A REAL-TIME MULTI-SENSOR 3D SURFACE SHAPE MEASUREMENT SYSTEM USING FRINGE ANALYSIS

MOHAMMAD SALEH MAHMOUD AL SA'D

A thesis submitted in partial fulfilment of the requirements of Liverpool John Moores University for the degree of Doctor of Philosophy

General Engineering Research Institute (GERI)
Liverpool John Moores University

April 2011

UNIVERSITY HAVE REQUESTED THE FOLLOWING ITEMS TO BE REDACTED

FIG 2.4 P14

FIG 5.2 & 5.3 P137

FIG 5.4 P138

FIG 5.6 P139

FIG 5.8 P140

FIG 5.9 P142

FIG 5.10 P143

FIG 5.12 P146

FIG 5.14 P150

FIG 5.17 & 5.18 P154

FIG 5.20 P155

TABLE 5.2 P157

To Japan who have been hit by the catastrophic earthquake and tsunami, and their subsequent devastation every waking day since March.

To my parents, who taught me that the real success in life is to be measured by the obstacles which I overcome while trying to succeed, and the utmost knowledge to have is that which is learnt for its own sake.

Abstract

A Real-Time Multi-Sensor 3D Surface Shape Measurement System Using Fringe Analysis

Mohammad Al Sa'd
Ph.D. Thesis

This thesis presents a state-of-the-art multi-sensor, 3D surface shape measurement system that is based upon fringe projection/analysis and which operates at speeds approaching real-time. The research programme was carried out as part of MEGURATH (www.megurath.org), a collaborative research project with the aim of improving the treatment of cancer by radiotherapy. The aim of this research programme was to develop a real-time, multi-sensor 3D surface shape measurement system that is based on fringe analysis, which provides the flexibility to choose from amongst several different fringe profilometry methods and to manipulate their settings interactively. The system has been designed specifically to measure dynamic 3D human body surface shape and to act as an enabling technology for the purpose of performing Metrology Guided Radiotherapy (MGRT). However, the system has a wide variety of other potential applications, including 3D modelling and visualisation, verbatim replication, reverse engineering and industrial inspection. It can also be used as a rapid prototyping tool for algorithm development and testing, within the field of fringe pattern profilometry.

The system that has been developed provides single, or multi-sensor, measurement modes that are adaptable to the specific requirements of a desired application. The multi-sensor mode can be useful for covering a larger measurement area, by providing a multi-viewpoint measurement. The overall measurement accuracy of the system is better than 0.5mm, with measurement speeds of up to 3 million XYZ points/second using the single-sensor mode and rising to up to 4.6 million XYZ points/second when measuring in parallel using the three sensor multi-sensor mode. In addition the system provides a wide-ranging catalogue of fringe profilometry methods and techniques, that enables the reconstruction of 3D information through an interactive user selection of 183 possible different paths of main combinations.

The research aspects behind the development of the system are presented in this thesis, along with the author's contribution to this field of research, which has included the provision of a comprehensive framework for producing such a novel optical profilometry system, and the specific techniques that were developed to fulfil the aims of this research programme. This mainly included the following advanced methods: a transversal calibration method for the optical system, an adaptive filtering technique for the Fourier Transform Profilometry (FTP) method, and a method to synthetically restore the locations of the triangulation spots. Similarly, potential applications for the system have been presented and feasibility and accuracy analyses have been conducted, presenting both qualitative and quantitative measurement results. To this end, the high robustness levels exhibited by the system have been demonstrated (in terms of adaptability, accuracy and measurement capability) by performing extensive real experiments and laboratory testing. Finally, a number of potential future system developments are described, with the intention of further extending the system capabilities.

Acknowledgements

The author wishes to express his deepest gratitude to his supervisory team, Dr. Francis Lilley, Professor David R. Burton and Dr. Munther Gdeisat. It would have been next to impossible to complete this work without their abundant help and invaluable guidance. Special thanks to Professor Michael J. Lalor for his gracious mentorship during this research programme.

Additionally, the author wishes to thank all the members of the General Engineering Research Institute for affording assistance and dialogue along the way and most importantly for providing a friendly atmosphere that is convivial to excellent research. Special thanks to Mohammad Qudeisat for his collaboration and untold hours of system calibration. Also, special thanks to Miss Helen Pottle for her continuous help.

Financially, the author would like to recognise the support of the Engineering and Physical Sciences Research Council and the National Institute for Health Research for funding the MEGURATH project and the NEAT programme, respectively. The author also wishes to convey thanks to the members of the Developing Technologies section at The Christie Hospital, especially Professor Christopher J Moore and Dr. Gareth Price, for their invaluable expertise in the subject of Metrology Guided Radiotherapy.

I would like to express my admiration to Dr. Saleh Al-Sa'ad, my father, who has always supported, encouraged and believed in me, in all my endeavours.

Finally, I would like to thank my friends, Dr. Mohammad Al-Awamleh, Dr. Amer Mofleh, Dr. Tayseer Al-Ahmad, Dr. Tareq AbuOrabi and Dr. Mohammad AlOun, for their encouragement and support.

Table of Contents

Chapter Four: Specifications and Applications of the System

Chapter Five: Hardware Design of the System

Chapter Six: Software Design of the System

Chapter Seven: Measurement Techniques and Algorithms

Chapter Eight: Experimental Results and Discussion

Chapter Nine: Conclusions and Recommendations for Further Work

Appendix

List of Figures

Chapter Two

Chapter Three

Chapter Four

Chapter Five

Chapter Six

Chapter Seven

Chapter Eight

Appendix

List of Tables

Chapter Two

Chapter Five

Chapter Seven

Chapter Eight

List of Abbreviations

1D-CWT	One-Dimensional Continuous Wavelet Transform
2D-CWT	Two-Dimensional Continuous Wavelet Transform
CBCT	Cone-Beam Computed Topography
CBI	Cone Beam Imaging
CCD	Charge Coupled Device
CMM	Coordinate Measuring Machine
CMOS	Complementary Metal Oxide Semiconductor
CMS	Central Measurement Server
CPU	Central Processing Unit
CSU	Camera Synchronisation Unit
CT	Computerised Tomography
CTV	Clinical Target Volume
CWL	Centre Wavelength
CWT	Continuous Wavelet Transform
DLP	Digital Light Processing
DMA	Direct Memory Access
DMD	Digital Micromirror Device
DWT	Discrete Wavelet Transform
FFT	Fast Fourier Transform
FIFO	First-In-First-Out
FL	Focal Length
FOV	Field Of View
FTP	Fourier Transform Profilometry
FWHM	Full Width At Half Maximum
GigE	Gigabit Ethernet
GPU	Graphics Processing Unit
GTV	Gross Tumour Volume
GUI	Graphical User Interface
GVSP	Gige Vision Stream Protocol
IDE	Integrated Development Environment
IGRT	Image Guided Radiotherapy

InSAR	Interferometric Synthetic Aperture Radar
LCD	Liquid Crystal Display
LCOS	Liquid Crystal On Silicon
LMS	Least Mean Square
LPC	Linear Prediction Coding
MeV	Mega Electron-Volt, 1 X 10^6 Ev
MGRT	Metrology Guided Radiotherapy
MLF	Multi-Leaf Collimator
MRI	Magnetic Resonance Imaging
OS	Operating System
PBS	Polarisation Beam Splitter
PCG	Preconditioned Conjugate Gradient
PMP	Phase Modulation Profilometry
PT	Peak Transmission
PTV	Planning Target Volume
RMSE	Root Mean Square Error
ROI	Region Of Interest
SDK	Software Development Kit
SNR	Signal-To-Noise Ratio
SPS	Spatial Phase Shifting
SPU	Sensor Processing Units
TCP	Transmission Control Protocol
TOF	Time-Of-Flight
TPS	Temporal Phase Shifting
UDP	User Datagram Protocol
USB	Universal Serial Bus
WD	Working Distance
WFT	Windowed Fourier Transform
WTP	Wavelet Transform Profilometry

Chapter One

Introduction

1.1 General Background

The reconstruction of 3D surface shape is an important and continuously developing subject that is applicable to many fields, including medical, design and manufacturing, heritage archiving, entertainment, etc. Optical profilometry methods that are based on fringe pattern projection are amongst the most advanced techniques and hold the highest potential and are becoming widely used nowadays. This is due to their associated advantages of high-resolution, full-field and non-contact measurement, high accuracy, fast measurement speeds, operational safety for both the operator and the scanned artefacts, and low setup costs. However, as they are optical techniques, it is obvious that regions of the object's surface that are invisible to the camera, or which are not exposed to illumination by the projector, cannot be measured. This is an inherent limitation of all optical profilometry methods. Moreover, nearly all current optical profilometry systems that are based on fringe analysis tend to be designed and optimised for a particular application using a single specific method of fringe analysis.

This thesis is concerned with the research aspects behind the development of a multi-sensor, 3D optical surface shape measurement system that is based upon fringe projection/analysis and which operates at speeds approaching real-time. It also demonstrates the system's potential value in that it can be applied to a variety of different applications. This optical profilometry system was designed to simultaneously measure surface shape by employing a multi-view measurement approach using three individual sensor units acting together cooperatively, in order to provide a greater area of measurement coverage for the object that is undergoing measurement. Because the fringe profilometry methods and techniques have their own distinct strengths and weaknesses, the system was designed to offer a selectable choice from within a broad set of profilometry methods and the ability to manipulate

their settings interactively. Thus, the measurement results can be optimised, in relation to the desired application-specific levels of accuracy and speed, by selecting the most appropriate combination of processing algorithms. This offers a multi-purpose profilometry system with a high degree of adaptability so as to fit the measurement requirements of various applications.

This research programme has formed part of the MEGURATH[1] project (EPSRC EP/D077702/1), in order to meet the functional requirements for surface reconstruction of the human body, in terms of robustness and speed, for the purpose of performing Metrology Guided Radiotherapy (MGRT). MEGURATH was a UK project, funded by the EPSRC and it built upon and extended the work that was accomplished in two previous European framework research projects INFOCUS[2] (EU FP4, BMH4950567) and ARROW[3] (EU FP4, BMH4983660) in order to create a new generation of 3D optical sensors for real-time monitoring of patient position during the delivery of radiotherapy treatments for cancer. The system that was developed as part of this research programme has subsequently been further developed by the author for another project called "A real-time visual feedback device for reducing patient movement during radiotherapy". The project is funded by the New and Emerging Applications of Technology (NEAT) programme from the National Institute for Health Research (NIHR). The further development of this work has focused on speeding up the measurement process, in order to provide patients with visual feedback information throughout their radiotherapy treatment session.

1.2 Brief Introduction to the System and its Applications

Various fields of research have been studied for the purpose of the design and development of the optical profilometry system that was produced during this research programme. Hence, a multi-disciplinary approach has been required in integrating and harmonising skills and knowledge sets from the various disciplines that are related to the design and development of such a profilometry system. This has included the following fields: optics, electronics, illumination, software development, human-computer interaction, and systems integration. The

[1] http://www.ljmu.ac.uk/GERI/MEGURATH.htm
[2] http://www.ljmu.ac.uk/GERI/INFOCUS.htm
[3] http://www.ljmu.ac.uk/GERI/arrow.htm

measurement system that is described here builds upon a culmination of over 25 years of combined knowledge and collaborative research that has been carried out at what is now the General Engineering Research Institute[4], in the fields of fringe pattern analysis, applied optics, precision measurement and computer vision.

The measurement system was designed to offer a high degree of adaptability in order to meet the requirements of various profilometry applications. This was achieved by providing a broad set of selectable fringe analysis methods and techniques, and the ability to manipulate their settings interactively. The system features the capability to measure both static and dynamic objects. It also features the ability to cover a significantly larger measurement field-of-view than that which would be offered by typical single-sensor profilometry systems, by using a multi-sensor measurement approach. The flexibility and high accuracy of the measurement system are demonstrated by extensive real experiments.

The author's contribution to this field of research included the provision of a comprehensive framework for producing such a novel optical profilometry system, and the specific techniques that were developed to fulfil the aims of this research programme. This mainly included the following advanced methods: a transversal calibration method for the optical system, an adaptive filtering technique for the Fourier Transform Profilometry (FTP) method, and a method to synthetically restore the locations of the triangulation spots.

The system has a wide set of potential applications, including medical, 3D modelling and visualisation, verbatim replication, reverse engineering, and industrial inspection. It can also be used as a rapid prototyping tool for algorithm development and testing, within the field of fringe pattern profilometry. Because this research programme has formed part of the MEGURATH project (www.megurath.org), significant effort was concentrated on the development of this system in order to meet the functional requirements of the 3D surface reconstruction of the human body that is necessitated by Metrology Guided Radiotherapy (MGRT). This was delivered

[4] http://www.ljmu.ac.uk/GERI

in terms of high levels of robustness and speed for the real-time monitoring of patient position during the delivery of cancer treatment.

1.2.1 Background about Metrology Guided Radiotherapy

Nowadays, radiotherapy is a well-known and widely used method for cancer treatment. It is a localised treatment method, which may be used to destroy any cancer cells that were not removed after surgery, or to reduce the size of a large, inoperable tumour to a manageable size, thus enabling surgery. It may also be effectively used in combination with alternative techniques, such as chemotherapy.

Radiotherapy works by delivering high-energy rays of ionising radiation to cancerous tissue. The energy from this radiation destroys the genetic material of the diseased cells, and subsequently prevents them from growing and dividing. Unfortunately, the radiation also destroys healthy cells, and so correct targeting of the radiation is very important. However, the normal cells are able to repair themselves to some degree at least, whereas the diseased cells are not as efficient in terms of their recovery to radiation insult. Thus, after a specific period of time, the healthy cells will have recovered, whilst the tumour cells will die.

The planning of 3D radiotherapy treatment is defined in the International Commission On Radiation Units And Measurements (ICRU) reports ICRU 50 and ICRU 62. Firstly, a Gross Tumour Volume, or GTV, is defined by a clinical professional to delineate the extent of the disease. Next a slightly larger Clinical Target Volume, or CTV, is defined by adding a margin, typically of several millimetres, to the external boundary of the GTV. This accounts for any micro-spread of the disease. When the treatment is actually planned, a further margin (called the Planning Target Volume, or PTV) is added to the boundary of the CTV (usually increasing the boundary again by several millimetres) in order to eradicate all of the cancerous cells within the target volume with a high probability of success. This margin needs to be sufficiently large to account for patient setup-errors and any patient movement that might occur during treatment (such as respiration). However, patient movement both during and between radiation fractions still can degrade the quality of the treatment, both by decreasing the radiation dose that is delivered to the

tumour target and increasing the dose which may be delivered to surrounding healthy tissue.

Image Guided Radiation Therapy (IGRT) combines a radiotherapy treatment machine, essentially a linear accelerator producing megavoltage X-Rays, with a kilovoltage X-Ray imaging system (recently using Cone-Beam Computed Topography, or CBCT). In the last few years, IGRT has been developed and is used directly prior to each treatment delivery session in order to reduce patient setup inaccuracies. Hence, if the patient is inaccurately positioned upon the treatment table, then positional corrections may be made such that the patient can be treated according to the pre-treatment planning regime. Yet, during actual irradiation there is no effective monitoring of any movement by the patient (either externally or internally), and detailed dynamics are not addressed explicitly.

The MEGURATH project aimed to use optical metrology to measure the position of a patient's body surface *during* treatment, and to use detailed and dynamic computer simulation to model internal organ motion from the known changes in the measured body surface. By using the 3D optical body surface measurement system that was developed for this research programme as an optical metrology device, it is possible to dynamically measure any motion of the patient's body surface that occurs during treatment. Consequently, by using the IGRT image volume that is acquired immediately before treatment and the 3D external body surface that is acquired via optical metrology during treatment, a dynamic deformation model can be generated. This dynamic deformation model can be linked to the treatment planning data and used as a radiobiological model in order to predicate complications for the treatment that was actually delivered to the patient. This field of research is known as Adaptive Radiotherapy (ART) and it can be used to accurately verify the radiation doses that are actually received by patients and also to adapt future treatment fractions so as to take into consideration any previous inaccuracies. Thus, an accurately adjusted PTV margin would spare healthy tissues surrounding the tumour and would simultaneously increase the probability of eradicating the tumour, ultimately enabling more aggressive treatments to be employed with correspondingly higher probabilities of success.

1.3 Structure and Aims of the Thesis

The aim of this research programme was to devise a real-time, multi-sensor 3D surface shape measurement system that is based on fringe analysis. The system should provide flexibility in that it should be possible to choose from amongst several different fringe profilometry methods and it should also be possible to manipulate their settings interactively. The ultimate goal was to design the system in order to successfully measure dynamic 3D human body surface shape and such that the system would act as an enabling technology for the purpose of performing Metrology Guided Radiotherapy. For this application the system would necessarily have to be highly robust, in terms of both the nature of the algorithms that are used and the system hardware and optics, which must necessarily survive in such a harsh radiation environment. To this end, the adaptability, validity and high accuracy of the system have been demonstrated by performing extensive numbers of real experiments in addition to thorough laboratory testing. Similarly, other potential applications for the system have been presented, as will be detailed in Chapter Four. Feasibility and accuracy analyses have been conducted, presenting both qualitative and quantitative measurement results for the measurement system that has been developed in this programme of research, and these are described in Chapter Eight.

This chapter contains a background introduction to this research programme and also sets out the primary motivations behind this research. It includes a brief introduction to the system that was produced during this research program and its specific applications, but these are discussed at greater length in Chapter Four. It also states the aims and objectives of the research and lays down the structure of the thesis.

Chapter Two begins with a general review of non-invasive techniques for surface shape measurement and justifies the reasons behind adopting an optical fringe profilometry approach for this research. This is followed by a review of the different techniques that may be used to produce fringe patterns. Next, a comprehensive literature survey of the fringe analysis methods and the phase unwrapping algorithms that are used in the system is presented. Experimental analysis is presented as part of the comparisons between the adopted fringe analysis methods and phase unwrapping algorithms.

Until recently, in the great majority of the literature that is available in the field of fringe profilometry, an emphasis was placed solely upon the fringe analysis methods themselves and the associated phase unwrapping algorithms. Practically, unwrapped phase data is useless if it is not translated into real-world coordinates. In order to obtain this phase-to-coordinates mapping relationship, some form of camera-projector calibration method for the measurement system must be employed. Unfortunately, such calibration methods are complicated and are not adequately addressed by existing work in the literature. For these reasons and because a significant amount of effort was spent upon system calibration, an entire dedicated chapter was devoted to address this problem. Chapter Three describes the common approaches for camera-projector calibration of fringe projection measurement systems, and subsequently presents the calibration methods that have been designed and adopted for use in this system. The chapter starts with a review of the phase-to-height relationship and the relation between image plane coordinates and transverse spatial dimensions. Then it moves on to discuss the techniques for obtaining an absolute phase map from the relative phase maps that are typically produced by the phase unwrapping process. This is followed by detailed descriptions of the specific phase-to-height calibration method that was adopted for use in this measurement system and also the associated transversal calibration method that was developed here by the author.

The specifications of the system that has been produced during this research programme are reported as part of Chapter Four. This is followed by a quality assurance analysis to determine the degree of precision this system can practically offer, including repeatability, reproducibility and heat stability tests. Next, the role and significance of this system in the field of the Metrology Guided Radiotherapy is presented, along with a detailed description of the basic application problem. To demonstrate the flexibility and adaptability of the system, other potential applications (such as reverse engineering and 3D modelling) are reviewed and specific example measurements are presented.

Chapter Five describes the hardware architecture and physical geometry of the system. Choosing the specification of the sensor components (in this case a camera and projector pair) for any fringe profilometry system is an extremely significant

step. For this reason, Chapter Five starts with a review of the various currently available technologies that may be employed for digital fringe pattern projection and also for image capture, in terms of their functionality and their effectiveness for use in this system. Alongside this review, the formal specifications and the specific advantages of the various adopted hardware technologies are presented. Next, the mechanism is described that was adopted for minimising the level of crosstalk between the three individual sensors and the hardware synchronisation unit that was developed for the cameras is also described. The accuracy of the measurements that are produced when using this measurement system are directly determined by both the frequency of the structured lighting fringe patterns and also by the degree of precision associated with the components that are used in system calibration. Hence, the chapter ends with a detailed description of the hardware that was used for system calibration, including the custom elevator table that was designed and built specifically for the calibration of this system.

In spite of the high importance that must be placed upon selecting the right hardware components for building an optical-metrology system, it is the processing software that is considered to be the heart of every vision system. Hence, the software development process that goes into the creation of such a system was a significantly challenging task. Considerable effort was expended here, chiefly by way of optimising the measurement algorithms and in efficiently utilising the processing power that is afforded by any specific system computing hardware. Chapter Six presents the software developmental aspects of the system that was produced by the author during this research programme. The development framework and the hierarchy of the system software are reviewed in this chapter, along with the software engineering techniques that were employed. Also, the various programming languages and libraries that were used are discussed.

Chapter Seven introduces the various algorithms and fringe profilometry techniques that were either researched as part of this work programme in the form of completely novel techniques, or alternatively that were adopted from existing approaches that were developed, extended and optimised by the author. These included the solution for coping with the non-linear projection response of the projector, the pre-processing techniques that were applied prior to carrying out the fringe analysis

methods, and the proposed novel adaptive filter for the Fourier Transform Profilometry (FTP) method. The chapter also reviews the overall measurement procedure that is used for both the single- and multi-view measurement modes of this measurement system. Furthermore, the overall calibration procedure is reviewed in this chapter in detail.

Chapter Eight presents an exhaustive set of example measurement results that were produced using this profilometry system. The results are presented as a logical sequence of increasingly complex measurement targets. The chapter also presents an accuracy analysis for the proposed adaptive mode of the FTP method, and discusses the various sources of measurement errors and their respective significance. Later in the chapter the approaches that were used to increase the speed of surface measurement are considered.

Chapter Nine puts forth the conclusions that have been drawn from this programme of research. As a result of the findings that are detailed in this thesis, recommendations are subsequently made for any potential avenues of further research that are primarily aimed at improving the measurement system's robustness and measurement capabilities. In effect, the potential of the measurement system may be regarded as continually evolving, through a process of both technological advancements and the evolution of new techniques, in order to meet ever more stringent application demands, in terms of general robustness, speed and measurement capability.

1.4 Author's Publications

- Al Sa'd, M., Lilley, F., Burton, D. R., Lalor, M. J., Gdeisat, M., "**A Real-Time Multi-Sensor Optical System for Metrology Guided Radiotherapy**". Interdisciplinary Biomedicine: An International Conference on Shared Methods and Discoveries, 22-23 April 2010, San Jose, California, USA.
- Al Sa'd, M., Lilley, F., Burton, D. R., Lalor, M. J., Gdeisat, M., "**Intelligent Real-Time 3D Body Measurement System Using Fringe Analysis**". IOP Photon08 Conference, 26-29 August 2008, Heriot-Watt University, Edinburgh, UK.

Chapter Two

Review of Fringe Profilometry Techniques for Shape Surface Measurement

Fringe Profilometry techniques have been used for many years in various applications, including industrial inspection, reverse engineering, medical monitoring, artwork inspection, robot vision, target sensing and many others. The advantages of such techniques are the non-contact and full-field measurement, the low cost and the high speed in obtaining the three-dimensional information. This chapter provides an overview of 3D shape measurement using fringe profilometry techniques. It starts by generally reviewing the available optical 3D measurement methods, their characteristics and the influence of their specific working principles on the resultant measurement. Next fringe pattern generation methods are reviewed, along with their individual pros and cons. Finally, the most common fringe analysis techniques and phase unwrapping algorithms are discussed, both theoretically and experimentally, along with their respective advantages and disadvantages.

2.1 General Review of Non-Invasive Techniques for Shape Surface Measurement

A wide variety of 3D surface reconstruction systems and techniques have been developed (Rocchini *et al.*, 2001), they are principally categorised either under the groupings of contact, or non-contact methods. Contact measurement techniques have been used in industrial applications since 1960s (Peklenik and Kubo, 1968), however they suffer from some significant disadvantages, such as: slow performance, high cost of using mechanical arms and the impracticability of touching the object for many applications (Vanherzeele *et al.*, 2004). Non-contact techniques were developed in order to cope with these problems and they may be further divided into transmissive or reflective approaches. Transmissive technologies, such as Computer Tomography (CT) and Magnetic Resonance Imaging (MRI), usually provide tomographic internal section data for an object and are also able to provide significant material characteristics for the measured object like density, however they are limited to some specific applications due to their high setup costs, safety

considerations and low relative speeds of measurement. Reflective technologies use either optical or non-optical methods, a well-known example of the latter being Interferometric Synthetic Aperture Radar (InSAR), which uses non-visible radio waves from the electromagnetic spectrum in order to perform remote sensing. While reflective techniques use the light scattered from the object, measurement can be performed either in the presence of a dedicated source of illumination (active), or without such a dedicated light source (passive).

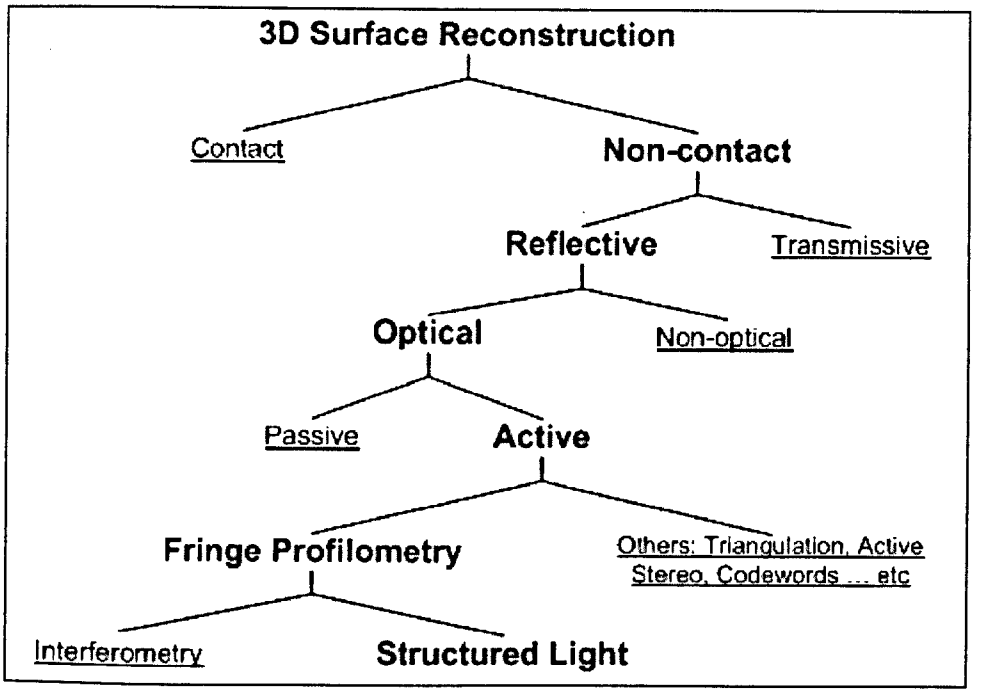

Figure 2.1 A general classification of surface profilometry techniques, showing the categories describing the system that was used in this research programme in bold.

In the passive approaches to reflective, non-contact measurement, the object is imaged by two or more cameras from different points of view (classical photogrammetry) and correspondences between the different images are found (Figure 2.2). The passive techniques suffer from the fact that they are sparse reconstruction problems, which complicates the process of finding correspondences when measuring surfaces with low levels of texture and easily recognisable features (Salvi *et al.*, 2010). On the other hand, active methods have been developed in order to provide denser spatial resolutions of measurement points and to give higher accuracy results. This is achieved by obtaining measurement information regardless of the presence, or absence, of any visual features on the object, and instead such methods depend on the additional information that is provided by the illumination source.

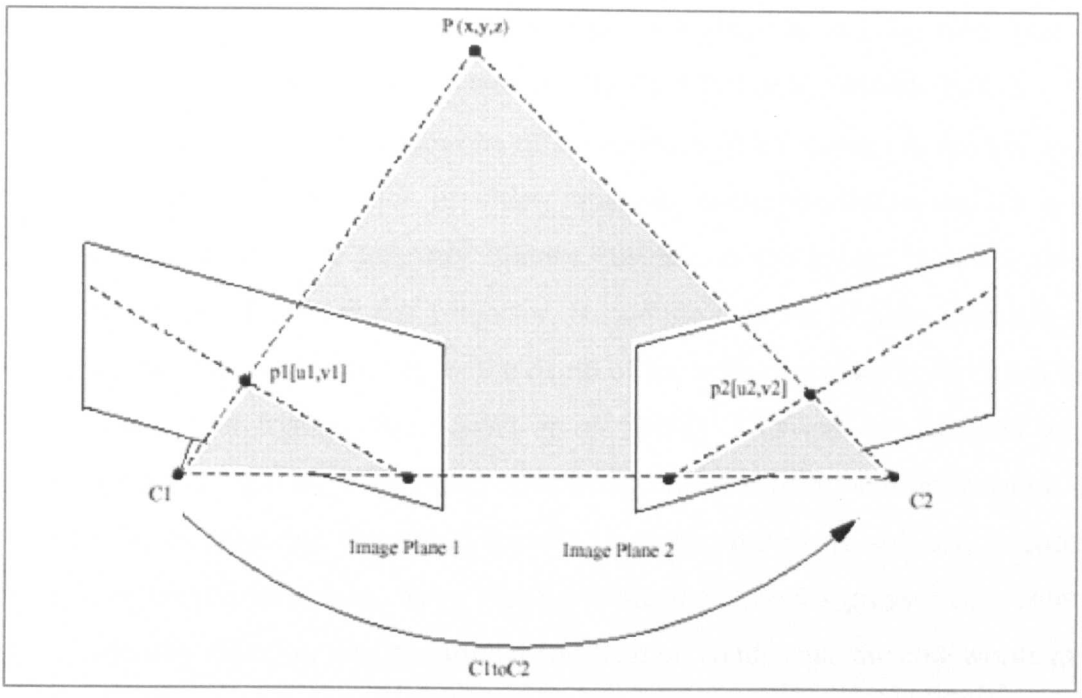

Figure 2.2 An example to demonstrate the passive stereo-vision technique.

The active optical approach is based on using a light source to emit some sort of known structured illumination that is projected upon the object to be measured. The illumination can be either coherent light (a laser beam) or incoherent light. Depending upon the nature of the projected light pattern (point-wise, stripe-wise or pattern-wise), the active optical profilometry techniques can be divided into two main streams: the scanning techniques and the full-field imaging techniques (Huang and Chiang, 1999). Scanning methods use either a point, or a stripe, typically of laser light, to measure depth based on the triangulation principle, where the relative positions of the emitter-sensor pair are already known. A Coordinate Measuring Machine (CMM) is a well-known example of a single laser point device, where a moving mechanical probe travels sequentially from point to point in order to synthesise the 3D shape, whereas for the case of stripe-based measurement methods (aka laser sheet-of-light techniques) there are some modern 3D cameras that can measure up to 329,000 profile points per second (Automation-Technology, 2008). However, it is necessary here to move either the camera-emitter pair, or the object, sequentially in order to generate the 3D shape of the whole object.

Laser scanning methods are insufficient in terms of measurement speed to allow dynamic shape monitoring. Full-field imaging techniques have been developed to overcome this measurement speed barrier, where it is feasible using some recently

developed methods to instantaneously measure 3D shape at a bandwidth that is determined by the frame rate of the camera. The main full-field methods include:

- Active stereo vision: where one of the cameras in the classic stereo vision is replaced by a projector in order to create correspondences and to give specific codewords to every unitary position in the image, given a fixed placement of camera and projector. Hence the location of any codeword on the measurement scene gives the depth of the subject surface based upon the principle of triangulation (Salvi *et al.*, 2003). This can be achieved with structured light by using either temporally encoded positional information of multiple projected patterns (Figure 2.3), or by employing spatially encoded positional information; using direct codification (pixel's greyscale or colour intensity value) or neighbourhood codification (represents the codewords in a unique pattern). Although the former gives the potential for dense 3D reconstruction, it has limitations when applied to measuring dynamic objects as it needs to project multiple frames of different patterns (Kawasaki *et al.*, 2008). Some researchers proposed using multiple cameras, together with structured light projection techniques. This eliminates the drawbacks associated with passive stereo vision due to a lack of corresponding points and also produces higher density reconstructions than the single camera and projector pair setup (Jecic and Drvar, 2003). However, stereo vision approaches still lack the capability to fulfil the accuracy demands of many applications, because the codewords are globally structured which makes it more complicated to map the corresponding coordinates of each pixel in the large patterns (Guan *et al.*, 2003).
- Time-of-Flight (TOF) sensors: which provide depth data at video frame rates by using the time-of-flight principle (Figure 2.4). A TOF camera actively illuminates a scene with an incoherent light signal (usually within the near infrared spectral range). The object's surface shape can be reconstructed by calculating the phase shift between the emitted and reflected signals at each pixel of the scene (Metrilus, 2009). Although this technology offers measurement that is independent of the object texture and can be performed at real-time speeds, the data markedly contains random and systematic measurement errors (Schuon *et al.*, 2008). Furthermore, currently available sensors provide only moderate resolutions (often limited to 320×240 pixels or fewer), which produces poor spatial resolution and makes the technology inappropriate for high quality 3D reconstruction.

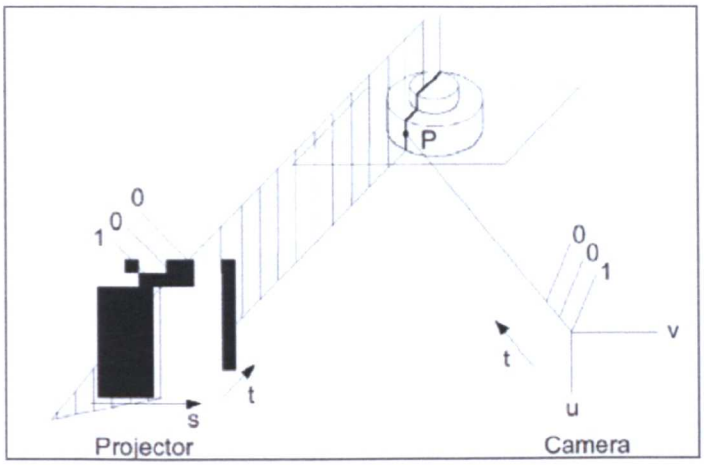

Figure 2.3 An example to demonstrate the temporally encoded stereo-vision technique (binary code-based); whereas set of patterns are projected onto the object's surface, the codeword for a given pixel is formed by the sequence of intensity values for that pixel across the projected patterns.

Figure 2.4 An example of shape reconstruction using a TOF camera (Schuon *et al.*, 2008).

- Fringe profilometry: also known as Phase Modulation Profilometry (PMP) depends on an optical heterodyne detection principle, whereby phase modulation and demodulation are utilised to accomplish the 3D surface measurement process. Basically, as illustrated in Figure 2.5, the phase is first constructed into a carrier with a sinusoidal intensity profile, constituting the source fringe pattern that is subsequently projected (using various methods which will be discussed further in Section 2.2) onto the object's surface. The object's 3D topography deforms the sinusoidal fringe pattern when viewed off-axis by phase modulating the fringe pattern with the 3D height information from the object's surface. Then the reflected intensity image of the phase modulated fringe pattern is grabbed by a camera and may be subsequently processed by demodulation in order to extract the phase

distribution (Zappa and Busca, 2009). Most techniques render discontinuities (wrapped modulo 2π) in the extracted phase, so phase unwrapping techniques (which are discussed in Section 2.4) are used to produce a continuous phase map (Zhou *et al.*, 2009). The height information is then calculated from the continuous phase distribution, either using simple triangulation or more complex phase-to-height relationship techniques (as discussed in Chapter Three) depending on the configuration of the measurement system and the complexity of the application. The interest in fringe profilometry techniques has been increased by the recent advances in pattern projection and image acquisition technologies (Zhang, 2010). The specific process that is used to determine the phase distribution is the main difference among the several fringe projection techniques (discussed in Section 2.3).

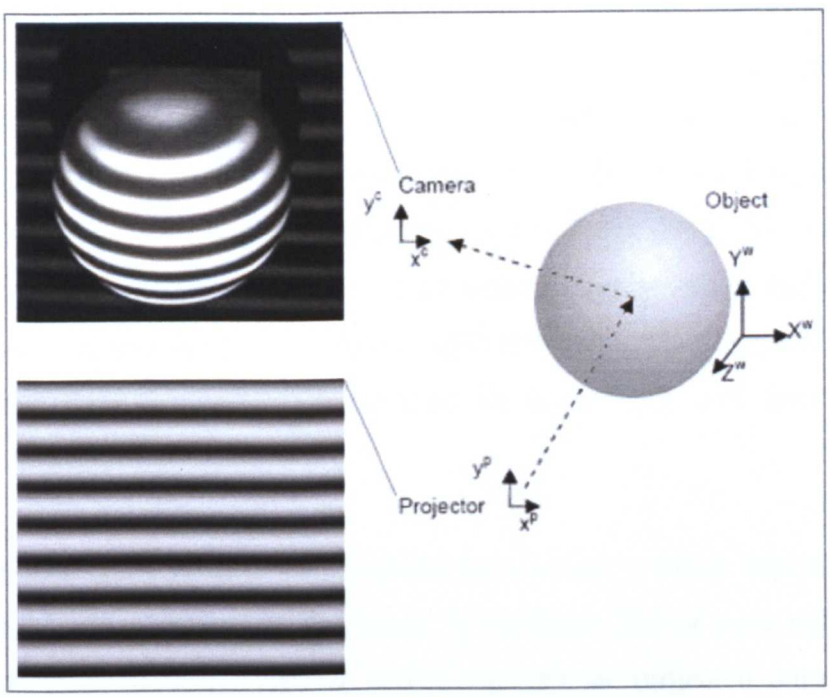

Figure 2.5 Illustration diagram for the fringe profilometry method.

Fringe profilometry techniques are the approach that has been adopted for the 3D shape reconstruction in this research programme. The justification for this lies in the fact that they can provide higher quality results than stereo vision or TOF, except in certain cases like the measurement of uneven surfaces that provoke shadowing and which render outliers due phase unwrapping problems (Su and Chen, 2001). Moreover, the maximum density resolution of the object's surface that can be measured depends on the characteristics of both the fringe generation device (the maximum spatial frequency) and of the image capture optics, as will be described in

detail in Chapter Five. Figure 2.6 illustrates the procedure of obtaining a reconstructed 3D surface measurement, based on the fringe profilometry techniques and algorithms that were employed as part of this programme of research. This illustration is adopted as a top level overview and reference resource showing the interconnectivity of the individual processing stages that will be described throughout the rest of the thesis.

2.2 The Generation of Fringe Patterns

Different techniques may be used to produce structured lighting patterns and, if these methods are to be utilisable in a fringe profilometry system, they should take into account and be customised to the specific measurement conditions associated with the particular application, such as: the surface characteristics of the measurement object (e.g. its reflectance and constituent features) and the circumstances of the measurement scene (e.g. the levels of ambient light, etc.). Modern camera technologies to some extent can cope with these conditions, which makes the process of obtaining accurate and reliable measurement results depend significantly upon the quality of the projected fringe patterns (Gorthi and Rastogi, 2010). The key methods of fringe pattern production include: laser interferometry, white light and laser grating projection approaches, and digital video projectors (Harding, 2009, Rocchini *et al.*, 2001). This section briefly reviews those methods and their respective advantages and disadvantages.

The first method to be reviewed uses optical inteferometry, which depends upon the principle of the interference of light waves. It combines two or more coherent light waves to produce the fringe pattern which can then be projected onto an object. Different approaches have been adopted to generate various shapes of fringe patterns, Figure 2.8 illustrates one of the common approaches (Young's experiment). To produce a fringe pattern, the method uses two separate apertures (P_1 and P_2) to divide the primary wavefront of the light beam (usually a laser) into two secondary beams.

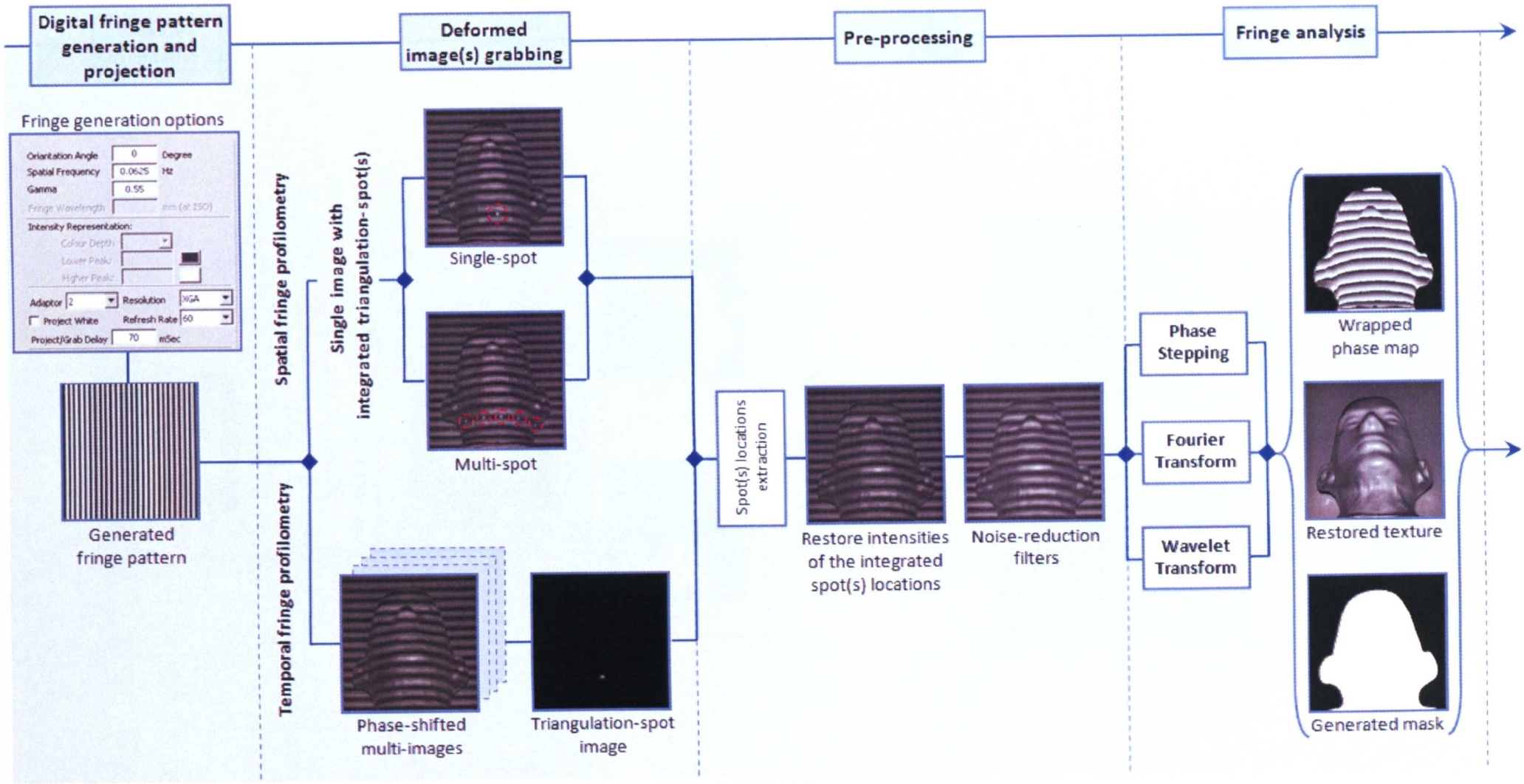

Figure 2.6 The workflow for the digital fringe profilometry algorithms and techniques, developed as part of this work. The rest of the diagram continues on the next page.

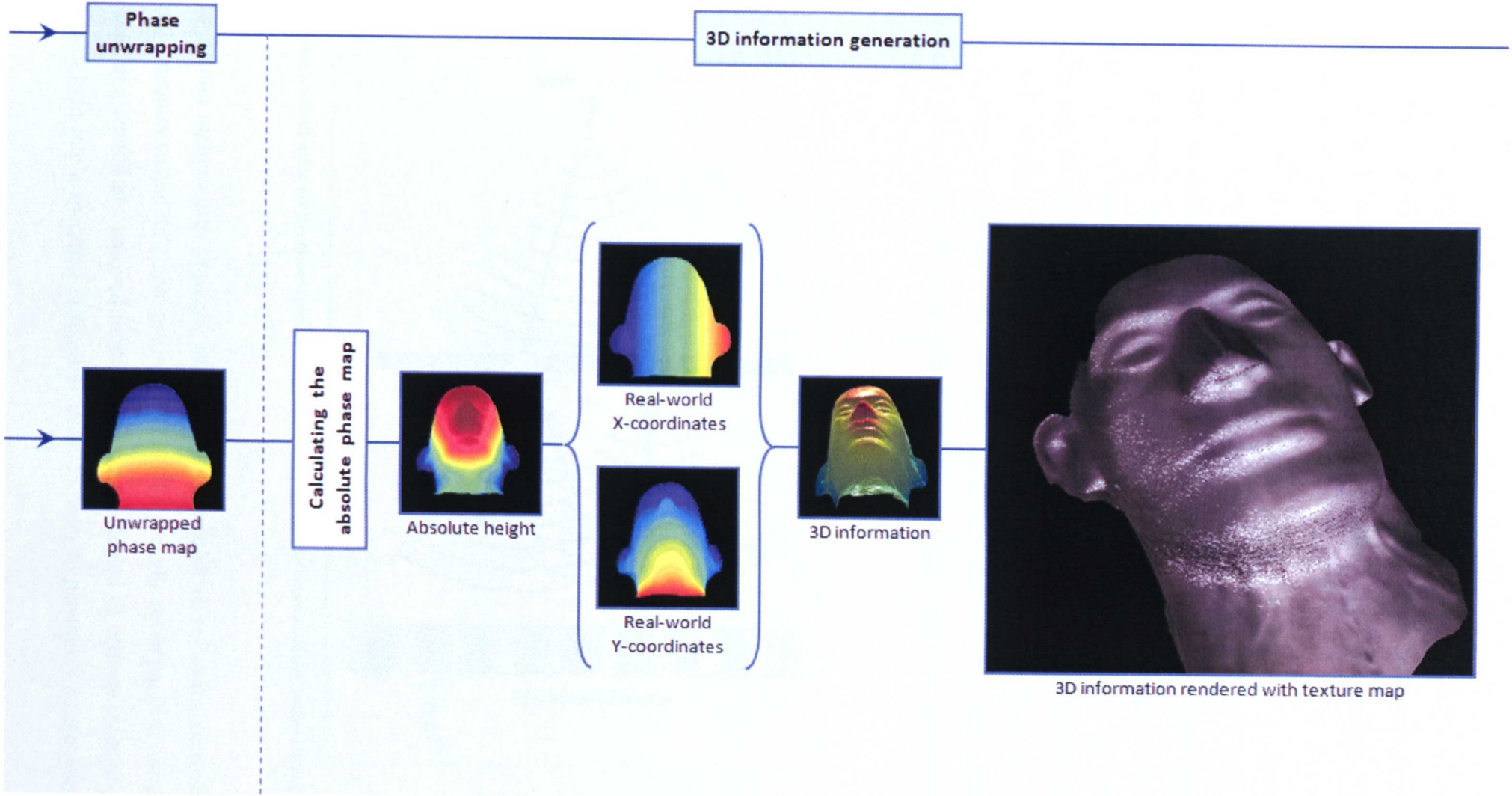

Figure 2.7 Continued from Figure 2.6.

The light waves passing through the apertures create an interference pattern of bright and dark bands in the far measurement field. The phase and spatial frequency of the generated fringes can be controlled by modifying the wavelength of the light source, the distance between the two apertures (either by a mechanical or an electronic actuator) or the distance between the measurement scene and the apertures (Robinson and Reid, 1993). Although this method is able to generate a very fine pattern with an unlimited depth of field, it also suffers from many disadvantages (Jecic and Drvar, 2003), such as: the stringent requirements for environmental stability make it impractical in many manufacturing applications, and the typical speckle noise associated with laser light gives rise to errors in phase measurement. Also, it is common with interferometric approaches that practical difficulties are likely to occur in providing the ideal beam geometry and also there are potential problems caused by self interference with reflected light from the measurement space.

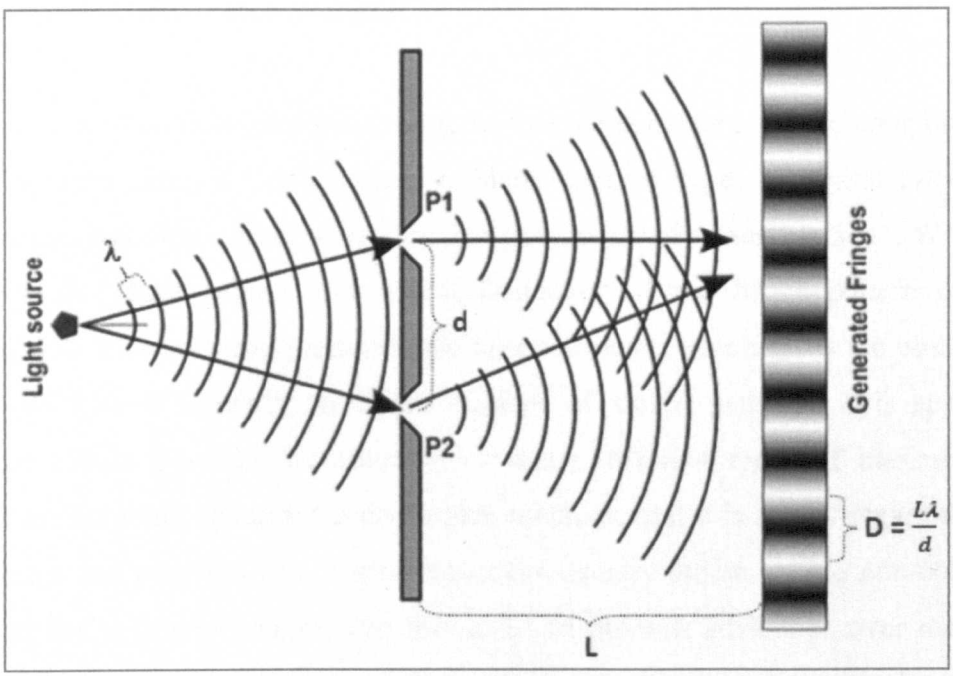

Figure 2.8 Illustration for the generation of fringe patterns using interferometry (Young's experiment).

The second method uses gratings, either using transparent or reflective substrates. Both transmissive and reflective gratings consist of a periodic set of parallel, closely-spaced and equidistant grooved lines, which can be shaped to diffract most of the incident light into a specified diffraction order. In order to generate a fringe pattern

either an incoherent (e.g. white light) or a coherent light source (e.g. laser) may be used. Several methods exist for fringe production using gratings, but typically the primary beam is spread into a line and then split into multiple lines using a grating to generate the fringe pattern (Hariharan, 2007). Specific line spacings may be fabricated in order to control the spatial frequency of the fringes, thus this method eliminates the complicated design requirements that are involved in the laser interferometry approaches when trying to obtain the specified spatial frequency. However, there are two main limitations of this method. The first lies in the difficulty of fabricating a very accurate grating, e.g. with a perfectly sinusoidal intensity profile, or with a consistent groove shape. The second drawback is the inflexibility of the technique in terms of it being very difficult to dynamically vary the phase and frequency of fringe pattern when using this method of fringe generation (Guo *et al.*, 2004). Harding (2009) also demonstrated that using a physical grating creates errors in phase calculations and the grating efficiency is primarily a function of groove shape.

The third method uses digital fringe patterns that are generated using a computer and then displayed using a video projector. Many specific types of digital projection technologies have been used, which are discussed in detail in Section 5.1.1. With this approach the shape, phase and spatial frequency of the fringe pattern can be manipulated arbitrarily and rapidly at the host computer, which gives the possibility to choose from a virtually unlimited number of varied patterns. This approach therefore makes possible the adoption of many different types of measurement technique, including advanced and complex methods, and it is in this regard that its true power and potential lies. Video projectors usually utilise visible non-coherent light sources (e.g. white light), and this gives an obvious advantage over the laser source of not producing speckle effects. However, the light intensity diminishes proportionally with the increased distance from the light source (Jecic and Drvar, 2003). In addition, the gamma nonlinearity of video projectors considerably decreases the accuracy of the measurement (Gorthi and Rastogi, 2010).

Taking into consideration the characteristics of the methods outlined above (and as summarised in Table 2.1), digital fringe pattern projection methods have been

adopted for use in this research programme. The effect of nonlinearity of video projectors is compensated for as is discussed in Section 7.2.1.

Method	Setup complexity	Quality of fringe pattern
Laser interferometry	high	suffers from speckles effect
Physical grating projection	moderate	hard to produce true sinusoidal waves
Video projectors	simple	suffers from gamma nonlinearity

Table 2.1 Brief comparison of the common fringe pattern generation methods.

2.3 Review of Fringe Pattern Analysis Methods

All fringe analysis methods share the core purpose of demodulating and extracting the phase signal, which has been modulated into the projected fringe pattern. These methods can be categorised into either spatial or temporal techniques. The methods adopted in the system, being used in this research programme, are not based on fringe skeletonising analysis (requiring fringe order identification or interpolation between the fringes), that are used in some holographic interferogram and Moiré fringe pattern methods (Ambrosini *et al.*, 2008, Zhang *et al.*, 2002). Accordingly, every pixel in the acquired fringe distribution image may give 3D information. This section reviews existing fringe analysis techniques and their characteristics. Finally, the implications of performing the specific process of demodulation using each method are discussed with regard to the quality of the final reconstructed 3D surface and these methods are also experimentally investigated.

2.3.1 Spatial Fringe Analysis

Spatial fringe analysis methods share the principle of extracting the phase spatially using various methods. Fundamentally, these methods need only one fringe distribution image (spatial carrier) to demodulate the phase information, which is separated across the image plane. A generalised equation for a captured fringe pattern for spatial fringe analysis (shown in Figure 2.9) may be expressed in the form:

$$I(x,y) = a(x,y) + b(x,y)\cos[\varphi(x,y) + 2\pi f_0 y] \quad \textbf{(2.1)}$$

where at each corresponding pixel $a(x, y)$ is a background intensity, $b(x, y)$ a fringe amplitude, f_0 is a spatial carrier frequency (which modulates the phase information along the y-axis), and $\varphi(x, y)$ is the unknown modulated phase signal that is to be determined. Coefficients a and b, and the φ should be slowly varying functions of x and y compared with the spatial carrier term $(2\pi f_0)$, which enables unique and monotonic determination of the phase value. Due to the periodic nature of the projected pattern, f_0 should be less than half of the sampling frequency (number of camera pixels) to satisfy the Nyquist rate condition and consequently to allow for a reliable phase demodulation (Takeda *et al.*, 1982). If the captured fringe pattern is projected orthogonally onto a plane surface, then a and b can be considered to be constant in each of the carrier fringe intervals (Moore and Mendoza-Santoyo, 1995). However, in this system due to the imposed system geometry, divergent and tilted fringes are used, hence a and b will not be constant. Besides, if the fringes are uniform across the image, then the phase φ is assumed to be linear across the y-axis in each interval.

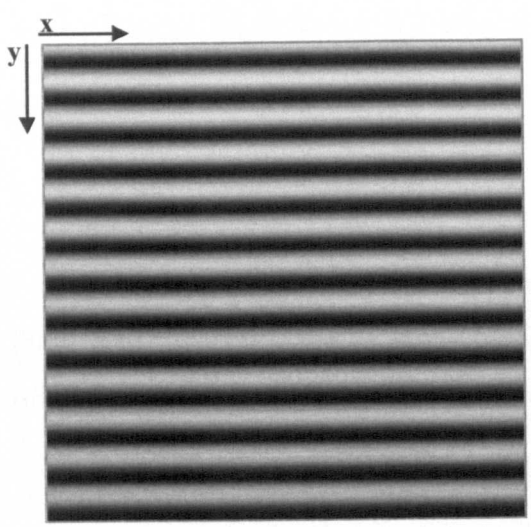

Figure 2.9 An example of a captured fringe distribution.

Due to the fact that the phase map is not directly accessible at each pixel (as it is in the case of temporal fringe analysis which is discussed in Section 2.3.2), the spatial fringe analysis techniques require more sophisticated processing than the temporal methods. The techniques that have been adopted for this system, within the spatial fringe analysis context, are the Fourier transform and Wavelet transform profilometry methods. The Windowed Fourier Transform (WFT) method (Qian,

2004) has been investigated by Huang *et al.* (2010), it surpasses the conventional Fourier transform method by producing better quality phase data (in terms of noise reduction). However, it has been excluded from the system that was developed during this programme of research as it requires long processing times, typically a matter of seconds or minutes (Qian, 2007) which makes it unfeasible for use in real-time measurement applications. Besides, the fact that the method uses a fixed window size is considered to be the main limitation of WFT (Yang *et al.*, 2009), hence it has been substituted for the wavelet transform profilometry method in this system.

2.3.1.1 Fourier Transform Profilometry (FTP)

Takeda *et al.* (1982) and Takeda and Mutoh (1983) proposed the 1D Fourier domain fringe analysis technique. Typically, to extract the phase the following process is carried out (this is illustrated schematically in Figure 2.10):

a. In the spatial domain, Equation (2.1) can be rewritten in the form:

$$I(x,y) = a(x,y) + c(x,y)\, e^{i2\pi f_0 y} + c^*(x,y)\, e^{-i2\pi f_0 y} \quad \textbf{(2.2)}$$

where * denotes a complex conjugate and

$$c(x,y) = \frac{1}{2}\, b(x,y)\, e^{i\varphi(x,y)} \quad \textbf{(2.3)}$$

Equation (2.2) may be transformed into the frequency domain by using the Fast Fourier Transform algorithm (FFT) with respect to the y-axis, which results in the following:

$$I(x,v) = A(x,v) + C(x,v - f_0) + C^*(x,v + f_0) \quad \textbf{(2.4)}$$

where A, C and C^* refer to the Fourier spectra, and v is the spatial frequency in the y-axis. The Fourier spectra in Equation (2.4) are separated by the carrier frequency f_0, provided that $a(x,y)$, $b(x,y)$ and $\varphi(x,y)$ are slowly varied compared with carrier frequency.

b. The phase component must be isolated in order to extract 3D shape information using some sort of filtering (e.g. Butterworth filter), where a filter $H(x,v)$ is used to select one of the two spectra on the carrier and filter out the unwanted background variation $a(x,y)$. Then the selected spectrum is frequency shifted by f_0 towards the origin to obtain $C(x,v)$. The spectral shift

by a distance f_0 in the frequency domain is equivalent to the subtraction of a linear component $2\pi f_0 y$ in the spatial domain.

c. The Inverse Fourier transform of the filtered and frequency shifted signal is then computed in order to obtain $c(x,y)$. Because the spectrum $C(x,v)$ is no longer symmetric about the origin, $c(x,y)$ has non-zero imaginary parts.. If the spectrum is not shifted in the frequency domain, then $c(x,y)$ will contain the carrier frequency $(2\pi f_0 y)$ (Moore and Mendoza-Santoyo, 1995).

d. The phase is calculated using the form:

$$\varphi(x,y) = \tan^{-1}\frac{Im[\mathrm{c(x,y)}\,]}{Re[\mathrm{c(x,y)}\,]} \qquad \textbf{(2.5)}$$

The resultant phase is called wrapped, as the arctangent function gives a principal value in the range -π to π. The continuous (true) phase can be obtained by using one of the phase unwrapping methods that will be discussed later in Section 2.4 of this chapter.

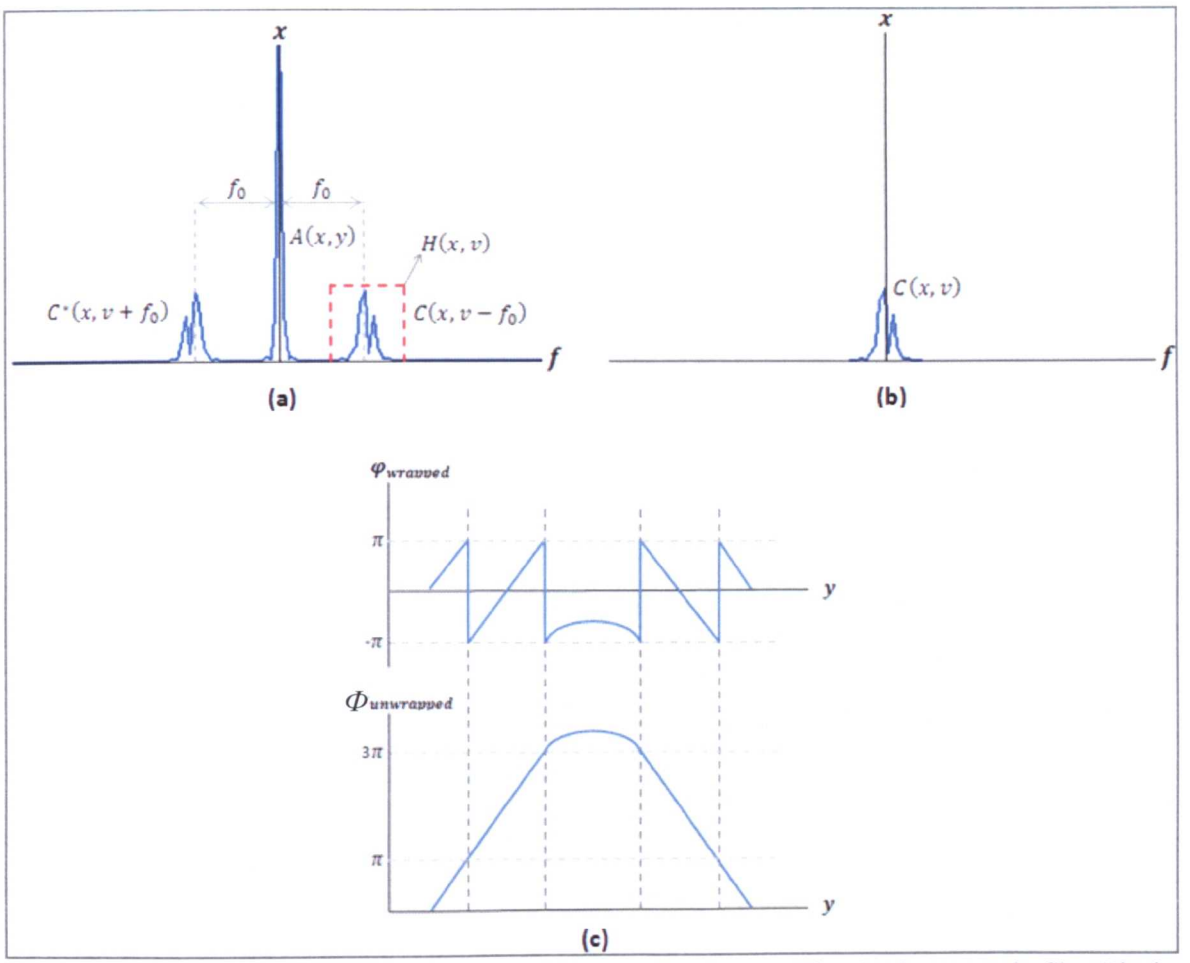

Figure 2.10 (a) Frequency spectra of a typical deformed fringe image, with a simple rectangular filter *H(x,v)* shown by the red dashed line. (b) the filtered and frequency shifted spectrum. (c) Calculated phase.

Various approaches have been researched that aimed to enhance the process of phase extraction using the conventional FTP method, and these may be summarised as follows:

- To provide an improved phase extraction process, with less noise, 1D analysis was extended to a 2D Fourier domain approach (Bone *et al.*, 1986, Lin and Xianyu, 1995).
- To increase the maximum measurable slope that was restricted by limitations of the sampling frequency and to reduce background noise, Guo et al. (1990) proposed the π-phase shifting FTP approach, which increased the measurable range of slope by three times. This method requires two fringe patterns to be projected upon the object, the second one being shifted by a half-period of the fringe spacing when compared to the first one. To retain the practical advantages that are usually associated with FTP, in that it only uses a single deformed fringe pattern for analysis, other approaches were proposed as a way of overcoming the requirement for a second captured frame in the π-phase shifting FTP method. One variation used two cameras to grab the measurement space from two-different angles (Hu and He, 2009), another approach combined patterns using colour (Chen *et al.*, 2006), and yet another used spatial frequency multiplexing like that illustrated in Figure 2.11 (Yue *et al.*, 2007).
- To measure objects that exhibit discontinuous height steps in their surface shape, Takeda et al. (1997) proposed using a spatial frequency multiplexing method.
- To measure dynamic objects and to reduce noise, Su et al (2001) proposed multiplying the spatial complex conjugate of the reference surface (or of the previous frame in the acquired sequence) by the spatial conjugate of the object being measured. Abdul-Rahman et al (2008) proposed using a single 3D volume for the analysis of dynamic objects (3D FFT and 3D filtering) not as a set of individual 2D frames. The 3D wrapped phase volume so obtained using 3D fringe analysis is equivalent in performance to the sequential 2D fringe analysis that was proposed by Su et al (Su and Zhang, 2010).

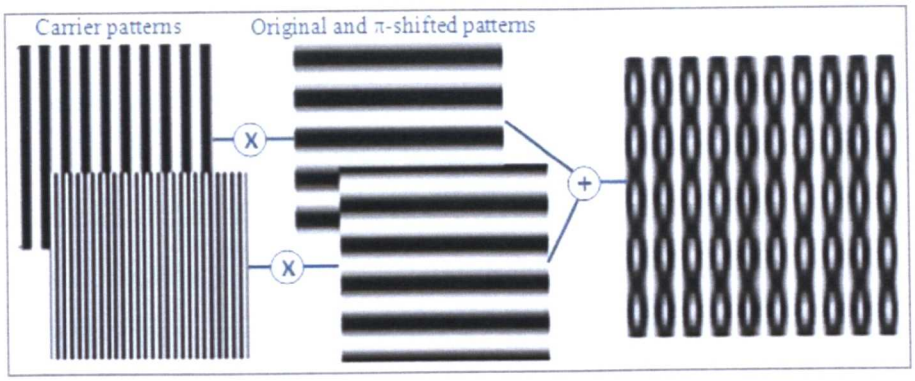

Figure 2.11 Frequency multiplexing approach used to decode the original and the π-shifted fringe patterns that are projected in a single pattern.

Nevertheless, the main challenge in the FTP process remains that of efficiently suppressing (filtering out) the background intensity signal $A(x, y)$, which in real-life measurement conditions normally overlaps with the fringe spectra in the frequency domain and thus makes it hard to isolate the modulated fringe phase signal. Common correlation filters used in the frequency domain are very sensitive to changes in their own parameters, and the presence of noise, which results in the production of regions with singularity neighbourhoods (regions of instability in the wrapped phase surrounding a phase singularity) appearing in the subsequent wrapped phase (Villa *et al.*, 1999). Consequently, the process of calculating continuous phase requires more robust and complicated unwrapping algorithms. Hence, different filtering techniques have been researched and these are summarised as follows:

- Lilley et al (2000) proposed subtracting the fringe distribution image from a fringe-free corresponding background image, which provides better component separation and filtration. However, this approach requires grabbing an additional image of the background data, which is disruptive and the pauses between fringe pattern acquisitions make it prone to introducing additional unwanted phase errors when measuring dynamic objects.
- To preclude disruptive pauses for collecting the background data of the above method, Moore et al (2001) proposed a method of extracting the background distribution data from the source fringe image using a randomised spread-based correction. However, any randomised processing may inescapably produce increased noise levels in the extracted background image. Chen et al (2005) proposed a method using the Windowed Fourier transform to extract the background distribution data and then subtracted it from the fringe data,

but this approach requires additional processing time which makes it impractical for dynamic measurement applications.

- Approaches were proposed using various filtration windows such as Hanning, Butterworth (Lilley *et al.*, 2000) and elliptical (Chen L.C. *et al.*, 2010) band-pass filter windows with manually adjustable parameters (i.e. cut-off frequency, bandwidth and n-order) that were required to be optimised for each object being measured. This approach introduces phase errors when measuring moving objects and lacks the flexibility required for measuring different objects, other than the one that was used to optimise the filter window. Besides this fact, with an optimal filter window, the phase errors that occur due to the random noise that is incorporated into the filter window are approximately equal to the errors that are produced due to the loss of filtered out information components (Bone *et al.*, 1986).
- Approaches were also proposed that sequentially applied filtering with adjustable parameters, an example being the use of regularised filters (Villa *et al.*, 1999). This approach, being iterative, needs additional processing time and these methods also still lack the capability to measure different objects whilst using a single set of filter parameters.

One more point that needs to be mentioned here, is that the FFT assumes that the data is continuous outside the finite block of data being transformed (Kujawinska and Wójciak, 1991). This assumption is satisfied if the sinusoidal image is periodic (i.e. having an integer number of fringes); if not then a frequency leakage effect will occur, which causes distortion and phase errors at the edges of the image (Perry and McKelvie, 1993). Whilst it is inflexible and impractical for many applications to grab an image containing an exactly integer number of fringes (i.e. a non-truncated fringe distribution pattern), a typical solution is that a windowing filter (e.g. Hamming, Hanning or Blackman) can be applied upon the spatial fringe pattern intensities prior to performing Fourier analysis (Vanherzeele *et al.*, 2008). Berryman et al (2004) studied the performance of applying different filters and concluded that the Blackman windowing filter gives the best results.

In this work, the 2D FFT is adopted and a state-of-the-art adaptive filter is researched providing an arbitrary determination of the information spectra (as will be discussed in Section 7.4.1).

2.3.1.2 Wavelet Transform Profilometry (WTP)

Using FTP with advanced adaptive filtration techniques is a powerful method for phase extraction. However, due to the nature of Fourier analysis, FTP performance is limited to images that contain stationary data. A stationary signal is a signal that repeats, i.e. its frequency contents do not change over time (Gonzalez and Woods, 2008). Fringe patterns tend to resemble non-stationary signals due the deformations caused by the shape of the object, which causes a frequency overlapping between the background signal and the fringe data. Consequently, this introduces phase errors when using FTP to filter out the background spectrum within the frequency domain (Zhong and Weng, 2004). Thus Wavelet transform profilometry (WTP) has been proposed by several researchers to overcome this problem (Watkins *et al.*, 1999, Afifi *et al.*, 2002, Ali *et al.*, 2004, Zhong and Weng, 2004).

Principally, wavelet analysis is used to divide a continuous signal into different multiple scale components (wavelet decomposition), where each component is assigned to a specific frequency range. The main reason behind the higher reliability of wavelet analysis when compared to standard FTP approaches lie in the fact that WTP deals with both time and frequency representations of a signal, whereas standard Fourier analysis only deals with frequency representation (Gonzalez and Woods, 2008). In the WTP technique, the continuous wavelet transform (CWT) is used to retrieve the phase map of a deformed fringe pattern, either using the one-dimensional continuous wavelet transform (1D-CWT) or the two-dimensional continuous wavelet transform (2D-CWT) (Gdeisat *et al.*, 2006b, Niu *et al.*, 2009). Gdeisat et al (2009) demonstrated that in most cases using the 1D-CWT is both more suitable and faster than using the 2D-CWT, unless low signal-to-noise ratios or slow phase variations are present in the deformed fringe pattern.

It is important to distinguish between the process of using wavelet analysis solely to extract the phase map and between the use of wavelet analysis in conjunction with

FTP. With the latter, wavelet analysis acts as a band-pass filter to extract and eliminate the zero spectrum, prior to the process of retrieving the phase using the FTP method. Gdeisat et al (2006a) used a 'Differential of Gaussian' as the mother wavelet for the 2D-CWT analysis process, with manual rotation and scale parameters that need to be determined for each object. To make the task of selecting those parameters more adaptive, Zhang et al (2009) proposed using the discrete wavelet transform (DWT) method.

The WTP method that was adopted for use in this system was the 1D-CWT analysis method, because the quality of the acquired fringe patterns are high and they are also free from speckle noise. Assuming that the orientation of the fringes in the images is vertical, the continuous wavelet transform of the fringe pattern is calculated on a row-by-row basis using a suitable mother-wavelet (e.g. Paul, Morlet or Shannon). Analysis using the Morlet mother-wavelet with a Gaussian window function is the technique adopted in this system for the WTP method, because the Morlet mother-wavelet provides superior localisation in both the spatial and frequency domains when compared to other mother wavelets and the Gaussian window type provides an optimal window shape (Ali *et al.*, 2004). The phase extraction process can be performed either by using the phase estimation, or by the phase gradient (frequency estimation) approaches. The phase estimation approach employs analytical mother wavelets to extract a phase signal that contains 2π discontinuities, which needs to be unwrapped in order to extract the true continuous phase. On the other hand, the phase gradient approach estimates and integrates the instantaneous frequencies in a fringe pattern in order to obtain the true continuous phase directly, without the need for unwrapping algorithms. In this system, the phase estimation method is adopted, as it offers higher quality phase measurement results in terms of noise performance (Gdeisat *et al.*, 2009).

The process of extracting the phase using the adopted WTP method (Figure 2.12) is summarised as follows (Abid *et al.*, 2008, Gdeisat *et al.*, 2009):

1. A Morlet mother-wavelet is generated, which is represented in complex form (the Fourier transformation produces zero values for the negative frequencies):

$$\varphi_M(x) = \pi^{-1/4}\, e^{i\omega_c x}\, e^{-mx^2} \tag{2.6}$$

where the first term ($\pi^{-1/4}$) is called the normalisation factor. The second term is the modulating harmonic signal with a centre frequency ω_c, which gives the number of oscillations of the Morlet wavelet within the Gaussian window. ω_c is chosen to be in the range 5-6, to satisfy the admissibility condition of the wavelet transform (i.e. the average of the wavelet itself must be zero). And the third term is the Gaussian envelope, where m is the bandwidth parameter which determines the spatial and frequency resolutions of the mother-wavelet (Addison *et al.*, 2002).

2. Next daughter wavelets $\varphi_{s,b}(x)$ are calculated by translation on the x-axis by a distance 'b' and by dilation by a factor 's' of the complex mother-wavelet $\varphi_M(x)$:

$$\varphi_{s,b}(x) = \frac{1}{s}\,\varphi_M\left(\frac{x-b}{s}\right) \tag{2.7}$$

in the WTP analysis of this work, the scale factor s is represented as a vector that varies from a starting scale s_0 to an ending scale s_n with a step of 1, default values for s_0 and s_n are 1 and 64 respectively.

3. The CWT coefficients are calculated, using the phase estimation approach, by projecting the fringe pattern $f(x)$ (on a row-by-row basis) onto the daughter wavelets $\varphi_{s,b}(x)$:

$$W(s,b) = \frac{1}{\sqrt{s}}\int_{-\infty}^{\infty} \varphi_M^*\left(\frac{x-b}{s}\right) f(x)\, dx \tag{2.8}$$

4. The phase of the coefficients are calculated using:

$$\varphi(s,b) = tan^{-1}\left(\frac{Im[W(s,b)]}{Re[W(s,b)]}\right) \tag{2.9}$$

where *Re* and *Im* are the real and imaginary parts of the CWT coefficients, respectively.

5. Finally, the wrapped phase values for each row are extracted by detecting the ridges (either from the modulus of the complex data, or from the phase) of each column in $\varphi(s,b)$, then the true phase map is obtained using a phase unwrapping algorithm for the entire wrapped phase map. In this system, two

algorithms were adopted: the direct maximum and the cost function ridge detection algorithms. The direct maximum algorithm is faster than the cost function algorithm, however it does not perform well against high noise levels when analysing data with low signal-to-noise ratios. The analysis of the two approaches are as follows (Abid, 2008):

a. **The direct maximum:** the maximum value of each column in the modulus array is located and then the corresponding phase is chosen from the phase array. In the case of a fringe pattern with a low signal-to-noise ratio, it is very likely that the magnitude of the CWT signal that is produced by the noise will exceed that which is contributed by the signal itself. In such cases, this may result in the system computing the phase of the noise and erroneously regarding it as representing the accurate fringe phase.
b. **The cost function:** this is capable of dealing with higher levels of noise than the direct maximum approach, due to the generic assumption that the unwrapped phase and its derivative are continuous. Dynamic programming is used to look for a set of optimum ridge paths through the local maxima in the modulus of the CWT. By using the cost function these paths are evaluated and the ridges with the minimum final cost are extracted.

The CWT modulus has a maximum value when the daughter wavelet frequency is very close to the frequency of the fringe pattern data, hence the performance of the WFT greatly depends upon the correct selection of the appropriate combination of its parameters, which are: the Gaussian bandwidth parameter (m), the scale value (s) and the ridge extraction algorithm that is employed.

The WTP method, similarly to the FTP method, produces phase errors at the image edges (Gorthi and Lolla, 2005b). Many approaches have been proposed to improve the retrieved phase at the image edges. Gdeisat et al (2009) demonstrated that using a Linear Prediction Coding (LPC) approach, which was first suggested by Federico and Kaufmann (2002) to extrapolate the fringes at the left and right borders of a vertically oriented fringe pattern, produces better results than other approaches, such as using the zero padding.

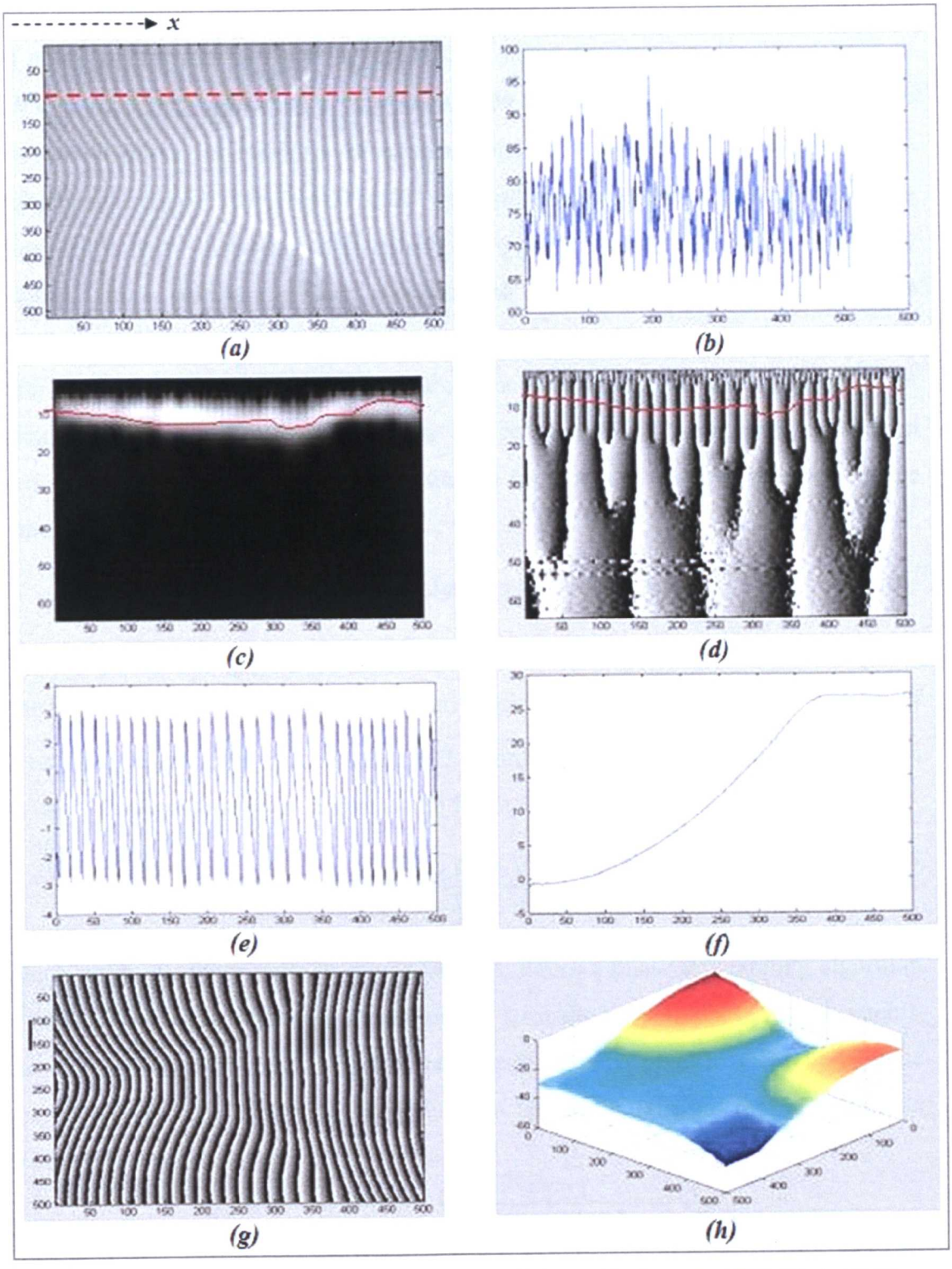

Figure 2.12 An illustrated example showing the process of phase extraction using WTP with the phase estimation method (Gdeisat, 2009): (a) a source fringe pattern, (b) intensity line plot of a selected row for demonstration purposes, (c) the path of the selected modulus of the 1D-CWT using a ridge extraction algorithm, (d) the extracted matching phase of the detected modulus, (e) extracted wrapped phase of the row, (f) the unwrapped phase of the row, (g) the entire wrapped phase map, (h) the entire unwrapped phase map.

2.3.2 Temporal Fringe Analysis

In phase modulation profilometry, temporal fringe analysis can be traced back to 1966 (Carré, 1966, Malacara *et al.*, 2005). This type of analysis directly extracts the modulated phase (in the form of wrapped phase, i.e. modulo 2π) by moving the reference wavefront with respect to the wavefront being analysed, thus introducing a phase difference. Measuring the intensity changes for various phase shifts drastically enables more accurate phase measurement than the spatial fringe methods (Yoshizawa, 2009). The fringe patterns are synchronously generated by correlating with sinusoidal signals of the same frequency and averaged over N periods of oscillation, such that N measurements are equally spaced over one modulation period. The acquired intensity distribution of horizontally oriented temporal fringe patterns can be represented in the form:

$$I_n(x,y) = I_0\{1 + \gamma(x,y)\cos[\varphi(x,y) + 2\pi f_0 y + \alpha_n]\} \quad \textbf{(2.10)}$$

where $n = 1,...,N$, I_0 is the background intensity, γ is the fringe visibility (modulation) and $\alpha_n = \frac{2\pi(n-1)}{N}$ is the known phase shift with respect to the origin. N is required to be larger than or equal to 3 in order to compute the phase distribution φ, using the least square technique in the form:

$$\varphi(x,y) = tan^{-1}\left[\frac{\sum_{n=1}^{N} I_n(x,y)\sin(\alpha_n)}{\sum_{n=1}^{N} I_n(x,y)\cos(\alpha_n)}\right] \quad \textbf{(2.11)}$$

which produces phase with 2π discontinuities, hence a phase unwrapping algorithm is needed to calculate the continuous phase. To make reliable phase measurements, the incident intensity must modulate sufficiently at each pixel to yield an accurate phase measurement. The fringe visibility can be calculated from the intensity data via the following equation:

$$\gamma(x,y) = \sqrt{\left(\sum_{n=1}^{N} I_n(x,y)\cos(\alpha_n)\right)^2 + \left(\sum_{n=1}^{N} I_n(x,y)\sin(\alpha_n)\right)^2} \quad \textbf{(2.12)}$$

The adopted phase shifting analyses that are used in this system depend on the number of required measurements N to calculate the phase and the fringe visibility, the equations of these methods are as follows:

a. **Three-frame technique:** two different phase shift values are employed using this method, either using $^{2\pi}/_{3}$ (120°) or $^{\pi}/_{2}$ (90°), for the first case when using 120° phase shifts:

$$\varphi = tan^{-1}\left(\sqrt{3}\frac{I_1 - I_3}{2I_2 - I_1 - I_3}\right) \tag{2.13}$$

$$\gamma = \sqrt{3(I_1 - I_3)^2 + (2I_2 - I_1 - I_3)^2} \tag{2.14}$$

and for the case when using 90° phase shifts:

$$\varphi = tan^{-1}\left(\frac{I_3 - I_2}{I_1 - I_2}\right) \tag{2.15}$$

$$\gamma = \sqrt{(I_3 - I_2)^2 + (I_1 - I_2)^2} \tag{2.16}$$

b. **Four-frame technique:** where a $^{\pi}/_{2}$ phase shift is used to give:

$$\varphi = tan^{-1}\left(\frac{I_4 - I_2}{I_1 - I_3}\right) \tag{2.17}$$

$$\gamma = \sqrt{(I_4 - I_2)^2 + (I_1 - I_3)^2} \tag{2.18}$$

c. **Five-frame technique:** where a $^{\pi}/_{2}$ phase shift is used to give:

$$\varphi = tan^{-1}\left[\frac{2(I_2 - I_4)}{2I_3 - I_5 - I_1}\right] \tag{2.19}$$

$$\gamma = \sqrt{[2(I_2 - I_4)]^2 + (2I_3 - I_5 - I_1)^2} \tag{2.20}$$

d. **Seven-frame technique:** where a $^{\pi}/_{3}$ (60°) phase shift is used to give:

$$\varphi = tan^{-1}\left[\frac{\sqrt{3}(I_2 + I_3 - I_5 - I_6) + (I_7 - I_1)/\sqrt{3}}{-I_1 - I_2 + I_3 + 2I_4 + I_5 - I_6 - I_7}\right] \tag{2.21}$$

$$\gamma = \sqrt{\left[\sqrt{3}(I_2 + I_3 - I_5 - I_6) + \frac{I_7 - I_1}{\sqrt{3}}\right]^2 + (-I_1 - I_2 + I_3 + 2I_4 + I_5 - I_6 - I_7)^2} \tag{2.22}$$

The process of extracting the phase is illustrated in Figure 2.13. Using digitally projected fringe patterns to perform phase shifting offers faster and more stable phase shifts than is the case for the classical inteferometry systems, as it does not

involve mechanical movements (Hu and Harding, 2007). However, video projectors tend to exhibit non-linearity in their response (as will be discussed in Section 7.2.1) which introduces phase errors into the measurement. With a higher number of measurements N, the effect of this non-linearity on the phase measurement is mitigated (Robinson and Reid, 1993). The three-frame techniques are found to be more prone to phase measurement errors, mainly due to the presence of second-order non-linearities (Yingsong, 2006).

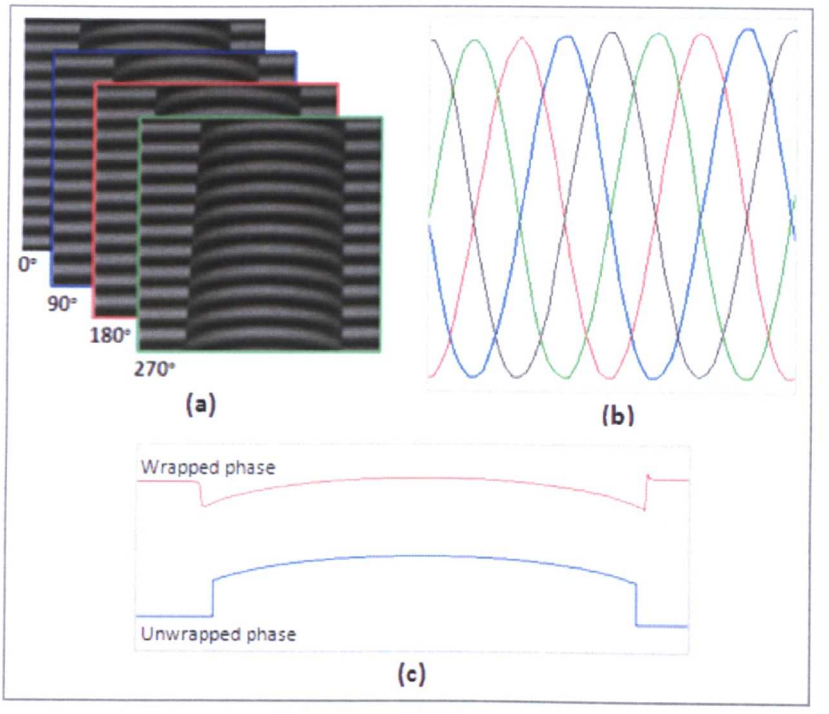

Figure 2.13 An illustrated example of temporal phase-shifting using the four-frame technique: (a) the grabbed four images, (b) vertical cross-section for the four images represented in a single plot to show the phase shift (90°), (c) horizontal cross-section for the extracted wrapped-phase and the unwrapped phase.

As the phase shifting technique depends locally on the intensity variation (phase deviation) at each pixel, it provides high precision and low sensitivity to noise in the measurements (Halioua and Liu, 1989). In addition, it is less sensitive to the image defocus problems that are associated with measuring objects that exhibit large depth variations (Huang *et al.*, 2005, Zhang and Yau, 2006). Using digital fringe projection to perform phase stepping on a fine scale, some researchers claim to achieve a measurement resolution of 50nm (Quan *et al.*, 2001). Furthermore, the texture of the surface can be restored simply by accumulating and averaging the N frames of the fringe images from each group of a fringe image series. To eliminate weak fringe

modulations, which may affect the behaviour and accuracy of the phase unwrapping process, a masking map can be generated depending on the calculated fringe visibility, with pixels below a certain visibility threshold being regarded as unreliable and hence being masked out from the resulting phase map.

Phase shifting profilometry can be employed either using temporal phase shifting (TPS) or using spatial phase shifting (SPS). In the TPS, multiple fringe patterns are sequentially projected onto the measurement space. While in the SPS, a single composite fringe pattern is used, which multiplexes the phase shifts either in colour space or in terms of frequency. The main SPS approaches that have been proposed to overcome the main drawback of the TPS methods, which is the requirement for the projection and capture of 3 or more patterns in order to achieve a measurement, are as follows:

- Chan et al (1995) suggested subdividing the fringe pattern into three component images, each with a different spatial carrier. Chan et al demonstrated that using this technique yields a loss of some local details, due to the reduction in resolution that is caused by the spatially divided original patterns. Consequently, the quality of the results obtained is of similar accuracy to that of results obtained by an equivalent system using FTP.
- Guan et al (2003) proposed combining the fringe patterns into a single composite pattern, as shown in Figure 2.14. Band-pass and low-pass filters are used to decode the original fringe patterns in the frequency domain. However, the bandwidth is divided to hold four frames, which reduces the measurement accuracy. Besides, the frequency filtering increases the complexity of decoding the fringe patterns of shapes with abrupt depth variation.
- Other approaches have been proposed that use colour space to separate the individual patterns of the three-frame technique, where each pattern can be isolated independently from the others by considering only the red, green, or blue channels of the captured compound image. The main drawback of this method is the colour-coupling problem, which even when employing customised cameras (like 3CCD technology-based cameras with special colour separation filters) still lacks accuracy in separating the combined colours (Pan *et al.*, 2006). In addition, colour patterns introduce a strong

dependence on the object's surface properties, such as coloration and luminance.

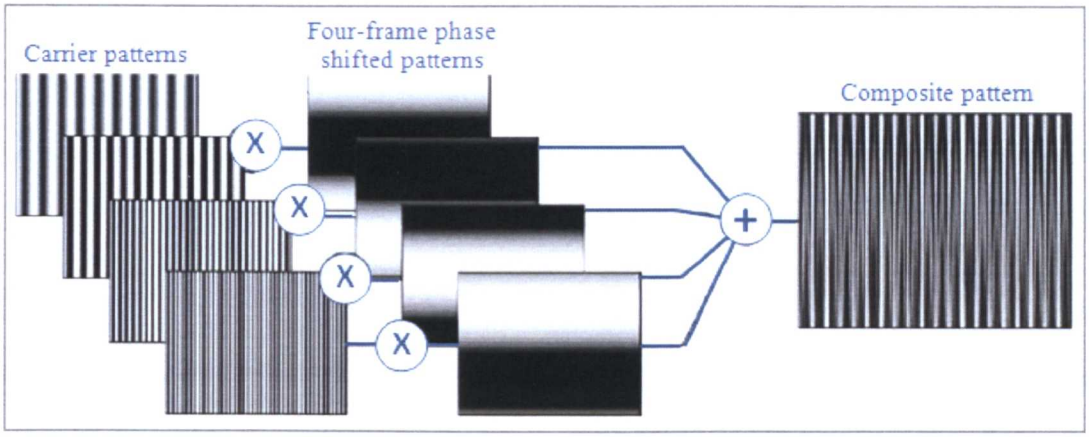

Figure 2.14 An illustration for SPS approach using frequency multiplexing.

Since the SPS approach requires an exact pixel-to-pixel correlation between the combined fringe patterns to form a single pattern, it is not an easy task to separate the deformed patterns of different object shapes, as the decoding process may require different filtration parameters for each object being analysed. In addition, this work depends upon a multi-view approach in order to cover the required large measurement field-of-view and does this by using three sensors (each fitted with chromatic filters in one of the primary colours in order to prevent any colour cross-talk between sensors). This makes it unfeasible to use the colour space approach for channel separation in the SPS method. Hence, only the TPS approach is adopted for this work.

2.3.3 Comparison between Different Fringe Pattern Analysis Techniques

The characteristics of the fringe profilometry techniques that have been described above differentiate the ability of each technique to fulfil the functional requirements of a specific measurement task. For instance, some temporal phase shifting (TPS) methods, particularly the more advanced error-compensating techniques, can enable more accurate measurement of the phase than is the case for both Fourier transform profilometry (FTP) and wavelet transform profilometry (WTP). They also provide simpler and faster computational loads for the analysis than is the case for FTP and WTP (Yoshizawa, 2009). The reason behind the more accurate phase measurement

using TPS is that it is locally dependant on each pixel (point-wise), whilst the spatial fringe analysis methods operate globally (Chan *et al.*, 1995). Analysing each pixel locally yields a higher measurement resolution (Zhu *et al.*, 2010a). On the other hand, analysing the fringe pattern globally has certain measurement implications, mainly due to the requirements for: a fringe pattern with higher spatial frequency than that required in TPS, a uniform fringe distribution (i.e. invariant light reflection by a test object), and more sophisticated processing. Hence, any inappropriate processing parameters for spatial fringe analysis techniques directly affect the extracted phase and produce incorrect results.

TPS techniques have another significant advantage over the FTP and WTP methods, which is the ability to simply generate both texture and mask maps for the object. By obtaining a binary mask, the mask can be employed to shorten the unwrapping process and to avoid errors that would result from noisy regions in the unwrapped phase. This is performed by tagging the valid unwrapping areas to avoid the phase unwrapping calculations in the invalid areas (Chen *et al.*, 2006). Berryman et al (2003) demonstrated that using the FTP method produces better results than TPS for simulated digital images with 10% or more added noise, Hu and Harding (2007) demonstrated that their modified three-frame TPS produces the best results in a real life application.

However, TPS techniques also have very significant drawbacks for certain applications. They need at least three fringe patterns to be captured in order to accomplish a measurement, which makes them infeasible when measuring dynamic objects, because subject motion introduces errors into the measurement during the multi-pattern scan process (Kreis, 1993). Thus, in this work the lack of dynamic operation by TPS was a major consideration and so TPS is only adopted for measuring static objects, while FTP and WTP have been adopted to perform measurements upon dynamically moving objects, because these methods only require the acquisition of a single fringe pattern. The WTP technique yields more accurate phase results than the FTP method, as it is more resistant to noise. Nevertheless, FTP offers a faster process for phase demodulation (Vanherzeele *et al.*, 2004). Consequently, selecting the appropriate fringe analysis method (and its processing parameters) becomes a compromise between speed and accuracy to meet

the requirements of the specific application. Table 2.2 summarises the main characteristics of the fringe analysis techniques adopted for use in this system (Kreis, 1993, Perry and McKelvie, 1993, Berryman *et al.*, 2003, Hu and Harding, 2007, Huang *et al.*, 2010, Quan *et al.*, 2010).

For FTP, texture and mask maps of the analysed object can be indirectly generated, by filtering out fringe data in the frequency domain and applying an inverse Fourier transform upon the rest of the data to get the texture map, then applying thresholding to generate the mask map. However, the restored texture image is blurred (due to the filtration process) and thus the mask data is not accurate. This will be discussed in further detail in Chapter Seven.

	FTP	WTP	TPS
No. of fringe patterns	1	1	≥3
Processing time	Short	Medium	Short
Ability to eliminate background	Low	Medium	High
Texture map	Possible but blurred	N/A	Simple and accurate
Mask map	Possible but not accurate	N/A	Simple and accurate

Table 2.2 A comparison of phase retrieval methods.

An experimental comparison was performed using the system that was developed during this programme, to demonstrate the strengths and the weaknesses of each of the fringe profilometry techniques used and their influence on the reconstructed 3D height information. The comparison is analysed in terms of both qualitative and quantitative height information metrics. Annotations for the implementations of the methods are as follows:

- The size of the images acquired in all cases was 512×512 pixels, with a bit depth equal to 8bits.
- Spatial frequency: $f_0 = 0.0625$ (such that the fringe period is 16 pixels).
- Unwrapping algorithm: using the reliability ordering technique by Herráez et al (2002).
- Phase-to-height conversion: using the adopted phase-to-height interpolation method (which will be described in Chapter Three).

- The points around image within a 10 pixel border are excluded from the comparison, due to the boundary effect of the FTP and the WTP methods.
- A plastic resin breast cast that was produced by rapid-prototyping from accurate CT scan data from a volunteer patient, exhibiting realistic curvature and steep features (Figure 2.15), was used as a measurement object.
- The analysed object is situated in the centre of the image (Figure 2.16).
- The computer specifications used for this analysis is described in Section 5.2.

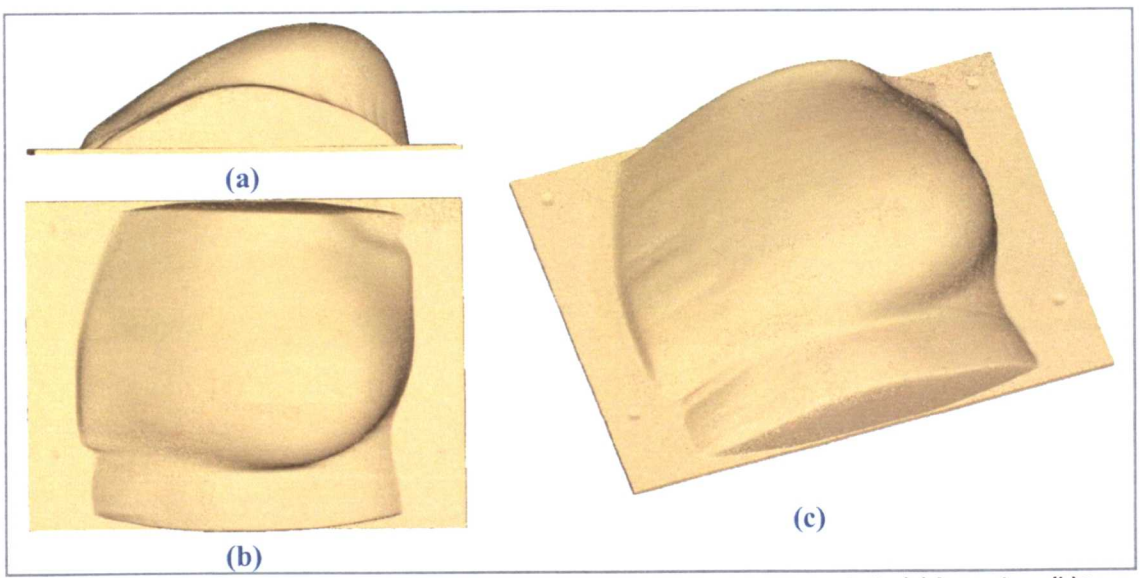

Figure 2.15 The breast phantom cast used for the comparative measurement analysis: (a) front view, (b) top view, (c) 3D isometric view.

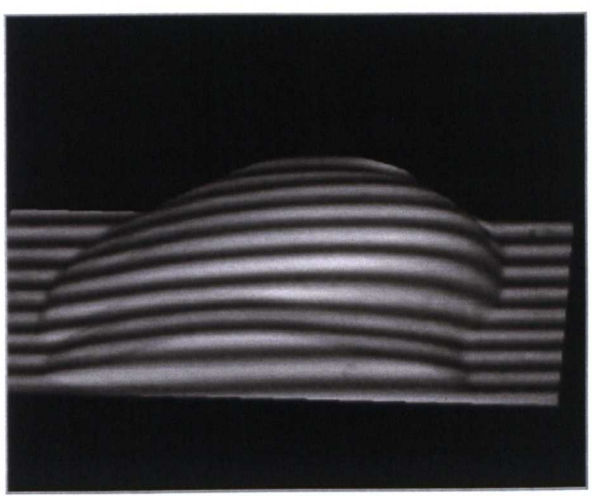

Figure 2.16 A captured image of a fringe pattern distribution projected upon the breast cast.

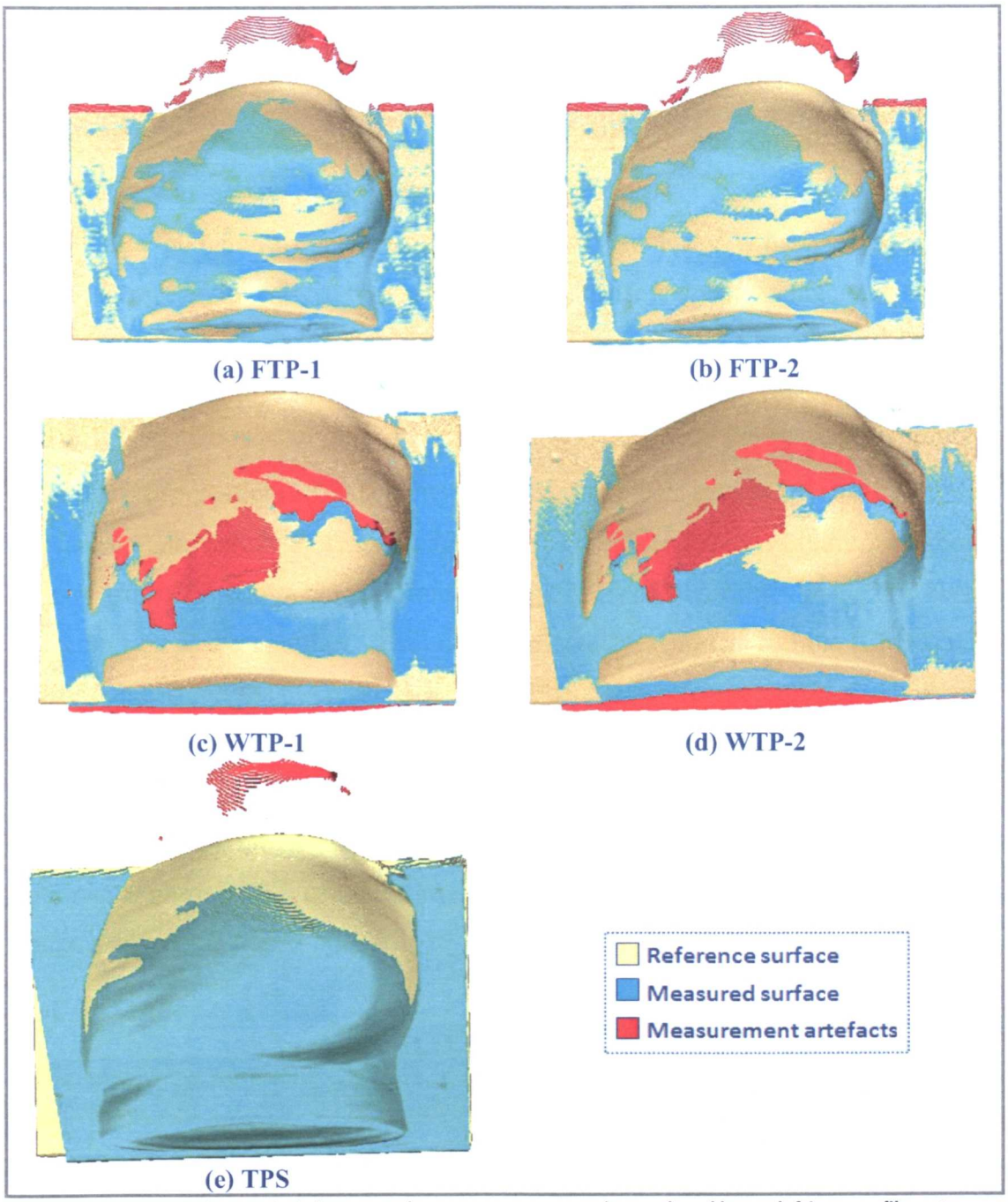

Figure 2.17 Deviation analysis between the measurement results produced by each fringe profilometry method and the real height information of the reference object.

The different methods that are being compared are defined below in terms of their specific processing parameters as follows:

- FTP-1: using FTP with Butterworth filter (Lilley *et al.*, 2000), filter parameters are selected for each object being analysed in order to minimise measurement error as far as possible (as described in Section 7.4.1).
- FTP-2: using FTP with the adaptive filter developed by the author (as described in Section 7.4.1.1).

- WTP-1: using WTP with the direct maximum ridge extraction approach, here the dilation vector s varies from 1 to 64 with a step of 1, and the bandwidth of the Gaussian envelope $m=1/2$.
- WTP-2: using the same parameters as in WTP-1, but instead using the cost function method for the ridge extraction process.
- TPS: as the influence of noise is noticeably alleviated if more phase-shifting frames are employed (Quan *et al.*, 2010), the four-frame technique is used for the TPS analysis, which is sufficient for suppressing the noise and the second harmonic artefact (Surrel, 1996).

Quantitative indications of the quality of the measurement results are used to express the measurement uncertainty using the methods compared above. Figure 2.17 shows a comparison of results from different fringe analysis algorithms using the breast phantom cast as a test object. A set of Coordinate Measuring Machine (CMM) data that was measured for the breast cast is used here as a reference surface, which was measured using an NVision 3D laser scanner with an overall measurement accuracy of 10 microns (NVision, 2008). The red colour represents the rendered measurement outliers, which are the points where the unwrapping algorithm failed to reconstruct a continuous phase result, using the wrapped phase that was generated by a particular fringe analysis method.

			The absolute height deviation from the reference surface			
Method	**Processing Time (ms)**	**RMSE[1] (mm)**	**Maximum (mm)**	**Average (mm)**	**PER[2] ≤0.5mm**	**PER[3] =0.0mm**
FTP-1	18	8.72	78.79	1.64	78.84%	1.59%
FTP-2	31	8.20	78.23	1.46	82.37%	1.89%
WTP-1	172	**5.66**	55.05	2.03	55.02%	0.58%
WTP-2	375	5.67	57.06	2.04	55.15%	0.59%
TPS	**15**	6.69	68.23	**0.89**	**93.50%**	**3.08%**

[1] RMSE is the root mean square error

[2] PER≤0.5mm is the percentage of points with deviation of 0.5mm or less from the reference surface

[3] PER=0.0mm is the percentage of points with deviation of 0.0mm from the reference surface

Table 2.3 Measurement results analysis produced by each fringe profilometry method.

The measurement results are shown in Table 2.3. Due to the presence of measurement artefacts, the percentage of number of points that lay within 0mm to

±0.5mm is the used here to represent the measurement accuracy. WTP methods result in the lowest RMSE and the lowest maximum error. However, this does not indicate the best measurement, as the percentage of number of points that lay within 0mm to ±0.5mm for WTP was only 55%. Hence, on this basis TPS is considered to produce the best results followed by FTP-2 and then FTP-1. It should be noted that although WTP algorithms are generally assumed to produce better results than FTP techniques in the presence of noise, this does not always hold true and is dependent upon the measurement object's surface topography. It is known that WTP approaches do not cope well with rapid phase variations in the sample data. It can be seen from the results presented here that the WTP methods have actually produced higher levels of error than the FTP algorithms. This is due to the rapid phase variations that are present in the sample data, which are caused by the steep curvatures present in the shape of the breast phantom measurement sample.

2.4 Review of Two-Dimensional Phase Unwrapping Techniques

The phase extracted using the above fringe analysis methods is indeterminate outside a range of 2π due to the fact that we are calculating the phase angle using the tangent trigonometric function, which gives a value ranging from $+\pi$ to $-\pi$. The resultant phase is called 'wrapped phase', or 'modulo 2π phase', which is in the general form of a sawtooth function (Figure 2.10c). In order to reconstruct the continuous (or true) phase, typically the phase discontinuities are located and a 2π value is then added, or subtracted, according to the sign of the phase change. In real-world applications false phase discontinuities might be detected due to the presence of corrupted data points (called *residues*) (Ghiglia and Pritt, 1998), which are caused by several factors, including: noise, phase discontinuities (such as holes and local shadows in the object's surface) and inconsistent phase gradients (such as rapid changes in the object's surface height and irregular surface brightness). Consequently, real phase jumps may become obscured and it is hard to distinguish between these and the false phase jumps. Hence, the reliability of a phase-unwrapping algorithm is determined by its ability to accurately detect the real phase jumps.

The phase unwrapping methods can be divided into path-dependent methods and path-independent methods. Path-dependent techniques are simpler than the path-

independent techniques. In the former, the unwrapping process involves scanning the wrapped phase map on a line-by-line basis to determine, and to compensate for, the modulo 2π jumps (Qian *et al.*, 2005). However, in the presence of noise (or surface defects) the errors in the resultant unwrapped phase propagate through the rest of the data and corrupt it (Gåsvik, 2003). Hence, only the path-independent techniques are adopted for use in the system being developed as part of this programme of research.

On the other hand, path-independent methods are where the phase is integrated along a pre-specified path (or series of paths). Typically, this path (or set of paths) is independently determined via scanning the wrapped phase data using a 3x3 window, to establish a relation between the phase value at the centre of the window and its neighbours, thereby identifying residues (Ghiglia and Romero, 1994). The key performance of this approach is dependent upon the technique that is chosen to establish the path(s) (Wu and Peng, 2006). Background information on the adopted phase unwrapping techniques for use in this work are reviewed in the following publications; (Judge and Bryanston-Cross, 1994, Ghiglia and Pritt, 1998, Karout, 2007, Zhu *et al.*, 2010b). The adopted algorithms are as follows:

A. Algorithms that use local integration, which involves integrating the wrapped phase data in a manner that is dependent upon the estimated phase gradients, travelling through a path starting from a certain point and then moving through all the rest of the pixels in the image. The Local integration phase unwrapping algorithms that have been adopted for use in this system are as follows:

   1. **Goldstein's branch-cut algorithm:** finds the residues within the wrapped phase data, and characterises them in terms of their polarity (which may be either positive or negative). Then, it locates close residues of the opposite polarity and connects the two residues together with a branch-cut line, thus joining each matched pair of residues via a separate set of branch cuts (thereby 'neutralising' the residues). These branch-cuts are then excluded from the unwrapping process, which can follow any path independently as long as it does not pass through a branch cut. This algorithm is the fastest among all those that are described in this thesis; however, it is limited to areas of wrapped phase data that contain only moderate residue densities.

Additionally, the incorrect selection of a single branch cut may cause errors to propagate over the whole data array.

2. **Quality-guided path following algorithm:** this depends upon a quality map that is produced for the wrapped phase data, which is generated using one of the methods that will be described later in this section. This method is a region growing method, which starts from a data point of highest quality and then moves on to unwrap the rest of the points in an order of descending quality, until it ends with the lowest quality point and in this manner prevents error propagation. As this method does not rely upon finding residues, the key success of its performance is directly dependent upon how accurately the quality map is generated.
3. **Reliability ordering algorithm:** this is analogous to the quality-guided path following algorithm, but it divides the data into regions (subsets of points) that are defined by the total reliability function of their edges. An edge is an intersection of two pixels that are connected horizontally or vertically. The reliability of an edge is defined as the summation of the reliabilities of the two pixels that the edge connects. Hence, an unwrapping path can be defined relative to the value of the reliability of the edges. Each region is then unwrapped in a descending reliability order until the region with the lowest reliability is reached.
4. **Flynn's minimum discontinuity algorithm:** which uses the quality map to guide the placement of every branch-cut. It starts from a point with a residue and follows the rest of the points with the lowest qualities until it finds another residue with an opposite polarity to form a branch-cut. The process is repeated until all the residues have been neutralised by branch-cuts, in order to unwrap as large as possible an area of the wrapped phase map. Because this algorithm relies on a quality map to find the branch-cuts, this can lead to a random and unpredictable arrangement of the branch-cuts, which is contrary to an intuitive view of where the branch cuts should lie.

B. Algorithms that use global integration, which formulate the unwrapping algorithm in terms of the minimisation of a global function, i.e. minimising the distance between the estimated phase gradient and the true gradient of the

yet undetermined unwrapped phase in both x and y directions. This can be performed by integrating over all the possible paths within the image, thus, smoother unwrapped phase data is produced than is the case when using local integration approaches. These algorithms are known to be more robust and accurate than the local integration algorithms, besides which, they produce an estimate of the unwrapped phase data that they fail to unwrap rather than simply returning an error as is the case when using the local methods. However, these methods are computationally more intensive and therefore are slower in terms of execution times than is the case for the local unwrapping algorithms. The global integration algorithms that have been adopted for use in this system are as follows:

1. **Weighted least-squares algorithm:** this uses a weighted least-squares method to minimise the distance between the phase gradient estimate (unwrapped phase) and the wrapped phase gradient, where the used weights are generated from quality maps. For this system, a preconditioned conjugate gradient (PCG) algorithm is adopted to iteratively solve the weighted least-squares problem. The main drawback of this method is the fact that if some residues are not masked out via the quality map, the resultant unwrapped phase will be severely corrupted. Moreover, PCG produces incongruent results (meaning that the unwrapped phase data are not phase matched to the wrapped data).
2. **L^p-Norm algorithm:** which uses a similar technique to the weighted least squares approach to minimise the difference between the phase gradients of the wrapped data and the gradients of the unwrapped phase result, however it computes the general minimum L^p-norm instead of the minimum L^2-norm. This method can generate data dependent weights, by computing the minimum L^p-norm where $p \neq 2$. These data dependent weights can efficiently eliminate the occurrence of residues within the resulting unwrapped data. This method can also optionally also use weights that are provided by a quality map in conjunction with the data dependant weights. This method is more robust than the weighted least-squares algorithm, however, it is highly computationally intensive and it can only find local minimums.

C. Algorithms that use both local and global integrations in a hybrid sense. These algorithms have been introduced to utilise the advantages of the above algorithms and aim to exclude their disadvantages. In essence, the result of using a global method at a given point is the average of all the solutions obtained by simple path-following (local method) radial paths from the point in question to the boundary. Several hybrid methods have been proposed, however, in this system only a single hybrid algorithm has been adopted:

1. **Synthesis algorithm:** this uses a local branch-cut algorithm in order to generate a mask of branch-cuts that may be used to balance all the residues within the wrapped phase data. This mask is zero-weighted and a zero-weighted quality map is added to it. Then, this compound mask is provided as a zero-weighted map to a globally weighted least-squares algorithm. Thus, all corrupted regions are masked out, which reduces the possibility of producing corrupted unwrapped data. Nevertheless, if the branch-cuts defining the zero weights are incorrectly placed, the phase error will be spread throughout the unwrapped phase data.

The majority of the above unwrapping techniques utilise quality map (or weight map) generation algorithms, to aid in isolating areas that are corrupted with residues. They do this by masking the residues out of the wrapped phase data to reduce their effect on the resulting unwrapped phase. Typically, quality maps are extracted from the wrapped phase data using general image processing techniques that are adapted for the phase unwrapping task. Quality maps are a vital factor in producing high quality results for the unwrapped phase and the performance of many advanced unwrapping algorithms relies heavily upon the efficiency of the quality maps that are employed (Karout, 2007). A quality mask can be generated by thresholding the quality map to exclude certain regions from the unwrapping process. In essence, different quality maps lead to different unwrapping results, yet, no single technique has been found that is able to automatically identify an optimal quality map for all cases (Ghiglia and Pritt, 1998). The quality map algorithms that have been adopted for use in this system are reviewed briefly as follows (Ghiglia and Pritt, 1998, Karout, 2007):

1. **Maximum phase gradient:** which measures the magnitude of the largest phase gradient (partial derivative or wrapped phase difference) in an m×m window, in order to indicate bad phase data.
2. **Phase derivative variance:** that calculates the statistical local variance of the wrapped phase derivatives in order to indicate bad phase data. It is considered to be the most reliable method for extracting the quality map from the wrapped phase.
3. **Pseudo correlation:** which attempts to mimic a correlation quality map estimate, but from the phase data itself, without the need for an extra set of data. It considers phase with uniform magnitude by using an m×m window, to indicate the good phase data.
4. **Second phase difference:** that uses the horizontal and vertical second differences of an m×m window to indicate bad phase data.

In addition, these algorithms can be combined together in order to provide more reliable quality maps (Su and Chen, 2004, Karout, 2007). The combinations that have been adopted in this system are:

1. Phase derivative variance and pseudo correlation methods.
2. Maximum of all quality maps.
3. Average of all quality maps.
4. Average of phase derivative variance and pseudo correlation methods.
5. Multiplication of all quality maps.
6. Minimum of all quality maps.

Finally, it is important to mention that there are other approaches that have been proposed that have the aim of over-riding the requirement for any phase unwrapping stage at all in the height recovery process, such as: using an additional colour coded pattern (Gorthi and Lolla, 2005a), or by using multiple fringe patterns with different spatial frequencies (Saldner and Huntley, 1997). Because these approaches unwrap the phase at each point independently over time, they are classified as temporal phase unwrapping methods, while the previously discussed approaches are classified as being spatial phase unwrapping methods. In the system that has been produced as part of this research programme, only spatial phase unwrapping approaches are employed.

2.4.1 Comparison among Phase Unwrapping Techniques

A general automated approach to the phase unwrapping in fringe analysis is considered to be impossible (Judge and Bryanston-Cross, 1994). To unwrap a distribution of wrapped phase data, that contains residue-rich regions, it is recommended to use global integration algorithms because they force unwrapping in these noisy regions, thereby providing estimates of the unwrapped phase data which are more accurate than that provided by the local methods. However, global integration algorithms are slower than local integration techniques, which makes them unsuitable for use in real-time applications (Zappa and Busca, 2008).

This section experimentally compares the unwrapping algorithms that have been adopted for this work, in terms of their performance and execution time. The comparison is analysed in terms of qualitative and quantitative metrics of the 3D height information that was produced by the measurements. These results are also compared against CMM measurements of the same object, rather than using synthetic images and using their known unwrapped data for comparison (Baldi *et al.*, 2002). Consequently, the behaviour of the phase unwrapping algorithms is studied according to their direct influence on the 3D height information that is output from the system. Another quantitative measure for comparison is to compare the unwrapped results against each other in terms of the number of remaining residues (or discontinuities) after unwrapping where the unwrapping algorithms have failed to obtain their unwrapped data. Parameters used in the implementations of the different unwrapping methods are for all cases as follows:

- The size of the images acquired was 512×512 pixels, with a bit depth equal to 8bits.
- Spatial frequency: $f_0 = 0.0625$ (such that the fringe period is 16 pixels).
- Fringe analysis technique: the phase was demodulated using the four-frame phase shifting technique, because it produces the most accurate wrapped phase results when compared to that produced by the FTP and the WTP methods, as was demonstrated in the previous section.
- The maximum phase gradient algorithm was used to generate the quality map for all unwrapping algorithms that depend upon weighted maps.

- Phase-to-height conversion: using the adopted phase-to-height interpolation method (as will be described in Chapter Three).
- The same plastic resin breast cast that was used in Section 2.3.3, exhibiting curvature and steep features (Figure 2.15), was used as the measurement object.
- The analysed object was situated in the centre of the image (Figure 2.18). A black electric cable was placed in the system's field of view over the object in order to provoke the production of residues and make the unwrapping task harder.
- The computer specifications used for the analysis is as described in Section 5.2.
- The algorithms have the following abbreviations:

GBC	Goldstein's branch-cut
QUG	Quality-guided
REL	Reliability ordering
FLN	Flynn's minimum discontinuity
PCG	Preconditioned conjugate gradient
LPN	Lp-Norm
SYN	Synthesis

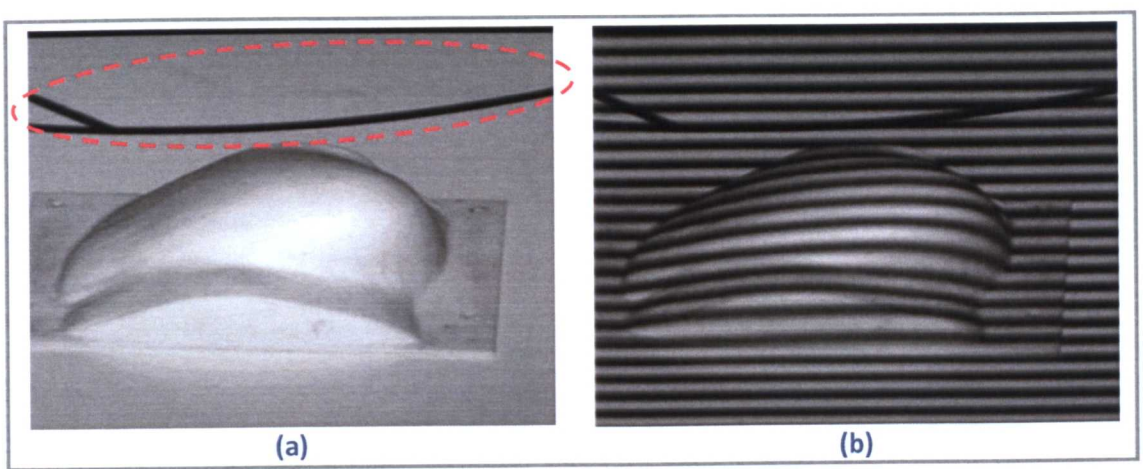

Figure 2.18 The analysed breast cast with a black electric cable present towards the top of the image to provoke residue production: (a) the texture image, (b) The captured fringe pattern distribution.

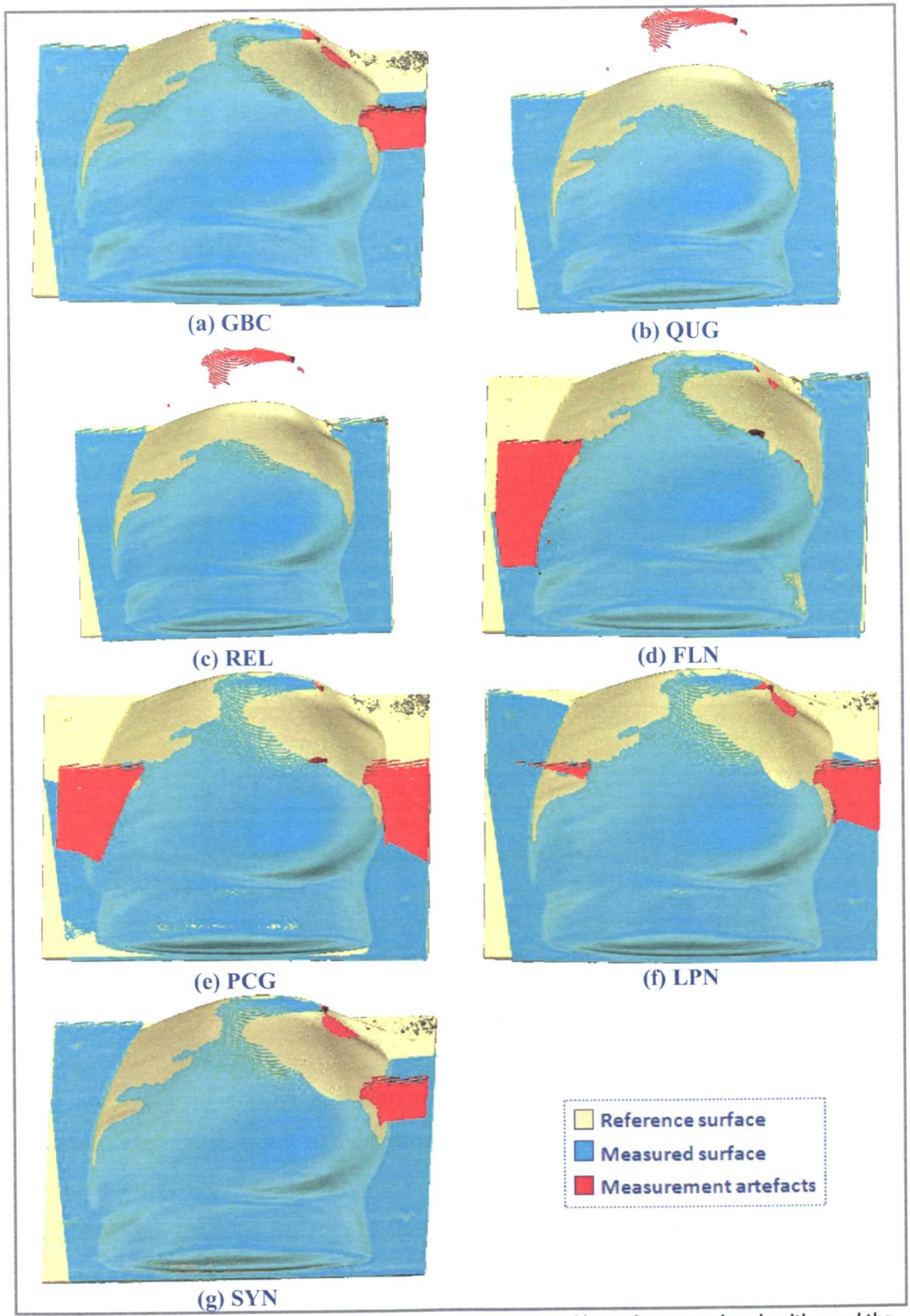

Figure 2.19 Deviation analysis between the measurements produced by each unwrapping algorithm and the real height information of the reference object as provided by CMM.

Figure 2.19 shows a comparison of results from different phase unwrapping algorithms using the breast phantom cast as a test object. Quantitative indications of the quality of the measurement results are used to express the uncertainty of measurement using the different algorithms listed above. A set of Coordinate Measuring Machine (CMM) data that was measured for the breast cast is used here as a reference surface, which was measured using an NVision 3D laser scanner with an overall measurement accuracy of 10 microns (NVision, 2008). The red colour represents the rendered measurement outliers, which are the points where the unwrapping algorithm failed to reconstruct a continuous phase result.

				The absolute height deviation from the reference surface			
Algorithm	**Processing Time[1] (ms)**	**2π jumps[2]**	**RMSE[3] (mm)**	**Maximum (mm)**	**Average (mm)**	**PER[4] ≤0.5mm**	**PER[5] =0.0mm**
GBC	**31**	153	**3.01**	40.46	**0.50**	92.61%	2.97%
QUG	234	**95**	6.69	68.21	0.89	**93.50%**	3.07%
REL	125	**95**	6.69	68.23	0.89	**93.50%**	**3.08%**
FLN	10953	113	3.95	**31.42**	1.03	88.26%	2.50%
PCG	1094	173	4.93	40.45	1.44	86.05%	2.35%
LPN	10281	249	3.49	40.49	0.67	91.40%	2.87%
SYN	965	153	**3.01**	40.47	**0.50**	92.62%	2.98%

[1] For the whole image (unwrapping process not masked)

[2] Number of points where the unwrapping algorithm failed to process the data

[3] RMSE is the root mean square error

[4] PER≤0.5mm is the percentage of points with deviation of 0.5mm or less from the reference surface

[5] PER=0.0mm is the percentage of points with deviation of 0.0mm from the reference surface

Table 2.4 Measurement results analysis produced by each phase unwrapping algorithm.

The measurement results are shown in Table 2.4, Goldstein's branch-cut and synthesis algorithms result in the lowest RMSE and average errors. However, this is not necessarily the best unwrapping result. Hence, the percentage number of points that lie within 0mm to ±0.5mm of the reference surface is used as a better indicator of the quality of the unwrapping process. Accordingly, the reliability-ordering and quality-guided algorithms commit less unwrapping errors and these also have the lowest number of 2π jumps.

2.5 Chapter Summary

This chapter has reviewed non-invasive techniques for 3D surface shape measurement and has concentrated upon fringe profilometry methods. The common methods of fringe pattern generation have been discussed, along with their respective advantages and drawbacks. Digital fringe pattern projection was selected as the fringe generation method that was to be used in the system being produced in this research programme, due to the significant advantage of its flexibility in being able to generate different patterns arbitrary and rapidly.

Three main fringe pattern analysis methods have been discussed, namely: FTP, WTP and TPS. These methods have been compared experimentally and as a result, TPS was shown to produce the best results (93.5% of the points of the tested sample are within ±0.5mm height deviation of the reference sample). However, due to its operational requirements for three, or more, different fringe patterns to be projected and captured, TPS is only used in the system for measurement of static objects. For the purpose of measuring dynamic objects, where the main interest lies in this research, FTP together with the adaptive filter that was developed by the author produced 82.37% of congruent points (±0.5mm) when compared to the height obtained independently using the 3D laser scanner for the object being analysed.

As the output of the fringe analysis methods is in the form of a modulo 2π wrapped phase distribution, some sort of phase unwrapping algorithm is required to recover the continuous phase. Various phase unwrapping algorithms have been reviewed and compared experimentally to demonstrate their robustness and processing speeds. Quantitatively, the quality-guided and reliability-ordering algorithms have shown that they produce the best results in terms of the maximum number of points of congruence with independently measured CMM data for the measurement object.

2.6 References

ABDUL-RAHMAN, H. S., GDEISAT, M. A., BURTON, D. R., LALOR, M. J., LILLEY, F. & ABID, A. 2008. Three-dimensional Fourier Fringe Analysis. *Optics and Lasers in Engineering,* 46, 446-455.

ABID, A. 2008. *Fringe Pattern Analysis Using Wavelet Transforms.* PhD Thesis, Liverpool John Moores University.

ABID, A. Z., GDEISAT, M. A., BURTON, D. R., LALOR, M. J., ABDUL-RAHMAN, H. S. & LILLEY, F. Year. Fringe pattern analysis using a one-dimensional modified Morlet continuous wavelet transform. *In:* SCHELKENS, P., EBRAHIMI, T., CRISTOBAL, G. & TRUCHETET, F., eds., 2008 Strasbourg, France. SPIE, 70000Q-6.

ADDISON, P. S., WATSON, J. N. & FENG, T. 2002. LOW-OSCILLATION COMPLEX WAVELETS. *Journal of Sound and Vibration,* 254, 733-762.

AFIFI, M., FASSI-FIHRI, A., MARJANE, M., NASSIM, K., SIDKI, M. & RACHAFI, S. 2002. Paul wavelet-based algorithm for optical phase distribution evaluation. *Optics Communications,* 211, 47-51.

ALI, D., SERHAT, Ö. & NECATI, E. F. 2004. Continuous wavelet transform analysis of projected fringe patterns. *Measurement Science and Technology,* 15, 1768.

AMBROSINI, D., PAOLETTI, D. & RASHIDNIA, N. 2008. Overview of diffusion measurements by optical techniques. *Optics and Lasers in Engineering,* 46, 852-864.

AUTOMATION-TECHNOLOGY. 2008. *3D sensors for three-dimensional high-speed measurement using the triangulation method* [Online]. Available: http://www.automationtechnology.de/cms/index.php?id=78&L=1 [Accessed 2 April 2010].

BALDI, A., BERTOLINO, F. & GINESU, F. 2002. On the performance of some unwrapping algorithms. *Optics and Lasers in Engineering,* 37, 313-330.

BERRYMAN, F., PYNSENT, P. & CUBILLO, J. 2003. A theoretical comparison of three fringe analysis methods for determining the three-dimensional shape of an object in the presence of noise. *Optics and Lasers in Engineering,* 39, 35-50.

BERRYMAN, F., PYNSENT, P. & CUBILLO, J. 2004. The effect of windowing in Fourier transform profilometry applied to noisy images. *Optics and Lasers in Engineering,* 41, 815-825.

BONE, D. J., BACHOR, H. A. & SANDEMAN, R. J. 1986. Fringe-pattern analysis using a 2-D Fourier transform. *Appl. Opt.,* 25, 1653-1660.

CARRÉ, P. 1966. Installation et utilisation du comparateur photoélectrique et interférentiel du Bureau International des Poids et Mesures. *Metrologia,* 2, 13.

CHAN, P. H., BRYANSTON-CROSS, P. J. & PARKER, S. C. 1995. Spatial phase stepping method of fringe-pattern analysis. *Optics and Lasers in Engineering,* 23, 343-354.

CHEN L.C., L.-C., HO, H.-W. & NGUYEN, X.-L. 2010. Fourier transform profilometry (FTP) using an innovative band-pass filter for accurate 3-D surface reconstruction. *Optics and Lasers in Engineering,* 48, 182-190.

CHEN, W., BU, P., ZHENG, S. & SU, X. 2006. Study on Fourier transforms profilometry based on bi-color projecting. *Optics & Laser Technology,* 39, 821-827.

CHEN, W., SU, X., CAO, Y., ZHANG, Q. & XIANG, L. 2005. Method for eliminating zero spectrum in Fourier transform profilometry. *Optics and Lasers in Engineering,* 43, 1267-1276.

FEDERICO, A. & KAUFMANN, G. H. 2002. Evaluation of the continuous wavelet transform method for the phase measurement of electronic speckle pattern interferometry fringes. *Optical Engineering,* 41, 3209-3216.

GÅSVIK, K. J. 2003. *Optical Metrology,* Chichester, Wiley.

GDEISAT, M. 2009. *Wavelet Transform Profilometry Using the Phase Estimation Method* [Online]. General Engineering Research Institute. Available: http://www.ljmu.ac.uk/GERI/98294.htm [Accessed 8 May 2010].

GDEISAT, M. A., ABID, A., BURTON, D. R., LALOR, M. J., LILLEY, F., MOORE, C. & QUDEISAT, M. 2009. Spatial and temporal carrier fringe pattern demodulation using the one-dimensional continuous wavelet transform: Recent progress, challenges, and suggested developments. *Optics and Lasers in Engineering,* 47, 1348-1361.

GDEISAT, M. A., BURTON, D. R. & LALOR, M. J. 2006a. Eliminating the zero spectrum in Fourier transform profilometry using a two-dimensional continuous wavelet transform. *Optics Communications,* 266, 482-489.

GDEISAT, M. A., BURTON, D. R. & LALOR, M. J. 2006b. Spatial carrier fringe pattern demodulation by use of a two-dimensional continuous wavelet transform. *Appl. Opt.,* 45, 8722-8732.

GHIGLIA, D. C. & PRITT, M. D. 1998. *Two dimensional phase unwrapping: theory, algorithm and software,* New York, Wiley.

GHIGLIA, D. C. & ROMERO, L. A. 1994. Robust two-dimensional weighted and unweighted phase unwrapping that uses fast transforms and iterative methods. *J. Opt. Soc. Am. A,* 11, 107-117.

GONZALEZ, R. C. & WOODS, R. E. 2008. *Digital Image Processing,* Prentice Hall.

GORTHI, S. S. & LOLLA, K. R. Year. A new approach for simple and rapid shape measurement of objects with surface discontinuities. *In:* OSTEN, W., GORECKI, C. & NOVAK, E. L., eds., 2005a Munich, Germany. SPIE, 184-194.

GORTHI, S. S. & LOLLA, K. R. 2005b. Wavelet Transform Analysis of Truncated Fringe Patterns in 3-D Surface Profilometry. *Optical Measurement Systems for Industrial Inspection IV* Bellingham, WA.

GORTHI, S. S. & RASTOGI, P. 2010. Fringe projection techniques: Whither we are? *Optics and Lasers in Engineering,* 48, 133-140.

GUAN, C., HASSEBROOK, L. & LAU, D. 2003. Composite structured light pattern for three-dimensional video. *Opt. Express,* 11, 406-417.

GUO, H., HE, H. & CHEN, M. 2004. Gamma Correction for Digital Fringe Projection Profilometry. *Appl. Opt.,* 43, 2906-2914.

GUO, L., SU, X. & LI, J. 1990. Improved Fourier transform profilometry for the automatic measurement of 3D object shapes. *Optical Engineering,* 29, 1439-1444.

HALIOUA, M. & LIU, H.-C. 1989. Optical three-dimensional sensing by phase measuring profilometry. *Optics and Lasers in Engineering,* 11, 185-215.

HARDING, K. Year. Comparison of projection means for structured light systems. *In:* HUANG, P. S., YOSHIZAWA, T. & HARDING, K. G., eds., 2009 San Diego, CA, USA. SPIE, 74320S-10.

HARIHARAN, P. 2007. *Basics of Interferometry,* Academic Press.

HERRÁEZ, M. A., BURTON, D. R., LALOR, M. J. & GDEISAT, M. A. 2002. Fast two-dimensional phase-unwrapping algorithm based on sorting by reliability following a noncontinuous path. *Appl. Opt.,* 41, 7437-7444.

HU, E. & HE, Y. 2009. Surface profile measurement of moving objects by using an improved [pi] phase-shifting Fourier transform profilometry. *Optics and Lasers in Engineering,* 47, 57-61.

HU, Q. & HARDING, K. G. 2007. Conversion from phase map to coordinate: Comparison among spatial carrier, Fourier transform, and phase shifting methods. *Optics and Lasers in Engineering,* 45, 342-348.

HUANG, L., KEMAO, Q., PAN, B. & ASUNDI, A. K. 2010. Comparison of Fourier transform, windowed Fourier transform, and wavelet transform methods for phase extraction from a single fringe pattern in fringe projection profilometry. *Optics and Lasers in Engineering,* 48, 141-148.

HUANG, P. S. & CHIANG, F.-P. Year. Recent advances in fringe projection technique for 3D shape measurement. *In:* CHA, S. S., BRYANSTON-CROSS, P. J. & MERCER, C. R., eds., 1999 Denver, CO, USA. SPIE, 132-142.

HUANG, P. S., ZHANG, S. & CHIANG, F.-P. 2005. Trapezoidal phase-shifting method for three-dimensional shape measurement. *Optical Engineering,* 44, 123601-8.

JECIC, S. & DRVAR, N. Year. The Assessment of Structured Light and Laser Scanning Methods in 3d Shape Measurements. *In:* The 4th International Congress of Croatian Society of Mechanics, 2003 Croatia.

JUDGE, T. R. & BRYANSTON-CROSS, P. J. 1994. A review of phase unwrapping techniques in fringe analysis. *Optics and Lasers in Engineering,* 21, 199-239.

KAROUT, S. 2007. *Two-Dimensional Phase Unwrapping.* PhD Thesis, Liverpool John Moores University.

KAWASAKI, H., FURUKAWA, R., SAGAWA, R. & YAGI, Y. Year. Dynamic scene shape reconstruction using a single structured light pattern. *In:* RYO, F., RYUSUKE, S. & YASUSHI, Y., eds., 2008. 1-8.

KREIS, T. M. 1993. Computer aided evaluation of fringe patterns. *Optics and Lasers in Engineering,* 19, 221-240.

KUJAWINSKA, M. & WÓJCIAK, J. 1991. High accuracy Fourier transform fringe pattern analysis. *Optics and Lasers in Engineering,* 14, 325-339.

LILLEY, F., LALOR, M. J. & BURTON, D. R. 2000. Robust fringe analysis system for human body shape measurement. *Optical Engineering,* 39, 187-195.

LIN, J.-F. & XIANYU, S. 1995. Two-dimensional Fourier transform profilometry for the automatic measurement of three-dimensional object shapes. *Optical Engineering,* 34, 3297-3302.

MALACARA, D., SERVÍN, M. & MALACARA, Z. 2005. *Interferogram analysis for optical testing,* New York, Taylor & Francis Group.

METRILUS. 2009. *Time-of-Flight Cameras* [Online]. Available: http://www.metrilus.de/time-of-flight-cameras/ [Accessed 8 April 2010].

MOORE, A. J. & MENDOZA-SANTOYO, F. 1995. Phase demodulation in the space domain without a fringe carrier. *Optics and Lasers in Engineering,* 23, 319-330.

MOORE, C. J., TORNOW, M., SHARROCK, P. J., LILLEY, F., LALOR, M. J. & BURTON, D. R. 2001. Dynamic Background Correction in 3Dt Body Surface Sensing & Visualisation. *Proceedings of the Fifth International Conference on Information Visualisation.* IEEE Computer Society.

NIU, H., QUAN, C. & TAY, C. J. 2009. Phase retrieval of speckle fringe pattern with carriers using 2D wavelet transform. *Optics and Lasers in Engineering,* 47, 1334-1339.

NVISION. 2008. *NVision 3D laser scanner* [Online]. nvision3d.com. Available: http://www.nvision3d.com/nvision-products.html [Accessed 2 May 2008].

PAN, J., HUANG, P. S. & CHIANG, F.-P. 2006. Color phase-shifting technique for three-dimensional shape measurement. *Optical Engineering,* 45, 013602-9.

PEKLENIK, J. & KUBO, M. 1968. A Basic Study of a Three Dimensional Assessment of the Surface Generated in a Manufacturing Process. *Annals of the CIRP,* 16, 257-265.

PERRY, K. E. & MCKELVIE, J. 1993. A comparison of phase shifting and fourier methods in the analysis of discontinuous fringe patterns. *Optics and Lasers in Engineering,* 19, 269-284.

QIAN, K. 2004. Windowed Fourier transform method for demodulation of carrier fringes. *Optical Engineering,* 43, 1472-1473.

QIAN, K. 2007. Two-dimensional windowed Fourier transform for fringe pattern analysis: Principles, applications and implementations. *Optics and Lasers in Engineering,* 45, 304-317.

QIAN, K., HOCK SOON, S. & ASUNDI, A. 2005. A simple phase unwrapping approach based on filtering by windowed Fourier transform. *Optics & Laser Technology,* 37, 458-462.

QUAN, C., CHEN, W. & TAY, C. J. 2010. Phase-retrieval techniques in fringe-projection profilometry. *Optics and Lasers in Engineering,* 48, 235-243.

QUAN, C., HE, X. Y., WANG, C. F., TAY, C. J. & SHANG, H. M. 2001. Shape measurement of small objects using LCD fringe projection with phase shifting. *Optics Communications,* 189, 21-29.

ROBINSON, D. & REID, G. T. 1993. *Interferogram Analysis, Digital Fringe Pattern Measurement Techniques*, Taylor & Francis.

ROCCHINI, C., CIGNONI, P., MONTANI, C., PINGI, P. & SCOPIGNO, R. 2001. A low cost 3D scanner based on structured light. *Computer Graphics Forum,* 20, 299-308.

SALDNER, H. O. & HUNTLEY, J. M. 1997. Temporal phase unwrapping: application to surface profiling of discontinuous objects. *Appl. Opt.,* 36, 2770-2775.

SALVI, J., FERNANDEZ, S., PRIBANIC, T. & LLADO, X. 2010. A state of the art in structured light patterns for surface profilometry. *Pattern Recognition,* In Press, Accepted Manuscript.

SALVI, J., PAGÈS, J. & BATLLE, J. 2003. Pattern codification strategies in structured light systems. *Pattern Recognition,* 37, 827-849.

SCHUON, S., THEOBALT, C., DAVIS, J. & THRUN, S. Year. High-quality scanning using time-of-flight depth superresolution. *In:* IEEE Computer Society Conference on Computer Vision and Pattern Recognition Workshops, 23-28 June 2008 Anchorage, AK USA. IEEE, 1-7.

SU, X. & CHEN, W. 2001. Fourier transform profilometry: a review. *Optics and Lasers in Engineering,* 35, 263-284.

SU, X. & CHEN, W. 2004. Reliability-guided phase unwrapping algorithm: a review. *Optics and Lasers in Engineering,* 42, 245-261.

SU, X., CHEN, W., ZHANG, Q. & CHAO, Y. 2001. Dynamic 3-D shape measurement method based on FTP. *Optics and Lasers in Engineering,* 36, 49-64.

SU, X. & ZHANG, Q. 2010. Dynamic 3-D shape measurement method: A review. *Optics and Lasers in Engineering,* 48, 191-204.

SURREL, Y. 1996. Design of algorithms for phase measurements by the use of phase stepping. *Appl. Opt.,* 35, 51-60.

TAKEDA, M., GU, Q., KINOSHITA, M., TAKAI, H. & TAKAHASHI, Y. 1997. Frequency-multiplex Fourier-transform profilometry: a single-shot three-dimensional shape measurement of objects with large height discontinuities and/or surface isolations. *Appl. Opt.,* 36, 5347-5354.

TAKEDA, M., INA, H. & KOBAYASHI, S. 1982. Fourier-transform method of fringe-pattern analysis for computer-based topography and interferometry. *J. Opt. Soc. Am.,* 72, 156-160.

TAKEDA, M. & MUTOH, K. 1983. Fourier transform profilometry for the automatic measurement of 3-D object shapes. *Appl. Opt.,* 22, 3977-3982.

VANHERZEELE, J., GUILLAUME, P. & VANLANDUIT, S. 2004. Fourier fringe processing using a regressive Fourier-transform technique. *Optics and Lasers in Engineering,* 43, 645-658.

VANHERZEELE, J., VANLANDUIT, S. & GUILLAUME, P. 2008. Processing optical measurements using a regressive Fourier series: A review. *Optics and Lasers in Engineering,* 47, 461-472.

VILLA, J., SERVIN, M. & CASTILLO, L. 1999. Profilometry for the measurement of 3-D object shapes based on regularized filters. *Optics Communications,* 161, 13-18.

WATKINS, L. R., TAN, S. M. & BARNES, T. H. 1999. Determination of interferometer phase distributions by use of wavelets. *Opt. Lett.,* 24, 905-907.

WU, L.-S. & PENG, Q.-J. 2006. Research and development of fringe projection-based methods in 3D shape reconstruction. *Journal of Zhejiang University - Science A,* 7, 1026-1036.

YANG, C., LU, Q., ZHAO, J. & MIAO, H. 2009. Window size selection in windowed Fourier transform for phase retrieval. *Optics and Lasers in Engineering,* In Press, Corrected Proof.

YINGSONG, H. Year. Improved Three-step Phase Shifting Profilometry Using Digital Fringe Pattern Projection. *In:* JIANGTAO, X., JOE, C. & ZONGKAI, Y., eds., 2006. 161-167.

YOSHIZAWA, T. 2009. *Handbook of Optical Metrology: Principles and Applications,* Boca Raton, CRC Press.

YUE, H.-M., SU, X.-Y. & LIU, Y.-Z. 2007. Fourier transform profilometry based on composite structured light pattern. *Optics & Laser Technology,* 39, 1170-1175.

ZAPPA, E. & BUSCA, G. 2008. Comparison of eight unwrapping algorithms applied to Fourier-transform profilometry. *Optics and Lasers in Engineering,* 46, 106-116.

ZAPPA, E. & BUSCA, G. 2009. Fourier-transform profilometry calibration based on an exhaustive geometric model of the system. *Optics and Lasers in Engineering,* 47, 754-767.

ZHANG, D., MA, M. & AROLA, D. D. 2002. Fringe skeletonizing using an improved derivative sign binary method. *Optics and Lasers in Engineering,* 37, 51-62.

ZHANG, Q., CHEN, W. & TANG, Y. 2009. Method of choosing the adaptive level of discrete wavelet decomposition to eliminate zero component. *Optics Communications,* 282, 778-785.

ZHANG, S. 2010. Recent progresses on real-time 3D shape measurement using digital fringe projection techniques. *Optics and Lasers in Engineering,* 48, 149-158.

ZHANG, S. & YAU, S.-T. 2006. High-resolution, real-time 3D absolute coordinate measurement based on a phase-shifting method. *Opt. Express,* 14, 2644-2649.

ZHONG, J. & WENG, J. 2004. Spatial Carrier-Fringe Pattern Analysis by Means of Wavelet Transform: Wavelet Transform Profilometry. *Appl. Opt.,* 43, 4993-4998.

ZHOU, G., LI, Z., WANG, C. & SHI, Y. 2009. A Novel Method for Human Expression Rapid Reconstruction. *Tsinghua Science & Technology,* 14, 62-65.

ZHU, F., LIU, W., SHI, H. & HE, X. 2010a. Accurate 3D measurement system and calibration for speckle projection method. *Optics and Lasers in Engineering,* In Press, Corrected Proof.

ZHU, Y., LI, A. & PAN, W. 2010b. Discussions on phase-reconstructing algorithms for 3D digitizing structure-light profilometry. *Optik - International Journal for Light and Electron Optics,* In Press, Corrected Proof.

Chapter Three

Camera-Projector Calibration for Fringe Measurement System

The fringe profilometry methods that were previously discussed in Section 2.3 result in the production of wrapped phase data. This wrapped phase data typically contains ambiguities in terms of the multiple phase cycles that may be present in the absolute phase signal, but which are hidden within the output signal due to the fact that it wraps back upon itself each 2π radian cycle. This means that the output is given only in terms of the fractional part of one phase cycle, ignoring any integer term of full cycles present, so that the output is limited to the range $[-\pi,+\pi]$. In order to remove these ambiguities, one of the phase unwrapping algorithms is applied (as was discussed previously in Section 2.4). The resultant phase data after the unwrapping process contains information about the profile of the object being analysed, but it does not yet represent true real world 3D information. Hence, a method is required to convert the phase values to 3D information, which is referred to as the calibration of the system. This involves two main stages, namely that of height calibration (for the Z-axis) and that of in-plane spatial calibration (for the X-axis and the Y-axis). System calibration was for many years trivialised as a process in fringe analysis and the production of accurate phase measurements was regarded as being itself the final goal, whilst completely ignoring the practical production of 3D heights from the phase signal. However it is anything but a trivial process and in recent years there has been an increase in research into system calibration and the production of practical measurement systems.

This chapter reviews the common approaches that address the phase-to-height relation in the literature, in addition to the techniques for obtaining the absolute phase. Then the process of the height calibration method that was adopted in this work is discussed in detail. Finally, the various methods for the transversal (X and Y

coordinate) calibration are reviewed, and the transversal calibration method that is proposed here by the author is discussed.

3.1 Review of Fringe Measurement Calibration

There are various methods available for calibrating a fringe profilometry system; one of the simplest and most straightforward methods is to place the projector and the camera at the same height while placing the projector at a position that is perpendicular to the measurement scene (as shown in Figure 3.1). This configuration enables the calculation of height information directly from the phase data (Hu and Harding, 2007), and the real-world XY-points, as follows:

$$x = i\,K_x \tag{3.1}$$

$$y = j\,K_y \tag{3.2}$$

$$z = \frac{L\,\Delta\varphi}{\Delta\varphi - 2\pi f D} \tag{3.3}$$

where at a pixel *(i, j)*: x and y are the transversal (lateral, or co-planar) coordinates which are relative to the pixel index, K_x and K_y are spatial magnification factors, z is the height which is proportional to the phase difference $\Delta\varphi$, L is the distance between the image plane of the camera and the reference plane, $\Delta\varphi$ is the phase difference from the reference plane (i.e. the phase after removing the carrier phase), f is the spatial frequency of the fringe pattern, and D is the distance between the centres of the projector and the camera lens.

For calibrating the lateral dimensions, Lilley *et al.* (2000) used an image of a black disk of precisely known diameter (placed on a matte white glass reference plane), then the image is binary thresholded and measured in pixel units in order to calculate the parameters K_x and K_y.

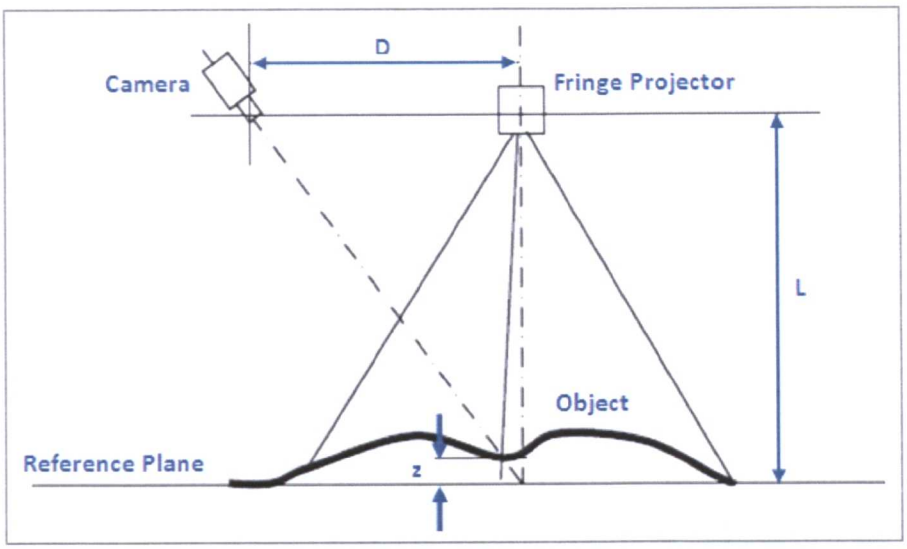

Figure 3.1 A simplified example for projector-camera configuration to calculate the height.

Equations (3.1)-(3.3) cannot provide the desired accuracy for critical optical metrology applications (such as those applications discussed in Section 4.3), because it is not easy to measure the parameters of these equations with great accuracy. Besides, it is hard to align the camera and the projector so that they are precisely at the same height and to ensure that the projector is exactly perpendicular to the measurement scene. Moreover, due to camera lens distortion, the magnification varies from pixel to pixel within the image frame and hence using globally constant K_x and K_y values results in the production of erroneous x and y coordinates. Likewise, the projector produces a divergent fringe pattern with a non-uniform fringe spatial frequency. For all of these reasons, any small errors in the parameters of these equations produces large errors in the resultant 3D information, and when these measurements are compared against Coordinate Measurement Machine (CMM) scan data for the same surface, these errors become noticeable.

This section reviews the approaches that have addressed the phase-to-height relationship as well as the conversion from image plane pixels to real world x and y coordinates, where the assumptions for simplified system geometries like that shown in Figure 3.1 do not need to be fulfilled (i.e. camera and projector may be placed arbitrarily). Figure 3.2 depicts the configuration of the sensor components for the system that was developed during this research program, wherein the phase-to-height relationship is non-linear (due to the divergence in the projected fringe pattern and

the non-uniformity of its spatial frequency), hence an advanced calibration process needs to be employed for this type of system geometry.

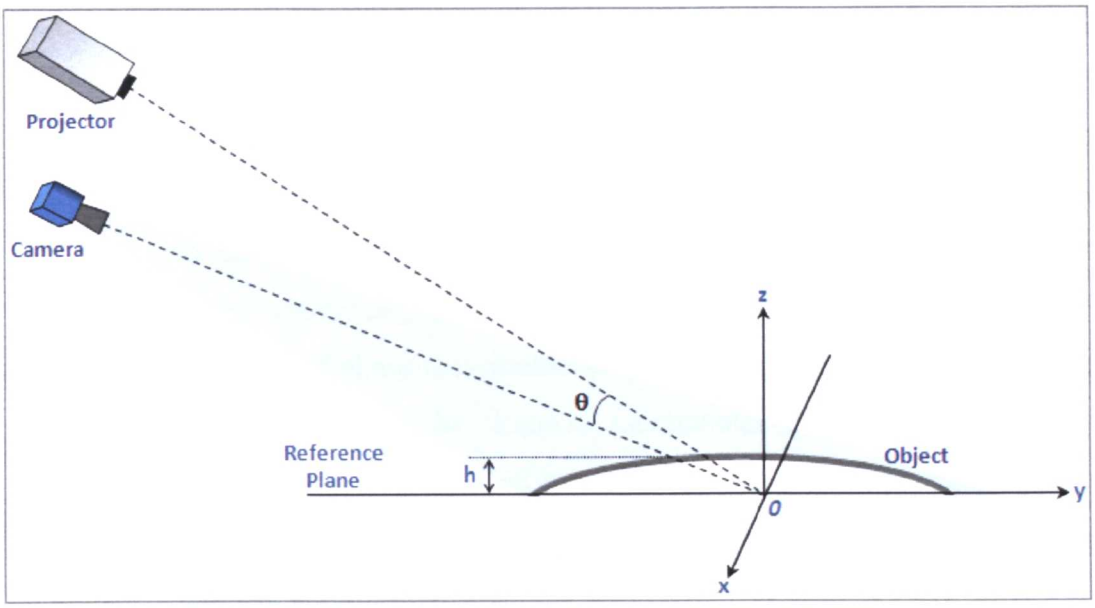

Figure 3.2 An illustration of the configuration of sensor components for the system that was developed during this research program.

3.1.1 Phase-to-Height Relation

In order to reconstruct the 3D height information of the object's surface, as shown in Figure 3.2, an algorithm for phase-to-height conversion is required. The form of this algorithm is usually related to the geometry of the camera and projector (in terms of parameters such as the angle between the axis of the camera and projector, the distance between the camera and the reference plane, the relative position of the camera and the projector, the focal length of the camera lens, and the spatial frequency of the fringe pattern). Research that has addressed the phase-to-height relation can be divided into three main approaches:

A. **Analytical methods**: which depend on the direct determination of the geometric parameters of the optical system, in order to establish an explicit mathematical model of the calibration coefficients for the phase-to-height relationship (Spagnolo *et al.*, 2000, Quan *et al.*, 2001, Zhang *et al.*, 2004, Halioua and Liu, 1989).

B. **Empirical methods**: which obtain a direct mapping of the phase-to-height relationship without an explicit determination of the parameters of the system

geometry, and wherein the calibration coefficients implicitly account for the system configuration. To determine the calibration parameters, empirical methods typically involve one of the following two general procedures:

1. A series of phase measurements are made by vertically translating the reference plane by known incremental height steps; wherein calibration coefficients are determined either locally for each pixel (Liu *et al.*, 2003, Reeves *et al.*, 2003, Guo *et al.*, 2005, Tavares and Vaz, 2007) or globally for the whole image (Lilley *et al.*, 2000, Srinivasan *et al.*, 1985).
2. A series of phase measurements are made by vertically translating the reference plane by known incremental height steps; wherein interpolation is employed to calculate the associated height value of each phase value, and hence, no calibration coefficients are required (Zhang *et al.*, 2005).

C. **Hybrid methods**: which basically measure the geometric parameters of the optical system to determine their approximate values, and then a series of phase measurements are performed by vertically translating the reference plane by known incremental height steps in order to estimate the geometric parameters (Hu *et al.*, 2003, Sutton *et al.*, 2001, Zappa and Busca, 2009).

The analytical calibration methods (approach A) cannot produce an exact representation of the phase-to-height relationship, as a direct measurement of system geometry parameters is required, which is a tedious and complicated procedure to perform accurately. Sensitivity analysis reveals that small errors in the measurement of these parameters produces potentially large errors in the calculated height value (Lilley *et al.*, 2000). Moreover, any non-simplified system geometry like the one that is depicted in Figure 3.2 typically requires a calibration model that is itself mathematically quite complex. This means that there is a significant chance of the model being inaccurate due to multiple aberrations in the optical imaging system and also makes it difficult to evaluate the influence of every system parameter upon the overall measurement error (Zhang *et al.*, 2004). Hybrid calibration methods, still require an initial measurement of the geometrical parameters of the system, hence any inaccurate determination of these parameters produces large corresponding errors in the resultant height values.

Empirical calibration methods (approach B) do not rely on the determination of geometrical parameters for the optical system, and thus they provide a more accurate representation of the phase-to-height relationship. Nevertheless, the accuracy of these methods depends on the precision of the elevation stage that carries the reference plane. Local calibration methods within the scope of this approach provide better results than global calibration methods, because the local calibration at each pixel accounts for local distortion effects that typically originate because of the divergence in the projected fringe pattern and the irregularity in terms of its spatial frequency. Empirical calibration methods that rely on the determination of calibration coefficients (approach B1) principally use least-squares algorithms, either for linear fitting (Guo *et al.*, 2005), or for higher order polynomial fitting (Liu *et al.*, 2003), however, these methods still rely upon the accuracy of the fitting algorithms that are used to generate the calibration coefficients. Hence, it would be better to avoid the complexity required for generating the calibration coefficients altogether, through the use of phase-to-height interpolation (as shown in approach B2).

Regarding the degree of accuracy required for obtaining height values using empirical calibration methods and in relation to the phase-to-height mapping linearly or nonlinearly, Jia *et al.* (2007) demonstrated that the accuracy of the linear calibration was similar to the nonlinear calibration at lower ranges of height (0 to 32mm), however, at higher height ranges the nonlinear calibration had noticeably higher accuracy. Jia *et al.* explained the difference in accuracy as follows, namely that when the measurement object approaches the camera and the projector for the higher range of height, the assumption of linearity based on a small divergence of light from the projector becomes less valid.

Empirical calibration using linear interpolation was the calibration method that was adopted for use in the optical profilometry system developed in this research programme (as illustrated in Section 3.2), wherein, the reference plane was elevated in short steps (typically $< \frac{1}{2}$ of the fringe spacing) in order to preserve the assumption of linearity for the phase-to-height mapping, and also to avoid using nonlinear interpolation, which may introduce Runge phenomenon artefacts (Fornberg and Zuev, 2007).

It should be stated here, that there is no explicit carrier phase component ($2\pi f_o$) removal technique used prior to the adopted height calibration method, neither at the calibration stage, nor at the measurement stage itself. In other words, carrier-removal techniques such as subtracting the unwrapped phase data of the reference plane from the unwrapped phase data of the object being measured or spectrum-shifting (as in the case of Fourier Transform Profilometry) are not employed explicitly for the adopted calibration methods. The disadvantage of the spectrum-shift approach is that the frequency of a carrier fringe cannot be accurately detected in practical measurements. On the other hand, the reference-subtraction approach requires two sets of measurements, which makes it less practical for the measurement of dynamic objects. Moreover, the phase measurement uncertainty is doubled in the subtraction process (Quan *et al.*, 2007). Instead, however, the unwrapped phase data (that is composed of the carrier and shape-related components) are directly mapped to the actual height.

3.1.2 Relationship between Image Plane Coordinates and Transverse Spatial Dimensions

Due to aberrations in the optics of the profilometry system (such as camera lens distortions, etc), the magnification varies from pixel to pixel throughout the image. Thus, when trying to use global magnification factors to map image coordinates to transverse spatial dimensions, this non-uniformity in magnification for each pixel produces invalid x and y measurement results. In addition, the relationship between image pixels and transversal spatial coordinates also depends upon the specific height and hence it should be expressed as a function of z. The process of establishing the relationship between the image-plane pixel coordinates and the transversal-dimensions is called camera calibration. In order to be expressed as a function of z, the camera calibration process is performed over a range of elevated heights.

Within the scope of the field of fringe profilometry, 2D camera calibration approaches can be categorised as follows:

A. **Photogrammetry**: which is the practice of determining the geometric properties of an object from its photographic images (Salvi *et al.*, 2001).

Camera calibration can be defined, within this context, as being "the process of determining the internal camera geometric and optical characteristics (intrinsic parameters) and/or the 3D position and orientation of the camera frame relative to a certain world coordinate system (extrinsic parameters)" (Tsai, 1986). Photogrammetry methods are employed for 3D geometric calibration, however, only 2D (or co-planar) camera calibration is used here, as height is obtained using a separate phase-to-height calibration. Typically, the process of calibration is divided into stages, firstly, to establish a camera model that deals with a mathematical approximation of the optical (intrinsic) and physical (extrinsic) parameters of the sensor. Secondly, to estimate the values of these parameters using direct iterative methods. Salvi *et al.* (2001) presented a detailed review of some of the most commonly used photogrammetrical calibration techniques, along with an evaluation of their accuracies. Salvi *et al.* demonstrated that Tsai's method (Tsai, 1987) provides the lowest mean error (0.0564mm) amongst all of the methods surveyed.

B. **Empirical mapping**: which establishes a mapping relationship between the world coordinate system and the image coordinate system. Principally, empirical mapping can be achieved in two stages; firstly, identifying features on the image of a calibration grid with known XY world coordinates and mapping those features to their corresponding pixels on the image plane. Secondly, a mapping relationship between the world coordinate system and the image coordinate system is established in order to calculate the XY world coordinate values of the rest of the image pixels. Zhang *et al.* (2005) used a calibration grid of black circles with precisely known diameters as calibration features, and they then established a mapping relationship using a least-squares method. Liu *et al.* (2003) used two sinusoidal gratings with their fringes parallel to the X and the Y directions respectively and with known fringe spacings. Using fringe analysis methods, the unwrapped phase data can then be used to map the image plane to the XY world coordinates.

Tsai's camera calibration technique was incorporated for the transversal calibration method of the system that has been developed by the author in this research programme. The transversal calibration is illustrated in Section 3.4.

3.2 Absolute Phase Measurement

As discussed previously in Section 2.4, the phase unwrapping techniques that have been adopted for this work produce the same relative unwrapped phase maps, i.e. the same form, but with different phase values. This is because the starting point for the phase unwrapping process is chosen arbitrarily. Hence, the resultant unwrapped phase map using these techniques is *relative* to the starting point of phase unwrapping process. The adopted phase-to-height calibration algorithm (as described in Section 3.3) requires the mapping of a fixed (*absolute*) phase map to its corresponding height value. Therefore, an absolute phase map must be obtained from the relative phase map, after the phase unwrapping process has been completed, in order to map the phase to height. The absolute phase map is directly related to the geometry of the optical system and it is independent of the starting points of the phase unwrapping algorithms.

An absolute phase map can be obtained from the relative phase map by incorporating the principle of triangulation into the system. A black frame containing a single high intensity spot (of known position within the frame) is projected onto the calibration plane at each discrete height step throughout the calibration range. The spot is aligned such that it falls at the centre of the minima of one of the fringes towards the middle of the fringe pattern, and it must remain on the same fringe throughout the measurement range. For each discrete height stage, the centre of the spot is determined by using standard image processing techniques and then the corresponding phase value at the location of the centre of the spot is subtracted from the entire relative phase map. Thus, the phase value at the location of the centre of the spot is deemed to be equal to a *zero phase* value and the phase maps that are subsequently produced after the global subtraction of this starting phase value are all now registered relative to that phase value.

However, the comparative luxury of using a dedicated projection frame for the triangulation spot, as illustrated above, is not suitable for performing dynamic measurements, due to time constraints. Zhang and Yau (2006) encoded the spot into the projected fringe pattern, in order to maintain the acquisition speed for dynamic objects, whilst still obtaining absolute phase maps. However, a single spot approach

is not practically reliable for use in real-life applications, because it can be difficult to determine the spot location due to noise and the presence of certain object features (such as high levels of curvature, the presence of bright and shadowed areas, etc) which would result in invalidating the resultant measurement if the location of the spot and hence the absolute phase datum were to be lost. In order to overcome this problem, a stripe (line) can be embedded into the fringe pattern instead of a single spot (Hu and Harding, 2007, Gai and Da, 2010), thereby building in a certain amount of redundancy. Here the relative phase values for any pixel on the stripe are equal and thus by subtracting the phase value of any of those pixels from the relative phase map it is possible to produce an absolute phase map.

Because we are using the approach of embedding a triangulation spot (or stripe) into the fringe pattern to encode absolute phase, this will produce phase errors at the pixel locations of the triangulation spot (or stripe) during measurement, as the fringe pattern has been compromised in these areas. Therefore, a novel approach was introduced by the author to restore the pixel values at the spot location, after determining its location using image processing techniques and prior to demodulating the phase using a spatial fringe analysis technique. Since restoring a whole stripe of pixels is a time consuming procedure, as well as being prone to errors, the author's approach was to use a multiple triangulation spot technique instead of employing a whole stripe.

The rest of this section addresses the author's approach for embedding and detecting the triangulation spot and this has been done in two discrete forms; the first when using a single spot and the second when using a multiple spot approach. The choice of which form to use may be adapted to the specific measurement application that the system is being employed for (as described in Section 4.1). The algorithm for restoration of the spot(s) location is illustrated in Section 7.3.2.

3.2.1 Single-Spot Triangulation

A single triangulation spot, for this work, can be projected either inside a separately projected black frame (for static object measurement using phase stepping profilometry), or within a fringe pattern (for dynamic object measurement using

spatial fringe analysis techniques). For both of these cases, the location of the spot is chosen to be at the centre of one of the fringes towards the middle of the fringe pattern at the reference plane. The chosen location remains the same throughout the entire calibration range. At the calibration stage the spot is projected inside a black frame, which produces a certain number k of detected x and y locations, where k represents the number of discrete elevated heights of the calibration plane as it is translated vertically throughout the entire calibration range. The size of the projected triangulation spot that was adopted for this work was 4×4 pixels, which was proven practically (by the author and for the system configuration described in Section 4.1) to provide a better detection of the spot within the acquired fringe pattern than a smaller size, as well as, providing a better restoration of the spot location than using a larger size.

For the first case where a dedicated frame is used for triangulation spot projection (at the calibration stage and at the measurement stage when measuring static objects), the location of the spot is obtained as follows:

1. Because the spot is projected with a high intensity value (255) within a dedicated black frame, its location can be determined by simply binary thresholding the acquired image, and then averaging the respective x and y indices in order to obtain the centre of the spot.
2. By using the corresponding wrapped phase map (respectively for either the calibration reference plane, or the measurement object, depending upon whether we are calibrating, or measuring), the location of the spot's centre is then *tuned* with sub-pixel accuracy so that it lies exactly at the edge of the phase wrap of the nearest fringe that was chosen to contain the spot and representing a known phase datum. The unwrapped phase value at the precise location of the spot's centre is then obtained by using linear interpolation.

On the other hand, at the measurement stage and for the second case where the spot is being projected within a fringe pattern, the processes of embedding the spot within the projected fringe pattern and of detecting the spot within the image that is acquired by the camera are as follows:

A. **Embedding process**: in order to achieve a reliable spot detection process, the spot is embedded into the low intensity area of one of the fringe minima and

this bright spot is surrounded by a black frame (with width of 1 pixel). Integrating the spot within the fringe minima makes it easier to detect the spot location than integrating it within the fringe maxima. Practically, the projected maximum intensity value of the fringe pattern was chosen to be less than the spot's intensity value by a greyscale value of at least 20.

B. **Detection process**: which includes the following steps:

1. The detected locations of the spot throughout the calibration range are used to generate a detection *trajectory* (or *epipolar track*) for the triangulation spot, by means of image processing techniques (see Appendix A1). The generated trajectory mask contains *1's* for locations where the detection will be performed and *0's* for where the detection will be excluded. The trajectory mask image is generated only once at the start up of the measurement software and is then stored in memory.
2. A series of image processing algorithms are applied to the grabbed fringe pattern with the embedded spot into it (see Appendix A2), mainly using smoothing and Laplacian filters, in order to enhance the visibility of the spot, hence, to provide a better detection.
3. The resultant image from Step 2 is multiplied by the trajectory mask image, which was generated in Step 1. Then the result of the multiplication is binary thresholded and the average of the x and y indices of the threshold results are used to obtain the centre of the spot.
4. The location of the spot's centre is *tuned* to a sub-pixel location using the wrapped phase map, in order to lie exactly at the edge of the phase of wrap of the nearest fringe that was chosen to contain the spot and representing a known phase datum. Then, the unwrapped phase value of the tuned location of the precise spot's centre is obtained using linear interpolation.
5. The location of the spot is synthetically restored (see Section 7.3.2) prior to applying the phase measuring fringe analysis method, in order to avoid producing erroneous phase values at the spot location.

3.2.2 Multi-Spot Triangulation

A multi-spot approach is used to add robustness and enhance the possibility of successful spot detection, as it is quite possible that one or more spots might be lost during the measurement stage, due to obscurement by the object's shape (e.g. curvature and shadows) and noise. The locations of the spot are chosen to be at the centre of one of the fringes that is located near the middle of the fringe pattern when it lies upon the reference plane. The chosen spot locations remain the same throughout the entire calibration range.

At the calibration stage, the number of triangulation spots (p) is selected in the way that the spots cover the measurement region-of-interest (i.e. to maximise the possibility of finding at least one spot). Each bright spot (S_p) is projected sequentially with a high intensity value (255) inside a dedicated black frame, which produces a number k of detected x and y locations for each spot, where k represents the number of elevated heights of the calibration plane throughout the calibration range. The adopted size of each of the projected triangulation spots for this work was 4×4 pixels. Practically, five spots were found to be sufficient to cover the measurement region-of-interest.

On the other hand, at measurement time, the process of embedding the spot into the fringe pattern and subsequently detecting the spot within the fringe pattern, are as follows:

A. **Embedding process**: all of the spots are embedded into the same fringe pattern; they are embedded into the low intensity area of the fringe minima and each spot is surrounded by a black frame (with width of 1 pixel) in order to maximise contrast. Practically, the projected maximum intensity value of the fringe pattern was chosen so that it was lower than that of the spots by a greyscale value of at least 20.

B. **Detection process**: which includes the following steps:

    1. The detected locations of all the spots as they pass throughout the calibration range are used to generate a number of different detection *trajectories* (one trajectory for each spot); by means of image processing techniques (see Appendix A1). The generated trajectories mask, contains *1's* for locations where the detection will be

performed and *0's* for where the detection will be excluded. The trajectories mask image is generated only once at the start up of the measurement program and stored into memory. Moreover, for each spot a detection a ROI is determined, which is used for locating the spot at the detection step.

2. A series of image processing algorithms, mainly consisting of smoothing and Laplacian filters (see Appendix A2), are then applied to the image of the acquired fringe pattern that contains the multiple embedded triangulation spots.
3. The resultant image from Step 2 is then multiplied by the trajectories mask image, which was generated using Step 1. Then, for each spot, the x and y indices for the maximum intensity value within the spot's detection ROI (which was determined in Step 1) is used as the centre of that spot.
4. Because all the spots lie on the same fringe, they are supposed to have the same unwrapped phase value. Therefore, a *reliability* value for each spot is calculated depending upon the unwrapped phase values of the adjacent points (of each spot) on the same fringe. The reliability value here indicates if the spot lies within a valid measurement area, hence, spots with high reliability values are assumed to lie within regions of a uniform unwrapped phase data. The reliability value (R_i) for each spot is calculated as follows:

$$R_i = 1 - \frac{|\Delta\varphi_i|}{\sum_{i=1}^{s}|\Delta\varphi_i|} \tag{3.4}$$

where for spot (i): $\Delta\varphi_i$ is the difference between unwrapped phase values of the adjacent points of the spot on the same fringe.

5. The location of the centre of the spot with the highest reliability value is then *tuned* to a sub-pixel location using the wrapped phase map, in order to lie exactly at the edge of the phase wrap of the nearest fringe that was chosen to contain the spot and representing a known phase datum. Then, the unwrapped phase value of the tuned location of the spot's centre is obtained by using linear interpolation.

6. The fringe pattern at the locations of the triangulation spots are then synthetically restored (see Section 7.3.2) prior to applying the fringe analysis method, to avoid the production of erroneous phase values at their locations.

3.3 Adopted Phase-to-Height Calibration Method

For an optical profilometry system that is to be used for applications that necessitate stringent accuracy requirements, such as the one that was produced during this research programme, it is essential to adopt a rigorous phase-to-height calibration method, which needs to fulfil the following criteria:

- Accuracy: which must be better than ±0.5mm to fulfil the requirements of the intended system application (Section 4.3).
- Practicality: which should not involve the requirements for any physical measurement of the parameters of the optical system.
- Maximised level of automation: which should not require any manual intervention throughout the calibration process.

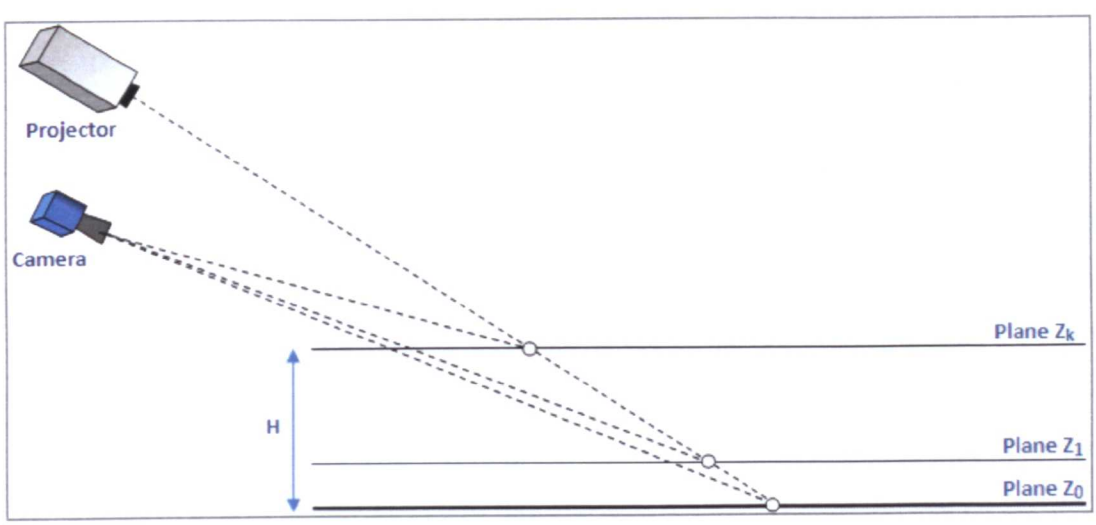

Figure 3.3 An illustration showing the vertical elevation of the calibration plane throughout the calibration range *H*.

Empirical calibration using linear interpolation is the calibration method that has been adopted for this work, and the calibration procedure is based on the empirical calibration approach that was proposed by Zhang *et al.* (2005). The reference plane is elevated in a number k of discrete height steps (see Figure 3.3) throughout the

required measurement range; the calibrated height range is called the *calibration range* (H). In order to generate a height calibration volume that implicitly represents the phase-to-height conversion for the optical system, the calibration procedure is as follows:

1. The calibration plane is elevated to the required height step (Z_k), whereas at the beginning of the calibration process it is set at the reference height (Z_0) and the plane is accurately and precisely levelled in order to insure that the height is the same across the entire plane. The reference height (Z_0) is chosen to be at the bottom. However, this configuration is customisable and the reference height can be chosen depending on the profilometry application requirements.
2. The phase is measured using a four-frame phase-shifting technique and then unwrapped using a reliability ordering phase unwrapping algorithm.
3. Multiple triangulation spots are sequentially projected on the calibration plane as illustrated in Section 3.2.2. The location of the spots is chosen to be spatially separated in such a way that they cover the measurement ROI (i.e. to maximise the possibility of finding at least one spot), and to be at the centre of one of the fringes towards the middle of the fringe pattern when it is projected at the reference plane (practically five spots were found to be sufficient).
4. One of the spot locations (usually one of the central spots) is determined by binary thresholding the individually acquired image that containing only that spot projected on a black background, and then averaging the x and y indices so as to obtain the centre of the spot. Then, using the corresponding wrapped phase map, the location of the spot's centre is tuned to a sub-pixel location so that it lies exactly at the edge of the phase wrap of the nearest fringe that was chosen to contain the spot and representing a known phase datum.
5. To obtain the absolute phase map using the unwrapped phase map, the unwrapped phase value of the tuned spot's centre (that was determined in Step 4) is globally subtracted from the entire wrapped phase map.
6. The resultant absolute phase map is stored inside the calibration volume and indexed with its corresponding height value (Z_k). Then steps 1-6 are repeated for a different discrete step height by using the elevator table to move the

plane, until the whole desired height measurement range (H) has been calibrated.

At the measurement stage, after obtaining the absolute phase map (as illustrated in Section 3.2), the absolute phase value of each point in the image is linearly interpolated in order to calculate its corresponding height value. The linear interpolation technique uses the corresponding index of each point in the image to find its surrounding relative phase values from within the calibration volume, then the upper and lower boundaries of the phase values and their height indices are used to calculate the height value of that point (illustrated in Figure 3.4), and as follows:

$$z_i = z_{i-1} - (\varphi_{i-1} - \varphi_i)\left(\frac{z_{i+1} - z_{i-1}}{\varphi_{i+1} - \varphi_{i-1}}\right) \tag{3.5}$$

where at point (i): z_i is the required height value to be obtained, using the corresponding absolute phase value (φ_i), and the upper and lower phase values (φ_{i+1} and φ_{i-1}, respectively) and their height indices (z_{i+1} and z_{i-1}, respectively).

This approach effectively accounts for local distortion effects. Moreover, the calibration process covers cases in which the measurement plane is not perpendicular to the optical axis of the camera lens, and involves no requirements for measuring or estimating the parameters of the optical system.

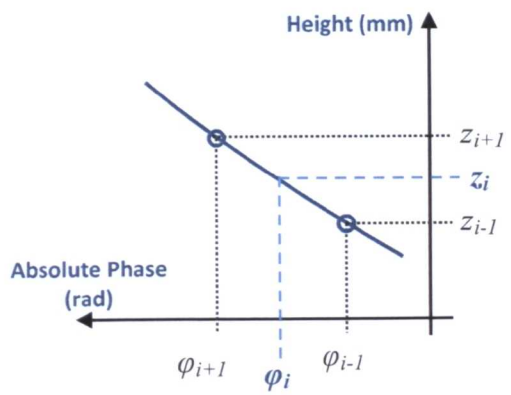

Figure 3.4 Illustration of the linear interpolation technique that is used to calculate the height value of a point in the image, where the upper and lower boundaries of the phase values and their height indices are used to calculate the height value of that point.

In order to eliminate any possible errors in the calibration process, the reference plane is elevated in small steps (typically < ½ of fringe spacing) in order to preserve the assumption of linearity for the phase-to-height mapping, and additionally to avoid having to use nonlinear interpolation, which may introduce Runge phenomena (Fornberg and Zuev, 2007). Furthermore, the uncertainty in the placement of the calibration plane (Zappa and Busca, 2009) was minimised by using a special calibration table with precise elevation accuracy and a float glass board (see Section 5.4 for more details), levelled via a high precision digital clinometer (with a measuring resolution of 0.01 degree). The specific clinometer that was used for calibration plane levelling was a Clinotronic Plus (WYLER-AG, 2009).

3.4 Developed Transversal Calibration Method

Tsai's camera model (Tsai, 1986, Tsai, 1987) was used for transversal calibration of the optical system that was developed in this research programme. Tsai's camera model was implemented into a C language version by Willson (1995), and Willson's C source code was integrated into the transversal calibration software that is used in this work. This section reviews briefly Tsai's method, and then describes the transversal calibration method that was developed by the author.

3.4.1 Review of Tsai's Camera Model

Tsai's camera calibration method models the radial distortion of the camera lens. It is based on the pinhole model of perspective projection. The detailed method is described by Tsai (1986, 1987). Basically, Tsai's model uses 17 calibration parameters; which are as follows:

A. Variable parameters, which are:
   - Intrinsic parameters, which describe the optical characteristics of the camera lens;
     - effective focal length of the pin hole camera (f),
     - first order radial lens distortion coefficient (k_1),
     - coordinates of the centre of the image plane (C_x, C_y),
     - horizontal scale factor (S_x).

- Extrinsic parameters, which describe the 3D position and orientation of the camera frame relative to a certain world coordinate system;
  - rotation angles for the transformation between the world and camera coordinates (R_x, R_y, R_z),
  - translational components for the transformation between the world and camera coordinates (T_x, T_y, T_z).

B. Constant parameters, which are:
- Number of the horizontal elements (pixels of the camera sensor (N_{cx}).
- Number of the horizontal pixels of the image plane (N_{fx}).
- Dimensions of the pixel of the camera sensor (d_x, d_y), which are provided by the camera manufacturer.
- Effective dimensions of each pixel (d_{px}, d_{py}) in mm/pixel.

In order to establish the camera calibration model (see Figure 3.5) the following steps are performed; firstly, the method employs an initial estimate of the calibration parameters, in addition to a set of feature points on the image plane (X_f, Y_f) with their known world coordinates (X_w, Y_w, Z_w). Secondly, the calibration parameters are iteratively and non-linearly optimised until the system converges. Two forms of calibration are possible; coplanar (where the feature points lie on the same height in terms of world coordinates) and non-coplanar (where the feature points occupy a 3D volume in terms of their world coordinates). Because Tsai's method is only used for transversal calibration of the optical system that is used in this work, only the coplanar form of calibration is employed here.

In order to obtain the feature points; a planar calibration grid is used, which is usually printed with a checkerboard, consisting of a white background with regularly spaced black squares of precisely known dimensions. Then, the image of the calibration grid is processed using image processing techniques so as to obtain the corners (as feature points) on the image plane. Consequently, a set of tuples of the feature points (X_w, Y_w, Z_w, X_f, Y_f) is obtained, where Z_w is set to zero since it is a coplanar calibration. The calibration procedure requires at least 11 feature points to optimise the calibration parameters (Willson, 1995).

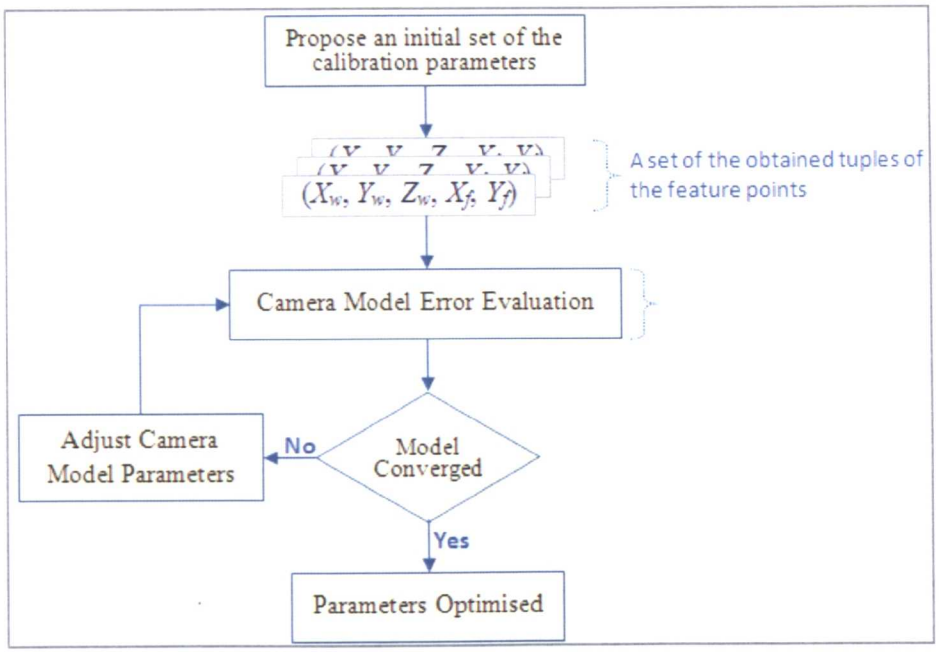

Figure 3.5 Flowchart for Tsai's camera model calibration method.

Willson's C code implementation (1995) of the Tsai method necessitates the provision of the following calibration parameters:

- The values of N_{cx}, N_{fx} and S_x are set to 1.
- C_x, is set to the full horizontal resolution divided by 2.
- C_y, is set to the full vertical resolution divided by 2.
- The algorithm will adjust S_x, C_x, and C_y to give a best fit set of the intrinsic parameters.
- d_x is set to the width of the camera sensor cell.
- d_y is set to the height of the camera sensor cell.
- d_{px} and d_{py} are set as described above; where an initial estimation of these values is required to allow the model to converge.
- The algorithm will automatically compensate for any errors in d_{px} and d_{py}.

3.4.2 Transversal Calibration Procedure

The transversal calibration method proposed by the author employs Tsai's camera model calibration method, with added enhancements to produce more accurate results. A checkerboard (consisting of eight rows, by eight columns of squares) was used as a calibration grid, made from hard PVC material that is 1mm in thickness. The size of the checkerboard tiles is 53×53 mm, however; smaller tile sizes (of

40×40 mm and 20×20 mm) have also been examined by the author and did not produce any difference in terms of the resultant 3D reconstruction. The maximum number of feature points (to be used as an input for Tsai's camera calibration method) is determined by the number of the internal corners of the checkerboard (there are 49 individual corners for this specific case).

The specific notations and settings that are used in the proposed transversal calibration method are as follows:

- The checkerboard is placed upon the calibration plane (which is used for the phase-to-height calibration) at the reference height (Z_0), such that one of its corners (usually the corner at the centre of the checkerboard) is used as the desired reference point (X_0, Y_0).
- As shown in Figure 3.6, the central corner (marked in red) is placed at the centre of the measurement ROI (marked in cyan).
- The feature points should be distributed within the desired measurement ROI.
- The chosen XY location of the checkerboard remains the same throughout the entire calibration range (H).
- The calibration plane is elevated in k height steps throughout the calibration range, and imaged at the full resolution of the camera for each step.
- The height elevation of each step is equal to 0.5 mm.

After grabbing k images of all of the k height steps throughout the full calibration range, each image is then processed in order to retrieve the X and Y coordinates for each step as follows:

1. The locations of the feature points (checkerboard corners) are extracted using image processing techniques. For this purpose, the OpenCV library (Bradski and Kaehler, 2008) is employed. Figure 3.7 shows an example of the extracted feature points (marked with green circles and the central point marked with a red circle).
2. To enhance the calibration accuracy of the Tsai's calibration method, the OpenCV library is used to refine the locations of the detected feature points to a sub-pixel accuracy.
3. As shown in Figure 3.8, the central horizontal and vertical axes of the measurement ROI (in yellow) are obtained by using the bounding feature

points (in green) that are detected at the ends of each axis within the area of the checkerboard.

4. Willson's algorithm (1995) is then used to optimize the model, and to obtain the corresponding X and Y world coordinates of any pixel in the acquired image.
5. The resultant X and Y world coordinates are relative to the central point of the checkerboard image, i.e. of the full resolution image. Hence, X and Y data are subtracted from the central axes of the measurement ROI in order to be registered relative to this point.
6. The X and Y surface data of the measurement ROI are clipped, and then stored inside individual X and Y calibration volumes. The calibrated X and Y surfaces are indexed inside the calibration volumes according to the corresponding value of their specific elevated height step.

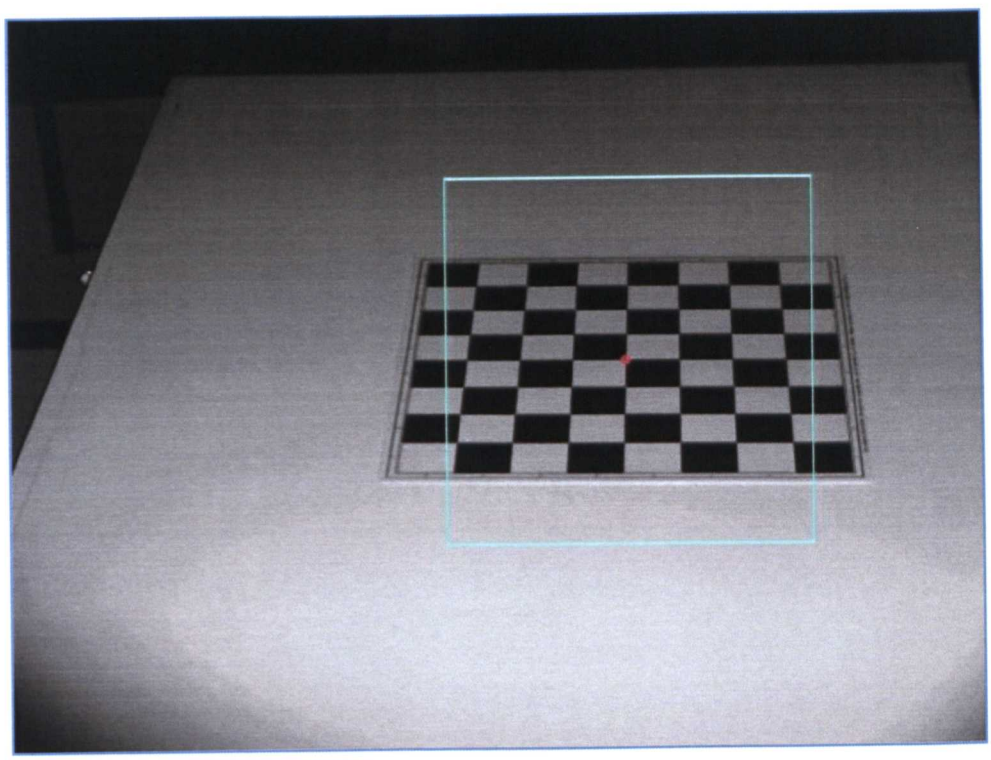

Figure 3.6 The checkerboard is placed on the reference plane at (Z_0), where the central corner (marked in red) is placed at the centre of the measurement ROI (marked in cyan).

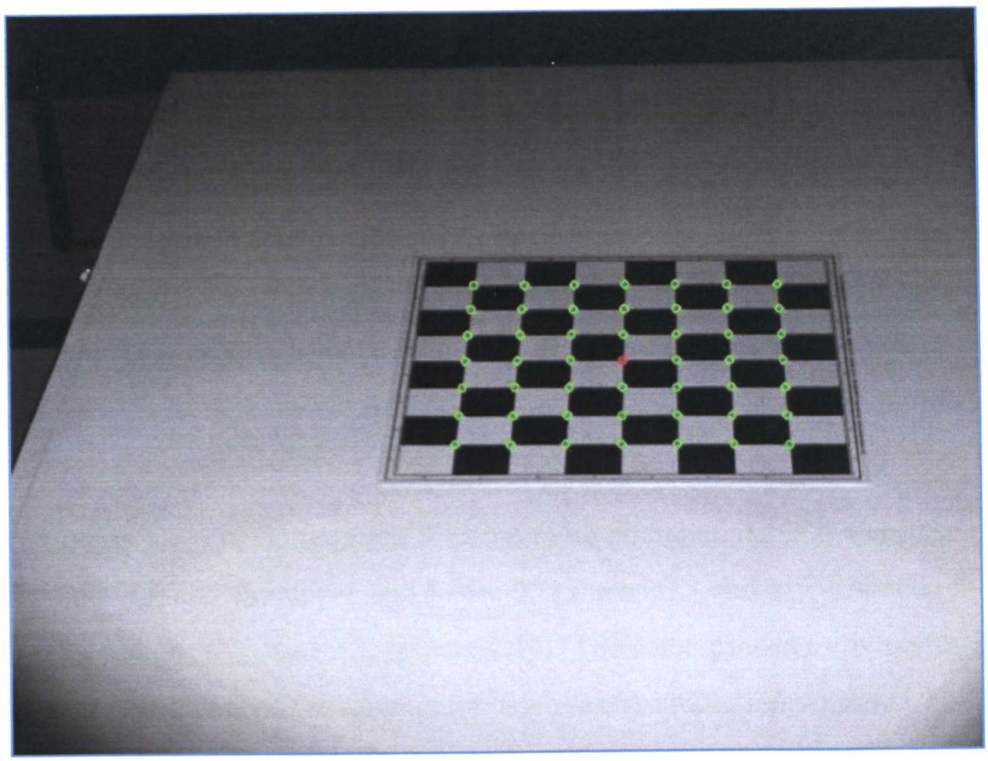

Figure 3.7 An example of the extracted feature points of the checkerboard, marked with green circles and with the central point marked with a red circle.

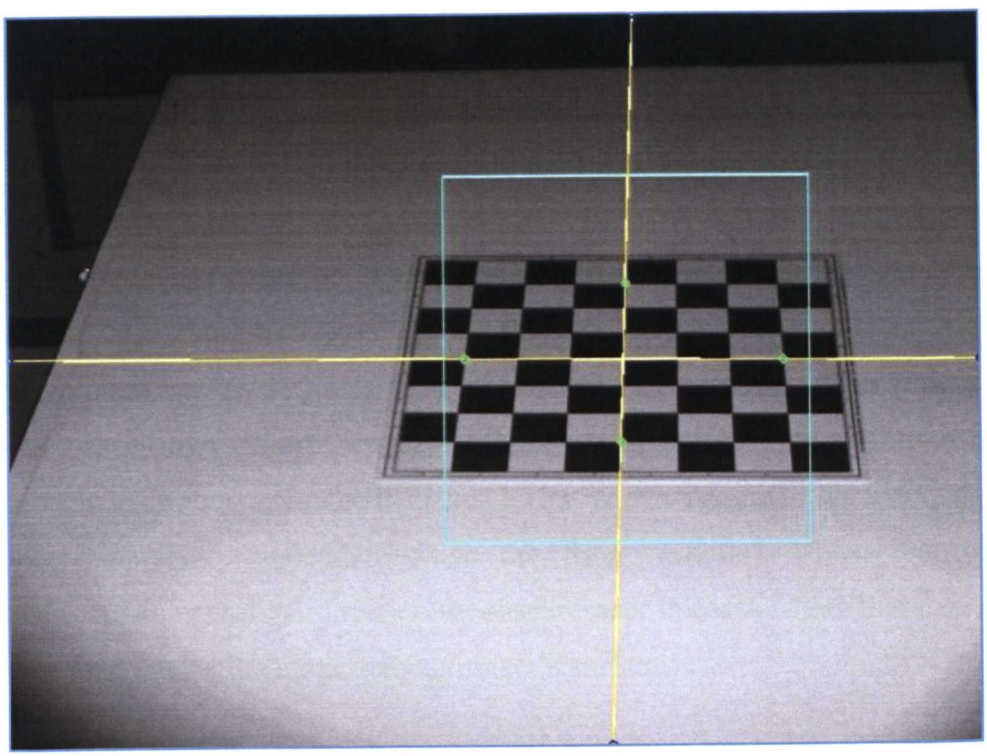

Figure 3.8 The central horizontal and vertical axes of the measurement ROI (in yellow), which was obtained by using the detected feature points at the end of each axis within the checkerboard area.

At the measurement stage and after obtaining the height map (as described in Section 3.3), the height value (Z) of each point in the image is linearly interpolated so as to calculate its corresponding X value. The linear interpolation technique uses the corresponding index of each point in the image to find its X value from inside the X calibration volume, then the upper and lower boundaries (of the X values and their height indices) are used to calculate the X value of that point, and as follows:

$$x_i = x_{i-1} - (z_{i-1} - z_i)\left(\frac{x_{i+1} - x_{i-1}}{z_{i+1} - z_{i-1}}\right) \tag{3.6}$$

where at point (i): x_i is the required X value to be obtained, using the corresponding height value (z_i), and the upper and lower X values (x_{i+1} and x_{i-1}, respectively) and their height indices (z_{i+1} and z_{i-1}, respectively). The same procedure is performed to obtain the Y coordinate of the same point using the Y calibration volume.

3.5 Chapter Summary

This chapter has shown that retrieving the 3D information from the unwrapped phase data is by no means a straightforward process. Hence rigorous calibration methods need to be performed for the optical measurement system in order to establish both the phase-to-height and the height-to-transversal coordinate relationships. Common approaches for calibrating both relationships have been reviewed in the chapter.

An absolute phase datum is needed to map the phase-to-height, because the unwrapping algorithms produce different unwrapped phase values, but with the same relative form of the phase maps. Two approaches were developed to produce the absolute phase map. Firstly, using a single triangulation spot (either inside a dedicated blank frame or embedded inside the fringe pattern). Secondly, using a multi-spot approach (embedded inside the fringe pattern), which reduces the possibility of losing the spot location by obscurement in cases where there are sharp edges, or shadows on the measurement object's surface.

For the phase-to-height calibration, an empirical calibration method was adopted. The method constructs a height (Z) calibration volume at the calibration stage. At the measurement stage, the height value of each point on the image is retrieved

individually using a linear interpolation technique. This approach effectively accounts for local distortion effects.

For the transversal calibration, X and Y calibration volumes are also constructed at the calibration stage. At the measurement stage, the height value of each point within the image is used to obtain the X and Y coordinates, again by using a linear interpolation technique.

The following chapter presents the specifications of the system that has been produced during this research programme, along with a quality assurance analysis to determine the degree of precision this system can practically offer. Additionally, two real-life applications of this system are reviewed, in order to show its full capability and its significant level of adaptability, so that it is able to meet the requirements of different surface measurement applications.

3.6 References

BRADSKI, G. & KAEHLER, A. 2008. *Learning OpenCV*, O'Reilly Media.

FORNBERG, B. & ZUEV, J. 2007. The Runge phenomenon and spatially variable shape parameters in RBF interpolation. *Computers & Mathematics with Applications,* 54, 379-398.

GAI, S. & DA, F. 2010. A novel phase-shifting method based on strip marker. *Optics and Lasers in Engineering,* 48, 205-211.

GUO, H., HE, H., YU, Y. & CHEN, M. 2005. Least-squares calibration method for fringe projection profilometry. *Optical Engineering,* 44, 033603-9.

HALIOUA, M. & LIU, H.-C. 1989. Optical three-dimensional sensing by phase measuring profilometry. *Optics and Lasers in Engineering,* 11, 185-215.

HU, Q. & HARDING, K. G. 2007. Conversion from phase map to coordinate: Comparison among spatial carrier, Fourier transform, and phase shifting methods. *Optics and Lasers in Engineering,* 45, 342-348.

HU, Q., HUANG, P. S., FU, Q. & CHIANG, F.-P. 2003. Calibration of a three-dimensional shape measurement system. *Optical Engineering,* 42, 487-493.

JIA, P., KOFMAN, J. & ENGLISH, C. 2007. Comparison of linear and nonlinear calibration methods for phase-measuring profilometry. *Optical Engineering,* 46, 043601-10.

LILLEY, F., LALOR, M. J. & BURTON, D. R. 2000. Robust fringe analysis system for human body shape measurement. *Optical Engineering,* 39, 187-195.

LIU, H., SU, W.-H., REICHARD, K. & YIN, S. 2003. Calibration-based phase-shifting projected fringe profilometry for accurate absolute 3D surface profile measurement. *Optics Communications,* 216, 65-80.

QUAN, C., HE, X. Y., WANG, C. F., TAY, C. J. & SHANG, H. M. 2001. Shape measurement of small objects using LCD fringe projection with phase shifting. *Optics Communications,* 189, 21-29.

QUAN, C., TAY, C. J. & CHEN, L. J. 2007. A study on carrier-removal techniques in fringe projection profilometry. *Optics & Laser Technology,* 39, 1155-1161.

REEVES, M., MOORE, A. J., HAND, D. P. & JONES, J. D. C. 2003. Dynamic shape measurement system for laser materials processing. *Optical Engineering,* 42, 2923-2929.

SALVI, J., ARMANGUÉ, X. & BATLLE, J. 2001. A comparative review of camera calibrating methods with accuracy evaluation. *Pattern Recognition,* 35, 1617-1635.

SPAGNOLO, G. S., GUATTARI, G., SAPIA, C., AMBROSINI, D., PAOLETTI, D. & ACCARDO, G. 2000. Contouring of artwork surface by fringe projection and FFT analysis. *Optics and Lasers in Engineering,* 33, 141-156.

SRINIVASAN, V., LIU, H. C. & HALIOUA, M. 1985. Automated phase-measuring profilometry: a phase mapping approach. *Appl. Opt.*, 24, 185-188.

SUTTON, M., ZHAO, W., MCNEILL, S., SCHREIER, H. & CHAO, Y. 2001. Development and assessment of a single-image fringe projection method for dynamic applications. *Experimental Mechanics,* 41, 205-217.

TAVARES, P. J. & VAZ, M. A. 2007. Linear calibration procedure for the phase-to-height relationship in phase measurement profilometry. *Optics Communications,* 274, 307-314.

TSAI, R. Y. Year. An Efficient and Accurate Camera Calibration Technique for 3D Machine Vision. *In:* Proceedings of IEEE Conference on Computer Vision and Pattern Recognition, August 1986 1986 Miami Beach, FL. IEEE, 364-374.

TSAI, R. Y. 1987. A versatile camera calibration technique for high-accuracy 3D machine vision metrology using off-the-shelf TV cameras and lenses. *IEEE Journal of Robotics and Automation,* RA-3, 323-344.

WILLSON, R. 1995. *Tsai Camera Calibration Software* [Online]. Available: http://www-2.cs.cmu.edu/afs/cs.cmu.edu/user/rgw/www/TsaiCode.html [Accessed 22 Apr 2007].

WYLER-AG. 2009. *Clinotronic Plus* [Online]. Available: http://www.wylerag.com/pages_eng/e4_331.html [Accessed 10 Feb 2010].

ZAPPA, E. & BUSCA, G. 2009. Fourier-transform profilometry calibration based on an exhaustive geometric model of the system. *Optics and Lasers in Engineering,* 47, 754-767.

ZHANG, S. & YAU, S.-T. 2006. High-resolution, real-time 3D absolute coordinate measurement based on a phase-shifting method. *Opt. Express,* 14, 2644-2649.

ZHANG, X., YUCHI, L., MEIRONG, Z., XIAOBING, N. & YINGUO, H. 2005. Calibration of a fringe projection profilometry system using virtual phase calibrating model planes. *Journal of Optics A: Pure and Applied Optics,* 7, 192.

ZHANG, Z., ZHANG, D. & PENG, X. 2004. Performance analysis of a 3D full-field sensor based on fringe projection. *Optics and Lasers in Engineering,* 42, 341-353.

Chapter Four

Specifications and Applications of the System

This chapter is devoted to presenting the features and the operational specifications of the fringe profilometry system that was developed during this research programme for 3D surface measurement. The chapter presents the algorithms and techniques that were adopted to perform the measurements, the types of supported measurement processes, the features provided for user interaction with the system hardware and the measurement process, and the available choices for visualising and/or storing the resultant data. The precision of the measurements obtained using this system is investigated in a dedicated quality assurance section, in terms of the repeatability and reproducibility of the system results. An analysis section is also included investigating thermal effects caused by heat dissipation in the sensor's projection hardware components in terms of the effect and impact upon the accuracy of the reconstructed 3D surface.

Finally, two real-life applications of this system are reviewed, in order to show its full capability and its significant adaptability so that it is able to meet the requirements of different surface measurement applications.

4.1 Specifications of the System

The system that was produced in this research programme has several advantages and characteristics, and these are as follows:

1. The system produces a multi-view 3D surface reconstruction with an accuracy of better than 0.5mm, with an XY sample point density of less than $0.7mm^2$ (0.64mm in X-axis and 1.07mm Y-axis; for measurement of a field-of-view of 330×550mm, with a grabbing resolution of 512×512 pixels and video projector resolution of 1024×768 pixels). In addition, the ability to measure dynamic events at a speed of up to 12Hz (using FTP for fringe analysis and Goldstein's branch-cut algorithm for phase unwrapping).

2. The ability to perform multipurpose optical profilometry, which enables qualitative and quantitative analysis of fringe patterns using a wide-ranging catalogue of fringe profilometry methods and techniques. Each technique has a great variety in terms of their processing parameters and hence this provides numerous paths of processing combinations for performing both static and dynamic surface measurements. The system can measure both full-field objects and partial-field objects.
3. A visual and interactive design, which enables the operator to interact with the system and to select the best possible combinations of processing methods and their parameters to meet the measurement requirements of an intended application.
4. Qualitative inspection, which is offered by means of the optional displaying of images of the results of the all processing stages of surface measurement process. In addition, the 3D rendering of the resultant reconstruction of object's surface.
5. Quantitative inspection, which is offered through the production of a cross-sectional graph plotting for the images of the individual processing stages and also for the final results of measurement process. The final measurement results are available as a full 3D point cloud height-map. In addition, the ability to store those images to be reviewed and further investigated using other programs.
6. Scalability, which is provided through the ability to perform the measurement either as a single-view approach using one of the single Sensor Processing Units (SPUs), as illustrated in Figure 4.2, or by using a multi-sensor approach in multi-view mode, running at the Central Measurement Server (CMS), as shown in Figure 4.1.
7. Adaptability, which is provided through the ability of the software system to automatically detect and adapt the available hardware resources (processors and memory), in order to optimise the measurement process.
8. The modular structure of the software (as discussed in Chapter Six) that provides the ability of achieving a desired 3D surface measurement for a specific application in the most efficient manner available for a given set of hardware resources.

4.1.1 Specifications of Measurement

Due to the significant flexibility of measurement available to the operator when using this system (in terms of the variety of available measurement algorithms and settings), the measurement specifications are mainly dependent on the following factors:

1. The intended application, which determines the combination of measurement algorithms that are used. For instance, when measuring dynamic objects; if an application favours speed over accuracy, then measurement speeds of up to 12Hz can be achieved; on the other hand, if accuracy is favoured over speed, then up to 5.35Hz measurement speeds can be achieved.
2. Elevation range of the calibration table, which for the current system is 500mm (see Section 5.4). The system can only produce accurate measurements for an object that lies within the bounds of the maximum volume over which the system was calibrated. Hence, the maximum height range that can be accurately measured is 500mm, i.e. the maximum calibration volume height, which is defined during the system calibration process, as discussed in Section 7.6. This applies also to the X and Y measurement ranges.
3. The system geometry (see Chapter Five), which directly determines the XY sample density of the reconstructed surface. The following factors determine the sample density of measurement:
    a. Zoom and focus settings of the camera lens, which is used to cover the required field-of-view of the measurement, and without compromising the depth-of-field; where a higher zoom setting for the camera lens enables the measurement to produce a greater sample density.
    b. Resolution of the projector display and zoom settings of the projector lens, where a higher display resolution (Section 5.1.1) and/or a lower zoom setting for the projector lens enables the measurement to produce a greater sample density.
    c. Working distance, which is the distance between the camera sensor and the measurement object; where a shorter working distance enables a higher sample density.

4. The physical Characteristics of the measurement object, such as: the object colour; for example in multi-view measurement of a dark coloured object, the image grabbing speed is slower than is the case for a light coloured object, because a higher exposure time for the camera sensor is needed. This directly affects the triggering frequency for synchronising the sensors (see Section 5.3). Hence, the level of light irradiance from the object's surface that reaches the camera(s) directly affects the measurement speed. Additionally, the object's curvature; where if it is higher than the maximum measurable curvature (see Appendix A3) then the fringe pattern will coalesce, hence, an invalid surface reconstruction will be produced.

The system is robust, in that the measurement process is stable and does not crash during the performance of a measurement. The accuracy of measurement is reliable, as the system has been tested against a set of Coordinate Measuring Machine (CMM) scan data that was measured using an NVision 3D laser scanner with an overall measurement accuracy of 10 microns (NVision, 2008). In addition, the validity of the pre-calibrated data of the system can be preliminarily verified by a simple visual inspection of the results of a multi-view measurement; wherein, if the calibration data are valid, then the reconstructed surface data using two or more sensors should overlay over each other (as discussed in Section 8.4.2).

The general measurement specifications for the system setup, as explained in Chapter Five, are shown below, whereas the sensor's camera (with an ROI resolution of 512×512 pixels) and the video projector (with a display resolution of 1024×768 pixels) are located approximately 2.7m and 2.9m from the artefact, respectively.

Z accuracy	< 0.5 mm
Z Precision (see Section 4.2):	
Repeatability	± 0.353 mm
Reproducibility	± 0.452 mm
Heat stability	± 0.092 mm
Number of sampled XYZ points	> 260,000 x,y,z points per sensor > 780,000 x,y,z points for all sensors
Measurement speed	≤ 12 Hz for single-view measurement ≤ 6 Hz for multi-view measurement

Number of measured XYZ points/second	≤ ~3.0 million x,y,z points/sec per sensor ≤ ~4.6 million x,y,z points/sec for all sensors
Field of view	≤ 330 mm × 550 mm
Spatial resolution XY mm/point	≤ 0.64 mm × 1.07 mm per x,y point
Coverage area	~220° around the object's volumetric centre
Maximum measurable body curvature	88° using single-sensor (See Appendix A3) > 90° using multi-sensor

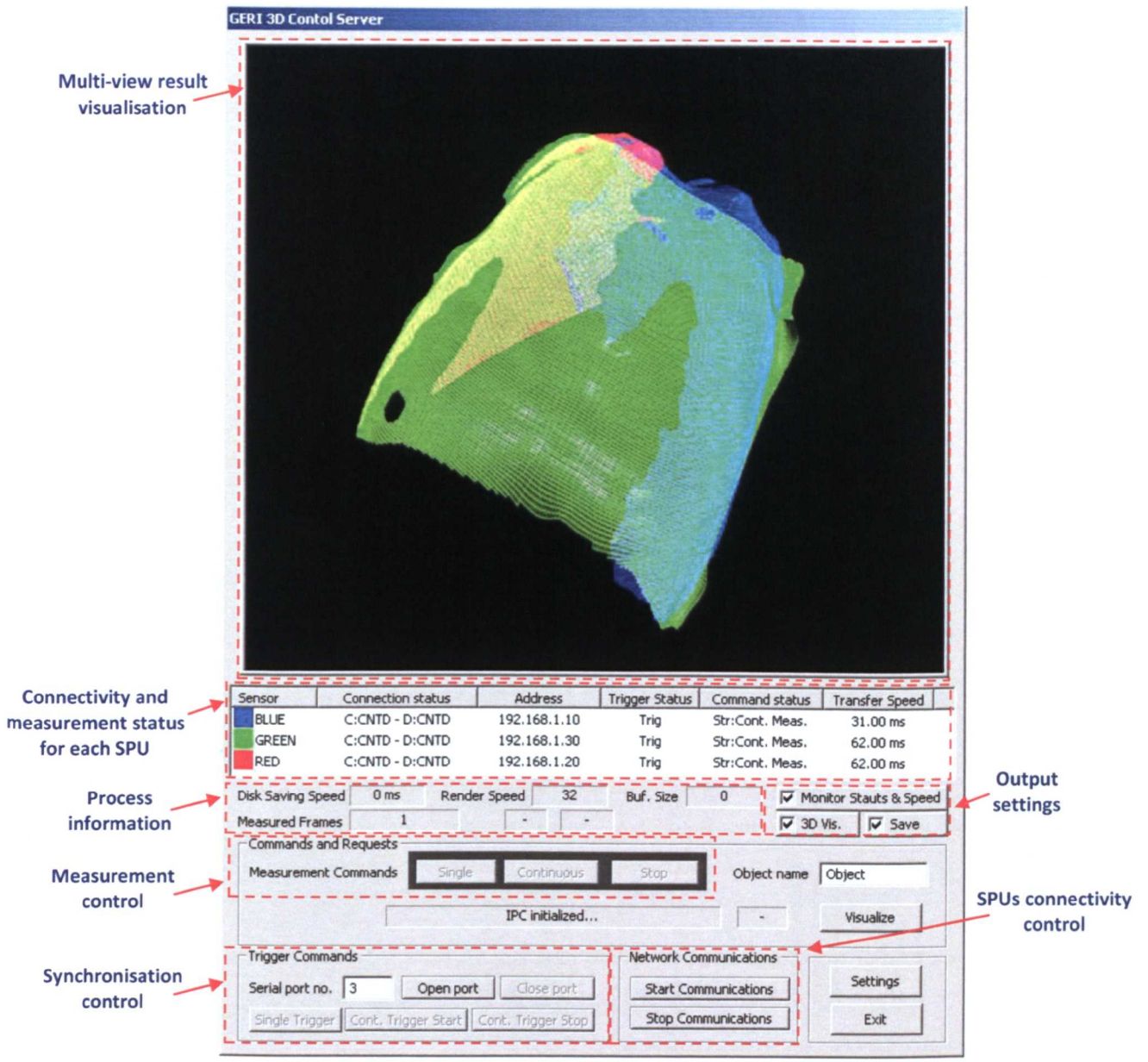

Figure 4.1 A screen capture for the CMS software that was developed by the author, showing a sample multi-view measurement process using a multi-sensor approach. The result of the surface reconstruction from each SPU is dynamically transferred to the CMS during the measurement process.

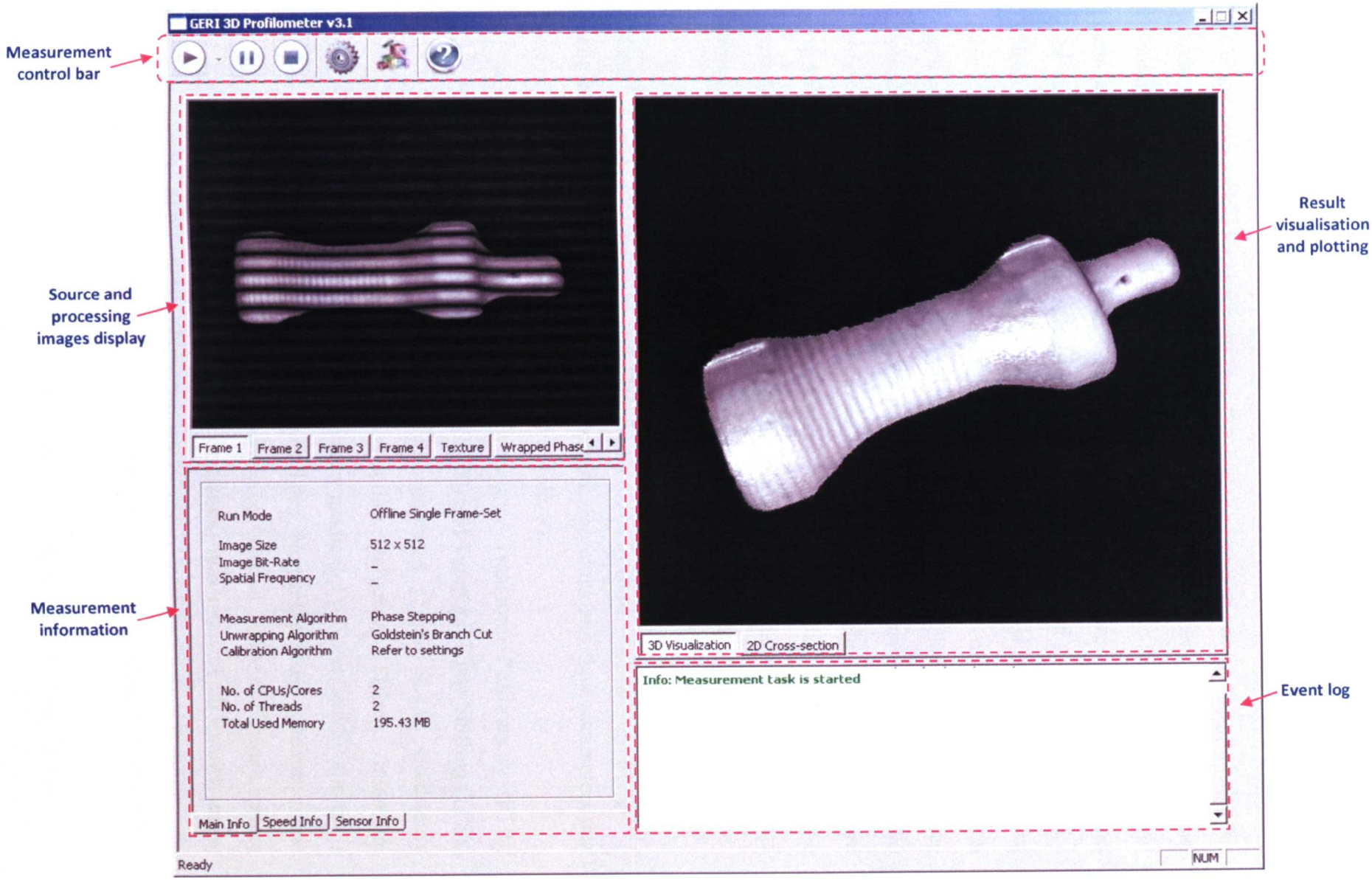

Figure 4.2 A screen capture for the software at each SPU as developed by the author, showing a sample single-view measurement process using a single-sensor approach.

It can be noticed from the measurement specifications that are listed above that the measurement speed degrades when using the multi-sensor measurement mode. This is due to the network transfer latency that is imposed by the network communications between the CMS and SPUs. As illustrated in Section 6.2.2, the CMS is responsible for synchronising the overall measurement process, and also for collecting the measurement results from the SPUs. Experimentally, the author has found that the network transfer latency ranges from 30ms to 85ms per frame, and this depends mainly upon the speed of the measurement process at each SPU and on the size of the measurement results that are being transferred to the CMS from the SPUs. It was found that a higher processing speed at the SPUs (and/or larger size of the measurement result data being transferred) slowed down the synchronisation process at the CMS, which in turn caused a processing bottleneck and hence introduced higher network transfer latency. At the worst case scenario, the processing bottleneck at the CMS end was found to reduce the measurement speed by 50%. However, because there are three sensors that are acting in parallel when the system is in multi-sensor mode, the overall measurement speed is approximately 1.5 times faster (i.e. 3 × 50%) than the single-sensor mode in terms of points measured.

4.1.2 Adopted Techniques and Algorithms of the System

The catalogue of fringe analysis measurement algorithms and their parameters that are offered by the system, are categorised as follows:

A. For fringe analysis (Figure 4.3): Fourier Transform Profilometry (FTP), Wavelet Transform Profilometry (WTP) and Temporal Phase Shifting (TPS).

B. For phase unwrapping algorithms supported (Figure 4.4a): Goldstein's branch-cut, Quality-guided, Reliability ordering, Flynn's minimum discontinuity, Preconditioned conjugate gradient, Lp-Norm, and Synthesis.

C. For quality map generation (Figure 4.4b): Maximum phase gradient, phase derivative variance, pseudo correlation, second phase difference, phase derivative variance and pseudo correlation, maximum of all quality maps, average of all quality maps, average of phase derivative variance and pseudo correlation, multiplication of all quality maps, and minimum of all quality maps.

D. For calibration (Figure 4.5): as described in Section 3.2 and Section 3.4.

This diversity of supported measurement methods enables the reconstruction of 3D information through 183 possible main combination paths. In addition, each fringe analysis method has its own processing parameters, which offers high flexibility to fit the requirements of various measurement applications.

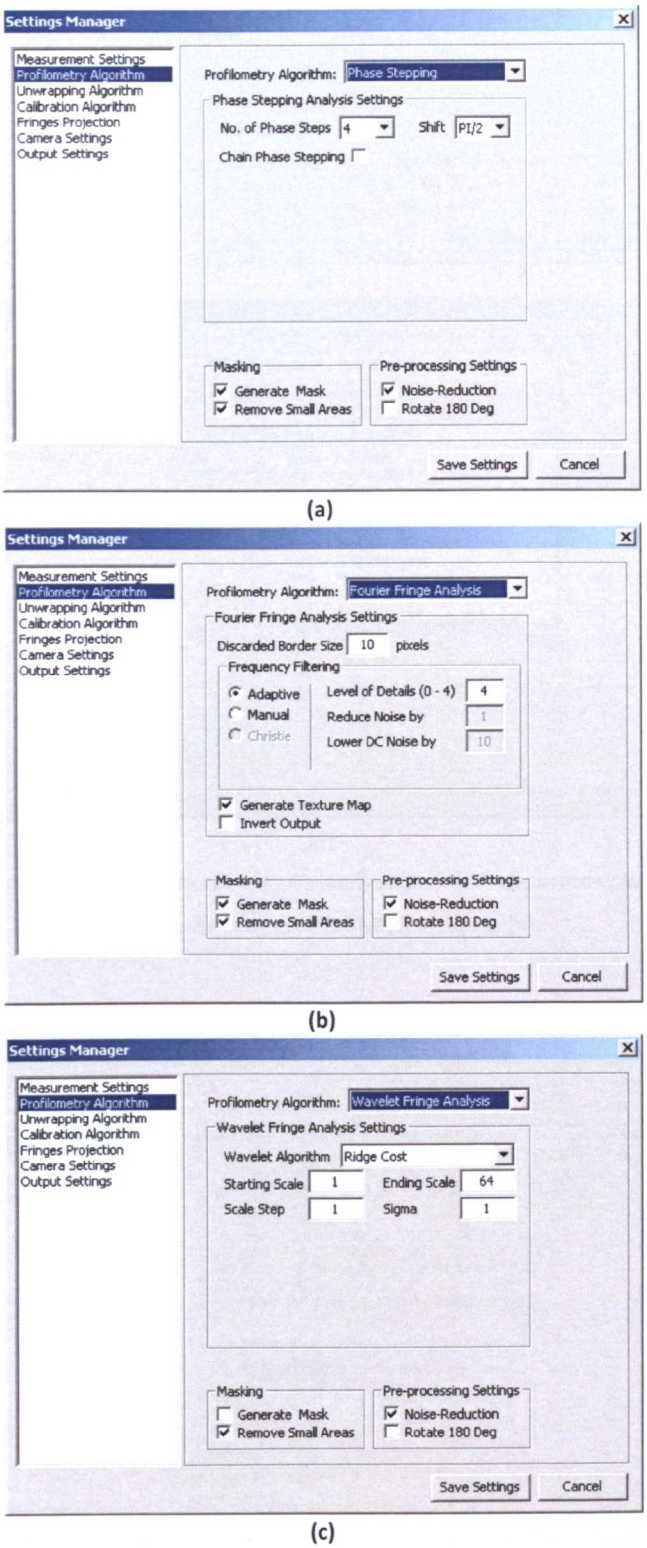

Figure 4.3 Screen captures for the settings dialog-boxes of the fringe analysis algorithms supported by this system: (a) TPS algorithm, (b) FTP, and (c) WTP.

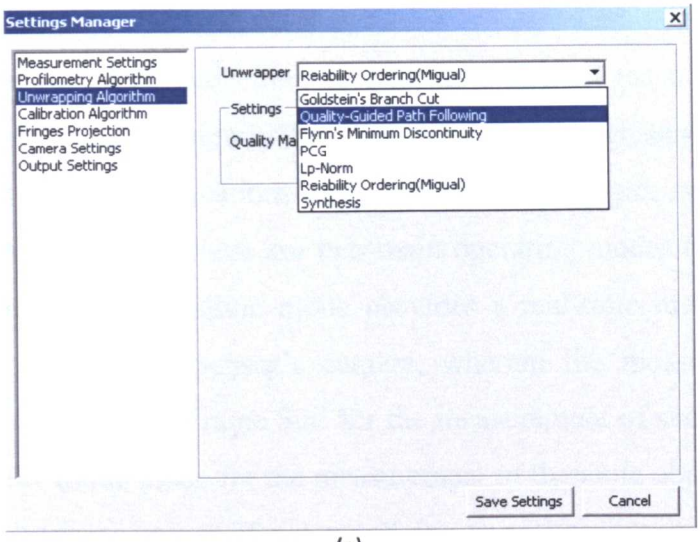

(a)

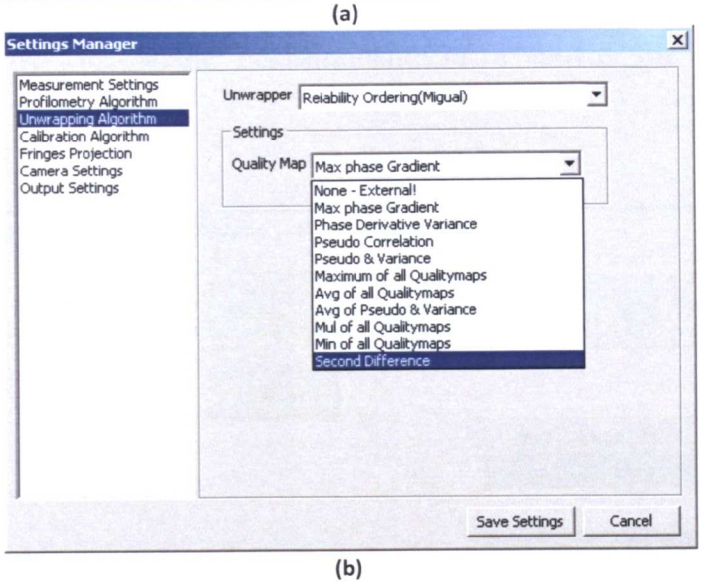

(b)

Figure 4.4 Screen captures for the system settings dialog-boxes of the supported unwrapping algorithms (a) and quality map generation techniques (b).

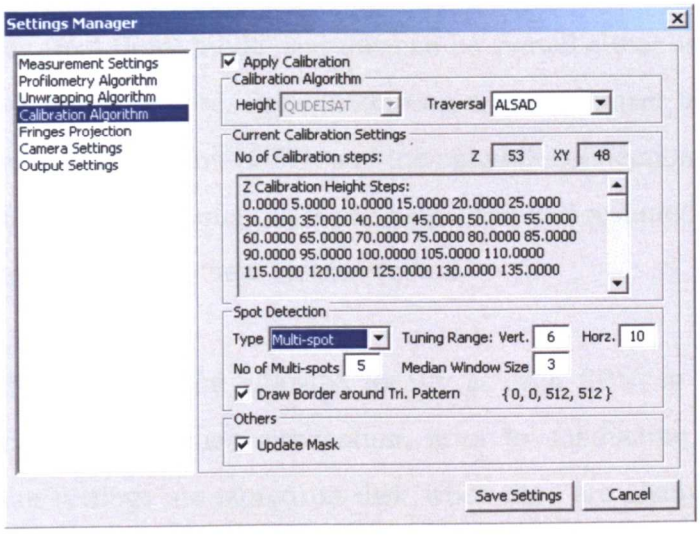

Figure 4.5 A screen capture for the dialog-box of the calibration settings and processing parameters.

4.1.3 Measurement Control and Settings

Measurement can be performed either locally at each SPU (as a single-view) or remotely via the CMS (multi-view). This approach offers a high scalability, in terms of using the system for applications that require either single, or multiple view measurements. At each SPU, there are two main operating modes (see Figure 4.6); 'Online' and 'Offline'. The online mode provides a real-time measurement from images grabbed live by the sensor's camera, wherein the measurement can be conducted either as a 'Single Frame Set' for the measurement of static objects, or in 'Continuous' multi-frame mode for the measurement of dynamic objects. The offline mode enables the measurement of pre-saved fringe pattern images, either using a single set of files for single measurement, or a movie file for continuous measurement.

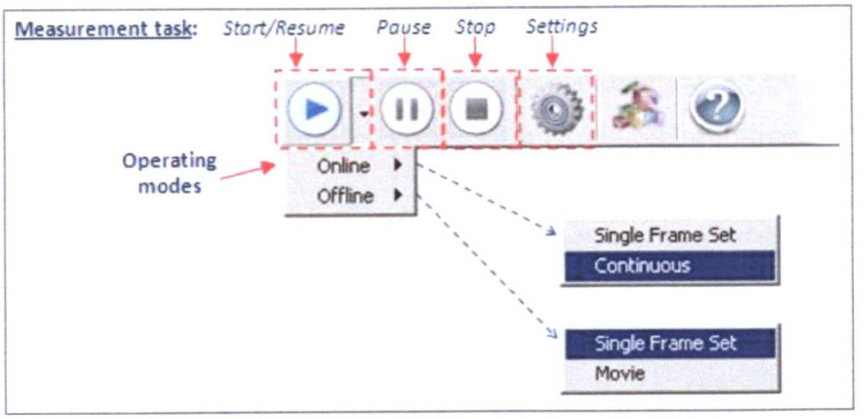

Figure 4.6 Measurement control and settings at each SPU.

On the other hand, multi-view measurement at the CMS (see Figure 4.1) is only available in online (real-time) mode, and this can be started either as a single frame, or continuous live frame capture. Prior to starting a measurement task at the CMS, the Camera Synchronisation Unit (CSU) and the network connections with the SPUs must be initiated. The measurement task can be paused and resumed by the operator for both single-view and multi-view measurements.

Measurement settings can to be adjusted locally at each SPU, in order to fit the desired requirements of a certain application, prior to conducting a measurement task. Measurement settings are stored on disk when they are changed by the user, and the last set that was used is re-loaded when the SPU software starts.

4.1.4 User Interaction

The system offers an advanced user interface, which enables the user to interactively manipulate measurement settings and parameters to fit the intended requirements (as shown in Figure 4.3, Figure 4.4 and Figure 4.5). Besides the ability of changing measurement settings and parameters, the user can adjust the following additional settings according to the desired preferences:

1. General settings (Figure 4.7), such as size of input images and multi-sensor mode settings.
2. The characteristics of the projected fringe pattern (Figure 4.8a), such as spatial frequency. Also the display settings of the sensor's video projector.
3. Camera settings (Figure 4.8b), such as exposure time, gain value and triggering mode.
4. Output preferences (Figure 4.9), which are divided into three parts, the first part shows the choices of displaying processing images (as shown in Figure 4.12). The second part shows the settings for data saving on disk, and the third part shows the options for visualisation and graph plotting.

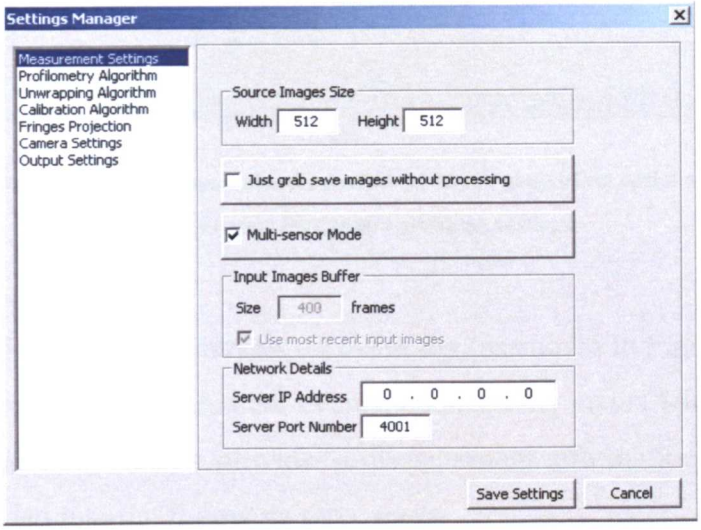

Figure 4.7 A screen capture for the general settings of a measurement task.

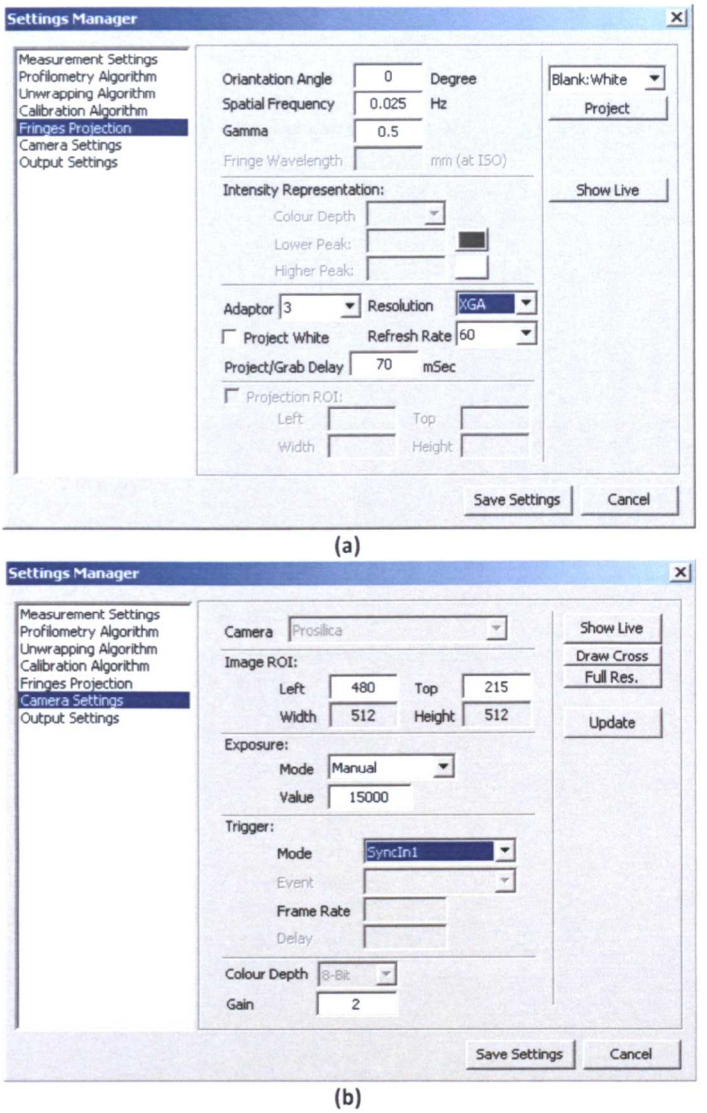

Figure 4.8 Screen captures for the settings dialog-boxes for: (a) Fringe generation options and video projector display settings, (b) Camera grabbing settings.

Moreover, the SPU software provides an event log (as shown in Figure 4.2) in order to notify the user about measurement events, connectivity status with the CMS and any errors encountered. Also, it provides a measurement information section (Figure 4.10) that is divided into the following three parts:

1. Main information, such as selected measurement algorithms and the available hardware resources.
2. Speed information, which in live mode shows the speeds of each stage of the measurement process, from image grabbing to output processing.
3. Sensor information, which continuously shows the status of the sensor components.

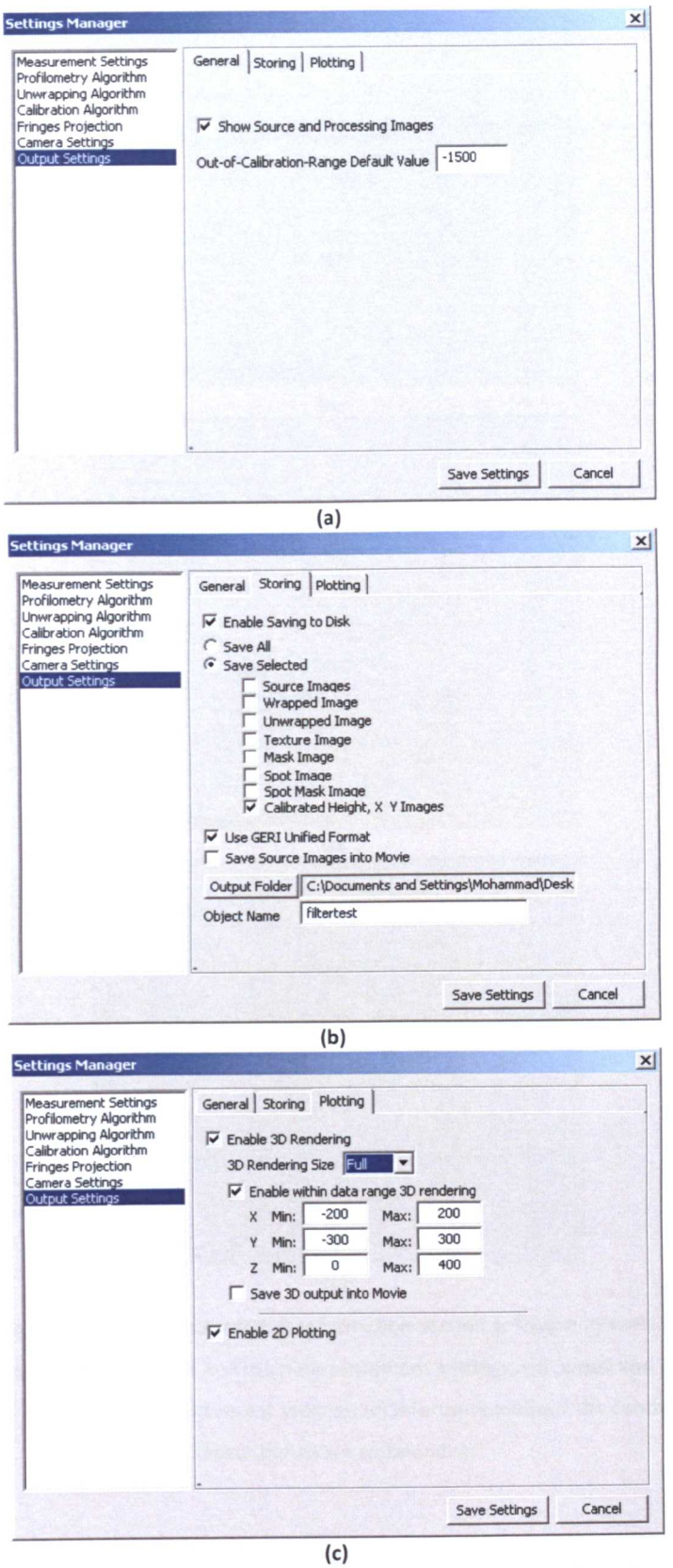

Figure 4.9 Screen captures for the available choices of output settings: (a) General output settings, (b) Storing to disk settings, (c) 3D visualisation settings.

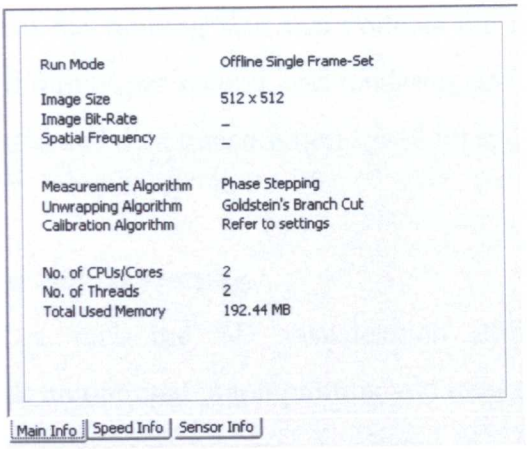

(a)

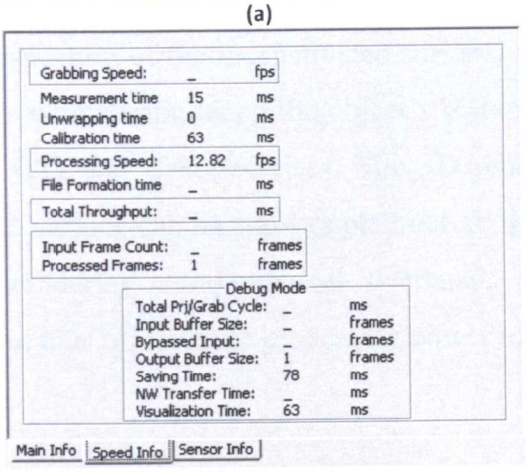

(b)

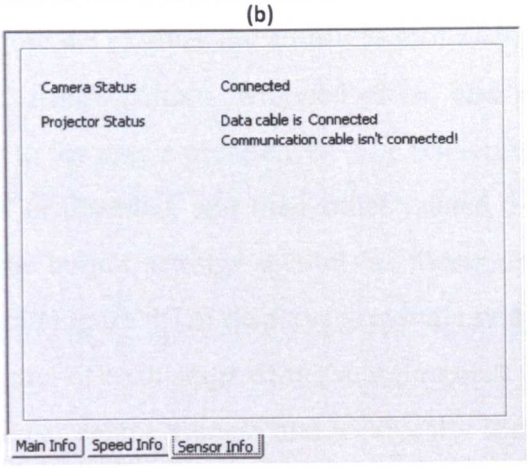

(c)

Figure 4.10 Screen captures for the measurement information section software at each SPU: (a) Information about processing system hardware and main measurement settings, (b) Speed and processing time information for each stage in the measurement process, (c) Information about the connectivity status of the sensor hardware components.

On the other hand, the CMS (Figure 4.1) provides the following user interaction facilities, in case of undertaking multi-view measurement:

1. 3D visualisation of the collected 3D information from the three SPUs.
2. The ability to change output settings, such as saving and visualising.

3. Information about the running task that collects the results from the SPUs, such as collected frames per second, and rendering and saving speeds.
4. Connectivity status and data transmission speed for each SPU.

4.1.5 3D Visualisation and 2D Plotting

The system includes a real-time 3D visualisation utility for the resultant measurements, alongside an optional graph plotting and image previewing capability for every stage in the measurement process. As shown in Figure 4.2, 3D rendering enables initial visual inspection of the reconstructed surface; it provides a variety of rendering choices, such as rendering using the object's texture and rendering within a specified range (of X,Y, and Z boundaries). The 3D rendering settings can be customised, wherein the surface can be sub-sampled before the rendering process in order to reduce the rendering computational overhead, which speeds up the visualisation process and thus offers more processing power to the core measurement process.

The 2D graph plot (Figure 4.11) gives the ability to plot a cross-section line (row or column) of the height, fringe pattern, wrapped phase and unwrapped phase data respectively, according to the user's preferences. The rendering and graph displaying options can be enabled or disabled, and their other related display settings may be adjusted, from inside the output settings section (as illustrated in Figure 4.9c). The image previewing utility (Figure 4.12) displays greyscale images of the input fringe pattern and also the results of each stage of the measurement process. This helps the user to examine the measurement process and to visually identify potential sources of any invalid reconstruction. As shown in Figure 4.9a, the image previewing feature can be enabled or disabled according to the user's preferences.

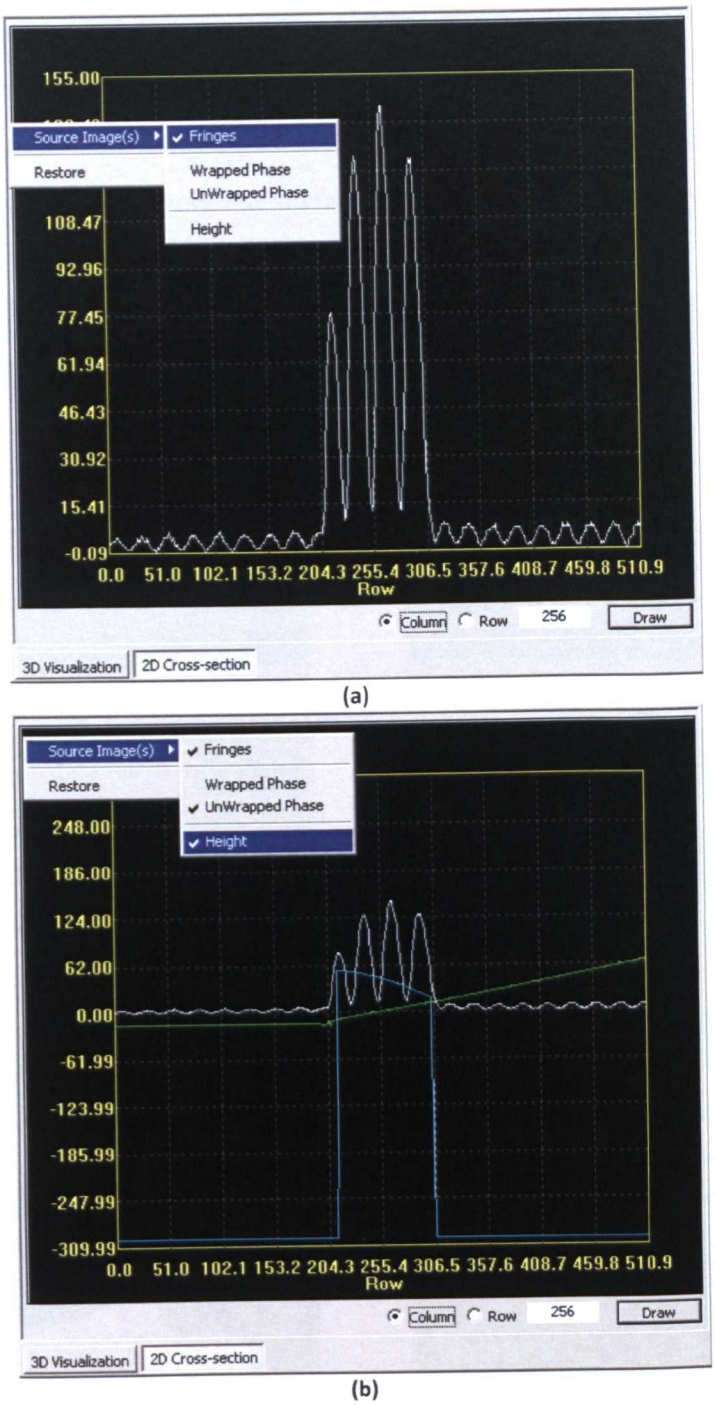

Figure 4.11 Screen capture for the cross-section graph plotting feature, showing the ability to select the number of the chosen row or column, in addition to the ability to select the source data to be plotted.

The CMS provides 3D visualisation of the collected multi-view measurements; each measurement is rendered using a different colour, which corresponds to the colour of the chromatic filters attached to the sensor head of each SPU, e.g. blue rendering colour is used for rendering the 3D information collected from the SPU with the blue chromatic filter. Because all of the three sensors are calibrated for their XY-coordinates using the same reference X and Y axis (as illustrated in Section 3.4), the

multi-view surface reconstructions are assumed to be overlaid and intersected with each other. In addition to affording a visual inspection, this approach helps in a preliminary validation of calibration; whereas in the case of an invalid calibration, this produces non-overlaid rendered surfaces.

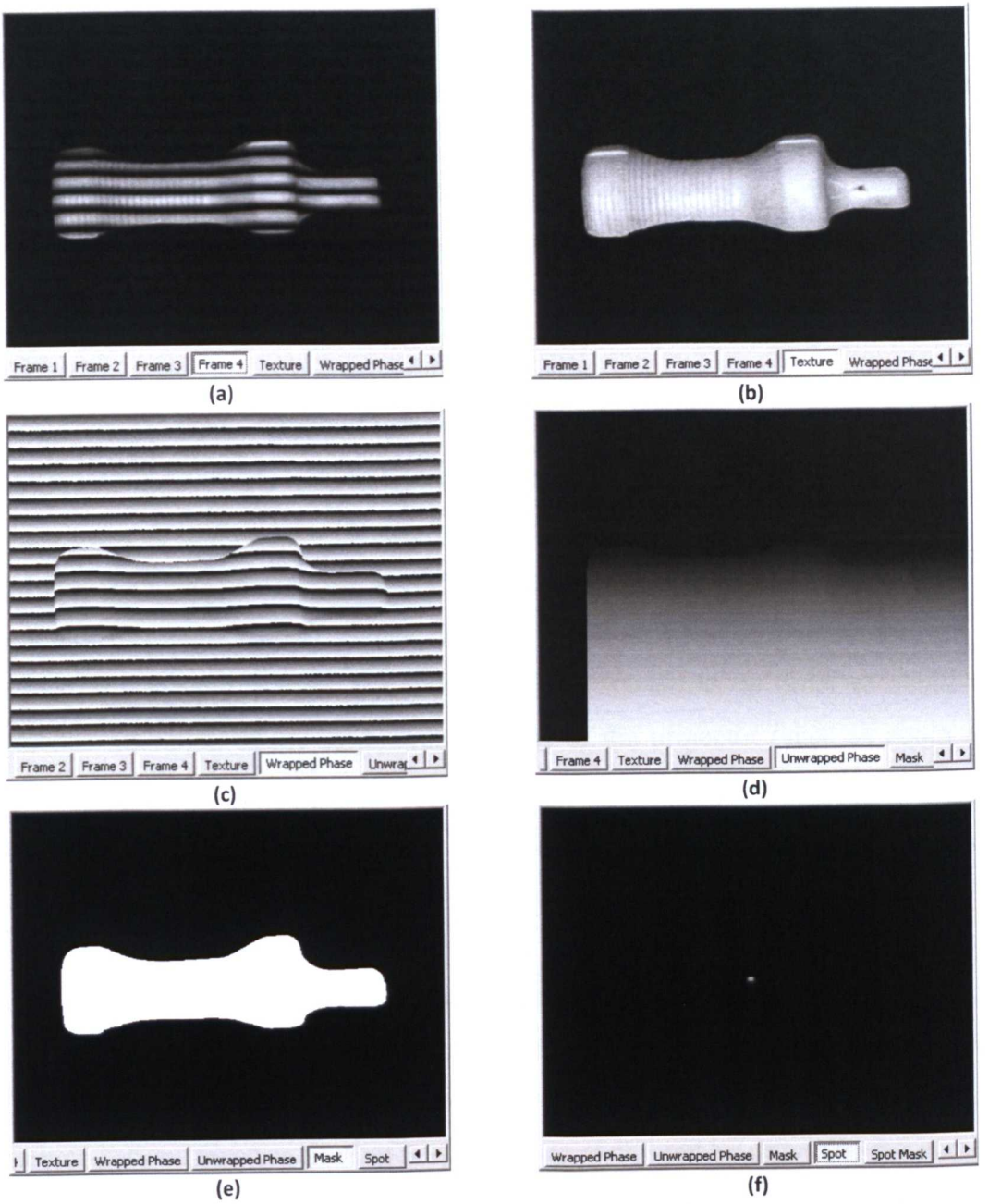

Figure 4.12 Screen captures for the 2D greyscale display of source and processing images: (a) Frame number four of a four-frame TPS, (b) generated texture map, (c) calculated phase map using TPS, (d) Unwrapped phase map, (e) generated mask map, and (f) triangulation spot image.

4.1.6 Storing of the Images

Storing of the measurement data and results is as necessary as the displaying capability, because it enables saving the data on disk for further analysis using other programs, or for future reprocessing using offline operating mode with the same, or different measurement settings. Figure 4.9b shows the variety of available choices for storing measurement data and results, whereas the data of each measurement stage can be selectively stored. Harvey *et al.* (2001) examined the effect of compression on fringe images to reduce the used disk space, and showed that the error introduced because of compression is about 0.14%. However, in this system source fringe pattern images are saved without any compression, either individually (as raw data or bitmap files), or as a video in a movie (AVI) file.

4.1.7 Sensor Hardware Control and Monitoring

The system provides software tools for manipulating the settings of the sensor hardware (projector and camera) independently at each SPU, performed via the system settings dialog box (Figure 4.8). Moreover, the sensor projector can be controlled remotely via the serial-port, using a specially developed programme by the author (see Figure 4.13). Hence, the projector's supplied remote control can be disabled and the programme can function as its substitute, in order to avoid the accidental alteration of the calibration settings of the projector (such as zoom and focus) by an unauthorised user. Additionally, the SPU programme provides a continuous monitoring of the sensor hardware. It automatically notifies the user about the status of both the projector and the camera.

The CMS programme enables direct control and monitoring of the network connections with the SPUs, by dynamically showing the status of these connections and data transmission speeds. It also controls the functionality of the Camera Synchronisation Unit (see Section 5.3), which is performed by providing the choices to start hardware camera triggering, either as a single, or as a continuous trigger. Single trigger option can be used to perform measurement only when the 'single trigger' button is clicked.

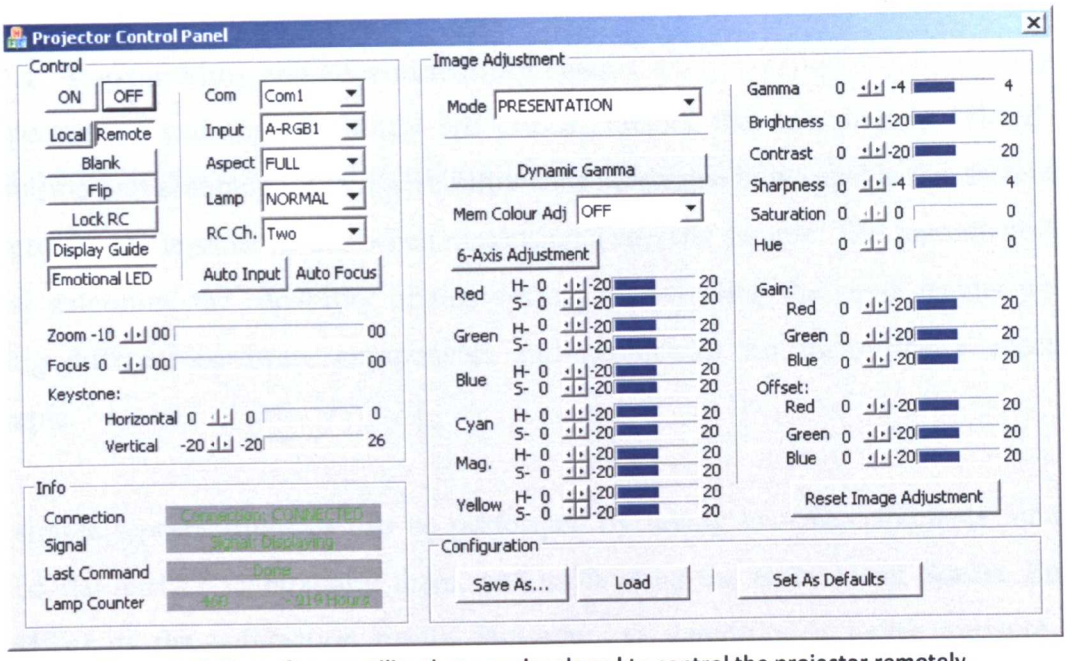

Figure 4.13 The software utility that was developed to control the projector remotely.

4.2 Quality Assurance

In order to determine the precision of reconstructed height information using this system, various quality assurance tests (repeatability, reproducibility and heat stability) were conducted by the author. This section reviews the details and results of these tests and provides quantitative measures of the degree of precision this system can offer.

For the all quality assurance tests in this section, the annotations for the implementations of the surface measurement are as follows:

- The size of the images acquired in all cases was 512×512 pixels, with a bit depth of 8bits.
- Spatial frequency: $f_0 = 0.0625\ ^{1}/_{\text{pixel}}$ (such that the fringe period is 16 pixels).
- Fringe analysis technique: the phase was demodulated using the four-frame phase shifting technique.
- Unwrapping algorithm: using the reliability ordering technique by Herráez *et al.* (2002).
- Phase-to-height conversion: using the adopted phase-to-height interpolation method (which is described in Chapter 3).

4.2.1 Repeatability and Reproducibility Tests

Repeatability and reproducibility are critical factors that are directly related to precision and accuracy. The repeatability tests determine how capable this system is of providing the same results when measuring a specific sample. The reproducibility tests determine the capability of this system of providing the same results when using different hardware components and geometries for measuring a specific sample.

A simple repeatability test can be performed by taking two measurements for the same flat surface, subtracting them, and calculating the Root Mean Square Error (RMSE) of the subtraction result. However, to determine a better measure of repeatability, the author conducted multiple set of measurements for a flat glass measurement plane, with its surface painted with matt white. A flat glass surface was used here so as to ensure that the reliability of the measurement was not affected in terms of the behaviour of the phase unwrapping algorithm, which may produce measurement errors if we were to use an object that has a surface shape that may produce residues (for example that exhibited abrupt changes in shape, shadows and holes, etc, in the object's surface).

The test consisted of 10 height measurement sets, where in each set the flat surface was consecutively measured twice over, and the measurements of each set are subtracted from each other. Hence, ten height deviation maps were obtained. The time between each of the two consecutive measurements within a single set was one second, and the time between each consecutive set of measurements was also one second, in order to eliminate any possibility of heat dissipation effects in the hardware. Measurements were performed after the projector had been switched on and running for one hour. The four-frame phase shifting method was used here for fringe analysis and the reliability ordering algorithm for phase unwrapping.

For each deviation map of each set of measurements, the following statistical calculations were performed: average error (Figure 4.14), RMSE (Figure 4.15), standard deviation (Figure 4.16), the probability of a reading lying within three standard deviations of the mean (Figure 4.17), and the percentage of the number of height deviation map points that were within ±0.5mm (Figure 4.18).

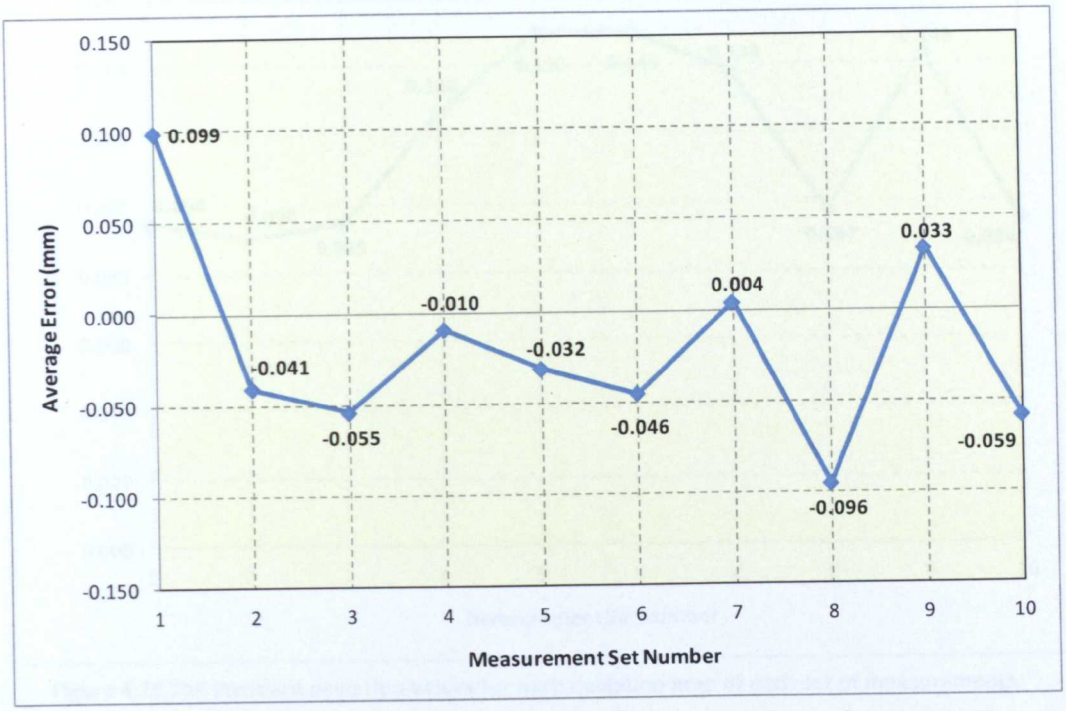

Figure 4.14 The calculated average error for each deviation map of each set of measurements.

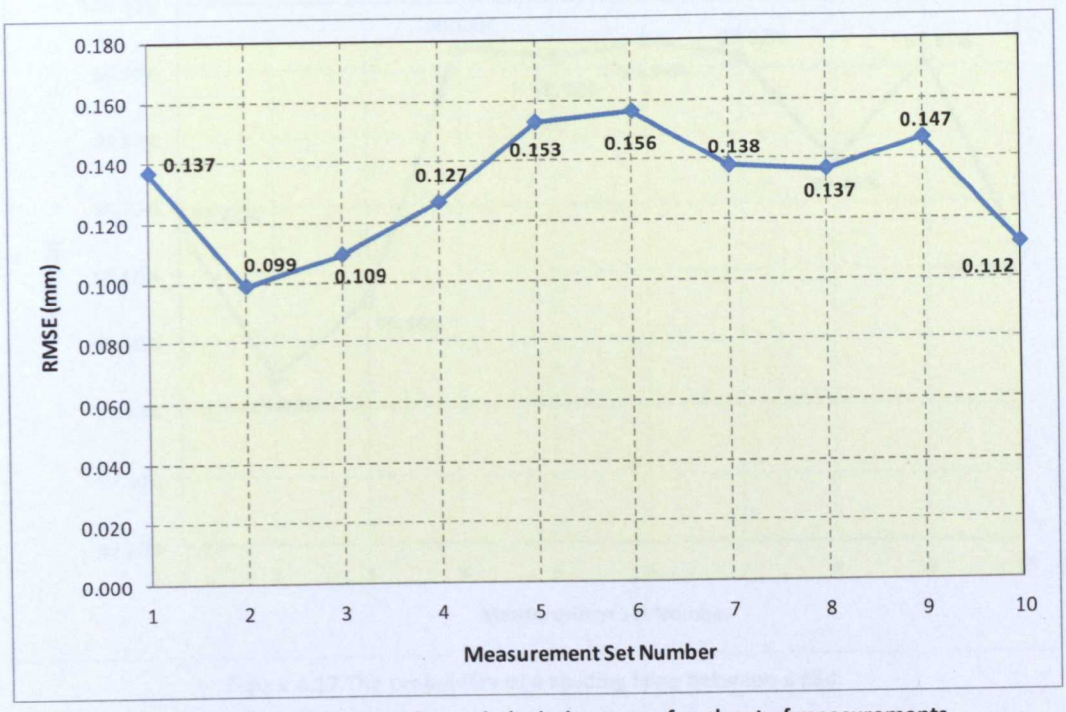

Figure 4.15 The RMSE values for each deviation map of each set of measurements.

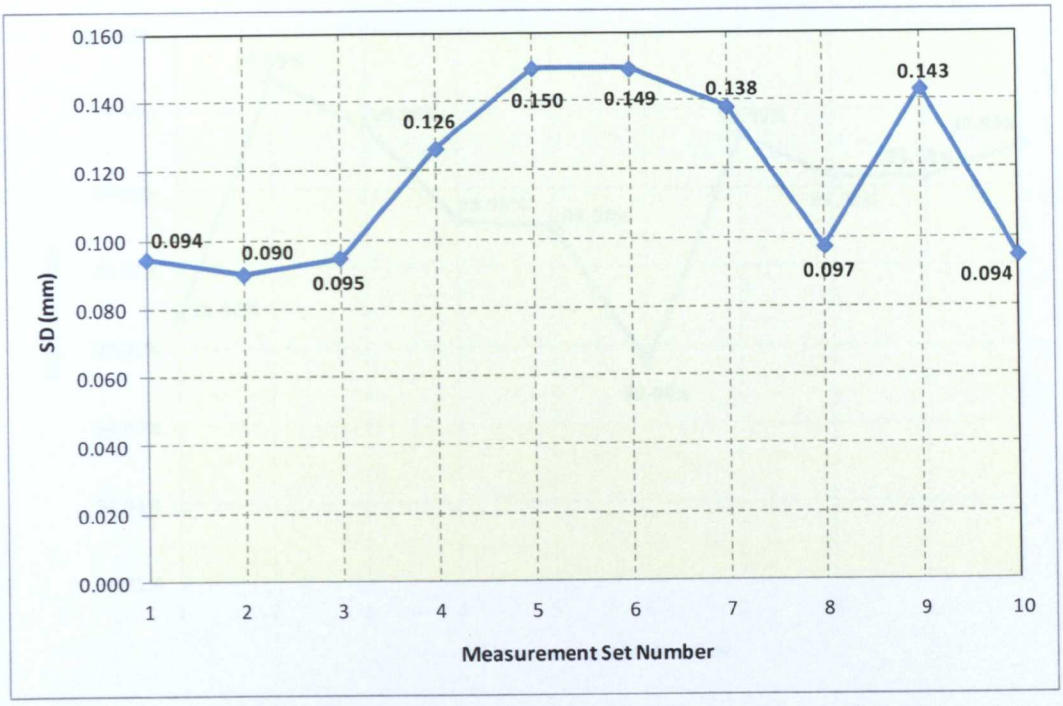

Figure 4.16 The standard deviation values for each deviation map of each set of measurements.

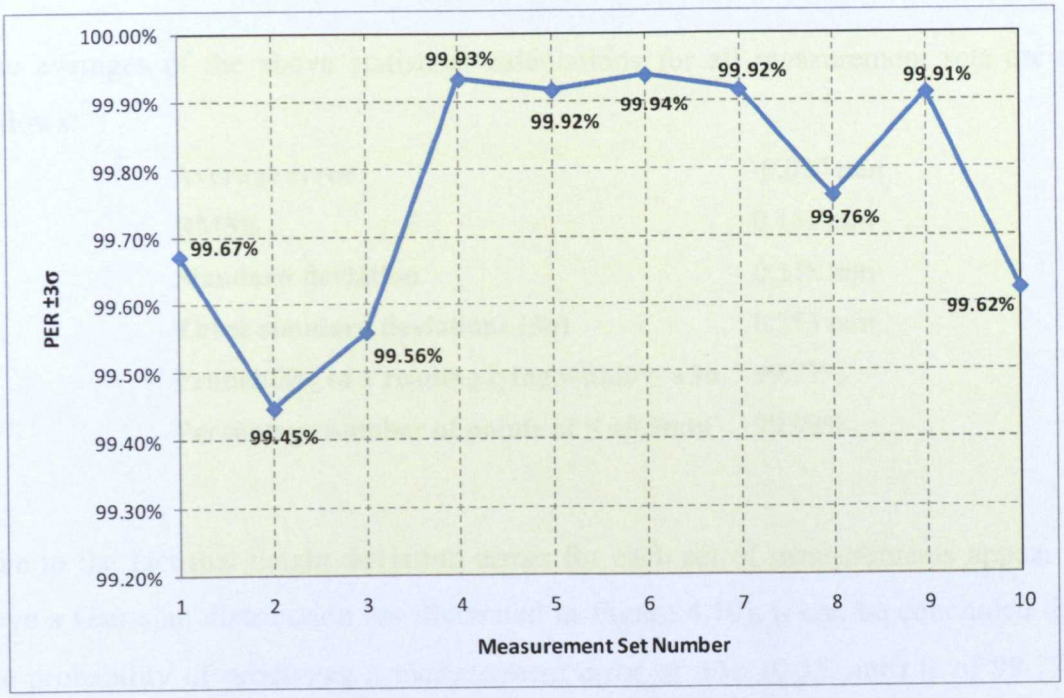

Figure 4.17 The probability of a reading lying between ≤ ±3σ.

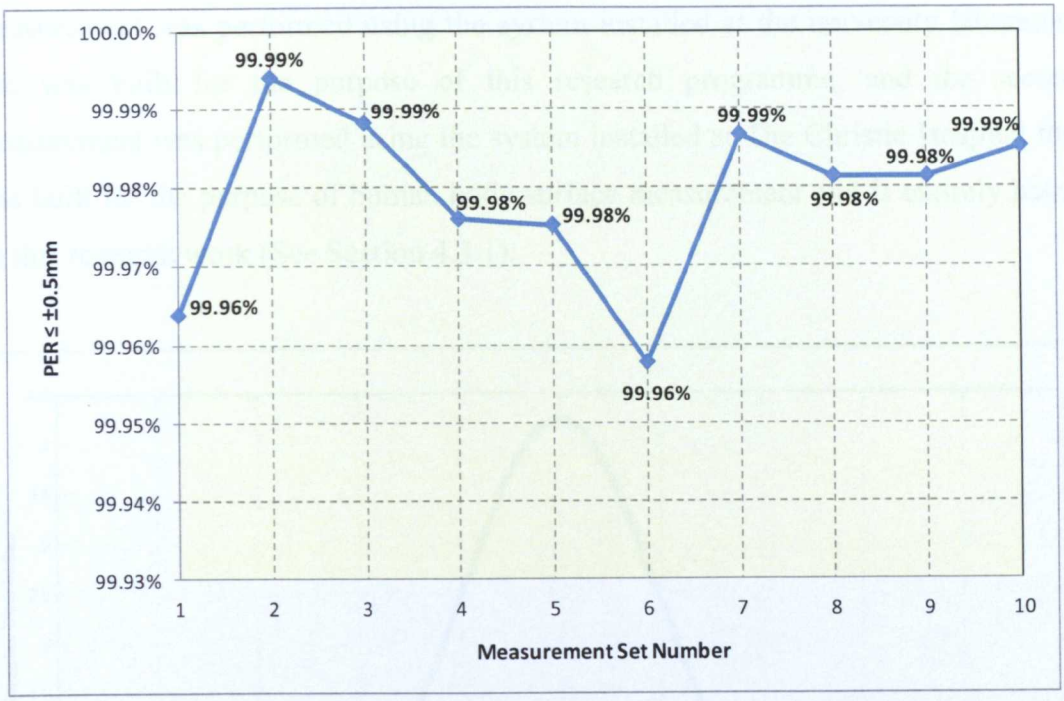

Figure 4.18 The percentage of the number of points that were within ±0.5mm, for each deviation map of each set of measurements.

The averages of the above statistical calculations for all measurement sets are as follows:

Average error	-0.020 mm
RMSE	0.131 mm
Standard deviation	0.118 mm
Three standard deviations (3σ)	0.353 mm
Probability of a reading lying within ≤ ±3σ	99.77%
Percentage number of points of ≤ ±0.5mm	99.98%

Due to the fact that height deviation errors for each set of measurements appear to have a Gaussian distribution (as illustrated in Figure 4.19), it can be concluded that the probability of producing a measurement error of ±3σ (0.353mm) is of 99.77% when the measurement is repeated for the same sample. Therefore, this test showed the repeatability of this system to be ±0.353mm.

Regarding the reproducibility test, a breast phantom cast was measured using two different systems with different sensor hardware components and geometries, but with the same make, model and specifications of system hardware. The first

measurement was performed using the system installed at the university laboratory that was built for the purpose of this research programme, and the second measurement was performed using the system installed at The Christie Hospital that was built for the purpose of human body surface measurement and is entirely based on this research work (See Section 4.3.1).

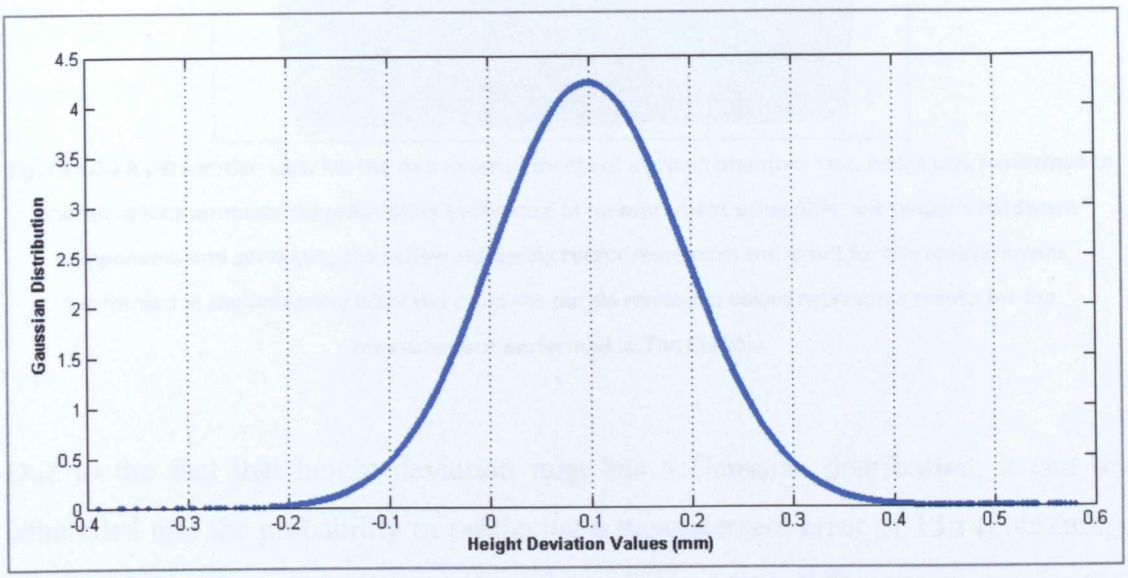

Figure 4.19 Gaussian distribution (or normal probability density function) of the first height deviation map, where it is apparent that the height deviation errors have a Gaussian distribution.

Figure 4.20 shows the results of the two measurements. A deviation map was calculated by subtracting the two results and the statistical characteristics for the difference were calculated, which are as follows:

Average error	-0.008 mm
RMSE	0.151 mm
Standard deviation	0.151 mm
Three standard deviations (3σ)	0.452 mm
Probability of a reading lying within ≤ ±3σ	98.68%
Percentage number of points of ≤ ±0.5mm	99.09%

Figure 4.20 A perspective view for the two measurements of a breast phantom cast, which was performed to calculate measurement reproducibility in the case of measurement using different sensor's hardware components and geometry; the yellow rendering colour represents the result for the measurement performed at the university laboratory and the purple rendering colour represents results for the measurement performed at The Christie.

Due to the fact that height deviation map has a Gaussian distribution, it can be concluded that the probability of producing a measurement error of $\pm 3\sigma$ (0.452mm) is of 98.68% when measurement is performed using two different systems for the same sample. Therefore, this test showed the reproducibility of this system to be ± 0.452mm.

4.2.2 Heat Stability Test

This system uses a video projector to generate and project fringe patterns onto an object being measured, as was discussed at length under Section 2.2 and Section 5.2.1. However, the video projector that was used was made out of plastic and basically optimised for office presentations or home uses, rather than for a scientific application. Thus, due the dissipated heat from projector's lamp, or electronic components, any drifts in image projection position and changes in light levels may have a great impact on the accuracy of the measurement performed using this projector in an optical profilometry system. Hence, a heat stability test was carried out, in order to study the effects of the dissipated heat of the projector used within this system, in terms of the accuracy of 3D surface reconstruction.

Measurement was performed over one entire day for a flat glass surface, painted matt white, and as the following time line: exactly at the time when the projector is turned on (zero hours and zero minutes, i.e. 0H:0M) when theoretically there was no heat effect yet on the measurement result, at 0H:15M, at 0H:30M, at 1H:0M, and then at every next hour until 24H:0M (one day) from the time when the projector was turned on. This produced a total of 16 height measurement results. By conducting this investigation into testing the thermal effects on the stability of the measurement results, the ideal time period to perform a measurement can therefore be determined.

The first measurement result (which was performed at 0H:0M) was used as a reference surface, and then all of the 16 measurements were subtracted from it in order to obtain 16 different height deviation maps. Then for each height deviation map, the following statistical calculations were performed: average error (Figure 4.21), RMSE (Figure 4.22), and percentage of the number of height deviation map points that were within ±0.5mm (Figure 4.23). The calculated averages of these results are as follows:

Average error	0.007 mm
RMSE	0.204 mm
Percentage number of points of ≤ ±0.5mm	98.16%

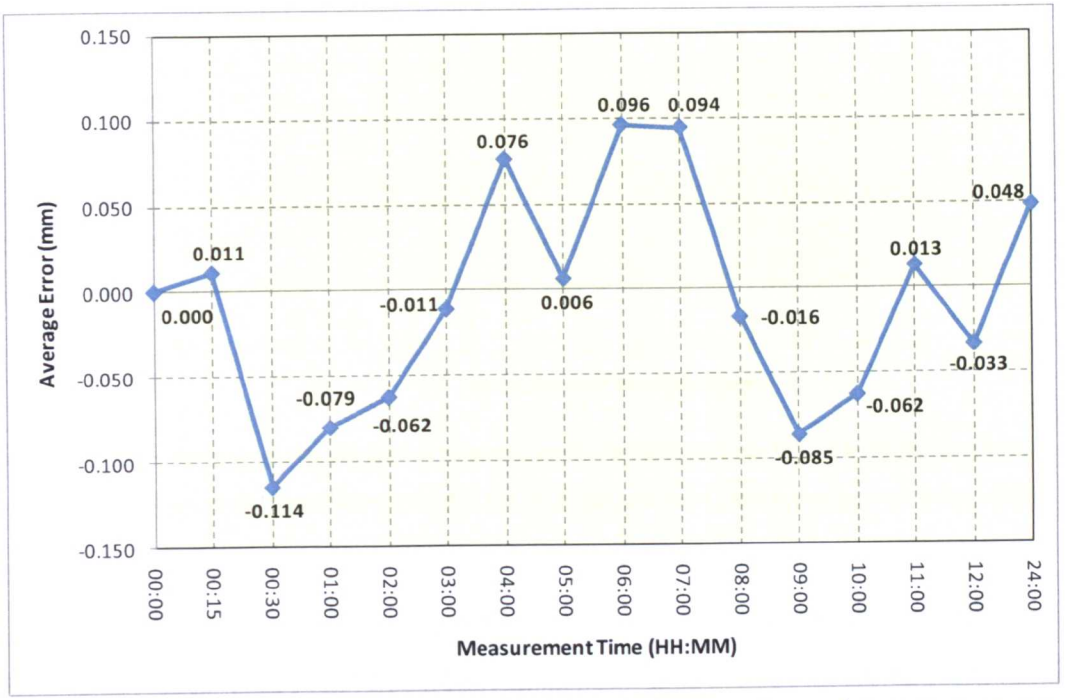

Figure 4.21 The calculated average error for each height deviation map, when each measurement was subtracted from the first measurement (which was performed at 0H:0M).

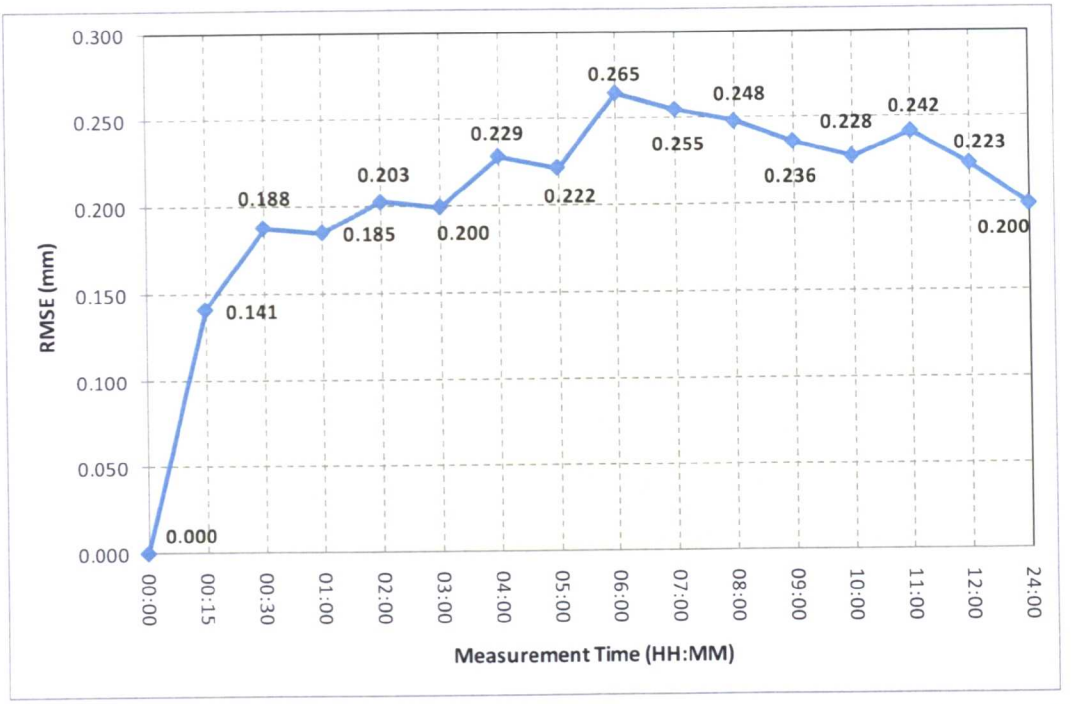

Figure 4.22 The RMSE for each height deviation map, when each measurement was subtracted from the first measurement (which was performed at 0H:0M).

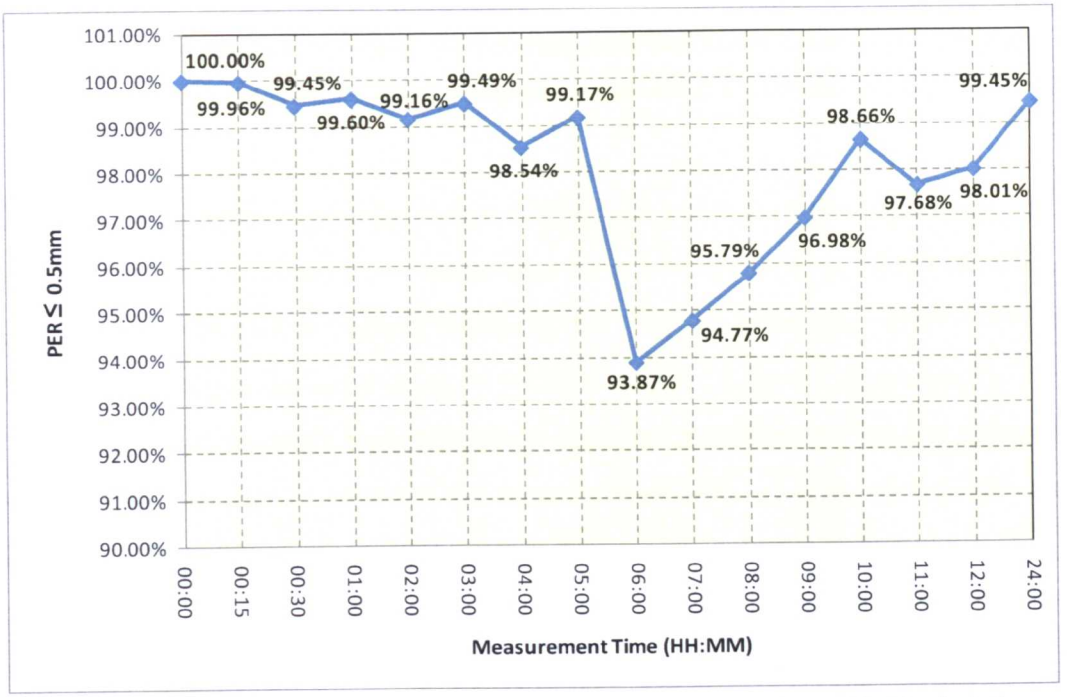

Figure 4.23 The percentage of the number of points that were within ±0.5mm for each height deviation map, when each measurement was subtracted from the first measurement (which was performed at 0H:0M).

In order to determine what is the best time period within which to perform the measurements, each of the measurement results was used as the subtracting reference measurement for height deviation calculations. The average of the percentage of the

number of height deviation map points that were within ±0.5mm for each reference surface is shown in Figure 4.24.

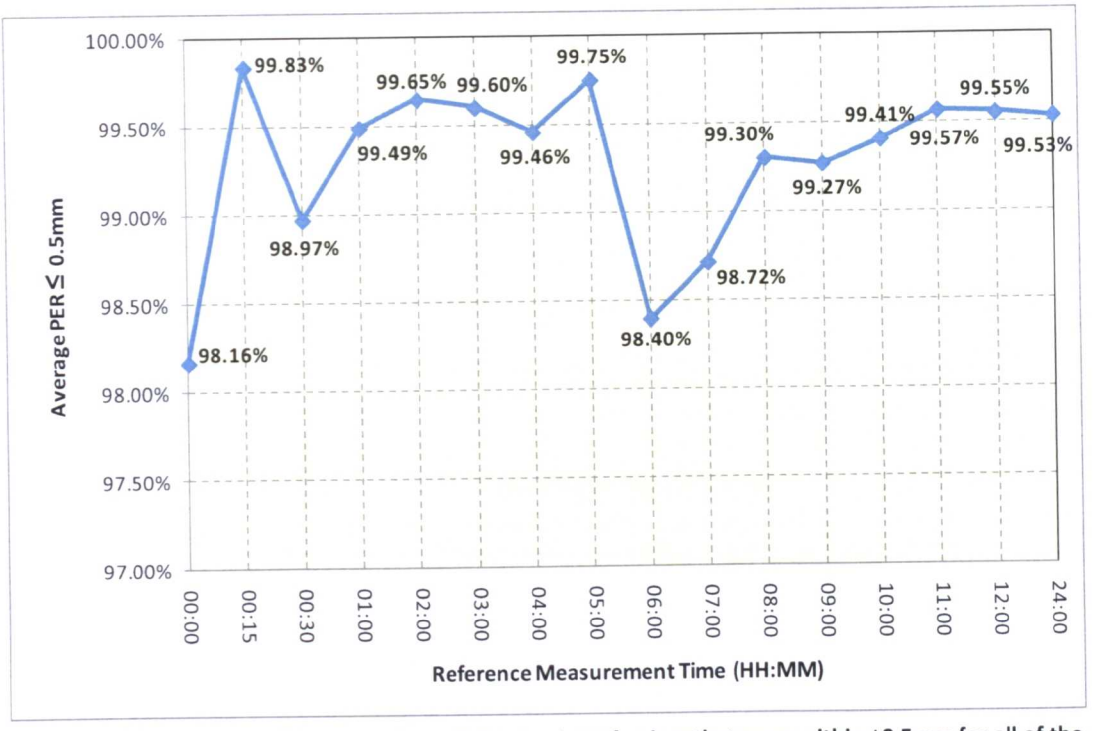

Figure 4.24 The average of the percentage of the number of points that were within ±0.5mm for all of the height deviation maps, when each measurement was used as a subtraction reference.

It can be noticed from Figure 4.24, that the highest average of the percentage of the number of height deviation map points that were within ±0.5mm, is obtained when using the flat surface measurement results at 0H:15M as a reference measurement for calculating the height deviation map (at 99.83% within ±0.5mm). Accordingly, it can be concluded that in order to obtain most accurate measurement results using this system, then it is best to perform the measurement after at least 15 minutes have passed since first turning on the video projector.

Figure 4.25 shows the percentage of the height deviation points that lie within ±0.5mm, when using the measurement result at 0H:15M as a reference measurement. Where, the average of the calculated RMSE values for each height deviation map was 0.153mm, the average standard deviation was 0.148mm, and the average of the percentage of the height deviation points that lie within three standard deviations ($\pm 3\sigma$ = 0.445mm) was 99.82%. This means that the probability of a reading lying within 0.445mm is 99.82%.

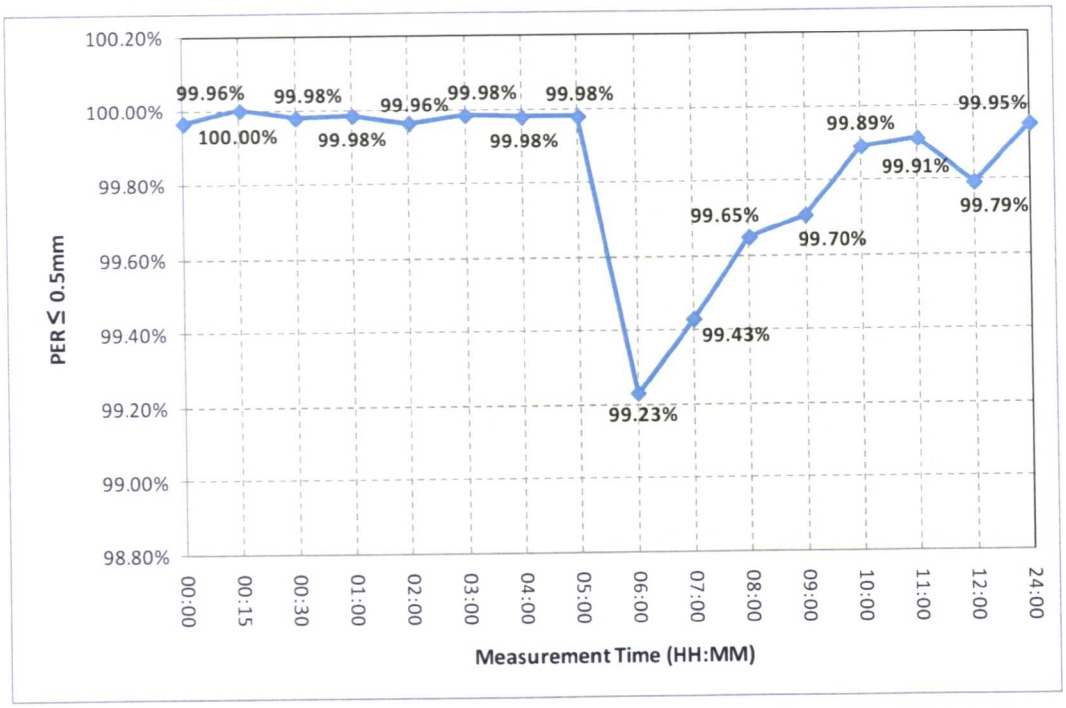

Figure 4.25 The percentage of the number of points that were within ±0.5mm for each height deviation map, when each measurement was subtracted from the second measurement (which was performed at 0H:15M).

It is important to mention that the error in the measurement results that is caused by thermal effects in the projector is actually even less than that which has been calculated above. This is because when the factor of repeatability is considered, and the results of the statistical calculations of the repeatability test are subtracted from their corresponding results in the heat stability test, then the actual effect of the projector's heat on the resultant measurement maybe measured statically as follows:

Average error	0.002 mm
RMSE	0.022 mm
Standard deviation	0.0307 mm
Three standard deviations (3σ)	0.092 mm

Hence, the thermal effects when using the projector that was adopted for this work (see Section 5.2.1) can be neglected.

4.3 Applications of the System

This system offers a high degree of adaptability to fit measurement requirements of numerous applications, in terms of its providing to a broad collection of profilometric methods and the ability to manipulate their settings interactively. Thus,

the measurement results can be optimised, in relation to desired accuracy and speed, by selecting the most appropriate combination of processing algorithms.

Two example applications for the system are discussed in this section. Firstly, in a human body surface measurement system in order to improve radiotherapy treatment of cancer, and secondly, in an object surface measurement system for general 3D modelling and reverse engineering applications. Experimental results for these two applications are reviewed and discussed in Chapter Eight.

4.3.1 Metrology Guided Radiation Therapy

As this research programme has formed part of the MEGURATH project (Lilley, 2009b), significant effort was concentrated on the development of this system to meet the functional requirements of surface reconstruction of the human body (in terms of robustness and speed) for the purpose of Metrology Guided Radiotherapy (MGRT). MEGURATH is a UK project, funded by the EPSRC and it builds on and extends the work accomplished in two previous projects INFOCUS (Lilley, 2006) and ARROW (Lilley, 2009a) in order to create a new generation of 3D optical sensors for real-time monitoring of patient position during the delivery of cancer treatment.

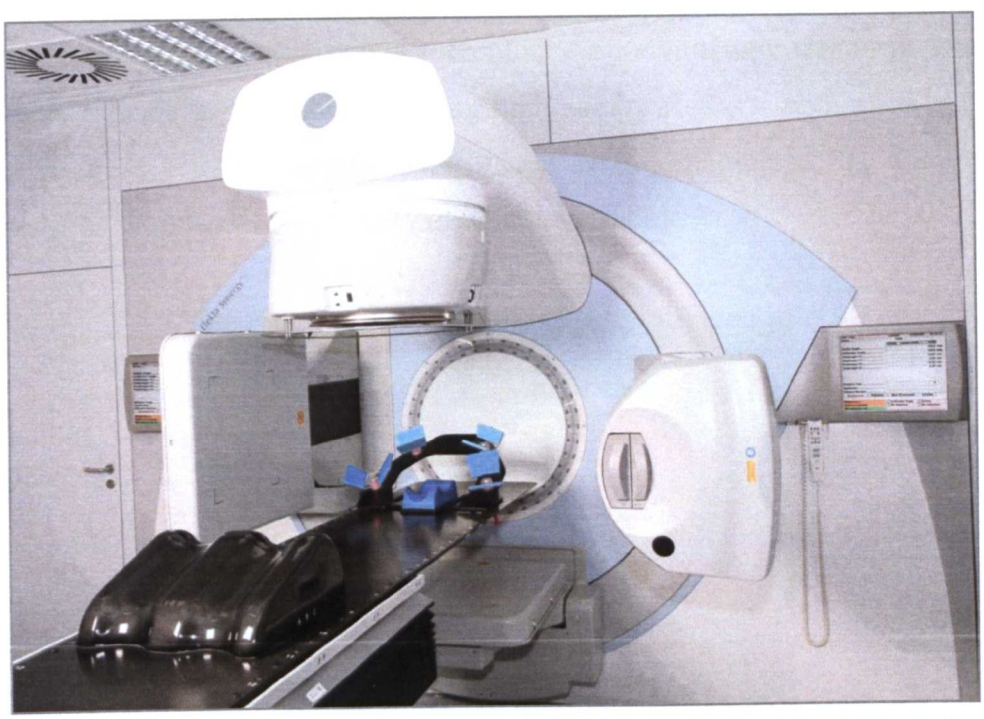

Figure 4.26 A typical radiotherapy treatment room (image courtesy of The Christie Hospital).

Radiotherapy has been in use as a treatment of a wide range of cancers for more than 110 years, with its earliest roots traced back to the discovery of X-Ray in 1895 (Pazdur *et al.*, 2009). Figure 4.26 shows a typical radiotherapy treatment room. The basic principle of radiotherapy is to repeatedly target the site of the cancer cells (a tumour) with small doses (fractions) of ionising radiation; which are typically delivered over a number of weeks in order to minimise damage to the surrounding healthy tissue. The radiation can damage healthy cells as it passes through normal tissue on its way to the tumour. To reduce this damage, the radiation is fired at the tumour from a series of different directions. This ensures that the cancerous tumour will receive a full dose whilst the surrounding healthy tissue receives a much lower dose. An image assisted pre-treatment planning stage is carried out using Computerised Tomography (CT) scans, to accurately define a tumour target and critical organs, such that the best possible beam fields and beam intensities can be determined. In addition, radiobiology is used to predict the probabilities of cure and complications (Bucci *et al.*, 2005). The radiation beams are shaped to conform more closely to the shape of the tumour using a Multi-leaf Collimator (MLC, shown in Figure 4.27) and this is called Conformal Radiotherapy.

Currently, when a patient is in position on the treatment table, and immediately prior to treatment, Image Guided Radiotherapy (IGRT) is used to optimise patient setup before therapy (Elekta, 2006). IGRT combines a radiotherapy treatment machine, essentially a linear accelerator producing high energy X-Rays, with a lower energy X-Ray imaging system, recently using Cone Beam Imaging (CBI). Figure 4.28 illustrates the workflow of a typical radiotherapy process.

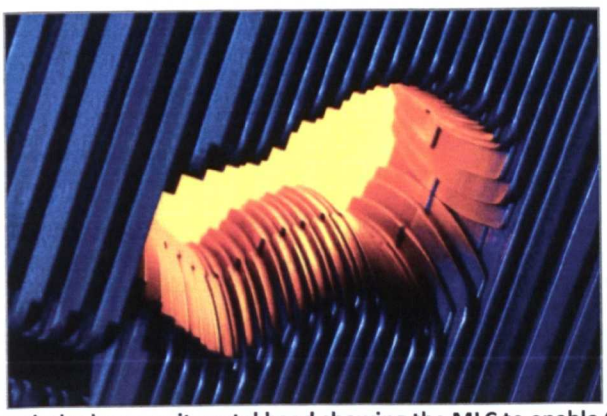

Figure 4.27 View underneath the beam exit portal head showing the MLC to enable Conformal Radiotherapy, image courtesy of Elekta.com.

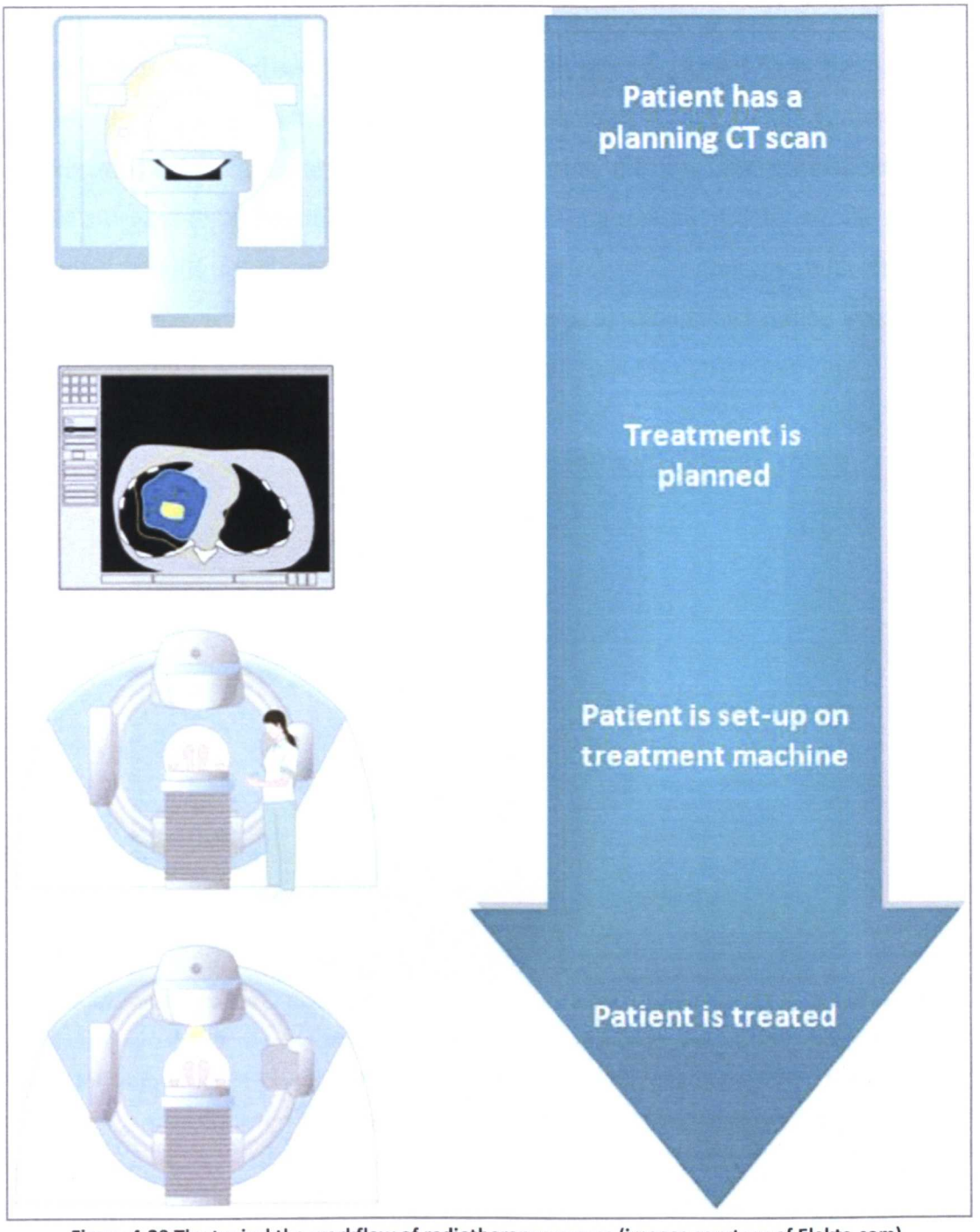

Figure 4.28 The typical the workflow of radiotherapy process (images courtesy of Elekta.com).

When radiotherapy treatment is in progress and radiation is being directed at the tumour, there is no effective dynamic monitoring of the patient's external body position, or internal anatomy. This means that a precisely planned treatment is in fact delivered in a manner that is effectively blind to the patient's internal and external body positions that were recorded in pre-treatment scans. At present, as a workaround to make treatment as accurate as possible, theoretical tolerance margins

around the tumour are specified at the treatment planning stage (Figure 4.29). In addition, radiotherapy moulds and masks are used to keep certain parts of the patient's body immobilised during treatment. On this simplified basis the patient is positioned prior to each treatment session. Nonetheless, due to the limitations of conventional methods in terms of not considering the dynamic movement of the patient's organs (e. g. breathing or peristalsis) during treatment delivery, the greatest challenge is still to attain the maximum probability of therapy with the least morbidity. Thus, it is crucial to establish a vigorous quality assurance system that allows corrections for routine setup variations and radiation target motion.

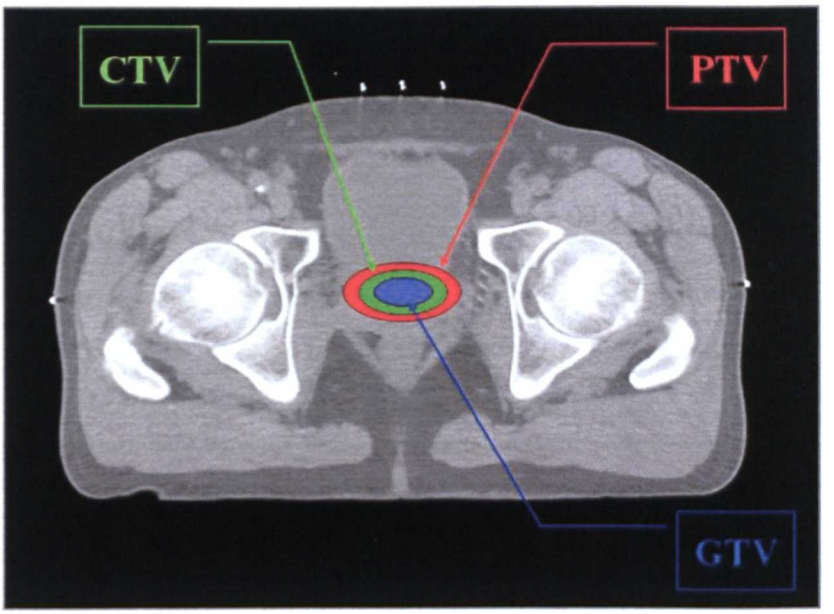

Figure 4.29 An illustration of the specified tolerance margins around the tumour: Gross Tumour Volume (GTV) represents the directly detectable volume of tumour, Clinical Target Volume (CTV) represents a GTV+ margin for micro-spread of disease, and Planning Target Volume (PTV) represents a CTV+ margin for motion and setup errors. Image reproduced with permission of The Christie Hospital.

As a collaborative research project, MEGURATH introduced MGRT where the patient is measured, imaged and modelled during treatment delivery. The project produced a non-invasive, radiation-free, real-time 3D patient positional monitoring system, based on surface body reconstruction using structured light. Dynamic reconstructed surface map and deformation modelling of the patient's external body surface are combined to quantify changes in the positions and shapes of the tumour and surrounding organs. Pilot work using sensor measurements to deform treatment plans has been reported by the project investigators, where for the first time a point

by point model of the patient during treatment has been constructed from live measurements (The-Christie, 2008). This enables clinical professionals to use radiobiology to determine the probabilities of tumour cure and complications for the treatment that was actually delivered, and to compare this with the treatment that was planned. Thus, MEGURATH established the foundation science for the development of adaptive radiotherapy.

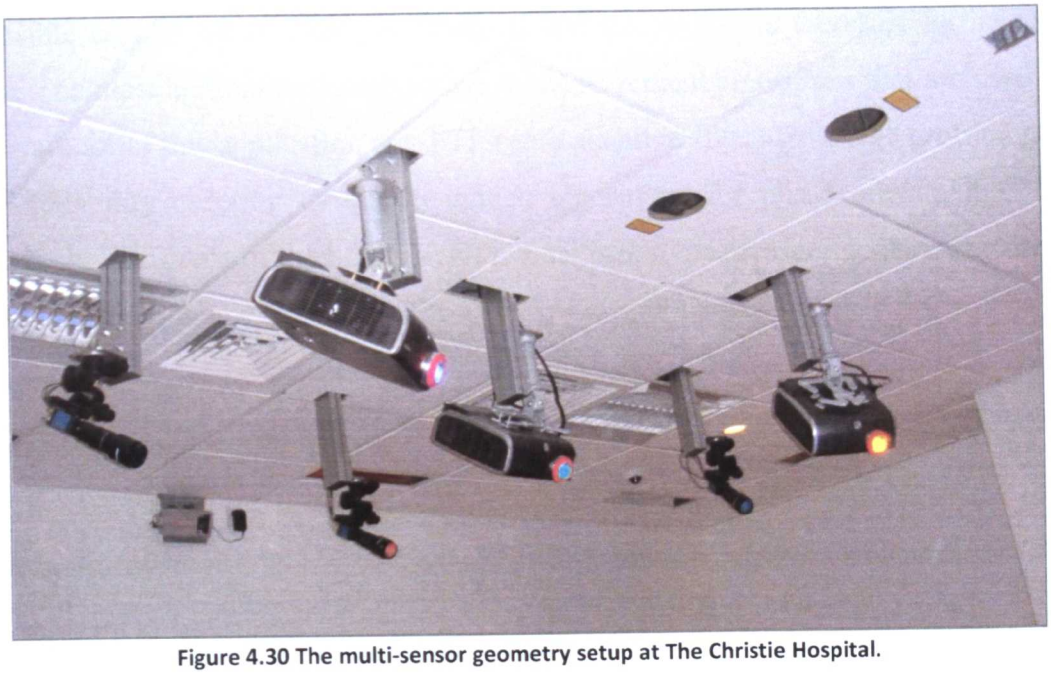

Figure 4.30 The multi-sensor geometry setup at The Christie Hospital.

The author's own role within the MEGURATH project involved working on all aspects of the optical, electronic, computing and software systems that are related to the task of dynamic body surface reconstruction using fringe analysis, at The Christie Hospital in Manchester. The profilometry system that is used at The Christie has the same hardware configuration for the sensor head components that is described in Chapter Five. Three sensor heads (Figure 4.30) are used to provide wider measurement coverage (about 220°) than would be achieved using a single sensor with up to 150° coverage around the centre of the radiation target (Iso-centre), where each camera and projector set of each sensor is attached to a chromatic filter of a different colour (Section 5.2.3) to provide simultaneous measurement without cross-talk. Moreover, this configuration accounts for sensor positioning redundancy, in the likely case of some obscurement by the treatment machine head as it rotates about its gantry. At the early stages of building this profilometry system, the sensor

hardware components were expected to be susceptible to the hostile radiation environment (4-20MeV) inside the treatment room and it was thought that they would only survive for a few weeks or months. However, they have proved to be resistant to radiation damage and are still fully functional after a period of more than two years.

The system uses structured patterns of projected white light, there are no lasers, invisible rays or other additions involved and the system is therefore intrinsically safe. The most appropriate combination of measurement algorithms that are used for the purpose of this application are: FTP (with adaptive filter) for fringe profilometry, and reliability ordering or quality-guided algorithms for phase unwrapping. The actual specifications of the MEGURATH final prototype measurement system are as follows:

Z accuracy	< 0.5 mm
Number of sampled XYZ points	> 260,000 x,y,z points per sensor > 780,000 x,y,z points for all sensors
Measurement speed	~5.35 Hz for single-view measurement ~4.5 Hz for multi-view measurement
Number of measured XYZ points/second	> 1.3 million x,y,z points/sec per sensor > 3.5 million x,y,z points/sec for all sensors
Field of view	≤ 400 mm × 660 mm
Spatial resolution XY mm/point	≤ 0.78 mm × 1.3 mm per x,y point
Coverage area	~220° around the Iso-centre
Maximum measurable body curvature	88° using single-sensor (See Appendix A3) > 90° using multi-sensor
Component cost	< £30,000

Several measurement tests have been performed using this system, and two different measurements are reported here. The first measurement was for a human's abdominal area, and the second measurement was for a radiotherapy RANDO phantom (a synthetic human dummy used in radiotherapy calibration and dosimetry, as shown in Figure 4.32). For the first measurement test, a full breathing cycle for a

human test subject's abdominal area was measured dynamically at a real-time speed for a duration of less than two seconds (i.e. here each inhalation and exhalation cycle took less than one second and the sensor was measuring at a rate of 5.35Hz), Figure 4.31 shows a cross-section graph plotting for the measurement results of the middle sensor.

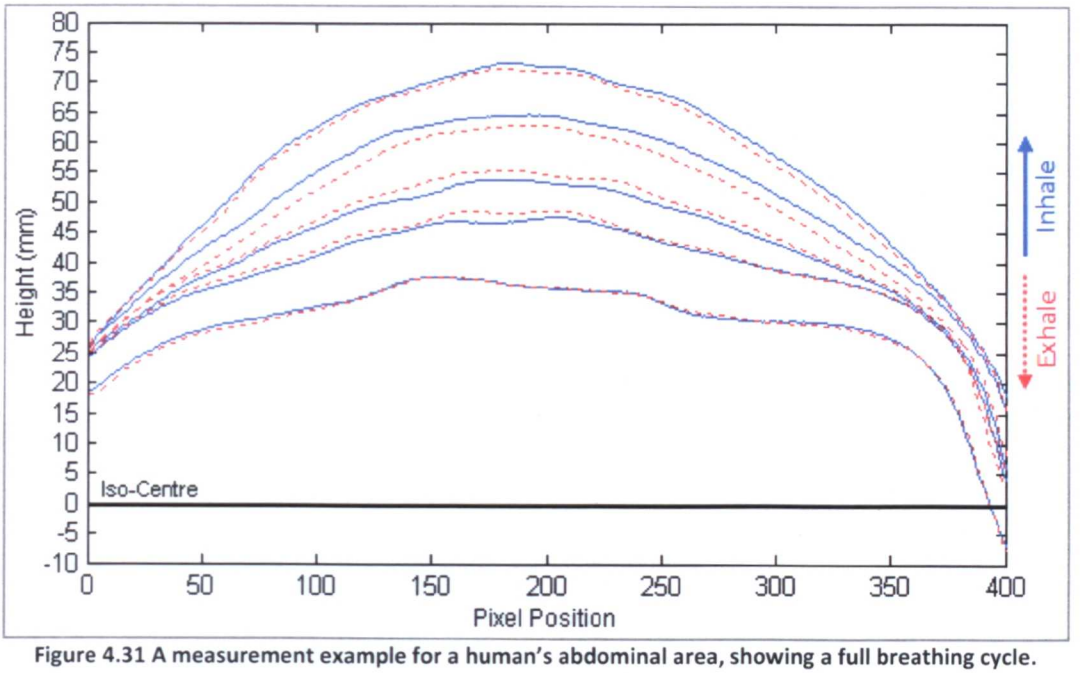

Figure 4.31 A measurement example for a human's abdominal area, showing a full breathing cycle.

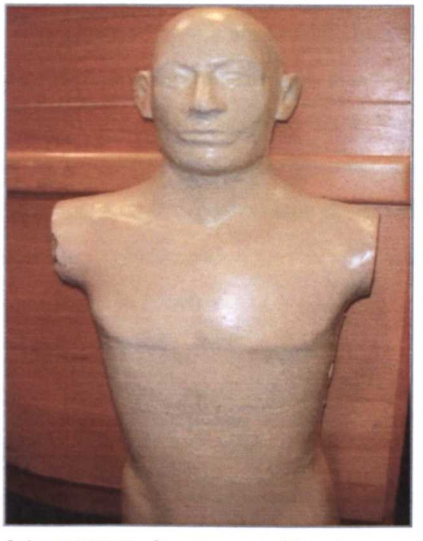

Figure 4.32 An image of the RANDO phantom used for the second measurement test.

In the second measurement test, the RANDO phantom was measured using a multi-sensor approach. A CT scan for the RANDO was used here as a reference surface, and the measurement results for the three sensors are illustrated in Figure 4.33.

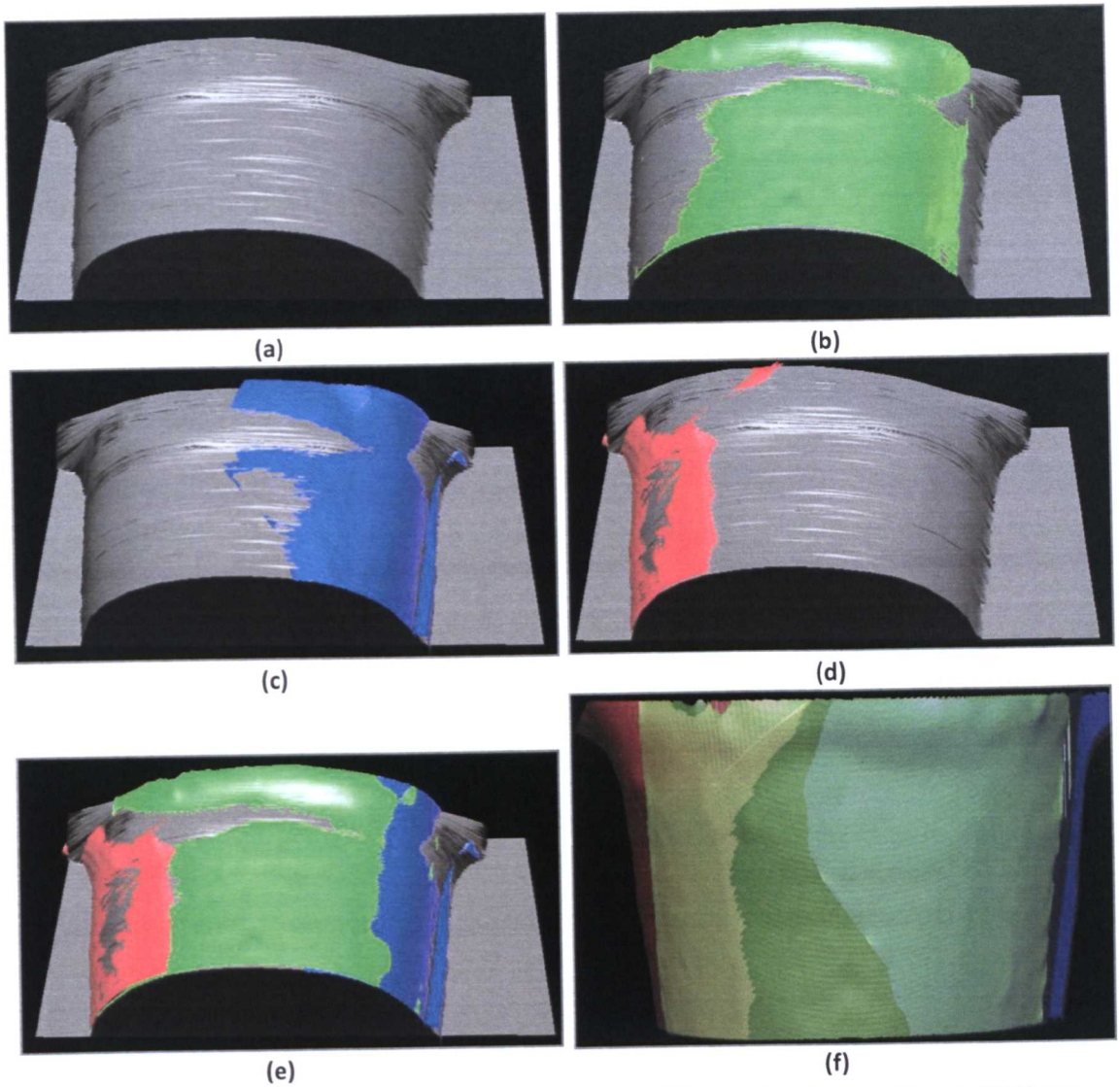

Figure 4.33 Measurement results of the RANDO phantom, overlaid over the reference CT-scan: (a) CT-scan results rendered in grey colour, (b) middle-sensor measurement result rendered in green colour, (c) right-sensor measurement result rendered in blue colour, (d) left-sensor measurement result rendered in red colour, (e) measurement results of the three sensors, (f) a transparent rendering of the results of the three sensors, showing a cyan colour for the intersection area between the measurement results of the middle and the right sensors, and a yellow colour for the intersection area of the measurements of the middle and left sensors.

4.3.2 3D Modelling and Reverse-Engineering

This system can be used to generate 3D digital models of measured artefacts; these digital models can be used for various applications, including:

- Visualisation: where models are used for display; such as 3D models for displaying sculptures and demonstration products.
- Verbatim replication: where models are used for fabrication back into physical parts; such as in designing medical prosthetics.

- Reverse engineering: where models are used to capture the engineering design intent, to be imported into a Computer Aided Design (CAD) environment.
- Inspection: where models are compared to a reference CAD model in order to confirm dimensional compliance.

The system, according to the geometry of the sensors (which is described in Section 4.1.1 and Chapter Five), is able to measure objects of a height of up to 500mm (due to the limitations of the calibration range), with an accuracy of better than 0.5mm, whereas the sample density can be controlled by adjusting the field-of-view for the measurement (typically 330mm×550mm). A better measurement accuracy and higher sample density can be obtained by reducing the working distance and adopting an orthogonal geometry for camera, or projector, however, the example measurements that are reviewed below were performed using the system hardware geometry that was described in Section 4.1.1 in order to provide a general overview of the capability of this system for use in the different profilometric applications that are described in this section. 3DReshaper application (3DReshaper, 2010) was used as a CAD environment for 3D surface analyses (e.g. alignment and deviation).

Example #1: 3D modelling for a glass Ball (sphere)

In this example and as shown in Figure 4.34, a single-view measurement was performed using this system to measure a segment of a glass sphere (sprayed with matt white paint), using the four-frame phase shifting algorithm for fringe analysis and the reliability-ordering algorithm for phase unwrapping.

Using the partial measured region of the surface of the sphere, four arbitrary points are needed to calculate the centre and radius of the sphere. The calculated geometric parameters of the sphere are as follows:

Centre	-13.98, 92.54, -170.81 (x,y,z)
Radius	~139.7 mm
Diameter	~279.4 mm
Area	245,241.15 mm^2
Volume	11,419,940.42 mm^3

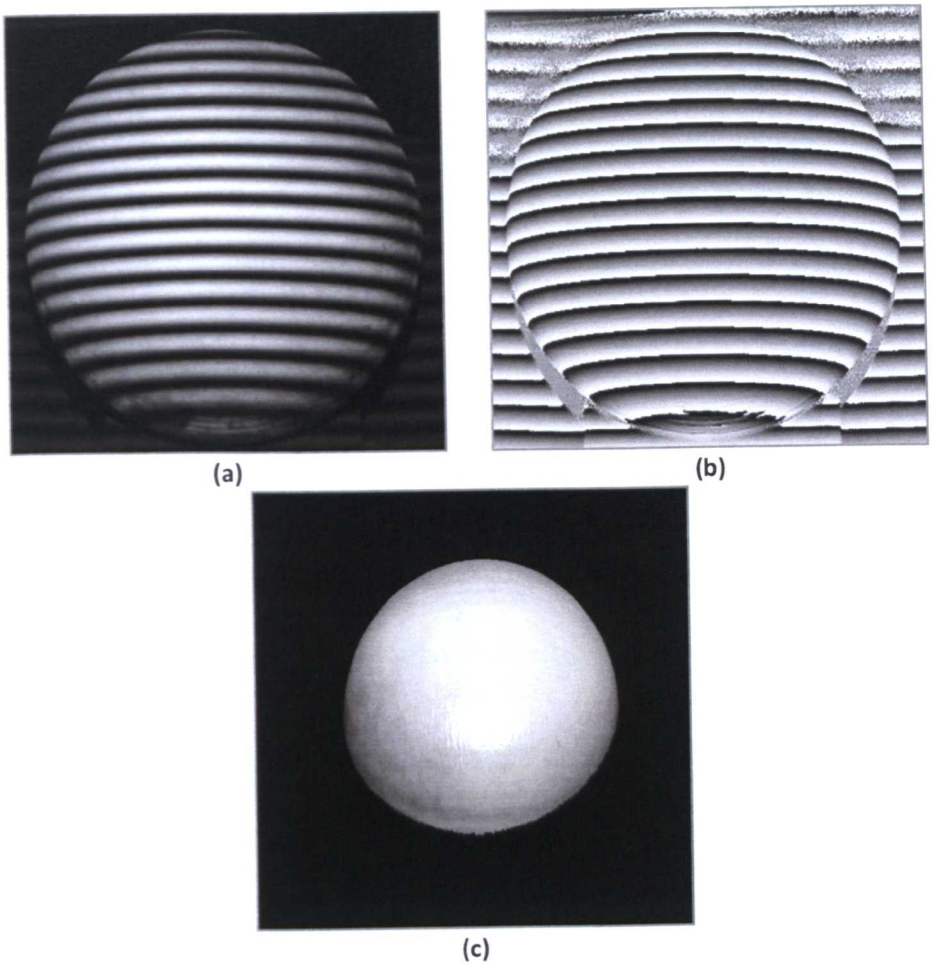

Figure 4.34 Measurement of a section of a glass sphere using a single-view measurement; (a) fringe pattern of the sphere, (b) retrieved wrapped phase, (c) 3D reconstructed surface, with texture rendering.

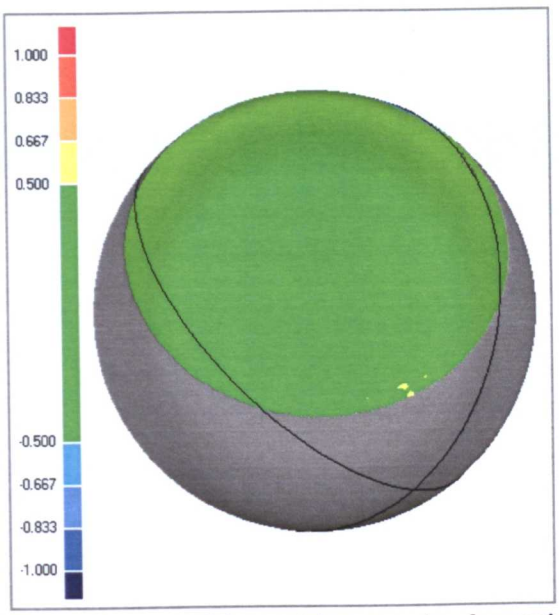

Figure 4.35 The calculated 3D deviation map of the partial measured surface region from the CAD reference sphere (units are in millimetres), where the coloured part represents the measured part of the sphere using the measurement system developed for this research programme, and the grey colour represents the generated CAD reference sphere.

Using the calculated centre and radius, a reference sphere CAD model was established in a CAD environment, in order to obtain the accuracy of the measured surface region. Figure 4.35 shows the 3D deviation map of the measured region from the reference sphere. The average and standard deviation errors of measurement were 0.018mm and 0.22mm, respectively.

Example #2: 3D modelling of a mechanical mould

In this example, a mechanical mould (shown in Figure 4.36) was measured using a single-view measurement, with the four-frame phase shifting algorithm for fringe analysis and the reliability-ordering algorithm for phase unwrapping. After 3D surface reconstruction, the x,y,z point cloud was imported into a CAD environment and some sample distances were calculated, as illustrated in Figure 4.37.

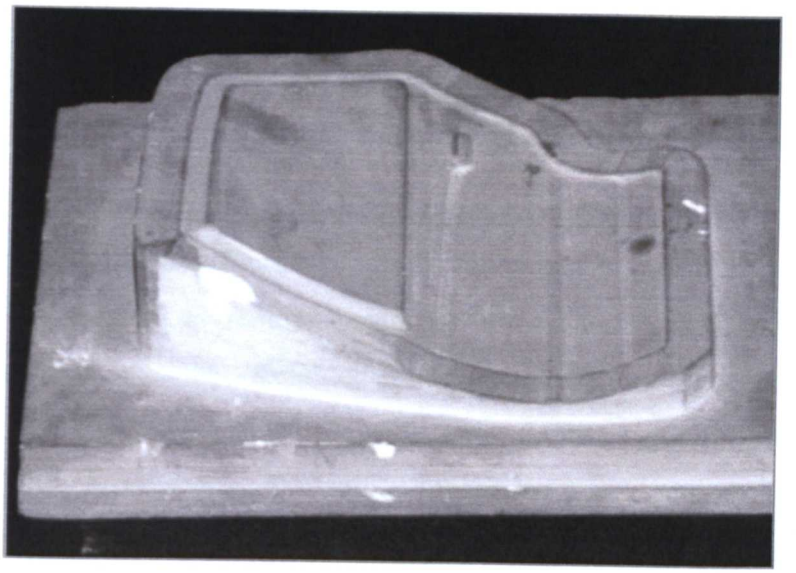

Figure 4.36 An image of the mechanical mould that was measured using the system, as illustrated in example #2.

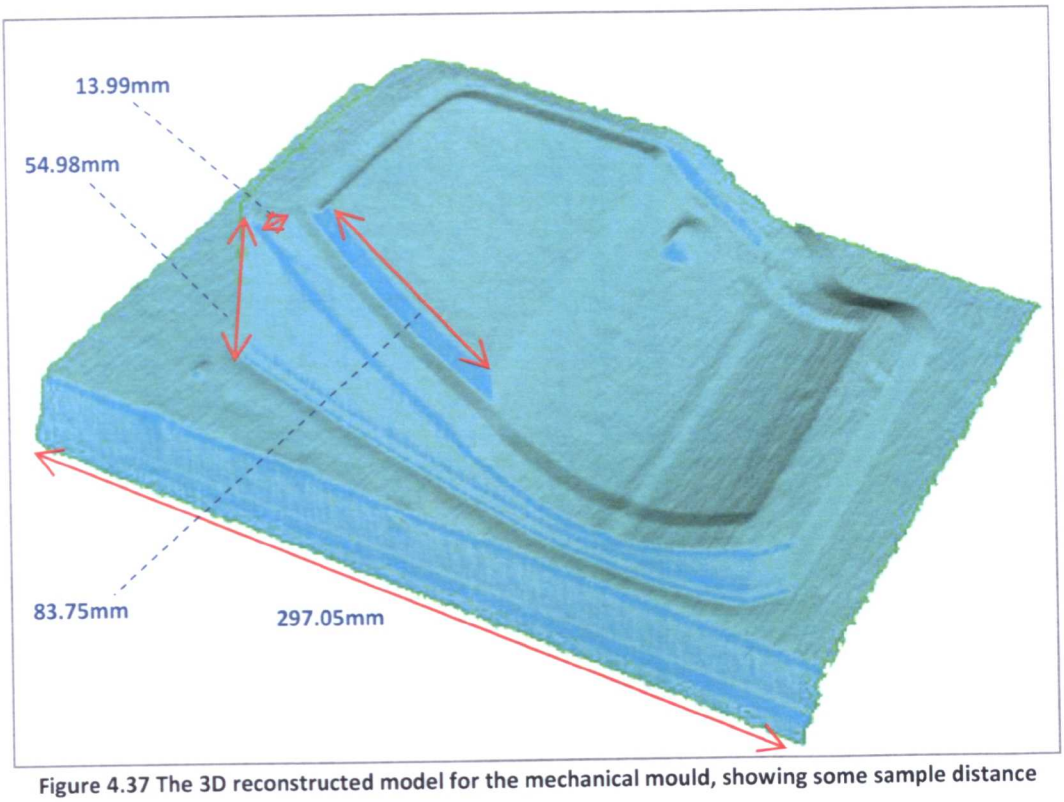

Figure 4.37 The 3D reconstructed model for the mechanical mould, showing some sample distance measurements.

Example #3: 3D modelling of a porcelain figurine of an owl

In this example, a porcelain figurine of an owl (shown in Figure 4.38) was measured using a multiple-view measurement, using the four-frame phase shifting algorithm for fringe analysis and the Weighted-least square (PCG) algorithm for phase unwrapping. The dimensions of the figurine were 400mm×300mm×200mm, width, height and depth, respectively. Two multi-sensor measurements were carried out, one for the front side of the figurine (Figure 4.38) and another for its rear side.

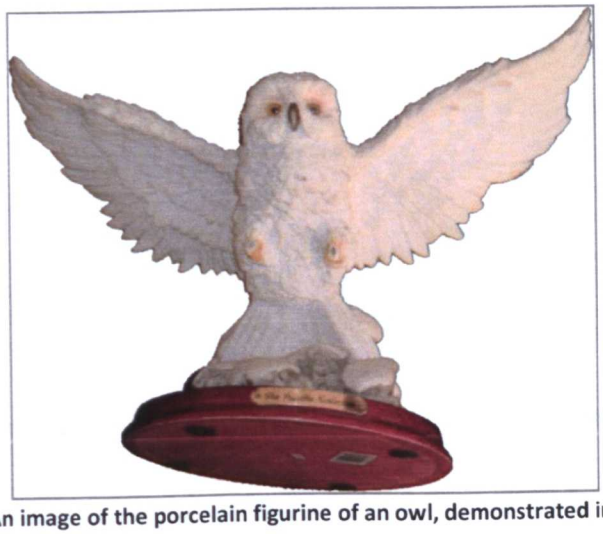

Figure 4.38 An image of the porcelain figurine of an owl, demonstrated in example #3.

The x,y,z point clouds of the two measurements were aligned and merged together to form a full 3D model of the figurine in a CAD environment, Figure 4.39 and Figure 4.40 show the merged 3D model of the two surface measurements obtained for the front and rear of the figurine.

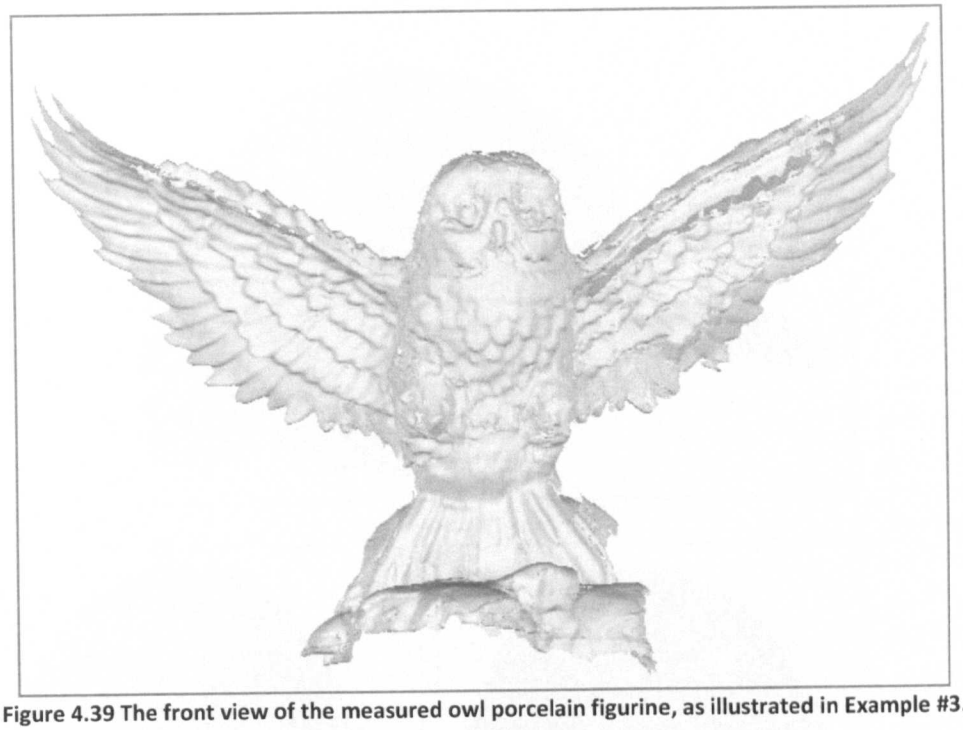

Figure 4.39 The front view of the measured owl porcelain figurine, as illustrated in Example #3.

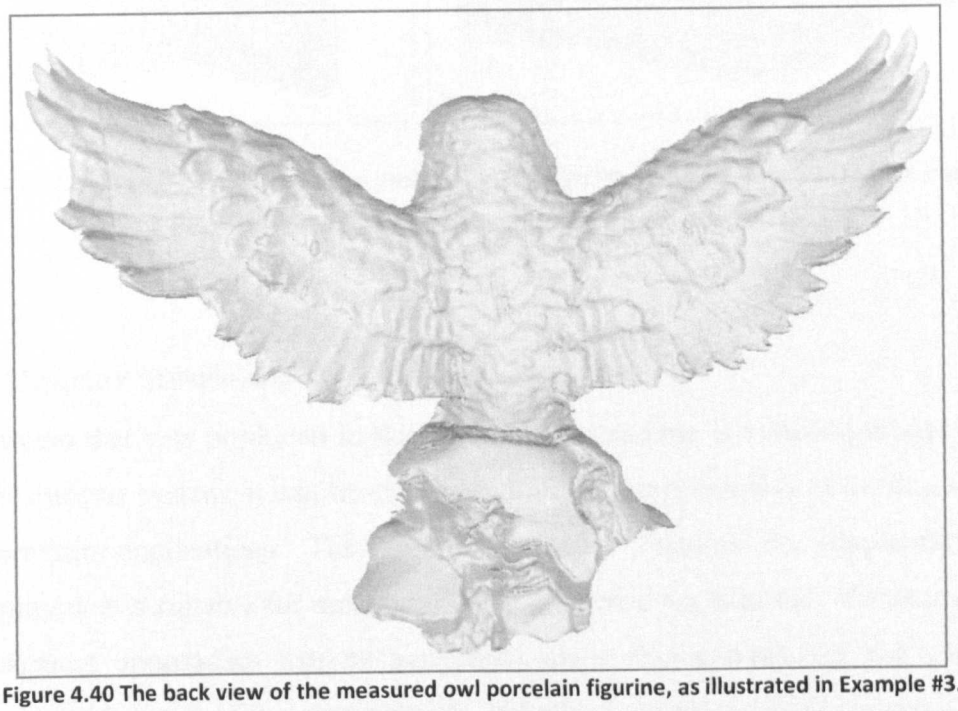

Figure 4.40 The back view of the measured owl porcelain figurine, as illustrated in Example #3.

Example #4: 3D modelling for a sport hat

In this example, a sport hat was measured by a single-sensor, using the four-frame phase shifting algorithm for fringe analysis and Flynn's algorithm for phase unwrapping. The 3D model of the measurement result is shown in Figure 4.41.

Figure 4.41 The 3D model for sports hat, as described in Example #4; (a) an isometric-view of the model, (b) front view with coloured texture rendering, (c) isometric-view with texture.

4.4 Chapter Summary

The system that was produced in this research programme is a multi-purpose fringe pattern analysis system; it can be employed to fit the requirements of various optical profilometric applications. The system generally features an adaptability and scalability that is suitable for most optical profilometric applications. Various surface measurement approaches can be performed using this system, via the use of a catalogue of fringe profilometry methods embedded within the single system, which can obtain the measurement through a combination of more than 183 different paths

of fringe analysis, phase unwrapping, and calibration algorithms and methods. In a measurement process it is beneficed to use a tangible visual display for what is actually a complex measurement process, so that the user can easily identify any sources of measurement errors and manipulate the parameters of the processing algorithms by way of a friendly and simple graphical user interface.

The height, or z accuracy of the measurements obtained using this system is better than 0.5mm, with an uncertainty of 0.353mm, and an XY sample density of better than 0.7mm. The uncertainty due to the heat dissipated by the video projector of the measurement sensor is ±0.092mm, and the uncertainty due to reproducibility is ±0.452mm. Speeds of measurements of dynamic objects primarily depend upon the choice of the fringe analysis and phase unwrapping algorithms that are used and their processing parameters, but up to 12 measurements can be achieved for a single-view measurement and up to six measurements for a multi-view measurement.

This optical profilometry system can be utilised for a large number of different applications, but to date it has primarily been used for dynamic human body shape measurement during radiation treatment, as it has formed part of a metrology guided radiotherapy application. Other possible uses for this system can be for the purposes of 3D modelling and reverse engineering applications.

The following chapter describes the hardware architecture and physical geometry of this system. It also reviews the various currently available technologies that may be employed for digital fringe pattern projection and for image capture, in terms of their functionality and their effectiveness for use in this system.

4.5 References

3DRESHAPER. 2010. *3DReshaper Application* [Online]. 3dreshaper.com. Available: http://www.3dreshaper.com/en1/En_software.htm [Accessed 2 Apr 2010].

BUCCI, M. K., BEVAN, A. & ROACH, M., III 2005. Advances in Radiation Therapy: Conventional to 3D, to IMRT, to 4D, and Beyond. *CA Cancer J Clin,* 55, 117-134.

ELEKTA. 2006. *Elekta Synergy* [Online]. elekta.com. Available: http://www.elekta.com/healthcare_international_elekta_synergy.php [Accessed 22 Jul 2007].

HARVEY, D. M., ARSHAD, N. M. & HOBSON, C. A. 2001. Image data compression and it's effect on the accuracy of fringe-based images for 3-D gauging using a phase stepping method. *Optics and Lasers in Engineering,* 35, 201-223.

HERRÁEZ, M. A., BURTON, D. R., LALOR, M. J. & GDEISAT, M. A. 2002. Fast two-dimensional phase-unwrapping algorithm based on sorting by reliability following a noncontinuous path. *Appl. Opt.,* 41, 7437-7444.

LILLEY, F. 2006. *INFOCUS - 3D Human Body Shape Measurement In Radiotherapy* [Online]. ljmu.ac.uk. Available: http://www.ljmu.ac.uk/GERI/INFOCUS.htm [Accessed 2 Oct 2009].

LILLEY, F. 2009a. *ARROW - Dynamic 3D Human Body Shape Measurement In Radiotherapy* [Online]. ljmu.ac.uk. Available: http://www.ljmu.ac.uk/GERI/arrow.htm [Accessed 2 Oct 2009].

LILLEY, F. 2009b. *MEGURATH - Metrology Guided Radiotherapy* [Online]. ljmu.ac.uk. Available: http://www.ljmu.ac.uk/GERI/MEGURATH.htm [Accessed 2 Oct 2009].

NVISION. 2008. *NVision 3D laser scanner* [Online]. nvision3d.com. Available: http://www.nvision3d.com/nvision-products.html [Accessed 2 May 2008].

PAZDUR, R., WAGMAN, L. D. & CAMPHAUSEN, K. A. 2009. *Cancer Management: A Multidisciplinary Approach*, Cmp United Business Media.

THE-CHRISTIE. 2008. *Metrology Guided Radiation Therapy - MEGURATH* [Online]. christie.nhs.uk. Available: http://www.christie.nhs.uk/pro/nwmp/dt/MEGURATH.aspx [Accessed 8 Jan 2009].

Chapter Five

Hardware Design of the System

One of the most crucial steps involved in building an optical-metrology system that is based on fringe analysis is to carefully choose the correct hardware components. In order to obtain the high levels of accuracy, reliability and automation that were required for this research project, the system hardware must be capable of the following functionality:

- Projection of high quality fringe patterns, in terms of truly and high resolution sinusoidal fringes that are free from any artefacts.
- Providing the highest performance source images that are captured by the system cameras, in terms of an accurate intensity distributions that are free from any optical aberrations, with prompt image transfer to the Sensor Processing Unit (SPU).
- Concurrent and low latency central synchronisation among the cameras and the Central Measurement Server (CMS), and among the SPUs.
- Real-time fast processing of the image data and visualisation of the results at each SPU, within the context of the system applications that are discussed in chapter Four.
- Real-time inter-communications among the SPUs and the CMS to ensure the fastest possible transmission data rate.
- Have the ability to control the beginning and ending of the measurement acquisition processing and also of visualising the integrated 3D results of all the sensors at the CMS.

Moreover, the sensor components should be able to operate under a hostile radiation environment in order to fulfil one of the system's potential applications which is that of metrology guided radiotherapy. The system consists of three sensor heads (a pairing of a single camera and a single projector comprising each sensor head). Figure 5.1 shows the geometry of the system that has been built as part of this programme of research. This chapter examines the currently available hardware

technologies in detail and justifies the selection of the system components that have been adopted.

5.1 Sensor Components

The sensor components form part of the low-level system architecture. As shown in Chapter Two, the captured image of a projected horizontal fringe pattern is represented by:

$$I(x,y) = a(x,y) + b(x,y)\cos[\varphi(x,y) + 2\pi f_0 y] \quad \textbf{(5.1)}$$

where $a(x,y)$ and $b(x,y)$ at each corresponding pixel, refer to the ambient light and modulation amplitude of the fringes respectively, f_0 is the spatial frequency of the projected fringes and $\varphi(x,y)$ is the phase modulation that is introduced as a result of the surface profile. Since the measurement of phase here assumes the presence of a sinusoidal intensity distribution in the fringe pattern, the accuracy of the phase measurement depends firstly on the ability of the projector to produce a fringe pattern with a sinusoidal intensity profile, and secondly, upon the ability of the image capture device to faithfully acquire the intensity distribution that was projected upon the object. The spatial resolution of surface measurements that are based on fringe projection methods depend mainly upon the fringe spacing. An extreme reduction of fringe spacing results in inaccurate measurements due to limitations in camera and projector resolution. Such implications should be thoroughly considered when designing fringe based optical profilometry systems.

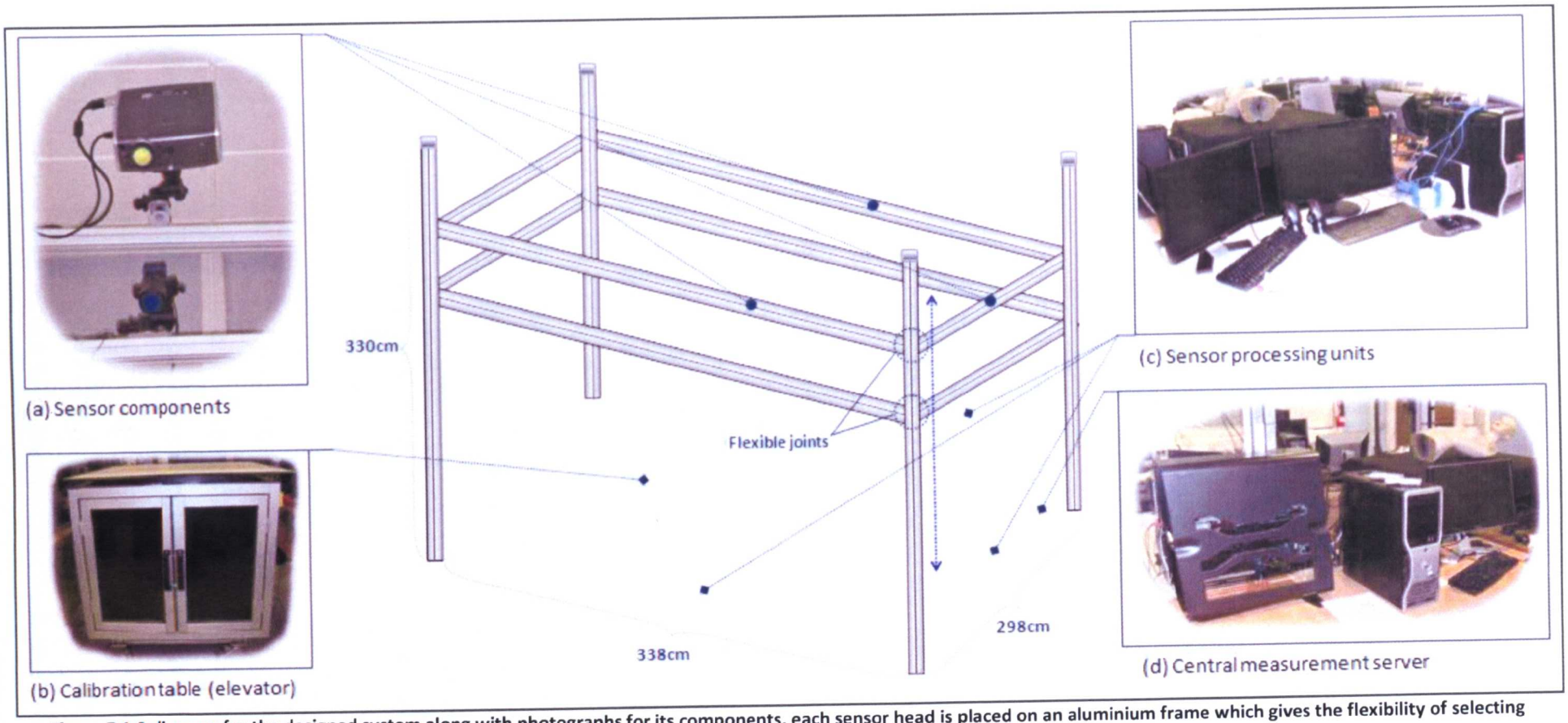

Figure 5.1 A diagram for the designed system along with photographs for its components, each sensor head is placed on an aluminium frame which gives the flexibility of selecting arbitrary position and orientation of both the camera and projector to fulfil various applications. (a) A single sensor head, shows the adopted projector (Canon XEED SX60), camera (Prosilica GE1380) and their mounts (Manfrotto 410 Geared Head). Each pair of cameras and projectors that comprise a single sensor head are both fitted with the same chromatic filter in one of the primary colours (red, green and blue). (b) The height elevation table used for system calibration. (c) One of the SPUs. (d) The central measurement server.

5.1.1 Fringe Pattern Projection

As discussed under Section 2.2, digital video projection methods are widely adopted nowadays as an alternative to other methods in optical metrology profilometry systems such as interferometric or grating projection techniques, due to their ability to manipulate fringe patterns simply and rapidly with high precision by software. Modern video projection technologies offer robust qualities in terms of high resolution, contrast ratios and sharp images. However, in regard to specific applications of fringe pattern projection, video projection often presents poor pattern geometric structure in terms of discontinuities and non-sinusoidal attributes (Baker *et al.*, 2005). The three leading technologies that are commonly used in the digital fringe projection are: Liquid Crystal Display (LCD), Digital Light Processing (DLP) and Liquid Crystal on Silicon (LCOS). This section reviews the functionality and contrasts these technologies through presenting their advantages and disadvantages generally, and specifically in the field of fringe pattern projection.

DLP technology is based on light reflection from an optical semiconductor called a Digital Micromirror Device (DMD) chip, 'it is perhaps the world's most sophisticated light switch' (Texas-Instruments, 2009). The DMD is a very precise light switch that enables light to be modulated digitally via up to 2 million hinge-mounted microscopic mirrors arranged in a rectangular array. Each mirror is spaced less than 1 micron apart. The individual micromirrors tilt either towards the light source to create a bright pixel or away from it to create a dark pixel. The bit-code of the streamed image entering the DMD directs each mirror to potentially switch on and off several thousand times per second, which enables the reflected light to be varied such that up to 1,024 individual shades of grey may be produced at every pixel location.

In order to generate coloured pixels DLP mainly uses two architectures, the single-chip and the three-chip methods. Figure 5.2 shows a schematic diagram for the single-chip system, where white light passes through a colour filter (wheel consists of red, green and blue colours that rotate sequentially to blend the required colour) then it is reflected via the DMD chip. Figure 5.3 shows a schematic diagram for the three-chip DLP system, where light generated by the lamp passes through a prism that divides it into the three primary colours (red, green and blue) and it then passes

to a dedicated DLP chip for each colour. The reflected colour of each of the three chips is combined and passed through the projection lens to form a colour output image.

Figure 5.2 Example of a single-chip DLP projection system (Texas-Instruments, 2009).

Figure 5.3 Example of a 3-chip DLP projection system (Texas-Instruments, 2009).

LCD projectors use transmissive technology, as opposed to DLP projectors where reflective technology is used. In LCD technology light shines through the polysilicon LCD panel, each individual cell thereof corresponding to a pixel. The panel contains polarising filters, where electric currents are used to switch individual pixels off or on, thereby letting the different colour light through to make up the output image. Most modern LCD projectors use three-LCD panels, which each process a different

primary colour (red, green and blue). Figure 5.4 shows a schematic diagram of a typical three-LCD technology architecture, the red, green and blue images from the LCD panels are combined and passed through the lens to project the image.

Figure 5.4 Example of a 3-LCD projection system (DeBoer, 2008).

LCOS (or LCoS) technology combines both transmissive and reflective technologies, usually the system consists of three LCOS panels, one for each red, green and blue channel respectively. Each panel has a liquid crystal layer which sits on top of a highly reflective substrate, and below the substrate there is another pixelated layer containing the electronics to activate the pixels. Figure 5.5 shows a schematic diagram for a typical LCOS technology architecture, where white light is divided into each of the primary colours and reflected onto the three LCOS panels, from which the reflected images are then combined in order to form the streamed output image.

Each of the DLP and LCD projection technologies has their respective advantages and disadvantages in the sense of the specific and intended applications they are principally designed for (DeBoer, 2008). LCD transmissive technology does not replicate the same high image contrast that is present in the DLP reflective technology, while LCD projectors generally produce brighter and sharper images than single-chip DLP which loses brightness due to the use of a colour wheel. However, single-chip DLP technology suffers from "Rainbow Effect" artefacts,

which appear as a rainbow or multi-colour shine that is briefly noticeable on the projected images, and which is produced because of the use of a colour wheel. Another important factor about the image quality of the two technologies is the Fill Factor, which represents the percentage of the active imaging area (pixel aperture ratio). A low fill factor causes an artefact called the Screen Door Effect, which is more noticeable in the case of LCD technology than it is for DLP (see Figure 5.6). The electronics surrounding the pixels in the LCD panel create an obstruction in the light path which results in a fill factor of only up to 73%, while the spatial separation between the micro-mirrors on the DMD chip of a DLP technology device gives a higher fill factor of typically 82%.

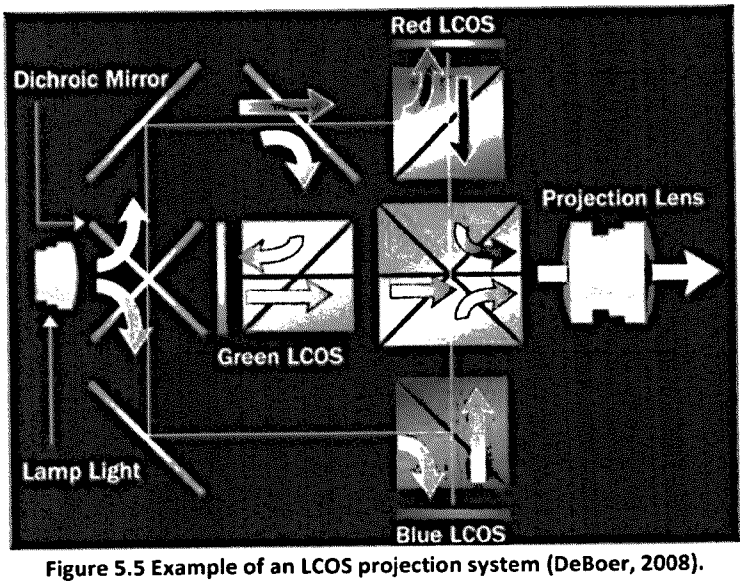

Figure 5.5 Example of an LCOS projection system (DeBoer, 2008).

Figure 5.6 Magnified region of two projected images using LCD and DLP technologies (DeBoer, 2008).

LCOS technology on the other hand overcomes the disadvantages of both DLP and LCD technologies. As it combines both transmissive and reflective technologies, it

produces high quality, bright and sharp images, that are free from the rainbow artefact (see Figure 5.7). Additionally, because the wiring and switching elements of the LCOS panel are placed under a reflective layer, the technology typically gives a fill factor in the region of 90% (see Figure 5.8 and Figure 5.9). This provides high-quality images with a minimum occurrence of artefacts compared to other currently available projection technologies (ProjectorPoint, 2009). Nevertheless, DLP still gives better contrast than LCOS technology and LCD still gives higher brightness than LCOS and these factors are considered to be the main drawbacks associated with LCOS technology.

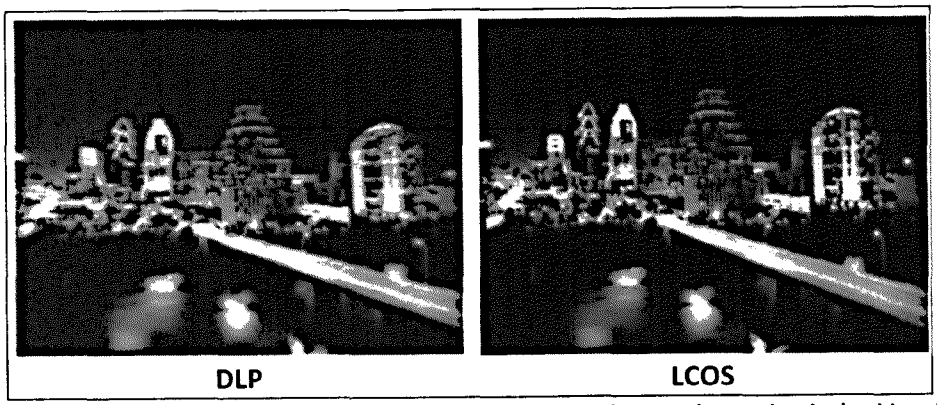

Figure 5.7 Colour appears blurred and broken in the DLP projected image due to the single-chip rainbow artefact, whilst the LCOS image appears crisp and sharp (ProjectorPoint, 2009).

Figure 5.8 The fill factor of the three dominant projection technologies. Circuitry lies around each pixel of the LCD device and causes spaces between the micro-mirrors of the DLP, thereby creating the screen door effect. However in LCOS, the circuitry is behind the panels and virtually eliminates the screen door effect (Canon, 2010).

These advantages and disadvantages for each technology, when assessed in terms of their effects on the accuracy of phase measurement based on projected fringe pattern profilometry, has been previously researched by several authors (Baker *et al.*, 2005,

Harding, 2009, Huang and Chiang, 1999). The major shortcomings to examine in this regard include the screen door effect, the rainbow artefact, the brightness and the contrast levels. These shortcomings affect the sinusoidal intensity of the projected fringe patterns in terms of poor contrast and brightness levels, consequently, errors in the phase modulation are introduced. The screen door effect and the rainbow artefact cause discontinuities in the projected pattern. Since the video projectors are basically designed and optimised for video presentation, the resultant non-sinusoidal projected fringe pattern is a substantial source of error in phase measurement when they are used for this scientific application. Baker *et al.* (2005) demonstrates that LCD projectors surpassed DLP projectors in producing better sinusoidal patterns with less phase error, producing a difference of average error of 0.06 radians. Harding (2009) shows that in some cases the significant effects of the low fill factor of the LCD projectors can be mitigated by defocusing the projected image, and the rainbow artefact of the DLP projectors can eliminated by removing the colour wheel filter. However, DLP projectors still exhibit the screen door effect, which is at a level less than that found in LCD projectors, but is higher than that found in the LCOS projectors.

A Canon XEED SX60 projector (Figure 5.10) has been adopted for fringe projection in the system that was produced during this research programme, because it uses LCOS technology. Moreover, this projector is powered by the Canon AISYS (Aspectual Illumination System) technology, which overcomes the traditional LCOS drawbacks of poor contrast and low brightness, by minimising the light leakage and enhancing the contrast. AISYS consists of a sophisticated optical array, including a specially designed Polarisation Beam Splitter (PBS). As a result, colours stay true to the source image and projection remains powerfully bright (Canon, 2010). The other main specifications and advantages of the adopted projector are summarised as follows:

- Native display resolution of 1400×1050 pixels (SXGA+), and a maximum resolution of 1600×1200 pixels (UXGA).
- 2,500 lumens output which produces vivid images, even in the presence of bright ambient light.
- 2000:1 contrast ratio which produces a true black colour.

- Compact and light design, weights 4.6kg.
- 2500H lamp life.
- Service port for input of serial commands, without using the remote control. This feature is crucial because when the projector is being used for fringe projection, the projector settings (such as zoom and focus) that are used at measurement time should exactly match the ones that were used at the calibration stage, and if the projector remote control is used incorrectly this may invalidate the calibration data. Moreover, in some applications the system computers are placed in another room (see Section 4.3.1) which makes it unreliable to select the best calibration settings for the projector using the remote control. Thus the remote control can be disabled, and a projector control software has been developed by the author (Figure 4.13), which is further discussed under Section 4.1.7.
- Ventilation vents, cooling fan, and layout of the optical array ensure better cooling and noise prevention.

Figure 5.9 Magnified region of two projected images using LCD and LCOS technologies (Canon, 2010).

Figure 5.10 The projector (Canon XEED SX60) that was adopted for fringe pattern generation (Canon, 2010).

However, although it can be seen that the image quality of this projector is very high, there remain other important shortcomings that the adopted projector shares with other digital projection technologies. These limitations are considered to be important to the performance of phase measurement techniques, based on digital fringe projection, and are as follows:

- Image non-linearity: as video projectors are generally designed to provide better quality images as perceived by the human eye, the projected images are pre-processed before projection. This introduces non-linearities that result in a deviation of the projected fringes from a true sinusoidal structure, which in effect introduces the presence of higher odd harmonics. This non-linear artefact can be mitigated by correcting the gamma value of projected pattern (Guo *et al.*, 2004). Gamma correction methods are further discussed in Section 7.2.1.
- Lower brightness levels in multi-sensor configurations: as the system uses three projectors, RGB chromatic filters in the three primary colours are attached to each projector. This lowers the brightness to about a third of the available light output of the projector, however this drawback can be overcome by increasing the gain value of the camera. Higher gain of the grabbing device introduces a lower SNR, but this still can be mitigated by pre-processing the acquired image using simple image filters. Section 7.3.1 discusses this issue in detail.
- Deficiency in terms of real-time projection: as video projectors are engineered for satisfying their customers in terms of video playback and

presentation, they process the streamed video images in multiple internal frame-buffers before projection in order to eliminate any flickering that might be noticed by the human eye. In most cases, this causes the projected fringe pattern (when using the phase stepping profilometry method) to interlace with the previously written image inside the memory-buffer. Consequently, the camera records a disturbed fringe intensity image (see Figure 5.11). To avoid such a large source of error, a simple synchronisation is used between the projector and the camera by setting a time delay (50-70mSec for the adopted projector) after the pattern projection and before the recording of the intensity distribution. This introduced delay because of projector latency hinders the use of measurement methods based on phase shifting profilometry for dynamic objects, so the phase shifting technique is only used for static, or very slowly moving subjects. Whereas for dynamic objects, other fringe profilometry techniques that are based on only a single projected fringe pattern (such as Fourier fringe profilometry) can be utilised without the need of invoking any delay between the camera and the projector.

- Thermal Drift effect: this is caused by the generated heat of the projection lamp and power supply circuits inside the video projector. This causes very slight movement of the lens and the internal components, which in turn induces a drift in the projected fringe pattern over the operation time. Harding (2009) shows that the short-term effect of thermal drift is negligible, while in the long-term it can produce a drift in the fringe pattern by an amount corresponding to one pixel. Section 4.2.2 shows the thermal drift effect on experimental results.

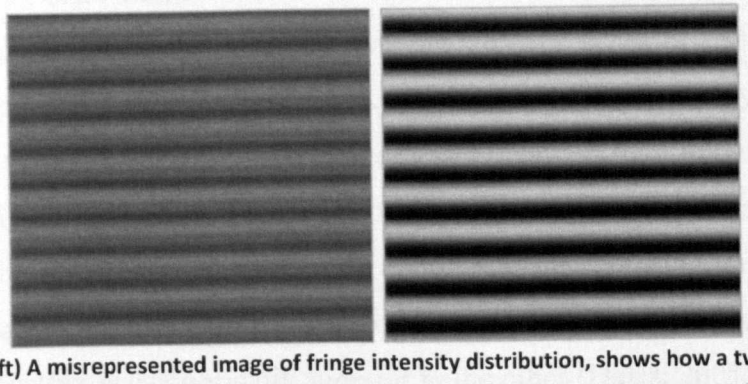

Figure 5.11 (Left) A misrepresented image of fringe intensity distribution, shows how a two subsequent projected patterns are interlaced as a result of multiple-frame buffering inside the projector. (Right) A well-represented fringe pattern with an accurate sinusoidal intensity profile.

5.1.2 Image Grabbing

Generally, modern industrial cameras offer potentially high quality images in terms of bit-depth, resolution, contrast, sensitivity, SNR, acquisition speed, dynamic range and data transfer speeds to the host computer. However, the selection of an appropriate camera technology depends totally on the intended application. This section reviews the currently available camera technologies, their advantages and disadvantages and the required features for achieving the best performance in the context of optical 3D surface measurement based on fringe pattern projection/analysis. The section ends by reviewing the adopted camera and its features.

Cameras are obviously dividable into two main groups; monochrome and colour. Monochrome cameras offer higher quality at low cost, but the ability to detect colour adds considerable flexibility. Nevertheless, because the system is designed to use three-sensors and each sensor (consisting of a paired combination of a single camera and a single projector) is fitted with chromatic filters in one of the three primary colours, the selection and discussion of the available choices lies only within the context of the digital area-scan monochrome cameras. There are three major factors that need to be considered when selecting a grabbing device for the modulated fringe pattern; firstly, the performance of the sensor and supporting electronics of the camera. Secondly, the interface technology responsible for how the image is managed and transferred to the computer and thirdly, the optical characteristics of the camera lens.

5.1.2.1 Sensor Performance

Modern digital cameras employ one of two fundamental types of solid-state sensor technologies, either Charge Coupled Device (CCD) or Complementary Metal Oxide Semiconductor (CMOS). Both of the image sensors convert light into electric charge via an array of photosensitive elements (pixels) and process it into electronic signals. However, each sensor employs different technologies for capturing images digitally. Each has unique strengths and weaknesses, giving certain advantages in different applications. Neither is categorically superior to the other (Dalsa, 2005).

In a CCD sensor, the built up charges of the imaging pixels are transferred using one of three common architectures: full-frame, frame-transfer, or interline-transfer. The full-frame architecture is the technology adopted in this system, due to its high sensitivity, the small size of its CCD sensor and its high fill factor (Andor, 2006). In the full-frame CCD (Figure 5.12) the accumulated charge of the array of pixels is shifted vertically, row by row, into the serial output register. Then for each row, the readout register is shifted horizontally, pixel by pixel, and in turn each pixel is fed into an analogue-to-digital converter and amplifier. While in a CMOS sensor, each pixel has its own analogue-to-digital converter (and often also includes amplifiers and other circuits such as those used for noise reduction), so the charge-to-voltage conversion is performed on a row and column basis and the voltages are read out in parallel rather than the sequential architecture that is used in CCD devices.

Figure 5.12 A CCD sensor moves photo-generated charge from pixel-to-pixel and converts it to voltage at an output node. A CMOS sensor converts charge to voltage locally at each pixel (Dalsa, 2005).

The differences in readout techniques of both CCD and CMOS sensors have significant implications for the resultant image quality. Table 5.1 summarises the main differences of both technologies in relation to the following factors on the image quality:

- Uniformity: which is the consistency of response for different pixels under identical illumination conditions. Ideally, CMOS uniformity is lower than that of CCD due to the spatial charge-to-voltage and amplifier variations.

- Fill factor (or well capacity): which is the percentage measure of the area of the pixel that can actually gather light. In CCD devices, all of the pixel area is devoted to capture light which gives a 100% fill factor. While in CMOS technology, only 20-50% fill factor is obtained because much of the pixel is occupied with local processing circuits (Stemmer-Imaging, 2010).
- Dynamic range: which describes the ratio between the smallest and the largest amounts of light that can be handled by the sensor. CCD gives an advantage by about a factor of two in comparable circumstances with CMOS, because of CMOS on-chip circuitry (Dalsa, 2005).
- Uniform shuttering: which is the capability to start and stop exposure arbitrarily. CCD delivers superior electronic shuttering with little fill-factor compromise, whilst implementing uniform electronic shuttering in CMOS requires even more on-pixel circuitry, which results in a compromise of an even lower fill-factor.
- Scan speed: CMOS offers higher scan speeds than CCD technology, because the digitisation process is performed locally at the same time for every pixel.

	CCD	CMOS
Uniformity	High	Low to moderate
Amplifier Mismatch	N/A	Moderate
Uniform Shuttering	Fast	Poor
System Noise	low-noise	More susceptible to noise
Fill Factor	High	Moderate
Dynamic Range	High	Moderate
Scan Speed	Moderate to high	Higher

Table 5.1 Comparison between CCD and CMOS imagers in terms of their readout techniques and their effects on the quality of output image.

Generally, the process of choosing the best imaging technology is totally dependent on the application. CMOS sensors are commonly incorporated into applications that require low power consumption or which have tight space constraints, whereas CCD sensors are usually used in applications that require higher image quality. Nevertheless, there are other important capabilities that need to be considered when

selecting an industrial camera that is based on CCD technology, for this type of application and these are discussed below as follows:

- Scan type: which is the method in which the image rows are scanned by the sensor and transmitted into the internal buffer of the camera. There are two scan types: interlaced and progressive. The interlaced technique scans the odd rows in one field and the even rows in another field, then integrates both fields together to produce a full frame which causes an interlace artefact when capturing moving objects, as each field of rows is exposed at a different time (see Figure 5.13). Whilst in progressive scan devices all rows are scanned sequentially and transmitted at once, which makes it ideal for high speed imaging applications.
- Quantum efficiency: is a property of the photovoltaic response defined as how well the pixels convert the incoming photons into stored electrons. So, if an imager has a quantum efficiency rating of 50% at a particular wavelength, it indicates that for every two photons striking a photodiode, one electron will be created in the pixel.
- Sensitivity: which is a measure of the minimum amount of light that is required for a sensor to produce an output with an acceptable SNR, and which is a critical factor, particularly for applications in the low light level region. The main related factors affecting overall camera sensitivity are fill factor, quantum efficiency, and charge conversion (JAI, 2007). Charge conversion is a measure of how much voltage is created from each electron that is generated by a pixel. Manufacturers usually use a light unit (lux) to represent the minimum illumination required at a specific aperture to produce a usable image.

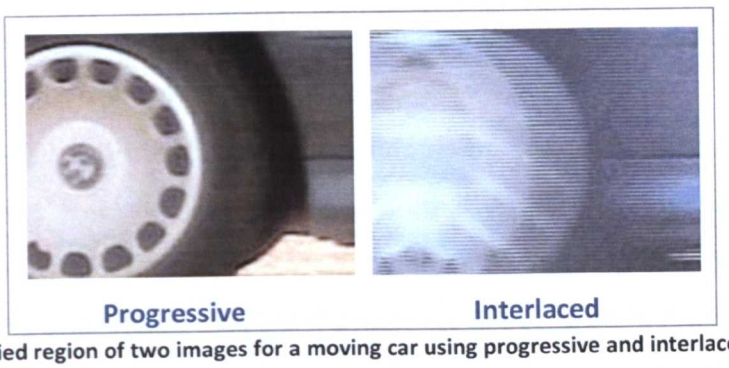

Figure 5.13 Magnified region of two images for a moving car using progressive and interlaced scan techniques (Stemmer-Imaging, 2010).

- Sensor noise: which is inherent to all electronic image sensors and arises from a variety of sources, which are discussed later under Section 7.3.1, along with the adopted techniques that are used for noise reduction. Noise usually occurs during the readout process and by the inherent background energy which typically increases heat (dark noise). The quality of a resultant image with regard to the level of noise is measured as the signal-to-noise ratio (SNR), where higher SNR produces more reliable images.
- Pixel and sensor chip sizes: the size of the sensor is represented in fractions of an inch, and the most commonly used sizes in machine vision applications are: 1/4", 1/2", 2/3"and 1". The size of the sensor elements (pixels) are measured in microns. Dynamic range and sensitivity are proportional to the pixel size, with larger pixel sizes producing higher quality images, whilst this decreases the sensor image resolution. Hence, sensor sizes of 1/2" and 2/3" are predominantly adopted in machine vision applications (JAI, 1998).
- Exposure time: which is the amount of time (usually measured in micro-seconds) that the sensor is exposed to light. Longer exposure times allow the sensor to gather more light, but generates more noise, bedsides causing exposure blur artefacts when acquiring images of moving objects. Typically, the exposure time for capturing moving scenes should be short enough so that the object moves by less than one pixel per frame acquired.
- Binning: which is the ability to combine the output of adjacent pixels into a single larger output (super pixel), for instance a binning of 2x2 represents the size of the cluster of pixels that is combined to output a super pixel. This technique is very helpful when used in low-light scenes, as it increases the sensor sensitivity as well as the SNR. However, the presence of a defective pixel in the binning group affects the resultant value.
- Triggering: which is the ability to initialise the exposure at a particular time, and is often called asynchronous reset.
- Resolution: which is the ability of an imaging system to resolve image details as separate features, for cameras it normally refers to the spatial number of active pixels in the sensor. Most machine vision applications require high resolution as it directly affects their performance (Figure 5.14). To determine the required resolution it is essential to consider the required field of view

and the smallest feature that needs to be determined. If the sensor lacks the ability to provide the required resolution, some manufacturers provide pixel jittering functionality, which increases the inherent resolution (typically by a factor of 4) but at the cost of reducing the number of frames delivered per second by a similar factor (i.e. typically 4 times slower) (Moshe, 2004).

Figure 5.14 Regions of two images with low and high spatial resolution sensors (Moshe, 2004).

5.1.2.2 Interface Technology

Historically, interfacing a camera to a host computer is performed by using an independent frame grabber to digitise the analogue signal produced by the camera, whilst modern cameras produce a digital output which is immediately available for transfer to the host computer.

Modern interface standards are reviewed as follows, along with their advantages and limitations (Stemmer-Imaging, 2010):

- CameraLink: which is based on Channel Link hardware technology, which uses serialised parallel data for transmission. The standard provides three levels of implementation: Base, Medium and Full, with bandwidths of 2.04 Gbit/s, 4.08 Gbit/s and 5.44 Gbit/s respectively. Selecting the level of implementation is dependent on the camera requirements, such as bit-depth, data transfer rate and number of channels. The maximum cable length is 10m over copper cabling and this can be extended over fibre cabling using repeaters and extenders. CameraLink requires the use of a frame grabber at the host computer, which increases installation expense and complexity.

- Universal Serial Bus (USB 2.0): which has a maximum throughput of 480 Mbit/s with a maximum cable length of 5m. For longer cables repeaters and active hubs are used.
- FireWire (IEEE-1394b): which was originally developed as a flexible interconnection bus for consumer peripherals and provides a bandwidth of up to 800 Mbit/s over cable lengths of up to 4.5m. Cable length can be extended using fibre optic extenders up to 100m. The standard can connect up to 16 cameras using an independent FireWire card installed on the host computer.
- Gigabit Ethernet (GigE): which is a serial network standard that has very high bandwidth (1Gbit/s) and allows for very long cable lengths (up to 100m) with Cat5e or Cat6 standard networking cables. It offers a low cost interface that is widely used in standard computer networking hardware. Using the GigE standard can exploit the processing power of hardware-based architectures simply by sending image data to multiple hosts simultaneously (Figure 5.15) through a GigE switch (multicasting capability).

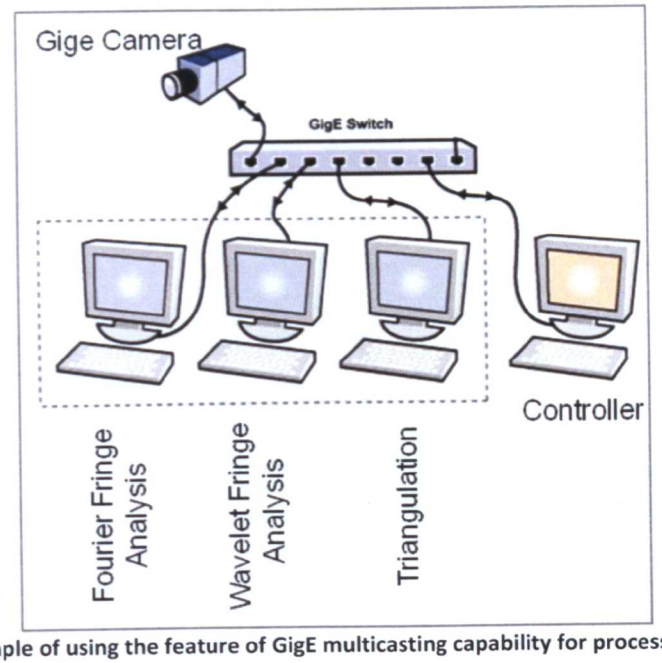

Figure 5.15 An example of using the feature of GigE multicasting capability for processing image data using different fringe analysis based techniques at a different dedicated host computer for each technique.

The interface technology that was adopted in this system is the GigE approach, due to its native long distance support, high data transfer rate and low complexity and expense. However, there are still some other capabilities that need to be considered

when selecting the appropriate GigE based camera for such a system, which mainly lie within the context of transmission performance and reliability. Most GigE camera vendors provide their own GigE driver to be installed on the host computer as the native Microsoft Windows stack driver does not efficiently interpret and transport the image gigabit data. So it is crucial to provide a dedicated GigE driver, to be installed under the Windows native stack driver, in order to deliver the higher performance and lower CPU load that is suited to demanding vision applications. The GigE driver uses a GigE Vision Stream Protocol (GVSP) filter driver installed on top of the regular NIC driver (Wilson, 2008). In operation, the specialised driver instantly recognises the packet header of incoming data. If the header belongs to a lower-performance protocol, such as the Transmission Control Protocol (TCP), the data are sent to the Windows IP stack for processing. If the header belongs to a performance-oriented protocol, such as GVSP, the data are forwarded to the GigE kernel and SDK (see Figure 5.16).

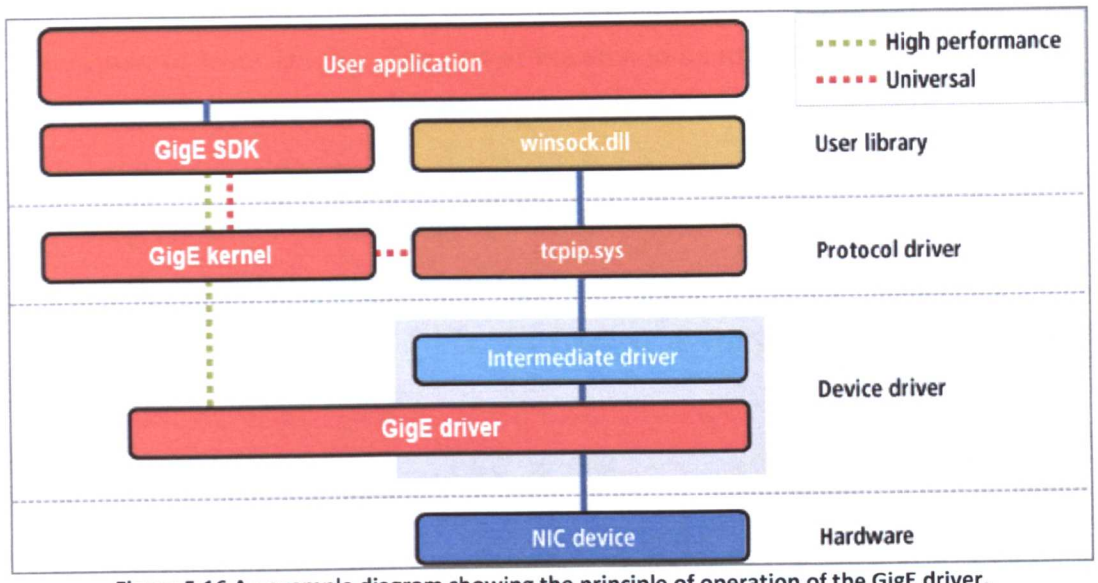

Figure 5.16 An example diagram showing the principle of operation of the GigE driver.

Another important parameter to be considered is the GigE camera support for high packet size of the data transfer stream. The standard packet size for Gigabit Ethernet cards is 1500 bytes, while most of the more reliable and specialised cards can provide higher packet sizes of up to 16 Kbytes. So it is essential to check the camera support for high packet sizes, as this reduces the load on CPU. Experimentally, it has been demonstrated by the author that using the Prosilica dedicated GigE driver with the highest supported maximum transfer unit (8 KBytes) reduces the CPU processing

overhead from 20% to 4%, which leaves the rest of the CPU processing power to be exploited by the vision application.

5.1.2.3 Camera Lens

Regardless of the camera technology, correct choice of lens is paramount, because no single lens can offer the perfect solution for all vision applications (Stemmer-Imaging, 2010).The lens is responsible for collecting the scattered light from the scene and presenting it upon the camera sensor. Lenses come with fixed or adjustable focal length capabilities, however for the purpose of building such a system for 3D surface measurement, lenses with adjustable focal lengths are commonly adopted to cope with the variety of different system applications, although the cost of this flexibility is the fact that imaging performance is often slightly compromised when compared to similar fixed focal length lenses. When selecting a lens some important factors need to be considered, in order to achieve the required performance and reliability, which are listed as follows:

- Field of View (FOV): The size of the area to be imaged.
- Focal length (FL): it is the distance between the camera sensor and the centre of the lens, the higher the focal length, the larger will be the image magnification. To determine the required focal length both the FOV and the working distance (WD) of the application are needed along with the size of camera sensor (Figure 5.17), the relation is represented mathematically as follows (Navitar, 2006):

$$FL = \frac{CCD \times WD}{FOV} \tag{5.2}$$

  where *CCD* is the width of the camera sensor.
- F-number: which defines the amount of light that can pass through the lens to the camera sensor. An adjustable diaphragm (or iris) inside the lens controls the aperture. The F-number is calculated by dividing the focal length of the lens by its effective aperture. So, the higher the F-number, the smaller is the iris aperture and the larger is the system depth of field.
- Depth of field: it is a measure of the range of object distances within which the image appears to be sharp and focused. It is mainly a function of the aperture of the lens and the working distance. To get an acceptable depth of

field it is necessary to compromise between the exposure time of the camera and the iris aperture.

- Image circle: light is projected as a circle onto the camera sensor because the lens is circular (Figure 5.18). The image circle must be larger than the sensor, because larger camera sensor results in dark corners within the image.
- Image quality: in terms of resolution and distortion, lenses with poor resolution or defects do not make full use of the camera potential, resulting in inaccurate measurements.

Figure 5.17 A distance diagram for Camera/lens pair (Navitar, 2006).

Figure 5.18 A diagram for an ideal image circle (Navitar, 2006).

5.1.2.4 Adopted Technologies for Image Grabbing

To adapt the functional requirements, in terms of optical surface measurement based on fringe pattern profilometry, the camera and lens pair must produce high quality images for static and dynamic object measurement applications. The adopted camera is a Prosilica GE1380 (Figure 5.19), its features are as follows (Prosilica, 2006):

- Sensor type: 2/3" CCD Sony ICX285, with progressive scan capability and quantum efficiency of 65%.

- Resolution: 1360×1024 pixels with the capability of region of interest (ROI) capturing.
- Pixel size: 6.45 x 6.45 (μm).
- Interface standard: GigE.
- Exposure range: 10μs to 60s.
- Gain range: 0 to 31dB.
- Trigger latency: 3.8 μs.
- Spectral sensitivity range: 400 - 1000 nm (Figure 5.20).
- Dynamic range: 72dB.
- Bit depth: Mono8 (8-bit - 256 grey levels) and Mono16 (12-bit - 4096 grey levels).
- Speed: 20 fps at full resolution and 35 fps at 512×512 pixels.

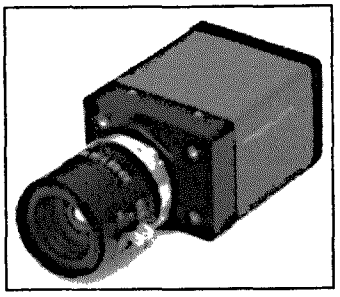

Figure 5.19 The adopted camera for the system, Prosilica GE1380 (Prosilica, 2006).

Figure 5.20 The monochrome relative spectral response of Prosilica GE1380 (Prosilica, 2006).

The lens needs to support a focal range of 22 mm to 66 mm in order to measure the surface of an object of dimensions 40 cm x 40 cm at working distance ranges from 1m to 3m, when using the Prosilica GE1380 camera. The adopted lens is a Navitar Zoom 7000, which offers a 6:1 zoom ratio over a focal range of 18 mm to 108 mm and a working distance of 12.7cm to infinity (Navitar, 2006). The adopted camera mount is a Manfrotto 410 geared head, which offers precise gear movement in three directions, pan, tilt and side to side tilt.

5.1.3 Chromatic Filters

As the system consists of three sensor heads it is necessary to minimise any potential chance for crosstalk amongst the sensors, and so each camera and projector set are fitted with colour separation filters. The colour filters on each sensor head enable simultaneous projection of the three different RGB coloured fringe patterns onto the object and ensures that each camera grabs only the intensity modulation of the correctly associated projector, without affecting the functionality of the other sensor heads. An additive colour separation model is adopted for the system using the primary colours: red, green and blue. The system performance, in terms of using multi-sensor profilometry, crucially depends on the degree of eliminating any overlapping wavelengths between the colours as well as the following characteristics of the chromatic filter:

- Centre Wavelength (CWL): which is the wavelength at the centre of the pass-band filter, that should be matched by the wavelength of each projected colour.
- Full Width at Half Maximum (FWHM): is the bandwidth at 50% of the maximum transmission. At this bandwidth there should not be any overlap between colour wavelengths.
- Peak Transmission (PT): it is the wavelength of maximum transmission, higher PT gives higher sensitivity and quantum efficiency.

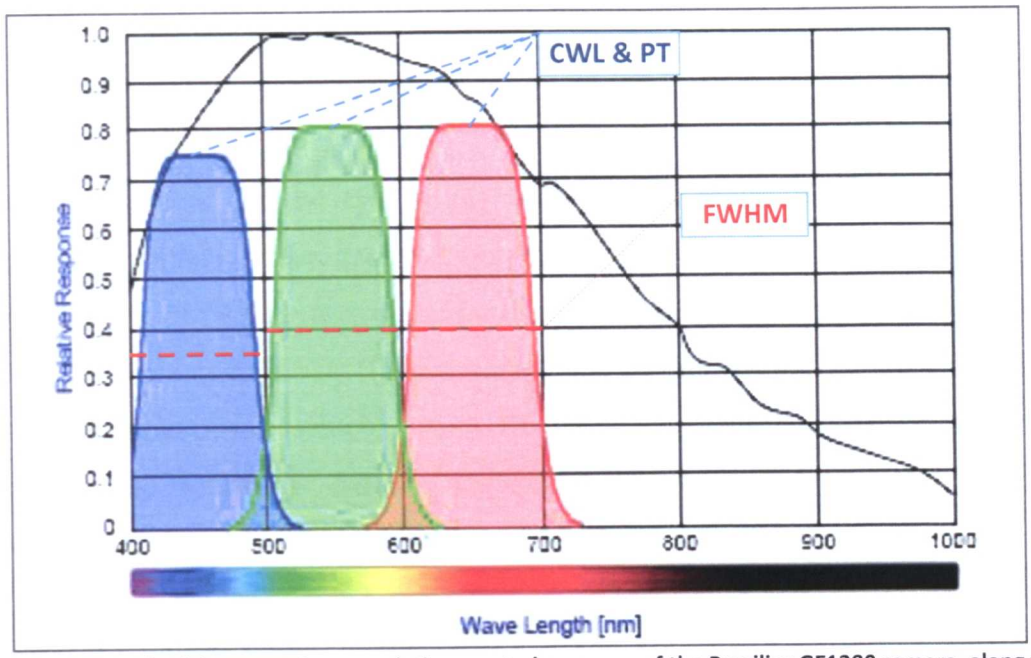

Figure 5.21 A graph of the monochrome relative spectral response of the Prosilica GE1380 camera, along with the resultant effect of using the colour filters on each channel.

The adopted filters have been carefully selected to eliminate any effect of colour crosstalk on the resultant measurement, Table 5.2 shows the characteristics of the adopted filter from Horiba Scientific and Figure 5.21 shows the resultant spectrum when applying the colour pass-band filters.

Table 5.2 The optical characteristics of the adopted chromatic filters (Horiba, 2007).

5.2 Processing Units and Networking Hierarchy among the Sensors

Modern advances in computer hardware afford both reliability and performance for demanding machine vision applications. This is in terms of the high processing power of modern multi-core CPUs, the huge capacities of cheap RAM and the fast transmission speeds of internal computer buses and network cards. These advances are crucial in building such a system, because each pixel of the image is independently processed. Moreover, advances in Graphics Processing Units (GPUs)

add an advantage for real-time projection of fringe patterns and visualisation of the resultant 3D data (Lau, 2010).

The adopted setup for the system (as illustrated in Figure 5.22) is to have an independent computer for each sensor head, which will be called the Sensor Processing Units (SPUs) and a dedicated computer for system management, the Central Measurement Server (CMS). Using this configuration, each sensor has its own processing power which allows the SPUs to mainly focus on achieving measurements, whilst the data management and user interfacing is channelled through the CMS. Each SPU has a dual Gigabit ports, one for the GigE camera and the other is connected to the CMS either via a Gigabit switch, or via a dedicated Gigabit port on the CMS. Both end-to-end Gigabit ports support Bus Mastering DMA (Direct Memory Access), which guarantees the lowest possible CPU integration into the transmission and receive operations (Intel, 2008). The specifications of the adopted computers are:

- SPU specifications:
  - Dell Precision T5400.
  - Intel Xeon E5420 Quad Core (2.50 GHz, 1333 MHz).
  - 4GB DDR2 667 MHz Quad Channel SDRAM memory.
  - 256MB PCIe x6 nVidia Quadro FX 570 graphics card with dual port, one for display monitor and another for fringe pattern projector.
  - Intel PRO/1000 MT dual port network adapter.
- CMS specifications:
  - Dell XPS 730X.
  - Intel Core i7 processor Extreme Edition 965 (3.20GHz).
  - 3072MB 1067 MHz Tri Channel DDR3 SDRAM memory.
  - Dual SLI 1GB DDR3 nVidia GeForce GTX285 graphics card.
  - Intel Gigabit ET quad port network adapter.

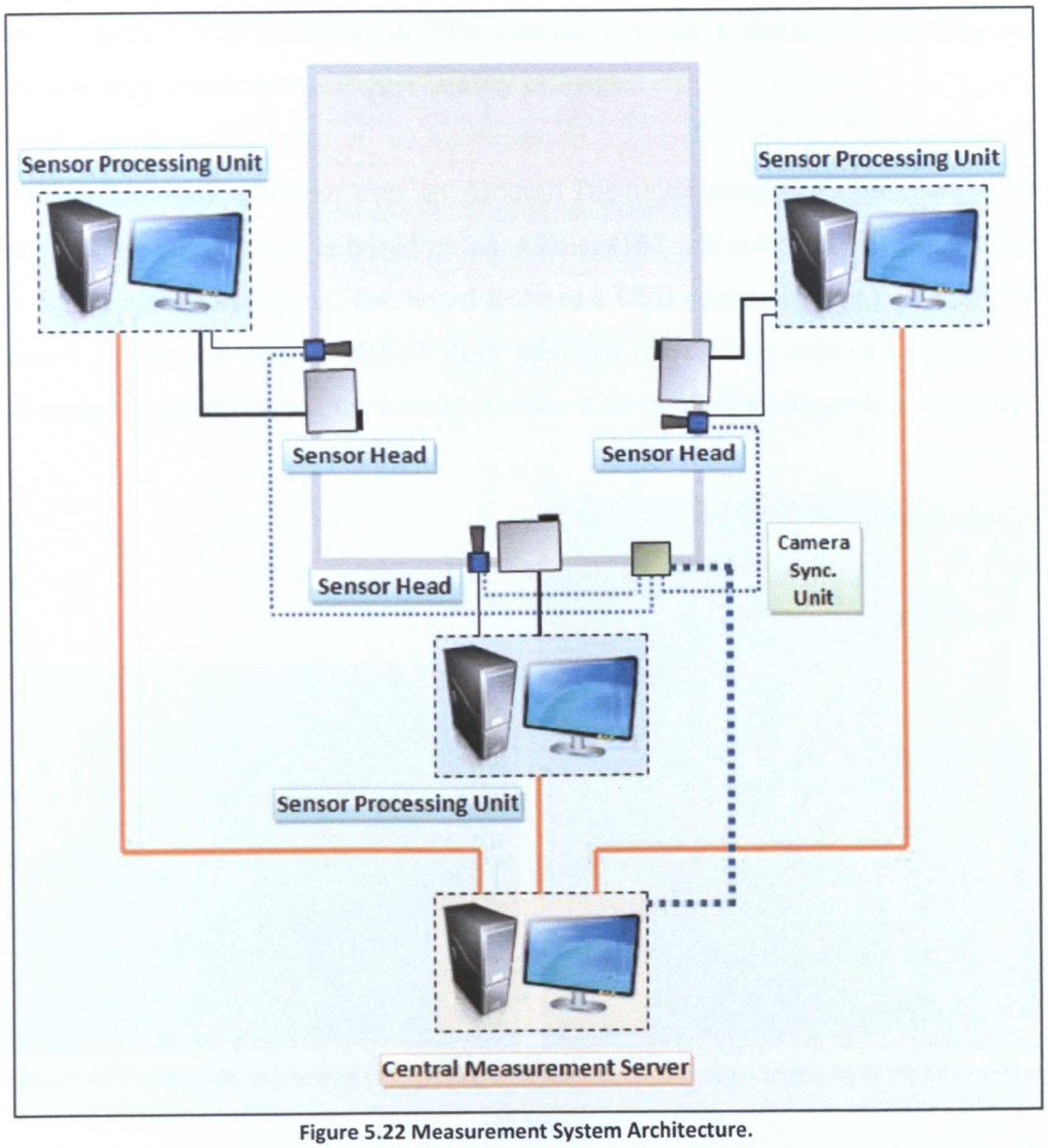

Figure 5.22 Measurement System Architecture.

5.3 Synchronisation Unit for the Cameras

For the purposes of the measurement of dynamic subjects with more than one sensor, it is vital to make sure that all sensor cameras grab the same scene simultaneously. This could be implemented by software triggering, initiated each time a new set of frames need to be captured by the cameras, as a command sent by the CMS to each SPU. However, because of the latency of network communications among the CMS and SPUs, hardware triggering is adopted and this offers high speeds and high precision in terms of the synchronisation of the cameras, with a synchronisation error in the order of under a microsecond. A dedicated triggering system has been designed by the author, which is controlled by the CMS and is connected to each

sensor camera. The Prosilica GE1380 cameras provide a dedicated asynchronous external trigger port, with a trigger latency of 3.8μs.

The synchronisation system uses an Arduino Diecimila general IO microcontroller board (Figure 5.23), that is based on an ATmega168 microcontroller, which offers 14 digital input/output pins. The board features a USB connection for power and IO control commands and 16 KB of flash memory for storing code. This gives the advantage of programming the board just once with the desired triggering frequency.

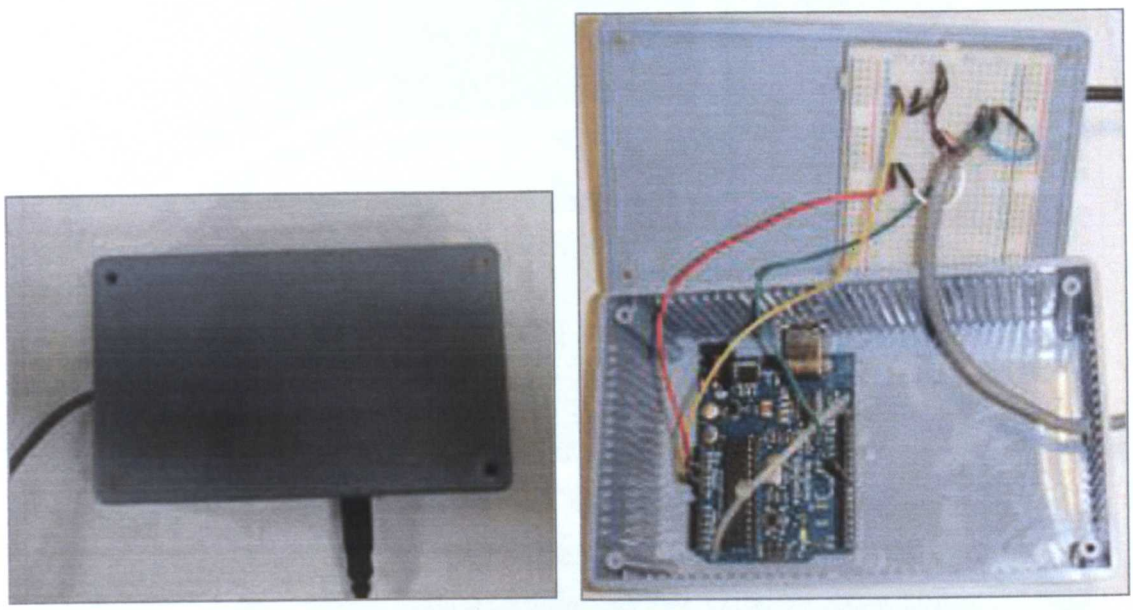

Figure 5.23 The specially engineered synchronisation system for simultaneous triggering of the three sensor cameras.

The triggering frequency should be carefully chosen as it is dependent on the actual camera grabbing speed and its exposure time. The max frame rate for the camera using the hardware trigger can be expressed as follows:

$$Max\ Frame\ Rate\ (Hz) = \frac{1}{Exposure\ Time\ (Sec) + \frac{1}{Actual\ Camera\ Speed\ (Hz)}} \qquad \textbf{(5.3)}$$

For instance, the actual grabbing speed for the Prosilica GE1380 is 35Hz at a resolution of 512x512 pixels, so if the highest exposure time for all of the sensor cameras is 0.032 Sec then the maximum frame rate that can be achieved with the hardware trigger is 16.5Hz. This means that the interval between each two successive triggering pulses should not be less than 60.57ms. To test the synchronisation accuracy of the system, the images of an LCD monitor with a

running timer application that is capable of millisecond temporal resolution are grabbed by the three sensor cameras (Figure 5.24). The cameras are set into hardware trigger mode, and triggered arbitrarily by the user at the CMS, through the triggering system.

Figure 5.24 An image shown to demonstrate the accuracy of the synchronisation (triggering) system, using a millisecond timer application.

5.4 System Calibration Hardware

As discussed in Chapter Three, the height and traversal calibration tasks for fringe based profilometry are performed by measuring the absolute phase and co-planar coordinates at different heights in order to construct the 3D calibration volumes. Three main factors are involved in obtaining accurate calibration volumes; firstly, how precisely the DC motor of the calibration elevator can move; secondly, the degree of flatness of the calibration surfaces; and thirdly, the degree of incline deviation of the calibration surface in both the horizontal and vertical axis.

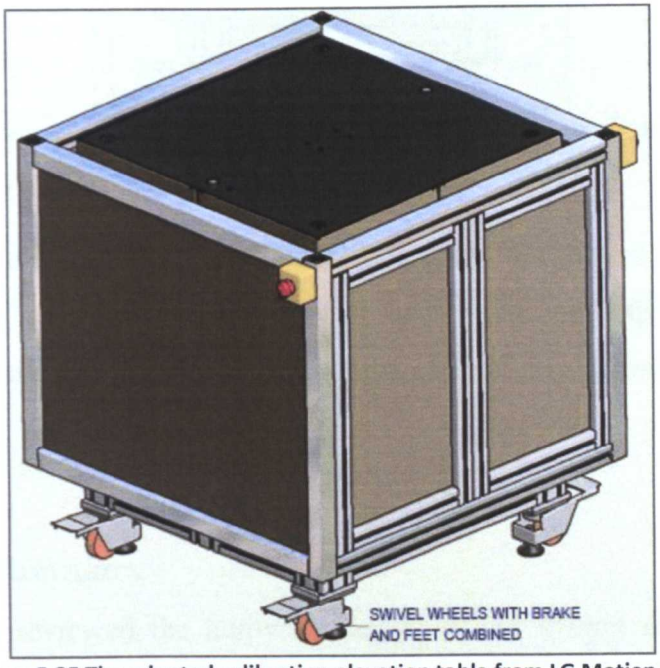

Figure 5.25 The adopted calibration elevation table from LG Motion Ltd.

In order to achieve the best results for the first and third of these factors, a customised calibration table (Figure 5.25) has been engineered by LG Motion Ltd (LG-Motion, 2009). The elevation motor is managed by a ViX Intelligent Microstep drive which can be controlled via a serial link to the CMS in order to perform the calibration of the three sensors at the same time. The drive can move the surface in micro-steps which gives an accuracy of 1μm for the movement of the calibration surface. The table height is 100cm with an elevation range of 50cm as illustrated in Figure 5.26. For ease of movement the table comes with swivel wheels as well as brakes with adjustable heights so as to obtain no deviation in the horizontal and vertical axes of the measurement.

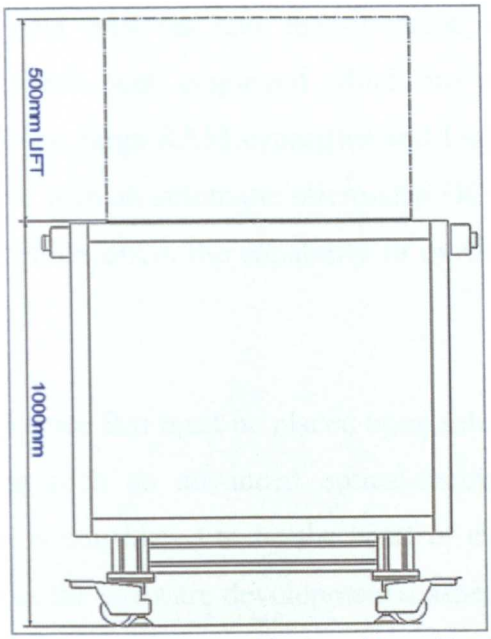

Figure 5.26 A diagram shows the side view of the calibration table.

Regarding the flatness of the optical calibration grids, toughened float glass with a thickness of 1cm, with surface painted with matt white for height calibration and with a checkerboard pattern for the transversal calibration, are used to offer a high level of flatness.

5.5 Chapter Summary

This chapter has reviewed the hardware design of the system that was produced during this research programme. Various hardware components, for the purpose of building such an optical metrology profilometry system, have been investigated in terms of their influence on the accuracy of measurement. For digital fringe pattern projection, the Canon XEED SX60 projector powered by LCOS technology has been adopted. LCOS projection technology provides better image quality than DLP and LCD technologies, in terms of higher fill factor and higher contrast and brightness levels in the images.

For the fringe pattern acquisition, the Prosilica GE1380 CCD-camera has been used as it provides a high image quality in terms of resolution, dynamic range, uniformity and SNR. In addition, it offers high speed image transfer to the host computer (1Gbit/s) using GigE technology, which enables the measurement process to be performed remotely from a distance of up to 100m using standard networking cables

(Cat5e or Cat6). For data analysis and measurement visualisation, advanced computing technologies have been employed which are powered with the most recent multi-core processors, large RAM capacities and high bus speeds. Finally, a customised elevation table with an automatic micro-step DC motor has been used in the calibration process, which offers the capability to move the calibration surface with a tolerance of $\pm 1 \mu m$.

In spite of the high importance that must be placed upon selecting the right hardware components for building such an advanced optical-metrology system, it is the processing software that is considered to be the heart of every vision system. The following chapter presents the software developmental aspects of this system, along with the software engineering techniques that were employed.

5.6 References

ANDOR. 2006. *CCD Sensor Architectures* [Online]. Andor Technology plc. Available: http://www.andor.com/learning/digital_cameras/?docid=314 [Accessed 2 Feb 2008].

BAKER, M. J., XI, J., CHICHARO, J. & LI, E. Year. A contrast between DLP and LCD digital projection technology for triangulation based phase measuring optical profilometers. *In:* HARDING, K. G., ed., 2005 Boston, MA, USA. SPIE, 60000G-12.

CANON. 2010. *Canon XEED Projector* [Online]. Available: http://www.canon.co.uk/For_Home/Product_Finder/Multimedia_Projectors/xeed/index.asp [Accessed 8 March 2010].

DALSA. 2005. *CCD vs. CMOS* [Online]. Available: http://www.dalsa.com/corp/markets/CCD_vs_CMOS.aspx [Accessed 22 January 2010].

DEBOER, C. 2008. *Display Technologies Guide* [Online]. Audioholics - Online A/V Magazine. Available: http://www.audioholics.com/education/display-formats-technology/display-technologies-guide-lcd-plasma-dlp-lcos-d-ila-crt [Accessed 1 Nov 2009].

GUO, H., HE, H. & CHEN, M. 2004. Gamma Correction for Digital Fringe Projection Profilometry. *Appl. Opt.*, 43, 2906-2914.

HARDING, K. Year. Comparison of projection means for structured light systems. *In:* HUANG, P. S., YOSHIZAWA, T. & HARDING, K. G., eds., 2009 San Diego, CA, USA. SPIE, 74320S-10.

HORIBA. 2007. *Colour Separation Filters* [Online]. Horiba Scientific Ltd. Available: http://www.horiba.com/uk/scientific/products/optical-filters/optical-filters-by-application/colour-imaging-filters/colour-separation-filters/ [Accessed 6 Mar 2010].

HUANG, P. S. & CHIANG, F.-P. Year. Recent advances in fringe projection technique for 3D shape measurement. *In:* CHA, S. S., BRYANSTON-CROSS, P. J. & MERCER, C. R., eds., 1999 Denver, CO, USA. SPIE, 132-142.

INTEL. 2008. *Intel PRO/1000 MT Dual Port Server Adapter* [Online]. Available: http://www.intel.com/products/server/adapters/pro1000mt-dualport/pro1000mt-dualport-overview.htm [Accessed 8 January 2010].

JAI. 1998. CCD Performance and the Pixel Size. Available: http://www.jai.com/SiteCollectionDocuments/Camera_Solutions_Application_Tech_Note/TechNote-TH-1084-CCDPerformance.pdf.

JAI. 2007. Camera Sensitivity Explained. Available: http://www.jai.com/SiteCollectionDocuments/Camera_Solutions_Application_Tech_Note/TechNote-TN-0701-SensitivityExplained.pdf.

LAU, D. 2010. *LEADING EDGE VIEWS: Structured Thinking* [Online]. Vision Systems Design. Available: http://www.optoiq.com/index/machine-vision-imaging-processing/display/vsd-article-display/9114323847/articles/vision-systems-design/volume-15/Issue_3/departments/Leading_Edge_Views/Structured_Thinking.html [Accessed 5 Mar 2010].

LG-MOTION. 2009. *Motion Solutions* [Online]. Available: www.lg-motion.co.uk [Accessed 10 July 2009].

MOSHE, B.-E. Year. Jitter Camera: High Resolution Video from a Low Resolution Detector. *In:* ASSAF, Z. & SHREE, K. N., eds., 2004. 135-142.

NAVITAR. 2006. *ProsilicaMacro Zoom Lenses - Zoom 7000* [Online]. Available: http://www.machinevision.navitar.com/pages/product_information/low_mag_video_lens/zoom_7000.cfm [Accessed 8 March 2010].

PROJECTORPOINT. 2009. *DLP and LCD Projector Technology Explained* [Online]. ProjectorPoint. Available: http://www.projectorpoint.co.uk/ProjectorLCDvsDLP.htm [Accessed 2 Nov 2009].

PROSILICA. 2006. *Prosilica - GigE Vision cameras - GE1380 high sensitivity CCD camera - 20 fps* [Online]. Available: http://www.prosilica.com/products/ge1380.html [Accessed 8 March 2010].

STEMMER-IMAGING 2010. *The Imaging and Vision Handbook*, STEMMER IMAGING GmbH.

TEXAS-INSTRUMENTS. 2009. *How DLP Technology Works* [Online]. Texas Instruments. Available: http://www.dlp.com/technology/how-dlp-works/ [Accessed 2 Nov 2009].

WILSON, A. 2008. *Driven to Distraction* [Online]. Vision Systems Design. Available: http://www.vision-systems.com/display_article/319428/19/none/none/Feat/Driven-to-Distraction [Accessed 1 Mar 2010].

Chapter Six

Software Design of the System

In spite of the high importance of selecting the right hardware components for building an optical-metrology system, it is the processing software that is considered to be the heart of every vision system. A particular problem associated with developing such a software system is the necessity to fulfil the requirements of various measurement applications and conditions upon the measurement process (see Chapter Four: Specifications and Applications of the System). These specific application requirements and measurement conditions may impose several constraints upon the measurement process, such as the characteristics of the object(s) being measured, the desired speed and accuracy of the measurement system, and the measurement scene conditions (for example illumination levels, etc). In order to effectively manage these different constraints, the software should provide an interactive Graphical User Interface (GUI) that is underpinned by a flexible and powerful processing core of software algorithms in terms of robustness and performance. Accordingly, the user can interactively select the best combination of image processing algorithms and their respective parameters in order to achieve a certain desired measurement task and in order to satisfy the particular constraints of the application.

This chapter presents the software development aspects of the system that was produced by the author during this research programme. The development framework and hierarchy of the system software are reviewed in this chapter, along with the software engineering techniques that were employed. Finally, the programming languages and libraries that have been used are discussed.

6.1 Development Hierarchy of the System Software

This section reviews the development hierarchy of the software system that was developed in this project, and this is shown in Figure 6.1. The lowest layer in the

hierarchy is the infrastructure layer, which includes: the hardware platform of the processing units (described in Section 5.2), the Operating System (OS) platform and the GigE camera driver (described in Section 5.1.2.2). The middle layer represents the development framework, which includes both the programming libraries that have been used (which are discussed later in Section 6.4) and the Software Development Kit (SDK) of the GigE camera. The top layer represents the measurement application that has been developed by the author, and here two different versions were developed, one for the Sensor Processing Units (SPU) and another for the Central Measurement Server (CMS). Each version has different core processing and Graphical User Interface (GUI) components, which are discussed in detail later in the next section.

The operating system platform that was used is Microsoft Windows XP Professional edition (32-bit). Other operating systems, such as Linux were excluded because of the lack support in terms of device drivers for the system hardware and a lack of compatible versions of the libraries used at the early stages of developing this system. However, it is recommended for any future work that the system functionality under Linux be examined, as a Linux OS system may have better capability in terms of utilization of the system hardware than is the case for Microsoft Windows operating systems. Windows XP running as a 64-bit operating system was also excluded for several reasons. Firstly, because, although it gives better performance for processing double precision (64-bit) floating point numbers, 32-bit floating point numbers provide adequate precision for the system applications (see Chapter Four) and so only 32-bit floating point numbers will be used in this system (with a precision of three decimal places), so it is logical to use a 32-bit OS. Secondly, 64-bit versions of Windows XP are designed for greater memory accessibility and memory management (National-Instruments, 2009), i.e. they can directly access memory more than the 32-bit versions that can address only up to 4GB of RAM. However, the memory usage of this system has been examined in detail by the author and this analysis has shown that it does not need more than 1.5GB of memory for most applications. Thirdly, the hardware devices used in the system require 64-bit drivers if they are to work on Microsoft Windows 64-bit OS versions (Microsoft, 2007); however, these drivers were not supported by hardware vendors at the early stages of this project. Finally, most of the system software

components (where possible, excluding those that were precluded due to lack of 64-bit drivers) were tested by the author under a Windows XP 64-bit OS and were found to give performance levels similar to those that were achieved under a 32-bit Windows XP OS version.

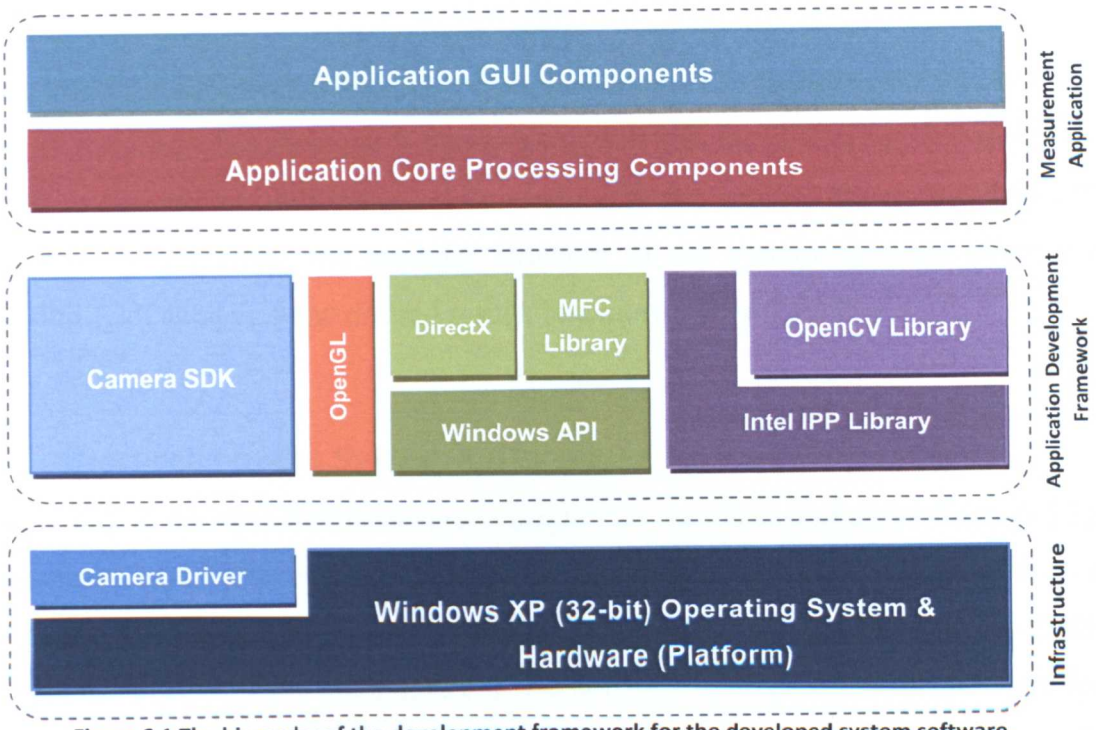

Figure 6.1 The hierarchy of the development framework for the developed system software.

Whereas the IDL (ITTVIS, 2010) and Matlab (Mathworks, 2010) programming languages were used for prototyping a number of different algorithms in order to rapidly find a sequence of image processing operations that satisfied certain specific tasks, C++ was the main programming language of choice that was used for the development of the system software due to its inherently high processing speed, which is well suited to dynamic applications. Some of the methods and algorithms that are related to 3D surface shape measurement using fringe analysis have been adopted from previous works, and these are listed as follows:

1. Fringe analysis techniques:
    a. Fourier Transform Profilometry (FTP) using manual Butterworth filter: code was provided by Lilley (1999) in the IDL language (ITTVIS, 2010), then exported to C++ by the author.

b. Wavelet Transform Profilometry (WTP): code was provided by Abid (2008) and Gdeisat *et al.* (Gdeisat *et al.*, 2009) in the C language, then converted to C++ by the author.

2. Phase unwrapping techniques: code was provided by Ghiglia and Pritt (1998) and Karout (2007) in the C language, then converted to C++ by the author.

The workflow for developing such a complicated piece of software has involved the use of software engineering techniques (as will be discussed later in Section 6.3) in order to provide flexibility and robustness across the entire software development process. Consequently, the modular structure of the system software offers the possibility of achieving the desired results in a most efficient manner.

6.2 Hierarchy of the System Software

According to the specified hardware configuration (as discussed under Section 5.2), the measurement process is performed independently for each sensor head at a dedicated SPU and then the results from the sensor heads are transferred to the CMS. Figure 6.2 illustrates the architecture of the software configuration; the software for each SPU is mainly responsible for performing the measurement task and optionally transferring measurement information to the CMS. Whereas the CMS is mainly responsible for coordinating multi-view measurement tasks that are distributed amongst multiple SPUs, and also for collecting the results to be optionally displayed, or saved locally to disk, according to the user's preferences. This scenario gives the flexibility for the user to run the measurement task either from a single SPU (as a stand alone sensor choice, i.e. a single-view measurement), or from the CMS (as a multi-sensor choice, i.e. providing a multi-view measurement). The task of measurement synchronisation of the three SPUs (in the case of a multi-view choice) is the responsibility of the CMS, and is achieved through the Camera Synchronisation Unit (CSU). The CMS is also responsible for harmonising the process of collecting the measurement results from the SPUs; by simultaneously signalling all of the SPUs to send their next set of results, and this is performed only after having received the entire set of results from the previous measurement.

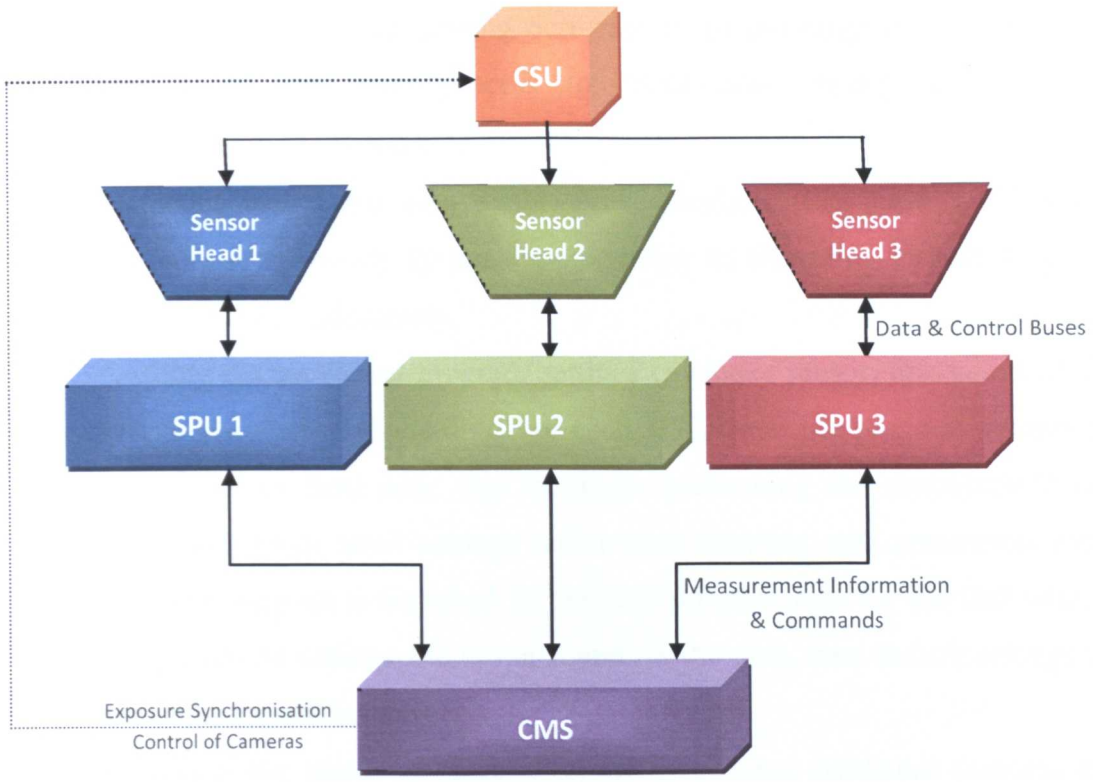

Figure 6.2 The architecture of the software configuration for the developed optical profilometry system.

The GUI for the system software was programmed so as to be as detailed as possible in order to provide the user with complete control and a very flexible means of interaction with the measurement process, whilst also giving the possibility to shield the complexity of the underlying core processing mechanisms from the user when under normal operation. This section reviews the software configuration for both the SPU units and the CMS. The software is categorised into two main parts, namely that of the core processing functions and the GUI components. The GUI section explains the configuration of the user interface of the system software, and the core processing section explains the mechanisms of the underlying processing tasks.

6.2.1 Sensor Processing Unit Software

6.2.1.1 Hierarchy of the Core of Processing

When the SPU program is launched, it performs the following tasks:

1. Setup the GUI components which are related to measurement (discussed later in Section 6.2.1.2).

2. Boosting the entire processing performance of the program; by setting the priority of the main process to "Real-Time" using Windows API *SetPriorityClass* function.
3. Detecting the number of available processors/cores that are installed within the current hardware system, which helps in allocating system hardware resources more effectively.
4. Loading the pre-saved program settings (includes sensor, measurement and output settings) from the disk. For each SPU, the entire program settings are stored on the hard disk; this facilitates performing the measurement task using previously used settings rather than selecting new parameters every time the program is launched. If the SPU program runs for the first time, or the pre-saved settings file is not found on the disk, then default settings for the program will be used.
5. Checking the status (connectivity) of the sensor hardware (camera and projector), and deploying their pre-saved settings.
6. Checking for the presence and validity of the calibration data files.
7. Initiating the networking thread (which is responsible for communication with the CMS).
8. Any errors encountered whilst performing the tasks above are reported to the user.

The user can start a measurement task according to the desired settings and preferences. Figure 6.3 shows a flowchart for the measurement task that has been developed by the author, where the user selects the operation mode: either online (using images acquired live from the camera), or offline (using previously acquired images that have been saved to disk) as a source of input images. Both measurement operational modes can be performed either once (on a single frame-set), or continuously (upon multiple frame-sets).The process of measurement is as follows:

1. A new measurement task is initiated according to the user's preferences and measurement settings. Three simultaneous threads are created in order to achieve the task, namely:

a. An image collection thread: which is responsible for collecting input images, either from the hard disk, or live from the camera, and storing them in an input buffer.
b. A processing thread: which is responsible for the core processing tasks associated with fringe profilometry.
c. An output manager thread: which is responsible for storing data onto the hard disk, displaying images and transferring data to the CMS.

2. The next step of initiating the measurement task is to initiate the fringe analysis, unwrapping and calibration algorithms. This is done by allocating their memory and deploying the measurement preferences to them. For the online operation mode, both the camera and the projector are prepared for measurement.
3. The image collection thread starts by collecting images inside the input buffer, whereas the processing and output manager threads are set to an idle state.
4. The processing thread is signalled by the image collection thread as soon as there is an "image-set" inside the input buffer. The number of images associated with each image-set for processing is variable and is determined by the selected fringe analysis method (e.g. we may be using only a single image for Fourier Transform Profilometry with integrated triangulation spots within the fringe pattern, or perhaps four images for three-frame Temporal Phase Stepping with a single extra dedicated frame for the triangulation spots, etc.). The image collection thread then either ends in the case when we are performing a single measurement, or else it keeps collecting images continuously until measurement is stopped by the user.
5. When the processing thread is signalled, it creates an output segment (*OutputFrame*) and attaches an image-set to it after removing it from the input buffer. The most recent image-set from the input buffer (i.e. the latest image set that has been grabbed from the camera) is selected to be processed by the processing thread.

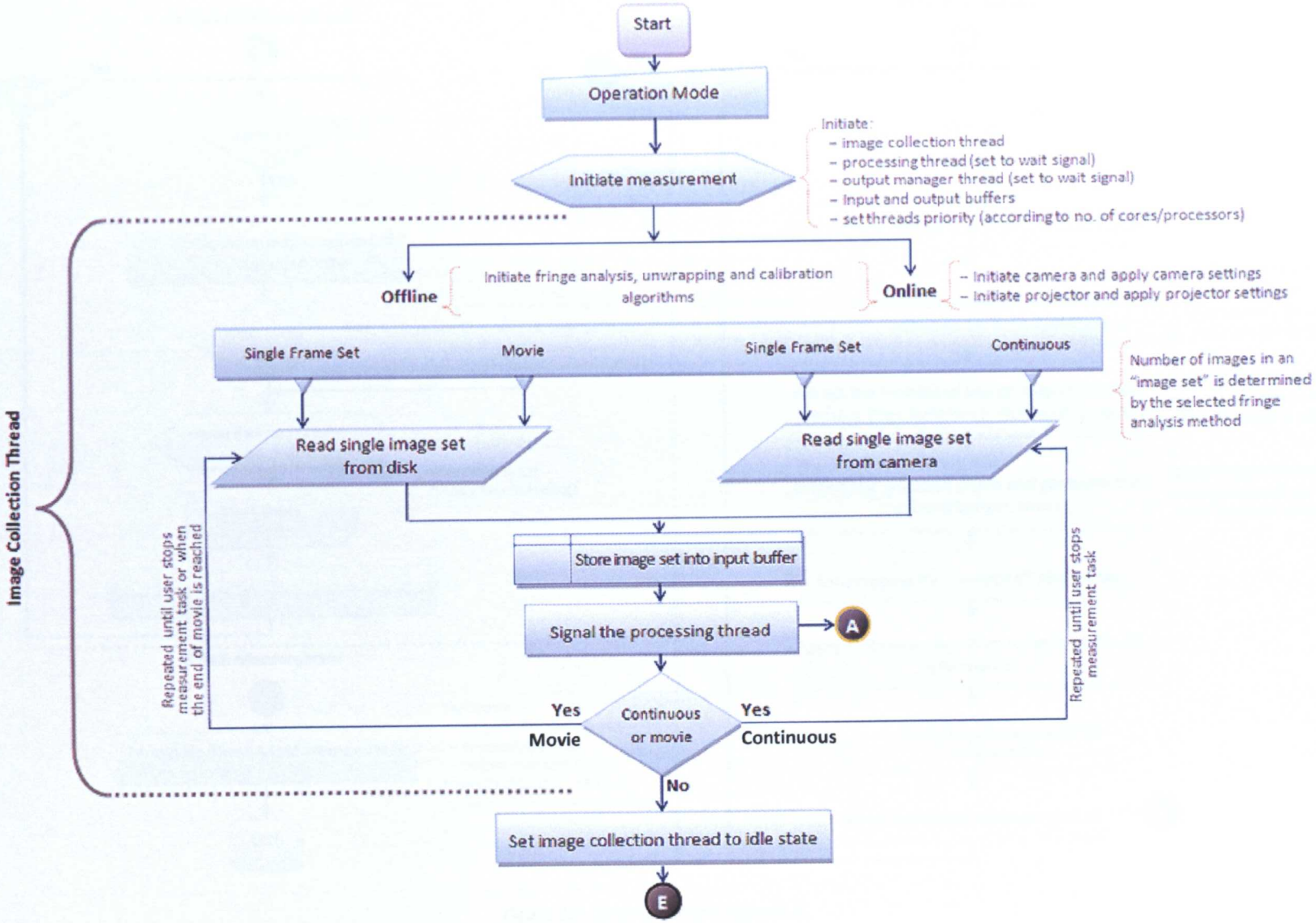

Figure 6.3 Flowchart for a measurement task running on an SPU, comprising three threads that are running concurrently.

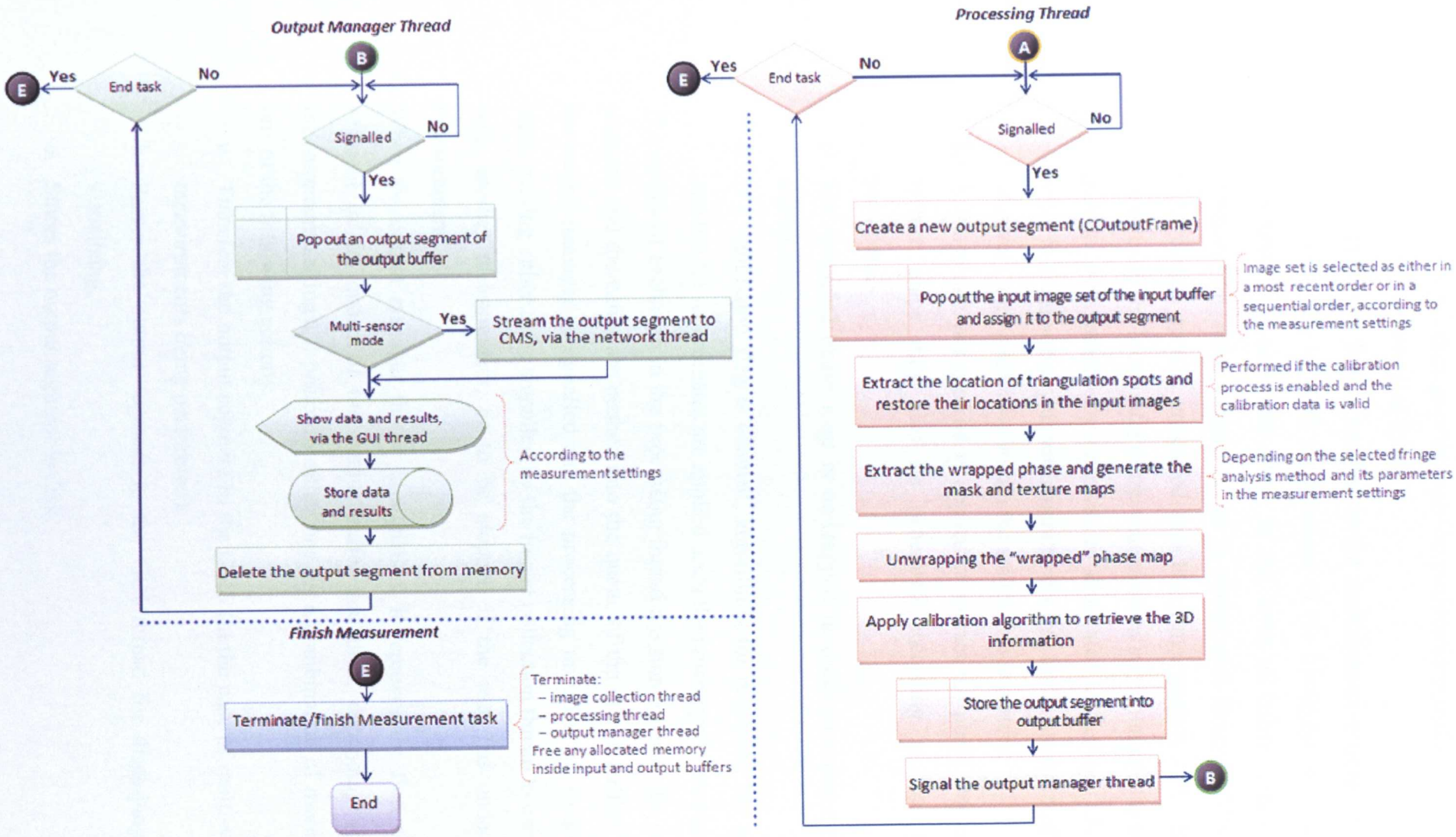

Figure 6.4 Continued from Figure 6.3.

6. The processing thread then goes through the profilometry analysis according to the measurement settings, as follows:
    a. If a calibration flag is enabled in the measurement settings and the calibration data is valid, the locations of the triangulation spots are detected. This may take place in the form of either a dedicated triangulation spot image, or as a compound image where the triangulation spot is integrated into the fringe pattern itself. In the latter case, the location(s) of the triangulation spot(s) inside the fringe pattern are synthetically restored (as illustrated in Section 7.3.2) in order to eliminate any measurement errors due to the presence of their relatively high intensities within the source fringe pattern.
    b. A fringe analysis method is applied to extract the phase. Mask and texture maps may also be generated according to the user's preferences.
    c. The extracted phase map is unwrapped in order to remove phase ambiguities.
    d. If a calibration flag is enabled, algorithms for retrieving the height and the XY-coordinates are applied upon the unwrapped phase map.

   The results of each step in the processing thread are stored inside the output segment and thereafter are pushed into the queue of the output buffer. Then the output manager is signalled and the processing thread is set to an idle state, waiting either to be signalled by the image collection thread to carry on with another measurement, or to be stopped if the user has ended the measurement.
7. When the output manager thread is signalled, it removes the first output segment in the queue of the output buffer and then, depending on the measurement settings, it performs either one, or a combination of more than one of the following actions:
    a. Transfers the output segment to the CMS (in the case of multi-sensor measurements being performed).
    b. Passes the output segment to the GUI thread for displaying and visualising.
    c. Stores the output segment to disk.

When the measurement task is ended (or terminated) by the user, the three task threads (for image collection, processing and the output manager respectively) are all stopped. Any memory that has been allocated to the measurement algorithms, and the input and output buffers is freed.

When the SPU program is closed it uninitialized any GUI components, saves the current measurement settings onto disk, stops the networking thread and deallocates any reserved memory.

6.2.1.2 Hierarchy of the Graphical User Interface

The GUI components of the SPU software are responsible for interacting with the user, as well as displaying information about the measurement (graphically and textually). The main five components of the SPU GUI (as shown in Figure 6.5) and their roles are as follows:

1. **User commands toolbar:** which is responsible for interacting with the user, performing tasks such as starting, pausing and stopping the measurement, with different options, or operating modes. The measurement settings dialog box is also categorised under this group of components. This category was developed using the Windows API, MFC and OpenCV libraries.
2. **Event log component:** which is responsible for notifying the user about specific errors, and event information such as the connectivity status of the sensor components, the network connection status to CMS, the validity of calibration data files, the starting and ending notifications of a measurement task, and any errors encountered in loading the settings file. This category was developed using the MFC library.
3. **Measurement information components:** which are responsible for displaying textual information about a measurement task and the hardware system being used. The components were developed using the MFC library and they are arranged into three groups as follows:
    a. Main information: shows the operation mode, the main characteristics of the input images (such as the resolution and fringe spatial frequency), the measurement methods used (for fringe analysis, phase unwrapping and phase-to-coordinates conversion), and the main

information about the hardware system being used. Memory usage by the program is also shown here, and this is updated dynamically to show the size of memory used for a measurement task. This group is updated when the program is launched and each time a measurement task is started.

b. Speed information: shows monitoring information for every step of the measurement process. This group is dynamically updated by all threads that are involved in measurement and includes the following:
    i. The grabbing speed and the number of image-sets inside the input buffer. These are updated by the image collection thread.
    ii. The time required for each of the fringe analysis, phase unwrapping and phase-to-coordinates conversion tasks is updated by the processing thread. In addition to this, the number of output segments inside the output buffer and the number of frames processed so far are displayed.
    iii. The output manager thread updates the time required for storing, visualising and transferring data.

c. Sensor information: shows the connectivity status of the sensor components.

4. **Image display components:** which is responsible for showing a monochrome display of the results of each step in the measurement process, including: grabbed fringe images, wrapped phase, unwrapped phase, mask map, texture map and triangulation spot images. This category was developed using the Windows API, and the MFC library. Images are arranged into a set of tabs, which can be browsed by the user.
5. **Result visualisation and plotting components:** which were developed using the Windows API, and the MFC and OpenGL libraries. They are arranged into two tabs as follows:
    a. 3D visualisation tab: the user can visualise the 3D information and adjust the 3D rendering parameters (such as rendering using texture and rendering ranges, etc.).
    b. 2D cross-section tab: the user can view graphical plots of the source images, wrapped phase, unwrapped phase and height information; by selecting the number of a row or column to plot.

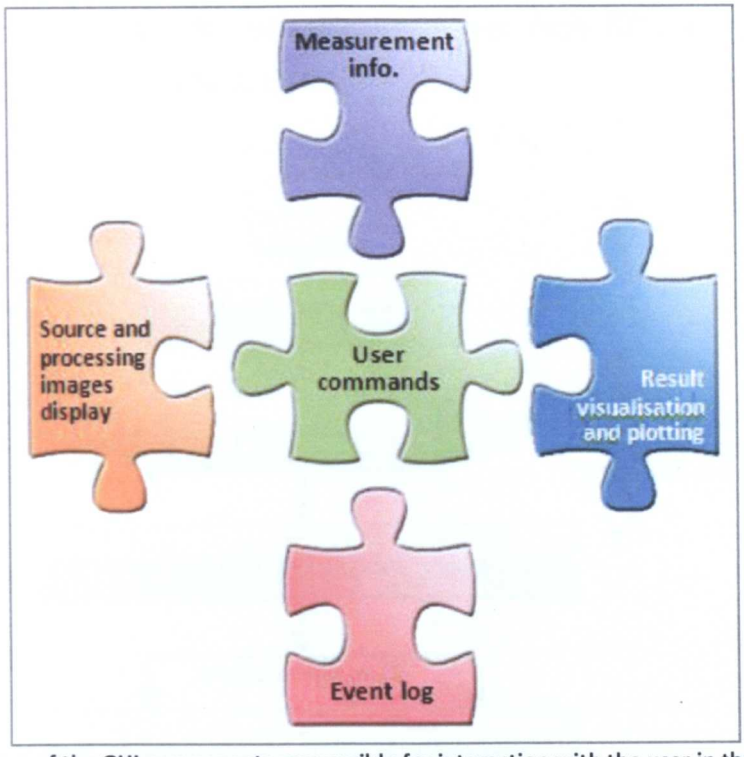

Figure 6.5 A diagram of the GUI components responsible for interaction with the user in the SPU application.

The GUI components were programmatically optimised in terms of memory usage and reliability in order to accommodate various measurement tasks. For instance, 3D rendering settings can be changed for faster rendering in a case where the system is performing dynamic measurement, or alternatively may be changed to a high resolution rendering setting when visually inspecting the measured objects. The components are functionally integrated with the core processing components, so as to provide the user with information interactively through the entire range of measurement stages.

6.2.2 Central Measurement Server Software

When the CMS program is launched, it initialises its GUI components, determines the number of installed processors/cores within the hardware system (to allocate them for its threads), allocates an input buffer (for result collection from the individual SPUs), and initiates the networking thread (to communicate with the SPUs). The software provides multi-view surface measurement functionality by employing a multi-sensor approach (in collaboration with the three SPUs). The CMS signals the SPUs to start and stop a measurement task, as well collecting the results to be displayed, and/or saved. Measurement can be performed either as a single shot

measurement, or alternatively continuously, where each SPU is responsible for sending the results individually to CMS.

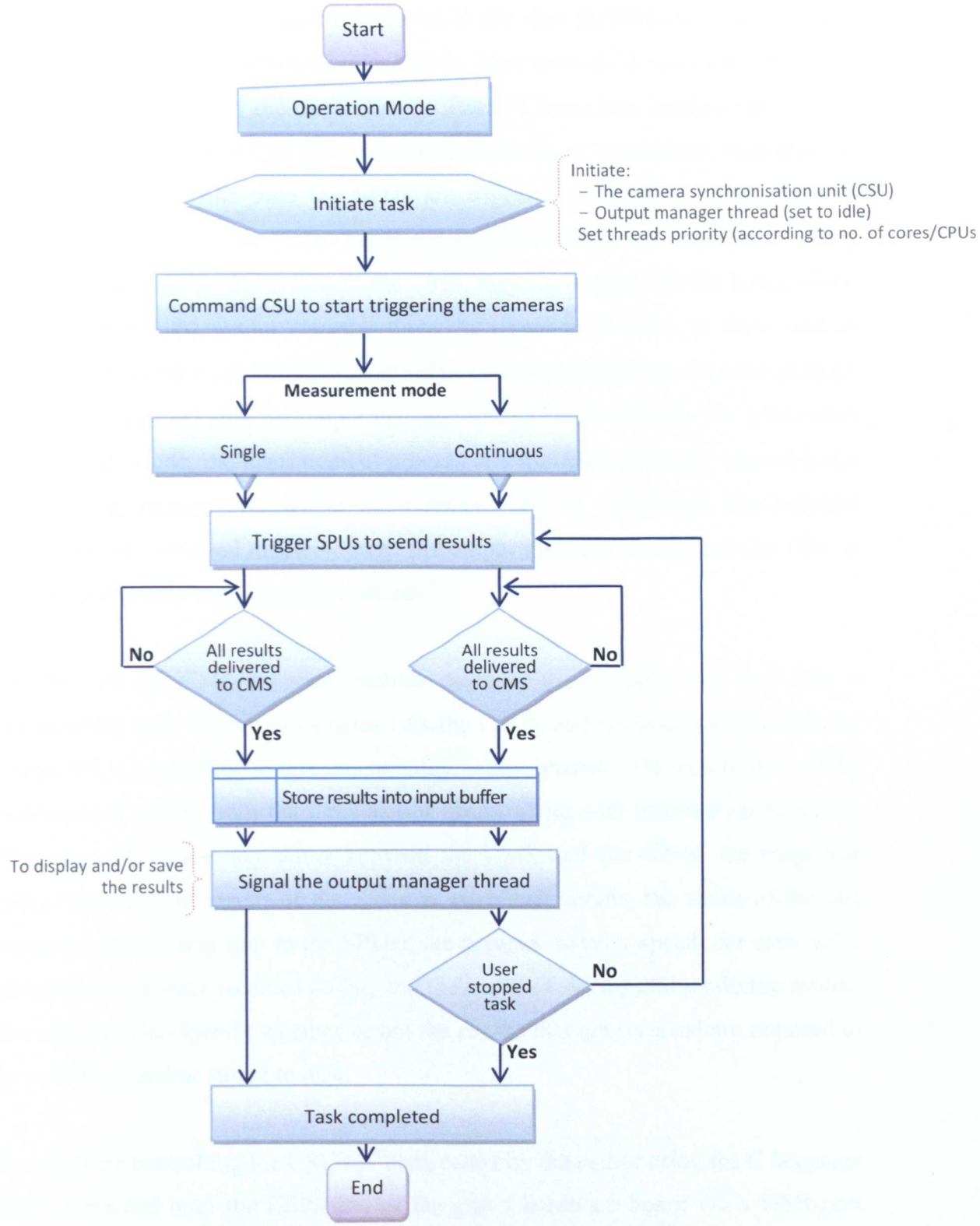

Figure 6.6 Flowchart of a measurement task running on the CMS.

Figure 6.6 shows a flowchart showing multi-sensor measurement being managed via the CMS. Upon selecting the type of measurement mode (single shot or continuous), a measurement task is begun by initialising a dedicated thread (output manager thread) to visualise, and/or store (according to the user preferences), the incoming measurement results from the individual SPUs. Next the CSU is commanded to start triggering the cameras of the three sensors. The SPUs are then commanded to start measurement (either in single shot measurement mode, or continuous measurement mode) and at the same time the SPUs are triggered to send the next available measurement results to the CMS. When the required results have been returned by all of the SPU's within the system to the CMS, they are pushed into the queue of the input buffer and the output manager thread is signalled in order to show, and/or store, the measurement information. For single measurement mode, the measurement process is completed after the output manager thread finishes its job. For continuous measurement mode, the measurement process is terminated when the user ends the measurement process. When the measurement task is completed, the program deallocates any reserved memory, stops the output manager thread, and the CSU is commanded to stop triggering the cameras.

The GUI of the CMS program enables the user to manually start and stop a measurement task, triggering cameras (via the CSU), and communications with the system SPUs. In addition to this functionality, it also provides 3D visualisation of the measurement results from the three sensor heads, along with information about the following: the connection status between the CMS and the SPUs, the triggering status (sent/acknowledged) of the SPUs to send their results, the status of the last command (which was sent to the SPUs), the network transfer speeds for each SPU, the number of results received so far, and the speed of storing and rendering results. The user can also specify whether or not the results that are received are required to be visualised, and/or stored to disk.

The software controlling the CSU has been coded by the author using the C language and is uploaded onto the EEPROM of the unit's hardware board via a USB port (serial-over-USB). The CMS sends commands to the board to start or stop triggering the cameras, and the hardware board itself is responsible for starting or stopping the "hardware trigger" of all the cameras concurrently. This scenario guarantees that the

system has as short as possible a level of triggering latency (as discussed in Section 5.3), as opposed to the case where the cameras are triggered directly by the CMS using a software triggering approach, in which case the triggering latency might become significantly higher.

6.3 Used Software Development Techniques and Approaches

It is important to observe good software engineering techniques when developing such an advanced and complex optical profilometry system. The software development for this project has addressed the following issues:

1. Real-time capability: which was achieved by concurrency processing to utilise multi-core processors.
2. Reliable memory utilisation: which guarantees that no memory "leaks" have occurred when a measurement task is stopped, or the program is ended.
3. Hardware-independent optimization: which should be achieved as much as possible, without any additional effort (i.e. development rework for specific hardware), or any significant loss of efficiency (i.e. by not utilising the available hardware resources efficiently).
4. Software maintenance flexibility: which simplifies any bug fixes, or hardware changes, without the need for re-writing large sections of code.
5. Hardware monitoring and error logging: which is essential in order to notify the user about any errors that may occur.
6. Interchangeable algorithms: which are invoked by various components of the measurement process, such as: memory allocation/de-allocation, the filtering and the pre-processing algorithms.
7. Reliable network transfer: which ensures the integrity of data transfer between the CMS and the SPUs, with the highest transfer rate that is affordable by the specific system hardware.

This section reviews the software development techniques that were adopted during the development of the software system that was produced as part of this work.

6.3.1 Object-Oriented Design

An object-oriented design methodology was adopted during the development of the software system. This helped in reducing the complexity of such an intricate software system, by breaking up the measurement process into clear and simple modules that serve specific purposes. This approach has advantages in terms of improved understandability and maintainability of the code, when it is compared to a conventional procedural approach, where variables and functions are distributed all over the code listing (Lafore, 1998). In addition, due to the feature of encapsulation of the code into modules, this approach ensures a reduced number of code defects and also facilitates the replacement of an existing module with a new implementation (Horstmann, 2006). For instance, the implementation of the SDK of the camera is not accessed directly; it is instead encapsulated inside a camera object (module), which is accessed directly by other parts of the software system. Thus, changing the camera hardware, or the camera SDK, only requires the changing of the SDK implementation inside the camera object, instead of changing all occurrences throughout the entire code of the system software.

The program modules were implemented programmatically as classes using the C++ language. Each class encapsulates the related process and data models (variables and functions), where they can be initialised, de-initialised and accessed. Figure 6.7 shows the classes (or objects) that are associated with the task of performing a measurement. This design plays an important role in separating the GUI from the other processing components, where only the "measurement task class" is used for communicating with the GUI components. The measurement task class, in its turn, acts according to the user commands that are received through the GUI components. For instance, upon receiving a 'start measurement' command, the measurement task class prepares the system for measurement, initialises the measurement algorithms and starts the measurement threads. Measurement settings (according to the user's preferences) are passed to the measurement task class; if the user wants to measure an object using Fourier Transform Profilometry (FTP), the measurement task class initialises an instance of the FTP class. Each individual class within the system software is responsible for the allocation and de-allocation of the memory that they use.

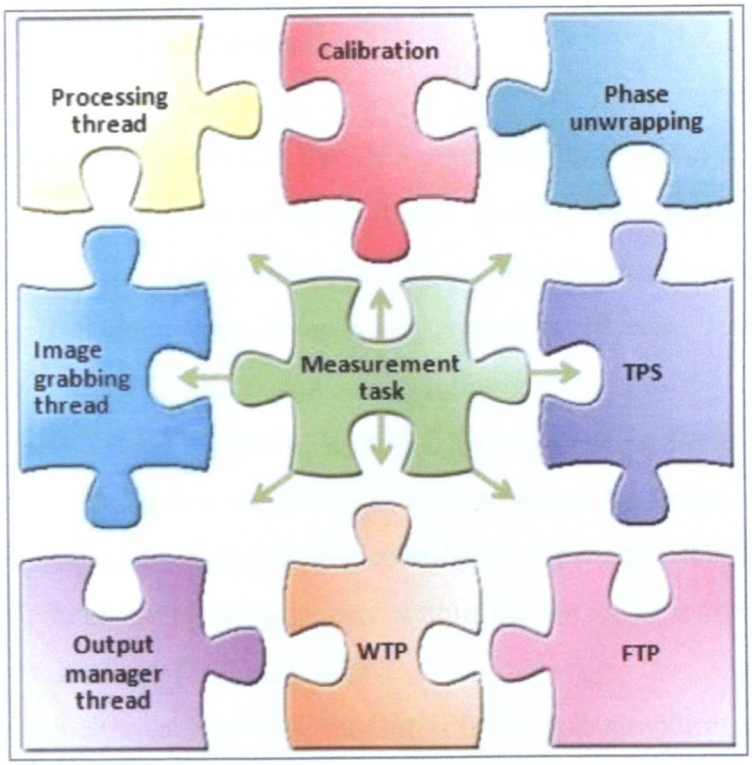

Figure 6.7 A diagram showing integrated modules (classes) in a measurement task running on a SPU.

C++ data structures were also used to organise several data items into a single module, in order to form a single entity. Examples of some data structures that were used in this software system are as follows:

1. System settings structure: which encapsulates all of the program settings, such as the user preferences for storing results into disk.
2. Projected triangulation pattern structure: which encapsulates the characteristics (size, location and intensity value) of a projected triangulation spot.
3. SPU network structure: which encapsulates the characteristics of the network connection between the SPU and the CMS, such as IP addresses, port numbers, connection status and other related data sets.

6.3.2 Data Structures

Data structures are the heart of any complicated program, because selecting the appropriate data structure affects the complexity of the resulting implementation (Skiena and Revilla, 2003). An incorrect selection in terms of data representation may increase the complexity of the implementation, hence it also makes software

maintainability and traceability more difficult, and additionally it may slow down the program's computational performance.

The containers (data structures) of the C++ standard library have been adopted to implement the data structures of the software system, because they offer thread safety (to be accessed from different threads simultaneously), self memory management and contain type-independent variables (Preiss, 1998). The C++ containers used in this software system are as follows:

1. List: this is a double linked-list, which was used as an input buffer to store images grabbed from the camera. It is accessed by image collection and processing threads. A list implementation was selected because it provides a faster element insertion (anywhere within the list) than is the case for other types of containers (Drozdek, 2004).
2. Queue: which is a First-In-First-Out (FIFO) data structure; where the first element added is the first one to be removed. A queue container was used to implement the output and network buffers, and to store and transmit the measurement results, respectively.

6.3.3 Real-Time and Multi-Thread Management

In computer science, a process represents an individual program, while threads are usually initiated within the boundary of a process. Nowadays multi-core architectures are widely available, and they can readily be utilised (using a multi-threading approach) to process multiple tasks, or large data-sets through multiple data paths (Liu, 2009). However, the development of a multi-threaded application is not a straight-forward task. The overall design of the software system needs to be modular in order to easily manage access to shared resources without causing deadlocks (Meyers, 2001). A deadlock happens when two or more threads are dependent upon each other, when accessing mutually-exclusive resources (Granatir, 2009). Mutually-exclusive access is used in order to prevent two threads from accessing a shared resource at the same time (Leiserson and Mirman, 2009).

A multi-threaded approach was used in programming this software system. For instance, the measurement task employs three threads in order to achieve the

measurement, whilst fully utilising the multi-core architecture. The three threads are the image collection, processing and output manager threads. The first two threads share the image grabbing input buffer, and the latter two threads share the result output buffer. In order to achieve a mutually-exclusive access to the input buffer, a Critical Section objects (Windows API: *CRITICAL_SECTION*) approach was adopted, because it offers a slightly faster, more efficient, mechanism for synchronisation than is the case for other approaches, such as the Windows API Mutex and Semaphore methods (Microsoft, 2006). In order to overcome a deadlock situation (whereas two, or more, threads are each waiting for the other to finish), an Event objects (Windows API) approach was used. A deadlock situation may occur between the image collection and processing threads, hence, the processing thread is initiated to await a signal from the image collection thread (when the input buffer is loaded). By using this scenario, the processing thread does not lock the input buffer whilst checking whether there is a new image-set inside the input buffer, hence it does not block (or delay) the image collection thread from inserting newly grabbed images into the input buffer, or from removing old images (for the purpose of only using the most-recently grabbed images).

For the access management of the output buffer, only Event objects are used, because the output results are stored in a queue (in the output buffer) and all of the results must be processed by the output thread manager. In this scenario, the output manager thread is set to wait for a signal from the processing thread, upon its finishing of the measurement. The software system does not rely statically on the number of available cores/processors, instead it has been programmed to dynamically detect the available number of processing cores and to allocate execution priorities for them.

In order to achieve a greater parallelism (such as optimising *for* and *while* loops), the Intel compiler was used so as to utilise the multi-core architecture. The Intel IPP (Integrated Performance Primitives) library was also used and both Intel products are discussed later under Section 6.4. The software system was also profiled in order to identify the most time expensive execution paths; where processing overheads

throughout the program were tackled and more efficient design and implementation were adopted where possible in order to reduce the overall execution time.

6.3.4 Memory Management

Memory management is the act of managing the main memory that is used by a program. This involves providing the most efficient ways to allocate and de-allocate segments of memory to a program, in terms of both reliability and access speed (Microsoft, 2005a). Hence, the efficient management of main memory was a vital task in the development of this real-time software system that demanded reliable, fast and dynamic usage of memory.

Software bugs that are introduced due to the allocation and de-allocation of dynamic memory are a common error in programming. These types of bugs are known as memory leaks. A memory leak occurs either when memory is not released, or when it is released inappropriately. Consequently, the allocated memory segment becomes unreachable for further use, and when this occurs repeatedly it causes a degradation in the performance of the system. For instance, a measurement task that is repeated several times without a proper release of dynamically acquired memory may significantly diminish the performance of the entire system. Throughout the coding stages of this software system, any memory leaks were diagnosed and fixed using various memory leak detection APIs (Microsoft, 2005b), in order to ensure that no waste in memory occurred during the continuous use of the measurement software.

The optimisation of dynamic memory, in terms of allocation and access speeds, plays an important role in enhancing the system performance. Merely using classic memory allocation functions (such as *malloc* and *memcpy*) may slow down the operation of tasks that use this memory (Kaspersky, 2003). Hence, more advanced functions (as provided by Intel IPP, with functions such as *ippsMalloc* and *ippsCopy*) were employed to offer the maximum performance that is available from the specific system hardware.

6.3.5 System Inter-Connectivity Networking

The network connection between each SPU and the CMS (as shown in Figure 6.2) was implemented programmatically by way of two data buses. The first bus transmits data sets (such as the output results being transferred from the SPUs to the CMS) and the second bus transmits commands and reports errors (such as the 'measurement start' command that is sent from the CMS to the SPU). The CMS and each SPU have two software network sockets, one for the data bus and another for the commands bus, and they were implemented inside a dedicated thread that is devoted to communications (for transmission and signalling other threads upon receiving data, or commands).

In order to implement network connectivity, the Winsock (Windows Sockets) API was adopted, which enables the creation of a network-capable application to transmit data, that is independent of the network protocol that is used (Microsoft, 2008). There are several common network protocols, such as TCP (Transmission Control Protocol) and UDP (User Datagram Protocol). TCP is connection-oriented, whilst UDP is message-oriented (Young, 2008). TCP was adopted for use in this project because it provides reliable data transfer and strict order-of-transmission delivery of data, which is not offered by UDP. However, TCP is slower than UDP, because every data packet that is received also needs to be acknowledged with an acknowledgement (ACK) packet (Bradford, 2007). TCP functionality was modified by the author to reduce the latency that is introduced by its acknowledgement mechanism and this was achieved by modifying its low level settings to provide a higher transmission speed without affecting reliability.

6.4 Programming Languages and Libraries Used

The C++ language was used in the development of the software system. C++ is considered to be a middle-level language, as it combines both high-level and low-level language features (Schildt, 2003). Using C++ gives the desired flexibility, reliability and speed for programming a real-time system. The development environment that was used was the Microsoft Visual C++ 2005 Integrated Development Environment (IDE), which natively provides the facility for using Windows API and the Microsoft Foundation Classes (MFC) library.

The application development framework (as shown in Figure 6.1) included the following libraries:

1. Windows API: which was used in programming multi-threaded tasks and for hardware access and monitoring (such as controlling the projector and the CSU via the serial port). In addition, Win API was used for network programming using Winsock.
2. MFC: which was used for creating the GUI platform (such as the user controls and dialog boxes) and for displaying measurement related images.
3. Intel Integrated Performance Primitives (IPP): which was employed to speed up algorithms, as well as being used for memory management purposes.
4. OpenCV: which was used to read and store bitmap images and video files (Bradski and Kaehler, 2008).
5. Direct3D: which was used for creating and rendering fringe patterns that were to be projected (Pazera, 2002).
6. OpenGL: which was used to render the resultant 3D information (Agoston, 2005).

Furthermore, the Intel compiler (v 10.1) was employed to optimise code, in terms of minimising its execution time.

6.5 Chapter Summary

It has been shown in this chapter that the performance of this advanced optical profilometry system is not only determined by the available hardware capabilities, but is also significantly affected by the system software, which forms a vital integration with the system hardware. The correct choice of operating system platform, programming language, compiler and supporting libraries determine application reliability. A modular-design was adopted for the system software, because it provides better code understandability and maintainability than is the case for a classical procedural approach. Multi-threading and advanced memory management techniques were also used, so as to optimally utilise the available system hardware resources for any specific set of system hardware.

In this chapter the hierarchy of both the SPU and the CMS applications have been reviewed, along with the software libraries and the programming techniques that were employed as part of the system software design strategy.

The following chapter introduces the novel algorithms and fringe profilometry techniques that were researched as part of this work programme. These included the solution for coping with the non-linear projection response of the projector, the pre-processing techniques that were applied prior to carrying out the fringe analysis methods, and the proposed novel adaptive filter for the Fourier Transform Profilometry (FTP) method.

6.6 References

ABID, A. 2008. *Fringe Pattern Analysis Using Wavelet Transforms.* PhD Thesis, Liverpool John Moores University.

AGOSTON, M. K. 2005. *Computer graphics and geometric modeling:implementation & algorithms,* London, Springer.

BRADFORD, R. 2007. *The Art of Computer Networking*, Pearson Education.

BRADSKI, G. & KAEHLER, A. 2008. *Learning OpenCV*, O'Reilly Media.

DROZDEK, A. 2004. *Data Structures and Algorithms in C++*, Course Technology.

GDEISAT, M. A., ABID, A., BURTON, D. R., LALOR, M. J., LILLEY, F., MOORE, C. & QUDEISAT, M. 2009. Spatial and temporal carrier fringe pattern demodulation using the one-dimensional continuous wavelet transform: Recent progress, challenges, and suggested developments. *Optics and Lasers in Engineering,* 47, 1348-1361.

GHIGLIA, D. C. & PRITT, M. D. 1998. *Two dimensional phase unwrapping: theory, algorithm and software,* New York, Wiley.

GRANATIR, O. 2009. *Multi-Threading is Easier Than Networking* [Online]. intel.com. Available: http://software.intel.com/en-us/articles/omg-multi-threading-is-easier-than-networking/ [Accessed 2 Nov 2009].

HORSTMANN, C. 2006. *Object-Oriented Design & Patterns*, Wiley.

ITTVIS. 2010. *IDL* [Online]. ittvis.com. Available: http://www.ittvis.com/ProductServices/IDL.aspx [Accessed 10 Mar 2010].

KAROUT, S. 2007. *Two-Dimensional Phase Unwrapping.* PhD Thesis, Liverpool John Moores University.

KASPERSKY, K. 2003. *Code Optimization: Effective Memory Usage*, A-LIST Publishing.

LAFORE, R. 1998. *Object-Oriented Programming in C++*, Macmillan Computer Publishing.

LEISERSON, C. E. & MIRMAN, I. B. 2009. How to Survive the Multicore Software Revolution. Intel.

LILLEY, F. 1999. *An Optical 3D Body Surface Measurement System To Improve Radiotherapy Treatment Of Cancer.* PhD Thesis, Liverpool John Moores University.

LIU, H. H. 2009. *Software Performance and Scalability: A Quantitative Approach*, Wiley.

MATHWORKS. 2010. *MATLAB - The Language Of Technical Computing* [Online]. mathworks.com. Available: http://www.mathworks.com/products/matlab/ [Accessed 10 Mar 2010].

MEYERS, S. 2001. *Effective STL: 50 Specific Ways to Improve Your Use of the Standard Template Library*, Addison-Wesley Professional.

MICROSOFT. 2005a. *Memory Leak Detection and Isolation* [Online]. microsoft.com. Available: http://msdn.microsoft.com/en-us/library/x98tx3cf%28VS.80%29.aspx [Accessed 10 Nov 2006].

MICROSOFT. 2005b. *Memory Leak Detection in MFC* [Online]. microsoft.com. Available: http://msdn.microsoft.com/en-us/library/c99kz476%28v=VS.80%29.aspx [Accessed 10 Nov 2006].

MICROSOFT. 2006. *Critical Section Objects* [Online]. microsoft.com. Available: http://msdn.microsoft.com/en-us/library/ms682530%28VS.85%29.aspx [Accessed 2 Mar 2007].

MICROSOFT. 2007. *32-bit and 64-bit Windows: frequently asked questions* [Online]. microsoft.com. Available: http://windows.microsoft.com/en-US/windows-vista/32-bit-and-64-bit-Windows-frequently-asked-questions [Accessed 8 Jan 2007].

MICROSOFT. 2008. *Windows Sockets 2* [Online]. microsoft.com. Available: http://msdn.microsoft.com/en-us/library/ms740673%28VS.85%29.aspx [Accessed 10 Jul 2008].

NATIONAL-INSTRUMENTS. 2009. *A Closer Look at 32-Bit vs. 64-Bit Windows* [Online]. ni.com. Available: http://zone.ni.com/devzone/cda/tut/p/id/5709 [Accessed 10 Dec 2009].

PAZERA, E. 2002. *Focus on 2D in Direct3D*, Premier Press.

PREISS, B. R. 1998. *Data Structures and Algorithms with Object-Oriented Design Patterns in C++*, Wiley.

SCHILDT, H. 2003. *C++: The Complete Reference*, McGraw-Hill.

SKIENA, S. S. & REVILLA, M. A. 2003. *Programming challenges : The Programming Contest Training Manual,* New York, Springer.

YOUNG, W. 2008. *Winsock Programmer's FAQ* [Online]. tangentsoft.net. Available: http://tangentsoft.net/wskfaq/ [Accessed 10 Jul 2008].

Chapter Seven

Measurement Techniques and Algorithms

This chapter is devoted to presenting the algorithms and fringe profilometry techniques that were either researched as completely novel techniques as part of this work programme, or that were developed, extended and optimised by the author. The chapter starts by reviewing the overall measurement procedure that is used for both the single- and multi-view measurement modes of the measurement system that was produced in this work programme. Then it moves on to discuss the method by which the fringe pattern is adjusted before projection in order to overcome the non-linear projection response of the projector. The pre-processing techniques that are applied prior to carrying out the fringe profilometry algorithms are also discussed, including the algorithms that were adopted for both noise reduction and also for the restoration of data within the triangulation spot's location in the source fringe pattern. The author's contribution within the scope of the fringe analysis methods themselves is presented, in terms of the proposed novel adaptive filter for the FTP method. Then the overall calibration procedure is reviewed in detail. Finally, the algorithms are presented that were developed for generating the texture and mask maps when using the adaptive FTP method.

7.1 Measurement Procedure

As illustrated in Section 4.1.3, the surface profilometry measurement procedure can be performed either locally at each SPU (as a single-view), or remotely via the CMS (in multi-view mode). For both modes, the measurement is performed locally at each SPU. However, in the multi-view mode, the measurement results are subsequently transferred via the system's network connections back to the CMS.

The single-view measurement cycle may be summarised in the following table;

	Step Details	Outcomes
1.	At the start up of the SPU measurement programme: a. If the pre-saved user settings file is available then it is loaded, otherwise default settings are used. b. If the files of the calibration volumes and settings are found then they are loaded, otherwise the conversion process to full 3D coordinates is disabled (which limits the measurement to produce unwrapped phase maps only). c. Trajectory images are established for the single and multiple triangulation spot modes.	- Measurement settings are loaded or set to default. - Z, X and Y calibration volumes are loaded into memory. - Camera ROI, gamma value, spatial frequency, locations of the projected triangulation spots and the calibration 3D coverage ranges are loaded into memory.
2.	The user can adjust the measurement settings (as illustrated in Section 4.1), such as fringe analysis method, unwrapping algorithm and output options.	
3.	User starts the single-view measurement task by selecting the desired operation mode: a. Online: *single* or *continuous*. b. Offline: *single* or *movie*.	
4.	Depending on the selected operation mode: a. Online: grab a live image from the camera. b. Offline: load a pre-saved image.	
5.	The measurement is performed (as illustrated in Section 6.2.1) for the current (grabbed or loaded) fringe pattern set, according to the user's preferences and as follows: a. If the calibration flag is enabled and the calibration files are loaded into memory, then extract the location of any triangulation spots and restore their locations in the input images. b. Extract the wrapped phase map and generate the mask and texture maps. c. Unwrap the "wrapped" phase map. d. After obtaining the absolute phase map, apply calibration algorithms to retrieve the 3D information. e. Store and/or display results locally at the SPU.	- Location(s) of the triangulation spot(s). - Fringe pattern without the triangulation spot(s). - Wrapped phase, mask and texture maps. - Unwrapped phase map. - Absolute phase map. - Z, X and Y information.
6.	If a continuous measurement was selected then go back to Step 4. Otherwise, the measurement task is finished.	

Table 7.1 The single-view measurement cycle.

The multi-view measurement cycle may be summarised in the following table;

	Step Details	Outcomes
1.	After starting the CMS programme, the user must: a. Start network communications, which starts listening to any network connection request by the SPUs (Figure 4.1). b. Initiate the CSU, by clicking on the open port button, and then starting continuous or single trigger mode (depending on the measurement application requirements).	- CSU started to trigger the cameras.
2.	The measurement programme is started at each SPU, which is the same programme used for the single-view measurement; a. The same initialisation shown in Table 7.1 – Step 1 is performed here, with the same outcomes for each SPU. b. User must select the "multi-sensor mode" (Figure 4.7) for each SPU. c. User can change measurement setting for each of the SPUs. Some settings such as fringe analysis method need to be the same for all of the SPUs.	- Each SPU is connected to the CMS through a dedicated network connection.
3.	User starts the multi-view measurement task by selecting the desired operation mode: *single* or *continuous*. Both modes are for live measurement only.	
4.	CMS signals all the SPUs to send their next set of measurement results	
5.	When all cameras are triggered to grab the same measurement scene simultaneously, Table 7.2 – Step 5 is performed, with the same outcomes for each SPU.	
6.	The SPUs send their measurement results to the CMS (as they were signalled to do this in Step 4).	
7.	When the CMS has received all the results from all of the SPUs, it displays them and/or stores them locally.	The following is received from each SPU: - Z, X and Y information. - Source fringe pattern - Mask map.
8.	If a continuous measurement mode was selected then go back to Step 4. Otherwise, the measurement task is finished.	

Table 7.2 The multi-view measurement cycle.

7.2 Generation of Fringe Patterns

The user can change the characteristics of the projected fringe pattern, including: fringe orientation angle, spatial frequency and gamma value (as shown in Figure 4.8a). However, at measurement time the first two settings must exactly match the corresponding values for these parameters which were selected at the calibration stage. This requirement is necessitated so that the calibration remains valid for the current measurement, whereas by not ensuring that these parameters are the same for both calibration and measurement would produce erroneous 3D information in the final measurement results. Slight changes in the gamma value (discussed later in this section) may produce better results, in terms of a reduction in any surface ripple effects.

In order to produce the desired fringe pattern the above settings are incorporated into the following equation:

$$I(x,y) = \left[\frac{1}{2}\{\cos(y2\pi f_0 \cos\theta + x2\pi f_0 \sin\theta) + 1\}\right]^{\gamma} \quad (7.1)$$

where f_0 represents the spatial frequency, γ represents the gamma value and θ represents the fringe orientation angle.

7.2.1 Gamma Correction

A digital video projector was used for fringe pattern projection within the measurement system that was developed in this work programme (Section 5.1.1). Digital video projectors and graphic adaptors were originally designed to provide high quality images for visual perception by the human eye, in terms of the perceived brightness of the intensity values. For this purpose, the manufacturers of display devices use a particular gamma value for each display device, and the graphic adaptors dynamically change this value to balance the visual effect upon the display output. Hence, gamma is used here to describe the nonlinearity of a display device, and the actual display output can be described as follows (Guo *et al.*, 2004):

$$w(x,y) = u(x,y)^{\gamma} \quad (7.2)$$

where, u represents the normalised pixel intensity value, w represents the normalised actual output and γ represents the gamma value that is used, which is specific for each display device.

In the field of fringe profilometry, the non-linearities in the display hardware (video projectors and graphic cards) that is used produce a non-sinusoidal fringe pattern. When the fringe pattern is acquired by the camera and its image is analysed using a fringe analysis method, the non-sinusoidal fringe pattern causes phase errors and consequently renders erroneous height values (distortions that appear as *ripples* similar in appearance to those caused by Gibbs ringing as shown in Figure 7.1) when converting the phase to height (Pan *et al.*, 2009). The effect of the projection non-linearity depends on the fringe analysis method that is used. For the temporal methods, the effect is severe because the method assumes that the fringes are sinusoidal (Miao *et al.*, 2007). On the other hand, for the spatial fringe analysis methods, and in the case when using the FTP method, the non-sinusoidal waveform introduces higher harmonic components that extend into the fundamental frequency component and hinders the extraction of the fringe data. In the case of the WTP method, this is less sensitive to the higher harmonics than the FTP method, and this is because the ridge has the highest amplitude within the spectrum which is usually not close to the harmonic components (Huang *et al.*, 2010) .

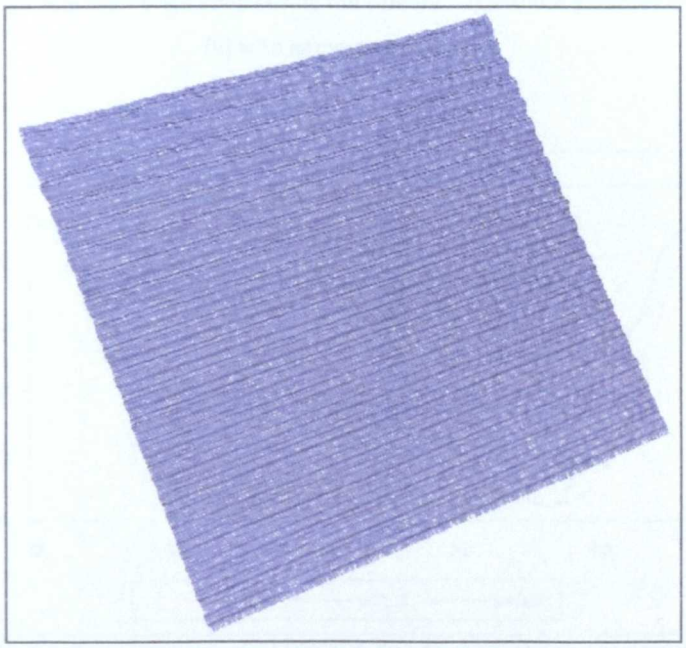

Figure 7.1 An example of the phase errors (ripples) introduced when measuring a flat surface with a non-sinusoidal fringe pattern, using four-frame phase shifting method.

In the literature, the problem of the non-sinusoidal waveform profile of the projected fringe pattern was addressed by compensating for the influence of the projector's non-linearity. Coggrave and Huntley (1999) proposed a method to determine the response curve of the overall system. At the calibration stage, a white surface is illuminated by the projector with the full range of the luminance values and the intensities are acquired using the camera to determine the response curve. At the measurement stage, the response curve information is applied to the acquired images in order to compensate for the projector's non-linearity. Guo, He *et al.* (2004) proposed an iterative procedure that is based on a statistical analysis of the acquired fringe images. At the calibration stage, they used a cumulative distribution function to build a lookup table of different applied gamma values (from 0.1 to 4.0 and sampled in increments of 0.01) to the projected fringe pattern and their corresponding measured phase distribution. At the measurement stage, an initial phase measurement was carried out and the cumulative phase distribution was used to find the best gamma value from the lookup table via interpolation.

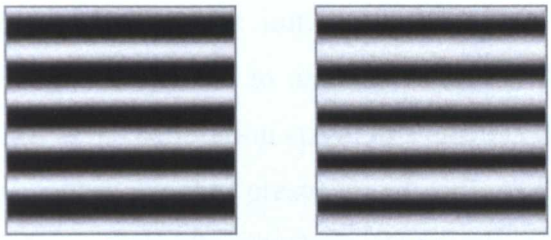

Figure 7.2 Subset of an acquired fringe image using the camera; (a) without gamma-correction (γ=1.0), and (b) with gamma-correction.

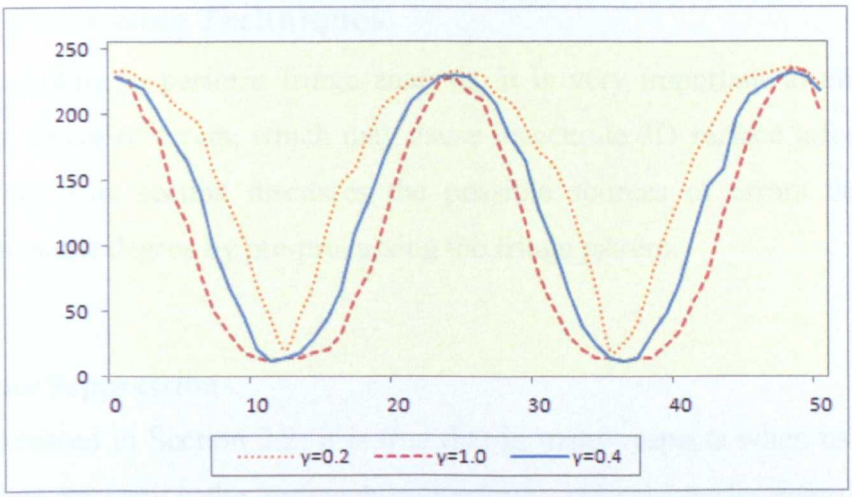

Figure 7.3 An example of deformed waveforms (with γ=0.2 and γ=1.0), and gamma-corrected waveform (with γ=0.4).

For the work presented in this thesis the author proposes a simpler solution than the above approaches, in which an initial value of gamma is set to 0.5 and this is applied to the fringe pattern prior to projection as shown in Equation (7.1). Then, different gamma values are used to compensate for the projected intensity, and their acquired images are examined visually until a sinusoidal fringe pattern is acquired. Figure 7.2 shows an example acquired fringe pattern before and after gamma-correction. As demonstrated in Figure 7.3, the cross-section for a fringe pattern with different gamma values is visually examined to select the appropriate gamma value; it can be noticed that using a gamma value of 0.4 for the projected fringe pattern produces a sinusoidal acquired fringe pattern. Practically, the process of estimating the appropriate gamma value is simple and does not require more than six attempts, and typically even fewer. Choosing the most appropriate gamma value is performed at the calibration stage and this is done for each sensor. Because the chromatic filters are used to eliminate any crosstalk between the sensors, the gamma value may differ from one sensor to another. The selected gamma value for each sensor is stored within the files of the calibration settings, and loaded into the measurement settings when the measurement programme is initialised. However, at the measurement stage, the user can change the gamma to another value (as shown in Figure 4.8a) than that which was used at the calibration stage; this enables flexibility in the ability to try other gamma values in the presence of different fluctuating ambient illumination levels that are dissimilar to those that were encountered during the calibration stage.

7.3 Pre-Processing Techniques

Before attempting to perform fringe analysis, it is very important to eliminate or reduce any source of errors, which may cause inaccurate 3D surface information to be produced. This section discusses the possible sources of errors that can be mitigated to some degree by pre-processing the fringe pattern.

7.3.1 Noise Suppression

As was discussed in Section 2.2, it is true that in many respects when using digital fringe pattern projection the approach outperforms optical interferometry methods, most importantly due the fact that such systems do not introduce the speckle noise

that is typically associated with laser light sources (Aebischer and Waldner, 1999). However, surface measurement using digital fringe pattern projection is by no means free from sources of noise. For example, in applications involving the measurement of relatively dark objects, a higher gain value for the camera needs to be selected (see Figure 4.8b) that has the effect of introducing an additive amplifier noise element (Gaussian) to the image. Consequently, the additional noise that is introduced adversely affects the accuracy of the 3D surface reconstruction.

In fringe profilometry, the signal-to-noise ratio needs to be maximised in order to avoid any possible errors in surface measurement (Robinson and Reid, 1993). Typically, a spatial smoothing filter is used to suppress the noise that was introduced into the acquired fringe pattern. However, the smoothing filter should be chosen carefully, such that it does not affect the fringe data and at the same time reduces the noise. Within the image processing field, there are three common smoothing algorithms, which are; Gaussian filters, median filters, and Wiener filters. Young, Gerbrands *et al.* (1998) examined those three filtering algorithms and concluded that using the Wiener filter resulted in the lowest RMS error when compared to the results of the other filters. Young, Gerbrands *et al.* also demonstrated that using the Wiener filter surpasses the other filters in preserving image features. This is because the Wiener filter performs adaptive noise filtering, in terms of preserving edges and other high frequency parts of an image (Kumar *et al.*, 2010). For this reason, the Wiener filter was the algorithm that was adopted in this work in order to reduce the noise within the source fringe pattern images. Figure 7.5 illustrates the introduced enhancement to the measurement results when using the Wiener filter (with a kernel size of 5×5), for a black phantom body (shown in Figure 7.4). For flexibility, the operator of the SPU can select whether to or not to apply the noise reduction algorithm at the pre-processing stage of the measurement process (see Figure 4.3).

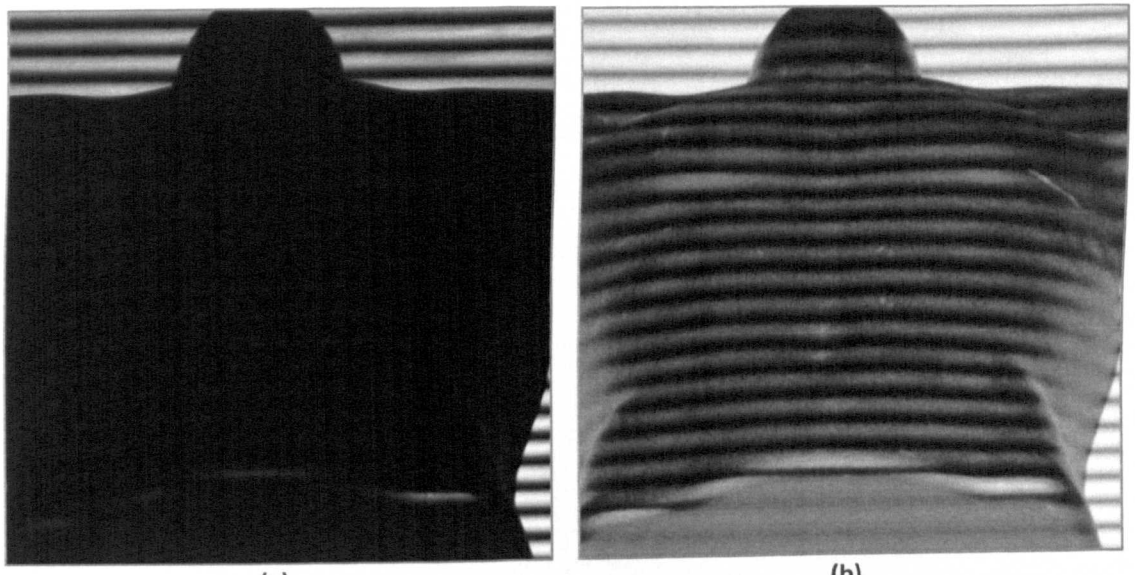

(a) (b)

Figure 7.4 Deformed fringe patterns for a black object; (a) using normal camera gain value, and (b) using a higher camera gain value, which introduces noise to the fringe pattern.

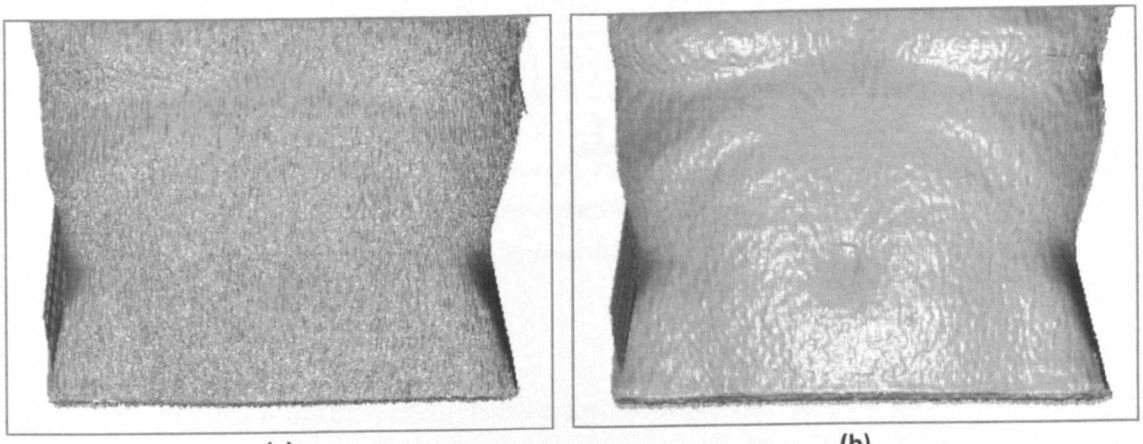

(a) (b)

Figure 7.5 3D reconstruction results for the example object shown in Figure 7.4b, using the four-frame phase stepping method; (a) without removing noise before applying the fringe analysis method, and (b) with noise removal via fringe pattern pre-processing using Wiener filtering.

For further analysis of the ability of the Weiner filter to produce better results than either Gaussian or median filters (in terms of noise suppression while preserving the fringe pattern data), the black plastic phantom upper human body cast (shown in Figure 7.4) was measured using each of these three filters (using a kernel size of 5×5). The four-frame phase stepping method was used for fringe analysis and the reliability ordering algorithm was used for phase unwrapping. To compare the height measurement results, a cross-sectional graph for the three measurement results was produced along with the measurement result without using any filtering. Figure 7.6 shows a graph plot of the row number 255, for a zoomed subsection of pixels 200-

300, for the results of the four measurements. It can be noticed that using the median filter destructively altered the fringe pattern, because it introduced invalid height measurement results. On the other hand, Weiner and Gaussian filters produced valid results. However, it can be noticed that the Weiner filter was more capable of producing smother results than the Gaussian filter.

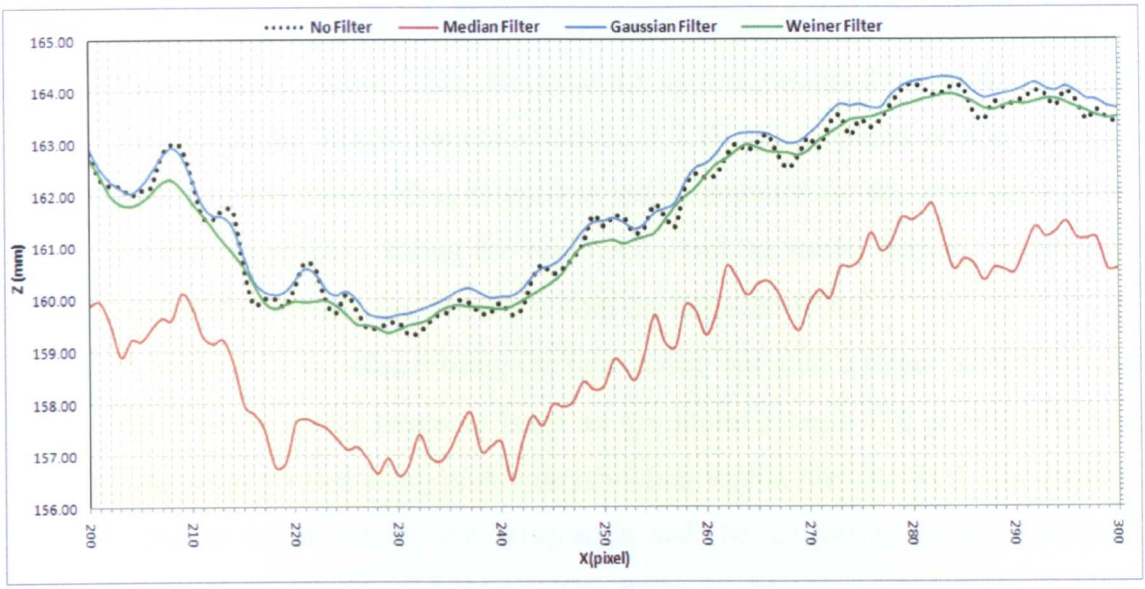

Figure 7.6 A cross-sectional graph showing the measurement height results using the three common smoothing algorithms; median, Gaussian and Weiner filters.

7.3.2 Restoration of the Triangulation Spot Locations

As was discussed previously in Section 3.2, a triangulation spot projection approach is used to enable calculation of an absolute phase map. In the case when we are integrating a single-spot (or multiple-spots) into the projected fringe pattern, the spot location itself disrupts the structure of the source fringe pattern and causes the production of erroneous phase values within the reconstructed 3D surface (as shown in Figure 7.9a). Hence, the location(s) of the spot(s) must be removed (restored) from the fringe pattern prior to the fringe pattern analysis being performed within measurement process.

For this work, the author has proposed an approach for restoring the location(s) of the spot(s), by extending the surrounding fringe intensity values to fill the unwanted spot(s) location(s) within the fringe pattern. After detecting the location(s) of the spot(s), their initial location(s) are used for the restoration procedure. Figure 7.7

shows a sample fringe pattern with a single embedded triangulation spot, and the restoration procedure in this case is as follows:

1. An initial ROI of the spot area is defined (see Figure 7.8a); using the pre-detected centre of the spot and an initial margin around the spot. Because the size of the projected spot is selected to be 4×4 pixels (Section 3.2.1), the initial margin is selected to be 5 pixels.
2. The ROI is binary thresholded to 99% of the maximum intensity value within the ROI (see Figure 7.8b). Because the spot is designed to be the brightest feature in the fringe pattern (Section 3.2.1), the centroid of the resultant points of the thresholding is used as the new centre for the next steps in the restoration process. Using the new centre and the initial margin, Figure 7.8c shows that the spot lies exactly within the adjusted ROI.
3. A larger ROI is defined using the new centre but with a larger margin around the spot, typically twice as large as the initial margin (10 pixels). Then, a mask is generated using binary thresholding within the new ROI. The mask is used to define where the restoration will be performed (1's to perform restoration and 0's to bypass). The mask is dilated to cover any possible pixels that belong to the spot (Figure 7.8d).
4. Depending on the orientation of the fringe pattern, the intensity value of a pixel with a mask value of 1 is calculated either using the horizontally adjacent pixels (for horizontal fringes), or the vertically adjacent pixels (for vertical fringes). Because the fringe orientation for this example is horizontal, the intensity value of each pixel (with a mask value of 1) is calculated by linearly interpolating the intensity values of the left two pixels within the new ROI. After performing the initial restoration, the intensity value of each pixel (with a mask value of 1) is recalculated by interpolating the intensity values of the pixels on the left and right-hand sides. Finally, a fully restored location is obtained as shown in Figure 7.8e-f.

Figure 7.7 A sample deformed fringe pattern with a single embedded triangulation spot.

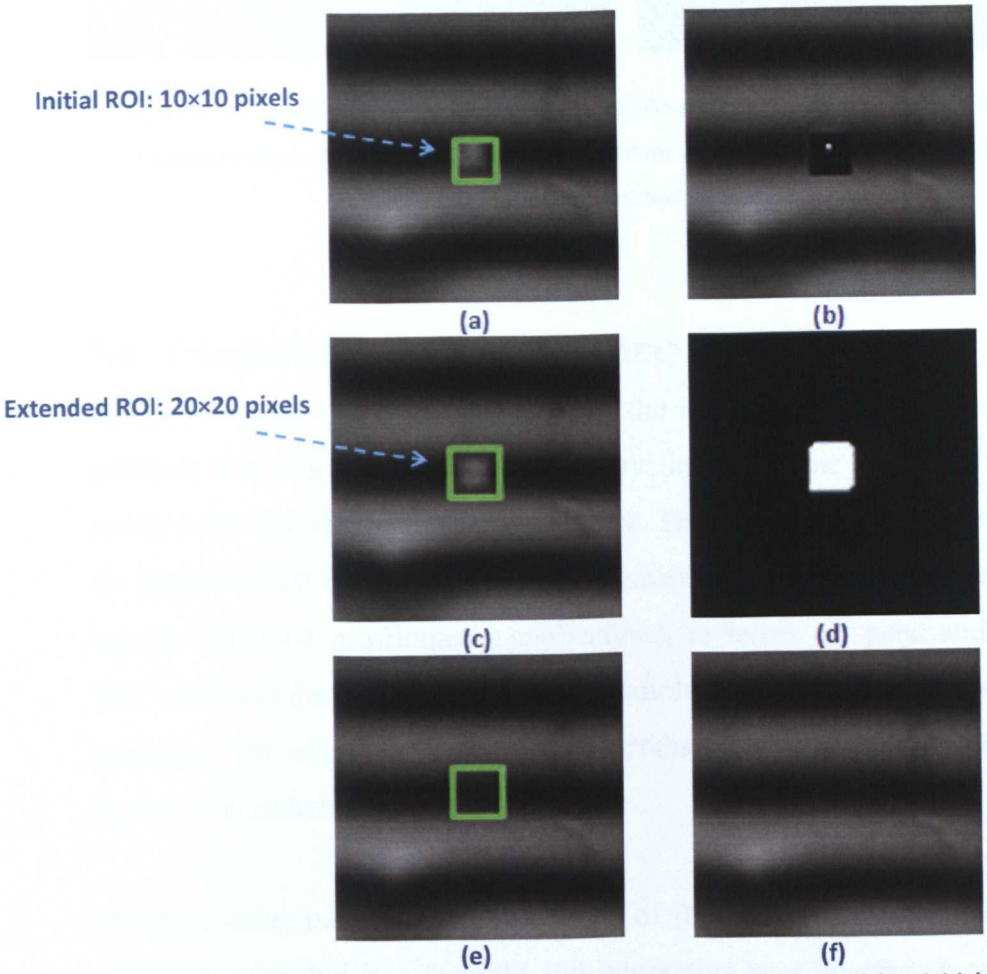

Figure 7.8 An illustration of the process of restoring a single-spot location; (a) an initial ROI is defined, (b) the binary thresholding result for the initial ROI, (c) a larger ROI is determined using the detected centroid, (d) a mask is generated using binary thresholding for the new ROI, (e) and (f) spot location is restored using interpolation.

For the multi-spot method, the procedure is repeated according the number of the embedded spots. Figure 7.9 shows the 3D surface reconstructions before and after restoring the multi-spot locations.

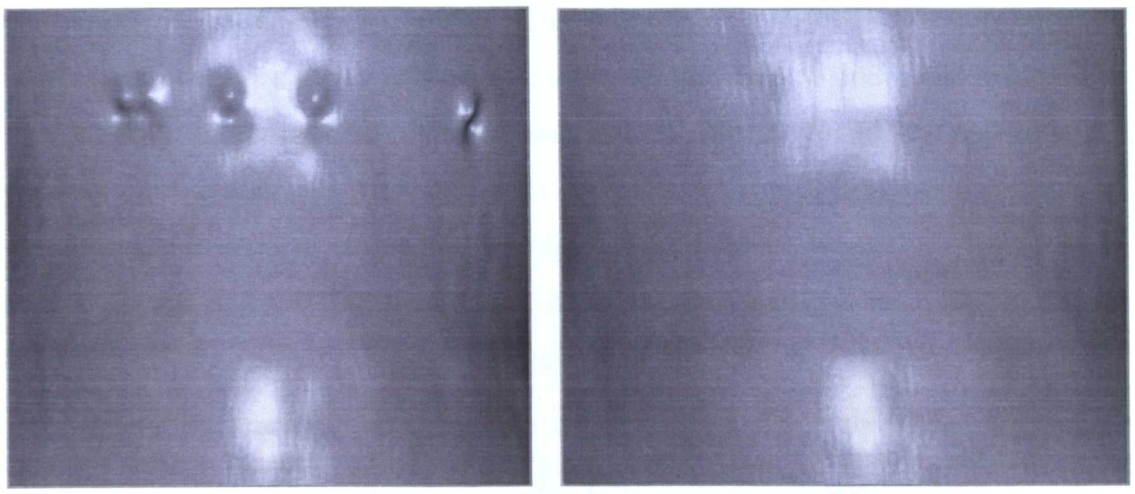

(a) (b)

Figure 7.9 The resultant 3D surface reconstruction; (a) without restoring the location of the spots, and (b) using the proposed technique to remove the locations of the spots prior to applying the fringe analysis method.

7.4 Fringe Profilometry Algorithms

As discussed previously in Section 6.1, the implementation of some fringe analysis methods was adapted from previous work; including the classic FTP method (using Butterworth filter) and the WTP method. These implementations were re-coded by the author in the C++ language and optimised in order to meet the requirements of various real-time profilometry applications, in terms of speed and robustness. The TPS method (Section 2.3.2) was also implemented by the author using the C++ language. The adaptive FTP method (introduced later in this section) was developed by and implemented by the author.

The processing parameters and settings of the fringe analysis methods used in this work are presented in a friendly and interactive user interface (see Figure 4.3) that has been developed by the author in order to provide a high level of flexibility allowing the user to manipulate these settings dynamically.

7.4.1 Fourier Transform Profilometry

For the FTP method, the background intensity signal of the fringe pattern must be suppressed prior to applying the method, because it usually overlaps with the fringe spectra and thus makes it hard to isolate the modulated fringe phase signal. As discussed in Section 2.3.1.1, many approaches were proposed for this purpose; however, these approaches require either the acquisition of additional images, or they involve increased calculation complexities. It was found by collaborating partners at the Christie Hospital[1] that using the Sobel filter produces similar measurement results to subtracting the background image from the fringe pattern image. Hence, a Sobel filter (with one of the kernels defined as shown in Figure 7.10) is spatially applied to the fringe image prior to using the FTP method.

$$\begin{bmatrix} 1 & 2 & 1 \\ 0 & 0 & 0 \\ -1 & -2 & -1 \end{bmatrix} \quad \begin{bmatrix} -1 & 0 & 1 \\ -2 & 0 & 2 \\ -1 & 0 & 1 \end{bmatrix}$$

(a) (b)

Figure 7.10 The kernel of Sobel filter that is used depends on the fringe orientation; (a) used for horizontal fringes, and (b) used for vertical fringes.

Moreover, because the FTP method uses a filtering function to extract the phase component within the frequency domain, the quality of the FTP result relies mainly on the filtering technique that is used. The SPU measurement software offers two different flavours of the FTP method; manual and adaptive (see Figure 4.3b). The two modes differ in the way that the information spectrum is determined. In the manual FTP method, a 2D band-pass Butterworth filter is used (Lilley, 1999) with three adjustable parameters, which are;

a. Filter DC width, which represents the number of rows (for horizontal fringes) or columns (for vertical fringes) of the half of the spectrum that are excluded from the filtering process.
b. Filter bandwidth (B), which used to calculate the filter cut-off frequency (w_c) as follows:

$$w_c = \frac{1}{(B\,N)} \tag{7.3}$$

[1] Prof. Chris Moore, North West Medical Physics, Christie Hospital, Wimslow Rd, Manchester. UK.

where, N represents the detected number of the fringes, which equals the index of the maximum value of the magnitude of half of the spectrum (with the exclusion of the DC width). The horizontal index within the magnitude image is used for horizontal fringes and the vertical index for the vertical fringes.

c. Filter order, which determines the amount of additional attenuation for frequencies higher than the cut-off frequency. Hence, using a higher filter order reduces other sources of noise (such as higher harmonics), but at the same time it compromises the information of the object's features.

The manual processing mode of the FTP method requires manipulating the above filtering parameters, which differ from one object to another, in order to compromise between the amount of suppressed noise and the reproduction of the extracted object's features. Adjusting the filter parameters for each object is tedious and impractical, hence the author has proposed an adaptive filtering approach that is described below.

7.4.1.1 Adaptive Filter for FTP

In digital image processing, an adaptive filter is basically a digital filter with self-adjusting parameters, i.e. its parameters adapt to the changing conditions of the input signal (Gonzalez and Woods, 2007). Typically, a Least Mean Square (LMS) algorithm is used iteratively to increase the SNR ratio of the output of the adaptive filter. For fringe pattern analysis, a spectral overlap occurs between the information and noise components, as well as the fact that the band occupied by the noise varies from object to another. Hence, using an adaptive filtering approach is supposed to produce better noise suppression. However, the process of filtering using an adaptive filter incorporates complex and iterative calculations to obtain the filter parameters.

To avoid the typical complexity and the iterative calculations involved in the use of adaptive filters, the author has proposed a state-of-the-art approach without introducing any significant added complexity, or requirements for computationally intensive and time consuming iterative calculations. The approach uses only a single parameter, which indicates the required level of details (an integer value within a

range of 0 to 4) to be extracted using the filter (Figure 4.3b). The lowest level of details (0) produces a high SNR ratio but at the cost of the lowest level of feature extraction, whilst the highest level of details (4) produces a high feature extraction level but with a correspondingly lower SNR ratio. Hence, practically by using a level of detail value of 2 or 3 typically offers a good compromise between SNR ratio and noise reduction so as to produce optimal results. The level of detail value is independent of the object's shape; hence there is no need to alter it for each object. As shown in Section 2.3.3, using the proposed adaptive filter produced better results than using the classic manual filter (described above), in terms of the fact that the percentage of number of points that lay within 0mm to ±0.5mm of the reconstructed surface is found to be higher for the adaptive filter.

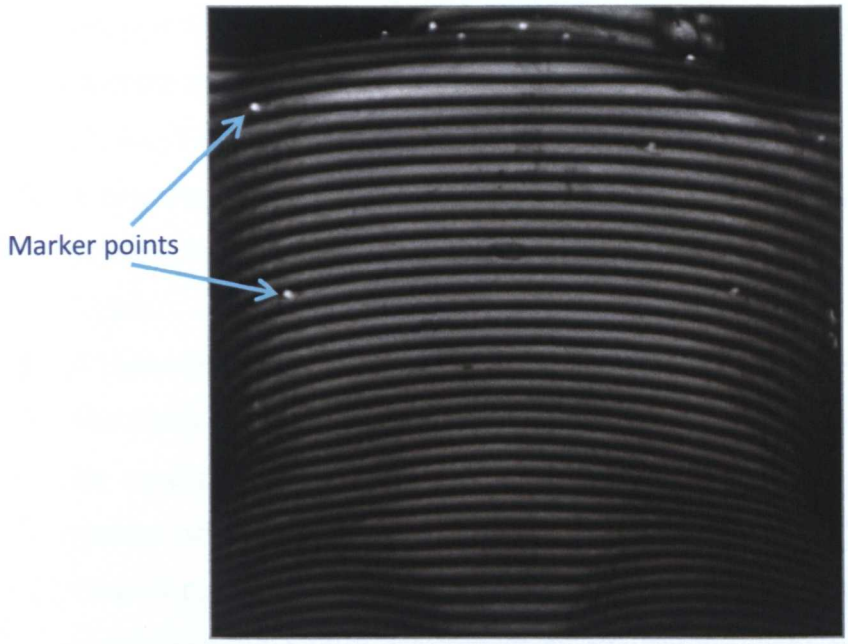

Figure 7.11 An example fringe pattern with added features (marker points) to demonstrate the proposed adaptive mode of the FTP method, using different filtering settings.

The filtering process for the proposed adaptive mode filter for use with the FTP method (for the example fringe pattern that is shown in Figure 7.11) is as follows:

1. The spectrum of the source fringe image (*source*) and its filtered output using the Sobel filter (*filtered*) are calculated using the FFT algorithm.
2. The spectral magnitude of the source image is subtracted from the spectral magnitude of the filtered image; this generates a magnitude difference image (see Figure 7.12a), where the positive values (in white) represent the phase

spectrum and the negative values (in black) represent the DC component and the unwanted noise spectrum.

3. For one of the halves of the magnitude difference image, the maximum value (the frequency pin of the phase spectrum) is determined. For horizontal fringes the upper half ROI of the image is used, whilst for vertical fringes the left half ROI of the image is used (see Figure 7.12b). Then the values of the other half of the magnitude difference image are set to zero.
4. The magnitude difference image is binary thresholded with a percentage of the maximum value (that was obtained in Step 3), where the level of detail value is mapped automatically to a particular percentage value (t). Experimentally, and by analysing a large number of samples; the adopted t values are: {4%, 2%, 1%, 0.5%, and 0%}, which are correspondingly mapped to the values of the level of details (0-4) respectively. For this example the selected level of detail value is 2, hence the mapped t value is 1% (see Figure 7.12c).
5. A filtering window is determined, which is the area where the results of the thresholding that have a value of 1 are located inside the image (see Figure 7.12d).
6. A Hamming window is applied to the filtering window (see Figure 7.12e).
7. The result of the Hamming window is powered to a number (n), this applies the concept of filter order, which is used in normal filters to reduce other sources of noise (such as higher harmonic components). The level of detail value is mapped automatically to a particular value of n, where the values of n were experimentally determined by analysing a large number of samples. The adopted n values are: {2.0, 1.5, 2.75, 3.0, and 6.5}, which are correspondingly mapped to the values of the level of detail (0-4). For this example the selected level of detail value is 2, hence the mapped n value is 2.75 (see Figure 7.12f).
8. The resultant filtering image is multiplied by the spectrum of the Sobel filtered image, and then the multiplication result is converted back to the spatial domain using the inverse Fourier transform in order to calculate the phase.

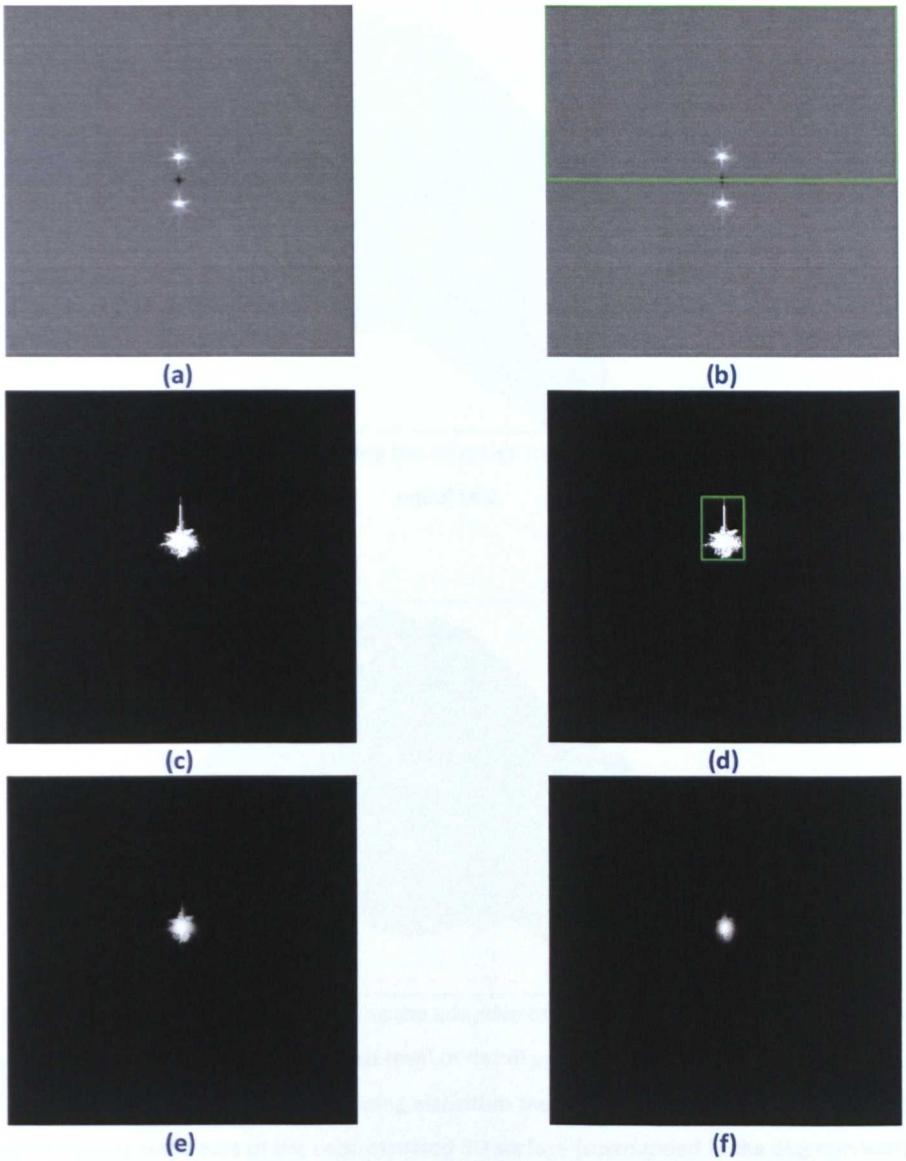

Figure 7.12 An illustration for the proposed adaptive mode for the FTP method; (a) the generated magnitude difference image, (b) the upper half is selected for processing because a horizontal fringe pattern has been used, (c) the result of binary thresholding for the selected ROI with t=0.01, (d) the determined filtering window, (e) the result of the Hamming window when applied to the filtering window, and (f) the results of the Hamming window being raised to the power of n=2.

Figure 7.13, Figure 7.14 and Figure 7.15 show the reconstructed 3D surface for the analysed example (Figure 7.11) using the adaptive mode of the FTP method, with a selected level of detail equal to 2, 0 and 4, respectively. It can be noticed that the marker points (shown in Figure 7.11) are more obvious when a higher level of details was used; however, some amount of noise is also introduced here. Hence, selecting the appropriate value for the level of detail is application dependent but not object dependent. An accuracy analysis of the proposed method using the adaptive mode for the FTP method is discussed further in Section 8.3.

Figure 7.13 The reconstructed 3D surface using the adaptive mode of the FTP method with a level of detail equal to 2.

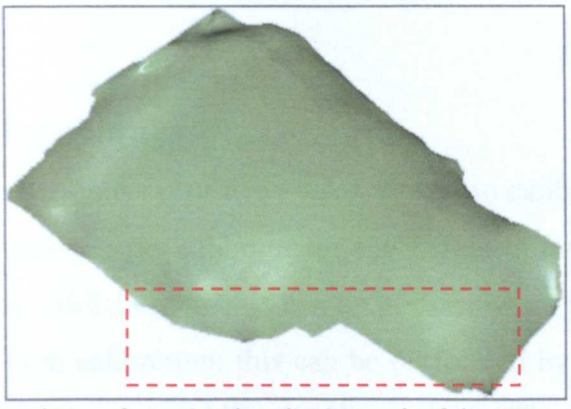

Figure 7.14 The reconstructed 3D surface using the adaptive mode of the FTP method with a level of detail equal to 0. For this measurement example, this level of detail produced wrapped phase data that introduced discontinuities to the result of the unwrapping algorithm that was used for analysis, and consequently resulted in missing out a part of the reconstructed 3D surface (surrounded in the diagram with a red rectangle).

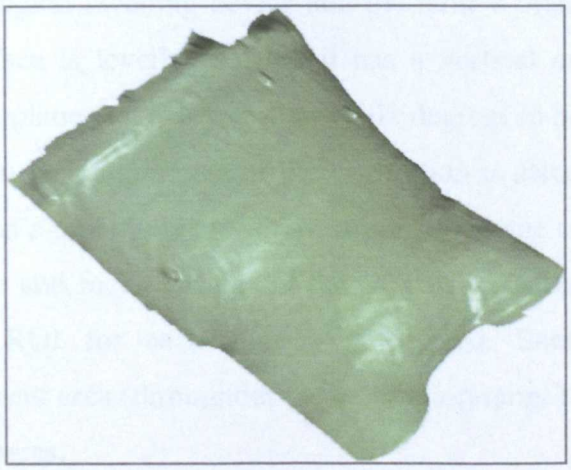

Figure 7.15 The reconstructed 3D surface using the adaptive mode of the FTP method with a level of detail equal to 4.

7.5 Phase Unwrapping Algorithms

The implementation of the phase unwrapping algorithms and their associated quality map generation techniques that were used in this work programme (as described previously in Section 2.4), were re-coded in the C++ language by the author. The new code was optimised and profiled in terms of speed, robustness and memory leak prevention (Section 6.3). The SPU measurement software offers a friendly user interface (Figure 4.4) for selecting these unwrapping algorithms and for manipulating their settings dynamically and interactively. The user of the SPU software can check the execution times (Figure 4.10b) of these individual algorithms and can visually inspect their results (Figure 4.2, Figure 4.11 and Figure 4.12).

7.6 Calibration Techniques

The calibration procedure consists of two cycles, firstly, to calibrate for the phase-to-height function and secondly to calibrate for the height-to-transversal coordinates function. A calibration validation process can be performed periodically to check for the validity of the system calibration; this can be performed by measuring an object which has precise and accurately known dimensions. The full phase-to-height calibration cycle is as follows:

1. Placement of the calibration plane:
    a. The plane is placed at the lowest height supported by the calibration table (Section 5.4).
    b. Using a digital levelling device and the table's brakes (Section 5.4), the table surface is levelled so that it has a vertical or horizontal gradient across the plane that is lower than ±0.01 degrees in both directions.
    c. The height coverage range of the calibration is selected according to the application's preferences (with maximum coverage range of 50cm).
    d. The zoom and focus settings of the camera for each sensor are adjusted, and the ROI for each camera is defined. Such that the required measurement area (throughout the calibration range) lays within the ROIs of all cameras.
    e. The reference height is selected (within the coverage range), and is pre-defined as $Z = 0$.
    f. The spatial frequency of the fringe pattern is chosen.

g. The height of the elevation step is chosen, such that it is less than the half of the length of the middle fringe of the projected fringe pattern.
h. The appropriate gamma value of the fringe pattern is adjusted for each sensor (Section 7.2.1).
i. The calibration plane is set at the reference height, and then the locations of the projected triangulation spots (for each sensor) are adjusted. Such that they cover the measurement ROI, and are at the centre of one of the fringes towards the middle of the fringe pattern.
j. The calibration plane is set at the lowest height of the calibration coverage range.

2. The calibration programme is initialised at each SPU. The calibration process (elevating the table and triggering the SPUs to measure the calibration plane) is automatically controlled via the network connections by either the CMS or one of the SPUs.
3. An absolute phase map of the calibration plane (at the current height) is obtained simultaneously at each of the three SPUs, and this is achieved via the following steps:
   a. An unwrapped phase map is obtained using four-frame phase-stepping as the fringe analysis method and using the reliability ordering algorithm for phase unwrapping.
   b. Triangulation spots are projected simultaneously for each sensor, and their locations are obtained (Section 3.2.2).
   c. One of the triangulation spots (usually the middle one) is used to calculate the absolute phase map.
4. The absolute phase map is stored locally at each SPU and is indexed according to the current height value of the calibration plane.
5. The calibration plane is raised using the elevator table to the next discrete height level within the pre-defined calibration range, and then steps 3 and 4 are carried out for the new height.
6. After obtaining the absolute phase maps of the calibration plane for all of the discrete height steps within the calibration range;
   a. The height (Z) calibration volumes for each SPU are constructed. Such that the absolute phase maps are indexed with their corresponding height value into the each height calibration volume.

b. The detected spot locations at each height step and for each SPU are stored.

These steps are summarised as a functional diagram in Table 7.3 along with the outcomes of each step.

	Step Details	Outcomes (for each sensor)
1.	Placement of the calibration plane: a. Plane is placed at the lowest height supported by the calibration table. b. Calibration table is levelled. c. The calibration range is determined. d. The zoom, focus and ROI settings of the camera for each sensor are determined. e. The reference height is selected and is pre-defined as Z = 0. f. The spatial frequency of the fringe pattern is chosen. g. The height of the elevation step is chosen. h. The appropriate gamma value of the fringe pattern is determined. i. The locations of the projected triangulation spots (for each sensor) are adjusted. j. Calibration plane is set at the lowest height of the calibration coverage range.	- Height calibration range - Height of the elevation step - Grabbing ROI - Spatial frequency - Gamma value
2.	Calibration programme is initialised at each SPU.	
3.	Absolute phase map of the calibration plane is obtained simultaneously at each of the three SPUs.	
4.	The absolute phase map is stored locally at each SPU.	
5.	Calibration plane is elevated using the table to the next height level.	
6.	For each SPU; construct the height (Z) calibration volumes and store the detected spot(s) locations.	- Height calibration volumes - X and Y spot locations.

Table 7.3 The summarised procedure for the phase-to-height calibration cycle, along with the outcomes of each step.

For the height-to-transversal calibration, the same calibration range and the reference height that were determined in the phase-to-height calibration are used. The full height-to-transversal calibration cycle is as follows:

1. The calibration plane is set at the reference height of the calibration coverage range. Where the height (or thickness) of the checkerboard is taken into account through lowering the reference height (and each elevation step) by the height of the checkerboard.
2. The checkerboard is placed over the calibration plane, such that one of its corners (usually the corner at the middle of the checkerboard) is used as the desired reference point (X_0, Y_0).
3. Calibration plane is set at the lowest height of the calibration coverage range.
4. Using the full resolution supported by the cameras, the images of the checkerboard are grabbed simultaneously by the three SPUs, and then stored locally at each SPU.
5. Calibration plane is elevated using the table to the next discrete height level, and then Step 4 is carried out for the new height.
6. After grabbing the images of the checkerboard for all of the height steps throughout the calibration range, X and Y calibration volumes for each sensor are constructed as follows:
   a. As illustrated in Section 3.4.2 the relative X and Y world coordinates for each height step are obtained using Tsai's calibration model, and then clipped to the same ROI that were determined in the phase-to-height calibration.
   b. The calibrated X and Y surfaces are indexed inside the X and Y calibration volumes, according to the corresponding value of the height step.

The calibration volumes and their settings (outcomes) of the above calibration cycles are stored locally into individual files at each of the SPUs. Those files are then used at the measurement time cycle.

7.7 Generation of Texture and Mask Maps

Texture and mask maps can be generated depending on the selected fringe analysis method, as will be discussed in detail later in this section. The processes of calculating these maps can be enabled or disabled for the measurement according to

the user's preferences (Figure 4.3). The resultant maps can be viewed dynamically by the user (Figure 4.12b and 4.12e).

7.7.1 Generation of the Texture Map

A texture map may be useful for some profilometry applications, especially when the 3D information of particular features on the object's surface needs to be obtained automatically. This can be performed by detecting the object's features on the texture image using image processing techniques, and then obtaining their 3D reconstructed information via their detected image coordinate indices. In the case of measuring static objects, a texture map can be grabbed as an individual image using the camera whilst projecting a blank white frame using the projector. Alternatively, and when using the TPS (Temporal Phase Shifting) fringe analysis method, the texture map can be generated by calculating the average of the TPS images. However, in the case when we are measuring dynamic objects, the generation of the texture map is not a straightforward process. This is due to the fact that neither the use of an additional image, nor the TPS method, are practical for use in measuring dynamic objects. Therefore, the texture map needs to be generated from the fringe pattern itself.

Many researchers have proposed various techniques for the purpose of retrieving the texture map using the fringe pattern. For instance, Moore *et al.* (2001) proposed a simple approach by spreading a random noise pattern across the fringe pattern image to detect and eliminate the peaks of the fringes, then smoothing the result to reduce the spread noise. Patricio and Joseph (2006) proposed using wavelet analysis to eliminate the fringes; however, their technique is only particularly useful for generating the texture map of relatively flat fields because the fringe spacings are easier to analyse than in the case of objects that exhibit significant surface curvature.

For this work, the texture map can be optionally generated according to the user preferences (Figure 4.3). However, in the case of dynamic measurement, the ability to obtain a texture map is only supported for the adaptive mode of the FTP method. For the manual mode of the FTP method and the WTP method, the texture map generation facility was left for future work. To reduce the calculation overhead, the

process of generating the texture map (for the adaptive FTP method) was implemented so that it was performed concurrently with the spectrum filtering process. The method of generating the texture map that was developed by the author may be described by the following steps:

1. The same magnitude difference image that was used to generate the adaptive filter (see Section 7.4.1.1) is used here. The example fringe pattern that was shown in Figure 7.11 is used here for demonstration.
2. The magnitude difference image (see Figure 7.12a) is binary thresholded with a thresholding value (t) to generate a texture filtering mask. Because the positive values in the magnitude difference image represent the phase spectrum and the negative values represent the DC component, choosing a negative value for t (towards the minimum value of the magnitude difference) eliminates more fringe data, but at the same time it produces a more blurred texture image. On the other hand, selecting a positive value for t (towards the maximum value) introduces more trace remnants of the fringes but at the same time it produces a sharper texture image. Experimentally, and via analysing a large number of samples, a t value of 1% of the maximum value of the magnitude difference was found to provide a compromise between sharpness and fringe elimination in the resultant texture image. Figure 7.16 shows the resultant texture filtering mask for the object being analysed in Figure 7.11.
3. The texture filtering mask is multiplied by the spectrum of the source fringe image, and then the multiplication result is converted back to the spatial domain using the inverse Fourier transform. The real part of the resultant image represents the generated texture map (see Figure 7.17).

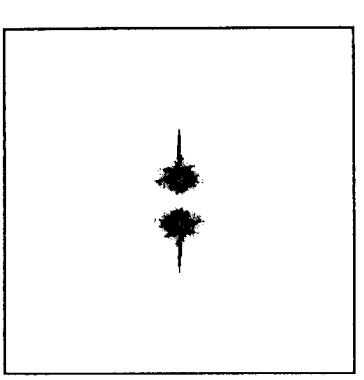

Figure 7.16 An example of a filtering mask produced as described previously, that is used in the process of generating a texture map.

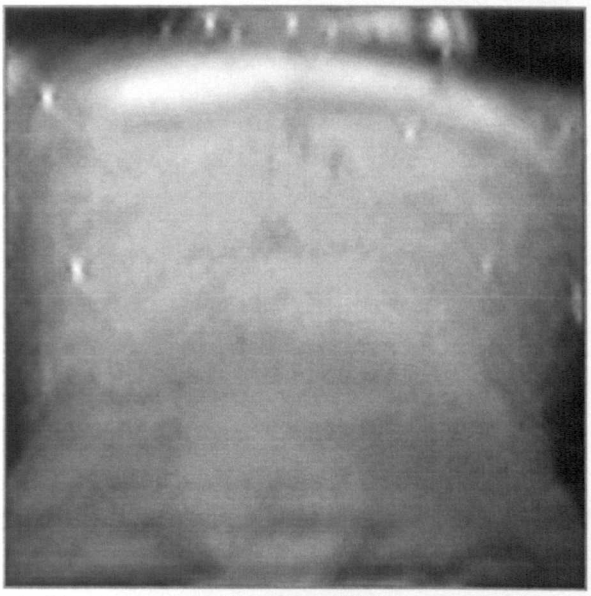

Figure 7.17 The generated texture map for the example fringe pattern that is shown in Figure 7.11).

7.7.2 Generation of the Mask Map

For this work, mask map is only generated when either the adaptive FTP or the TPS methods are used for measurement. It is generated by binary thresholding either the texture map (in the case when we are using the adaptive FTP method), or the result of the fringe visibility calculations (in the case where we are using the TPS method, as discussed in Section 2.3.2). For the other fringe analysis methods there is no direct algorithm available to calculate the mask map and hence it was left for future work. The mask map helps in excluding any unwanted areas of the fringe pattern from processing. This serves as an important tool for eliminating weak fringe modulations, which may affect the behaviour and accuracy of the phase unwrapping process. Moreover, using the mask map may help in increasing the processing speed, as the unwanted areas are automatically excluded from the computationally intensive unwrapping, phase-to-height and height-to-transversal coordinates processes. The image in Figure 7.18 shows the generated mask map for the example fringe pattern that was shown in Figure 7.11, produced by binary thresholding the texture map (Figure 7.17) that was generated using the proposed method as discussed earlier in this section.

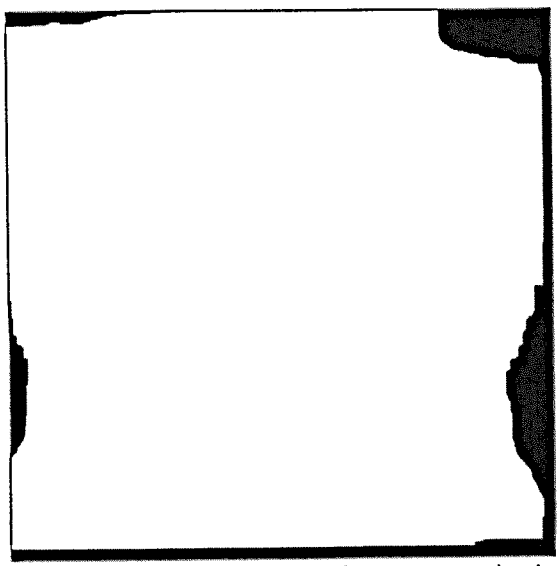

Figure 7.18 The generated mask map for the example fringe pattern that is shown in Figure 7.11.

7.8 Chapter Summary

Throughout this chapter, the specific contribution to the field of optical profilometry using fringe analysis has been presented. In terms of solving the problems caused by the non-sinusoidal intensity profile fringe patterns that are produced by digital projectors, a simple method has been proposed for adjusting the intensity of the projected fringe pattern prior to projection, which is based on the principle of gamma-correction of the display devices. For reducing the effects of noise on the resultant 3D surface measurement, which may be introduced in some fringe profilometry applications, the author has proposed using the Wiener filter at the pre-processing stage. Using the Wiener filter smoothes the source fringe pattern and at the same time it preserves the image features, and in such a manner it has been proven to practically outperform other filters such as the median filter. Some novel techniques were developed regarding the triangulation spots (implemented as both single and multiple spot modes) that are used to obtain an absolute phase map after the phase unwrapping process. The spots themselves must be removed from the source fringe pattern, after extracting their locations and prior to applying a fringe analysis method. This is required in order to avoid phase errors being produced due to the local disruption of the source fringe pattern in the vicinity of the spots. A method has been proposed for restoring the location(s) of the spot(s) using a simple interpolation approach.

A state-of-the-art adaptive filtering technique has been proposed for the FTP fringe analysis method, which only uses a single parameter (adjustable by the user depending on the application preferences) to compromise between the levels of extracted details and noise in the resultant 3D surface of the measurement object. For this adaptive mode of the FTP method, the author proposed another technique to extract the texture map, which eliminates the fringes from the fringe pattern within the frequency domain. All other fringe profilometry methods that were used in the system were re-coded in C++ and these were optimised to provide a maximum efficiency, in terms of speed and memory utilisation.

The cycles of both of the single-view and multi-view measurement procedures have been described in detail in this chapter. In addition the process cycles for the calibration procedures for the phase-to-height function and the height-to-transversal coordinates function have also been described.

The main novel intellectual contributions of this programme of research that have been presented in this chapter can be summarised as follows:

- A simple method for adjusting the gamma value of the projected fringe pattern prior to projection, in order to reduce the effect of the non-linearities in the display devices, and therefore to produce a true sinusoidal fringe pattern.
- A method to synthetically restore the locations of the triangulation spots, in order to avoid phase errors being produced due to the local disruption of the source fringe pattern in the vicinity of the spots.
- An adaptive filtering technique for the FTP method, which avoids the complexity of the relatively small number of existing attempts at producing adaptive filters and uses only a single parameter. At the same time, the technique is able to generate both texture and mask maps within the same process.

7.9 References

AEBISCHER, H. A. & WALDNER, S. 1999. A simple and effective method for filtering speckle-interferometric phase fringe patterns. *Optics Communications,* 162, 205-210.

COGGRAVE, C. R. & HUNTLEY, J. M. 1999. High-speed surface profilometer based on a spatial light modulator and pipeline image processor. *Optical Engineering,* 38, 1573-1581.

GONZALEZ, R. C. & WOODS, R. E. 2007. *Digital Image Processing*, Prentice Hall.

GUO, H., HE, H. & CHEN, M. 2004. Gamma Correction for Digital Fringe Projection Profilometry. *Appl. Opt.,* 43, 2906-2914.

HUANG, L., KEMAO, Q., PAN, B. & ASUNDI, A. K. 2010. Comparison of Fourier transform, windowed Fourier transform, and wavelet transform methods for phase extraction from a single fringe pattern in fringe projection profilometry. *Optics and Lasers in Engineering,* 48, 141-148.

KUMAR, S., KUMAR, P., GUPTA, M. & NAGAWAT, A. K. 2010. Performance Comparison of Median and Wiener Filter in Image De-noising. *International Journal of Computer Applications,* 12, 27-31.

LILLEY, F. 1999. *An Optical 3D Body Surface Measurement System To Improve Radiotherapy Treatment Of Cancer.* PhD Thesis, Liverpool John Moores University.

MIAO, H., QUAN, C., TAY, C. J. & FU, Y. 2007. Analysis of phase distortion in phase-shifted fringe projection. *Optics and Lasers in Engineering,* 45, 318-325.

MOORE, C. J., TORNOW, M., SHARROCK, P. J., LILLEY, F., LALOR, M. J. & BURTON, D. R. 2001. Dynamic Background Correction in 3Dt Body Surface Sensing & Visualisation. *Proceedings of the Fifth International Conference on Information Visualisation.* IEEE Computer Society.

PAN, B., KEMAO, Q., HUANG, L. & ASUNDI, A. 2009. Phase error analysis and compensation for nonsinusoidal waveforms in phase-shifting digital fringe projection profilometry. *Opt. Lett.,* 34, 416-418.

PATRICIO, M. R. & JOSEPH, H. 2006. A Method to Remove Fringes from Images Using Wavelets. *The Astrophysical Journal,* 649, 553.

ROBINSON, D. & REID, G. T. 1993. *Interferogram Analysis, Digital Fringe Pattern Measurement Techniques*, Taylor & Francis.

YOUNG, I. T., GERBRANDS, J. J. & VAN VLIET, L. J. 1998. *Fundamentals of image processing*, Delft University of Technology, Netherlands.

Chapter Eight

Experimental Results and Discussion

Previous chapters have reviewed fringe profilometry techniques and the camera-projector calibration for surface shape measurement. In addition, the specifications, applications, and hardware and software designs of the 3D surface shape measurement system that was developed as part of this programme of research have been presented. The preceding chapter has described the measurement techniques and algorithms that were developed as part of this work by the author.

This chapter presents results from both of the two 3D profilometry systems which were built during this research programme; the first system was built at the JMU university laboratory (Figure 5.1) and the second was constructed at one of the radiotherapy treatment rooms at The Christie Hospital in Manchester (Figure 4.30). The two profilometry systems have the same hardware configuration for the sensor head components that were described in Chapter Five. However, the profilometry system at The Christie Hospital features processing units with different computer hardware specification, which have been constantly upgraded to the most recent hardware technologies in order to accommodate faster measurement speeds. The results are grouped into two main categories of measurements, namely for static objects and dynamic objects respectively. In general, the test objects were selected to be either real, or simulated, human body parts. This choice was made in order to test the robustness of the system, in terms of accuracy and speed, within the field of human body surface measurement and specifically for the application of Metrology Guided Radiotherapy (discussed in detail under Section 4.3.1). The results are presented as a logical sequence of increasingly complex measurement targets.

This chapter also presents an accuracy analysis of the proposed adaptive mode of the FTP method, and discusses the sources of measurement errors. Finally, the approaches that were used to increase the speed of surface measurement are considered.

A large body of measurements have been carried out using the software and hardware that has been developed in this research programme, and these measurements were performed on both static and dynamic objects of various different shapes. As illustrated in Section 2.3.3, temporal phase shifting (TPS) methods are best suited to high accuracy measurements of static objects. The Fourier Transform Profilometry (FTP) method with the adaptive filter that was developed by the author, was designed for the measurement of dynamic objects. The software running at the CMS was designed so as to remotely measure dynamic objects simultaneously using multi-sensor mode and to collect the results from the individual SPUs, thereby enabling their centralised storage and/or visualisation. For the measurement of static objects using multi-sensor mode, the measurements are carried out locally at each SPU and the results are collected manually from the local hard disk of each SPU.

All of the results that will be presented in this chapter have some common features. Common annotations for the measurement results that are presented in this chapter are as follows:

- The size of the images acquired in all cases was 512×512 pixels, with a bit depth equal to 8bits.
- Spatial frequency of the fringes in all cases was: $f_0 = 0.0625\ {}^{1}/_{\text{pixel}}$ (such that the fringe period is 16 pixels).
- The resultant measurements produced using the multi-view approach are supposed to overlay over each other, assuming a valid calibration set is present (and that the positions of the sensor components have not been altered after calibration).
- The merging of the resultant point clouds as produced by the three sensors is not one of the issues addressed in this research programme. However, a CAD environment was employed to merge the point clouds in order to validate and carry out error analysis upon the measurement results. The 3DReshaper software application (3DReshaper, 2010) was used as a CAD environment for this purpose.
- The notations used in the analysis of the measurement results are as follows:

SD is the standard deviation error

PER≤1.0mm is the percentage of points of the 3D deviation map that are within a

tolerance of ±1.0mm

PER≤0.5mm is the percentage of points of the 3D deviation map that are within a tolerance of ±0.5mm

PER≤0.1mm is the percentage of points of the 3D deviation map that are within a tolerance of ±0.1mm

PER≤50μm is the percentage of points of the 3D deviation map that are within a tolerance of ±50μm

8.1 Static Objects

8.1.1 Breast Cast

Here is another plastic resin breast cast that was produced by rapid-prototyping from accurate CT scan data (that is typically accurate to a few microns) from a volunteer patient, exhibiting realistic curvature and steep features (Figure 8.1). The breast cast was used as a measurement object for this measurement example. The measured dimensions of the breast cast as defined in the CAD environment are; 292mm (L) × 230mm (W) × 89mm (H).

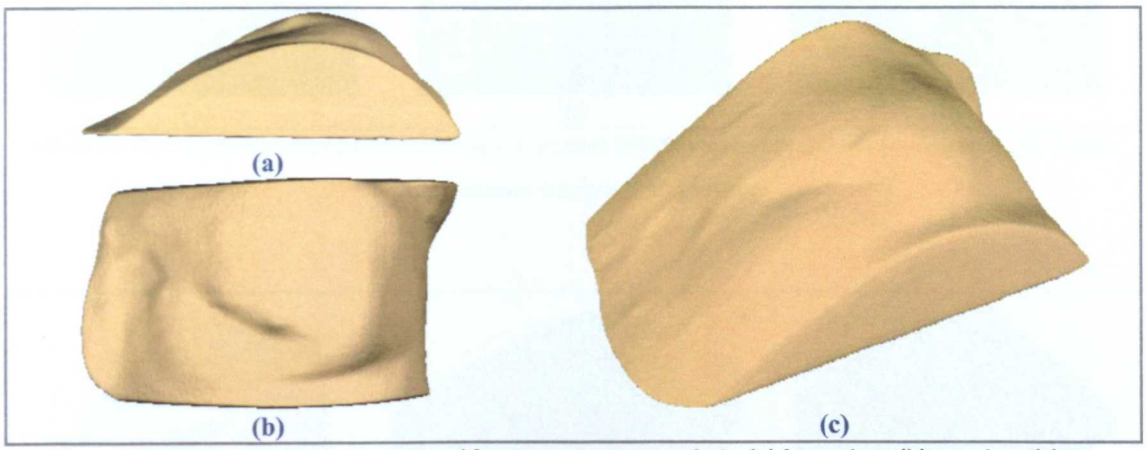

Figure 8.1 The breast phantom cast used for measurement analysis: (a) front view, (b) top view, (c) 3D isometric view.

The four-frame phase shifting method was used for fringe analysis and the reliability ordering algorithm was used for phase unwrapping. Figure 8.2 shows the first acquired fringe patterns (with 0 phase-shift) of this object, as obtained from the three individual sensors.

A black sheet was placed under the object in order to simplify the generation of the binary mask for the non full-field object used in this example. The breast cast was placed at the centre of the measurement ROI of the middle (green) sensor. Figure

8.3a-c shows the 3D point clouds of the measurement results for the left, middle and right-hand sensors, respectively. Because the transversal coordinates of the three sensors were calibrated simultaneously using the same central X and Y axis (as illustrated in Section 3.4.2), the measurement results of the three sensors overlay upon each other as shown in Figure 8.3d-e. Then under a CAD environment, the 3D point clouds were merged and aligned to the reference surface of the breast cast (Figure 8.4). A set of Coordinate Measuring Machine (CMM) data that was measured for the breast cast is used here as a reference surface, which was measured using an NVision 3D laser scanner with an overall measurement accuracy of 10 microns (NVision, 2008).

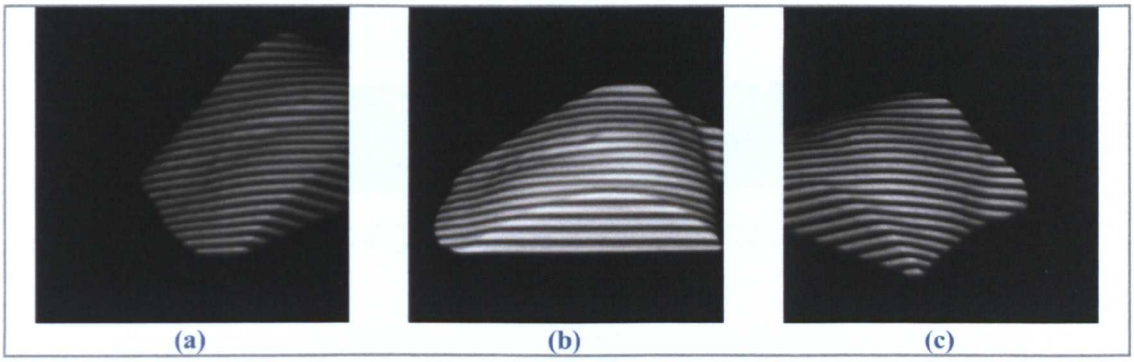

Figure 8.2 The acquired fringe patterns of the breast cast with 0 phase-shift: (a) left (red) sensor, (b) middle (green) sensor, (c) right (blue) sensor.

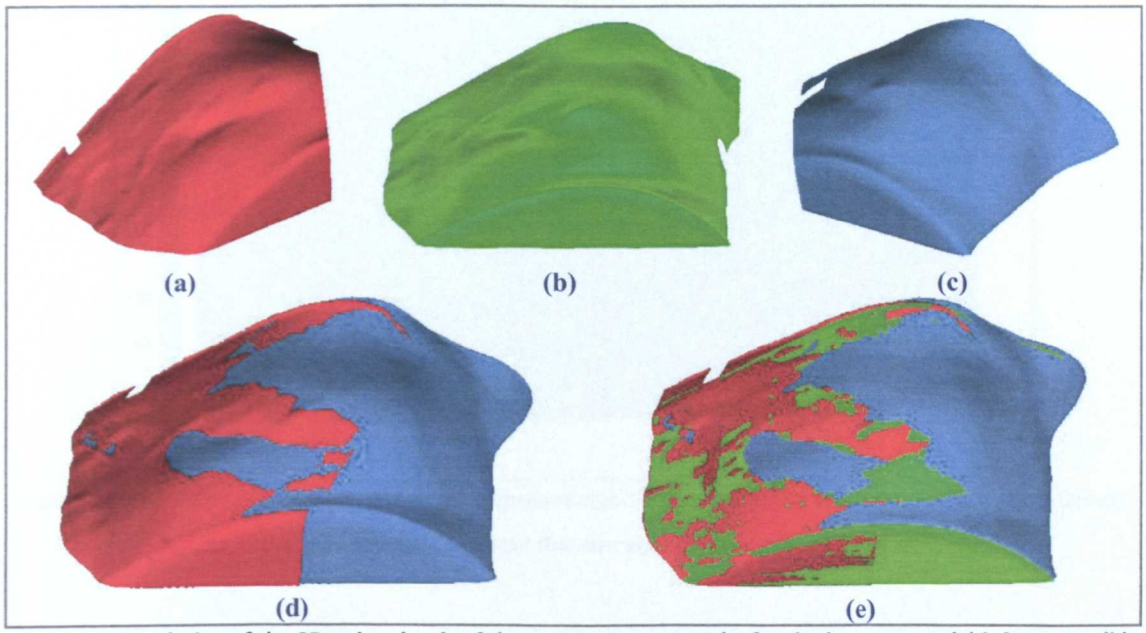

Figure 8.3 Rendering of the 3D point clouds of the measurement results for the breast cast: (a) left sensor, (b) middle sensor, (c) right sensor, (d) left and right sensor, (e) all sensors.

Figure 8.4 A perspective view for the merged three measurement results (in purple) of the breast phantom cast and its corresponding CMM reference surface (in yellow).

Using the CAD environment, the 3D deviation map between the three merged surfaces and the reference surface of the breast cast was calculated and is shown in Figure 8.5. The 3D deviation results are as follows:

The absolute 3D deviation from the reference surface					
Average (mm)	SD (mm)	PER ≤1.0mm	PER ≤0.5mm	PER ≤0.1mm	PER ≤50μm
0.090	0.092	100.00%	**99.36%**	67.72%	39.54%

Table 8.1 The 3D deviation results between the three merged surfaces and the reference surface of the breast cast.

Figure 8.5 The 3D deviation map between the three merged surfaces and the reference surface of the breast cast, the grey colour represents the reference surface of the breast cast.

The average number of points in each 3D point cloud of the three sensors was of the order of 120,000 points, which produced a merged surface with approximately

245,000 points. Hence, in addition to the advantage of wider coverage of the object's surface, there is another key advantage that arises when using the multi-sensor approach, which is the fact that we are increasing the measurement density at the shared areas of the individual measurement ROIs. However, merging surfaces that contain measurement outliers can detrimentally affect the final merged result, and consequently produce increased measurement errors.

8.1.2 Plastic Cast of Human Male Face

A plastic cast of human male face (Figure 8.6) with approximate dimensions of 155mm (L) × 222mm (W) × 85mm (H) was measured using the system. The four-frame phase shifting method was used for fringe analysis and the reliability ordering algorithm was used for phase unwrapping. Figure 8.7 shows the first set of acquired fringe patterns (with 0 phase-shift) for the three sensors. Figure 8.8a-c shows the corresponding 3D point clouds for the measurement results for left, middle and right sensors, respectively. Figure 8.8d-e shows how the reconstructed point clouds successfully lie over each other, for the left and right sensors and for the three sensors together, respectively.

Figure 8.6 Photograph of the plastic human face cast.

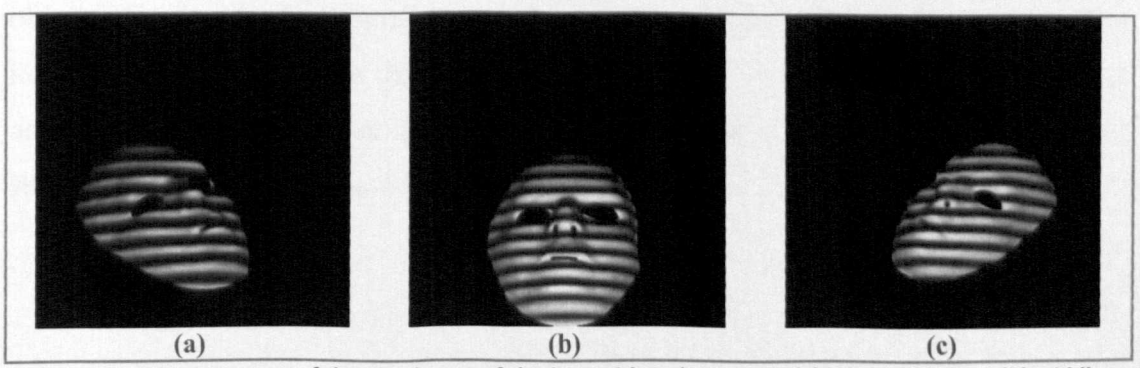

Figure 8.7 Fringe patterns of the plastic cast of the face with 0 phase-shift: (1) left (red) sensor, (b) middle (green) sensor and (c) right (blue) sensor.

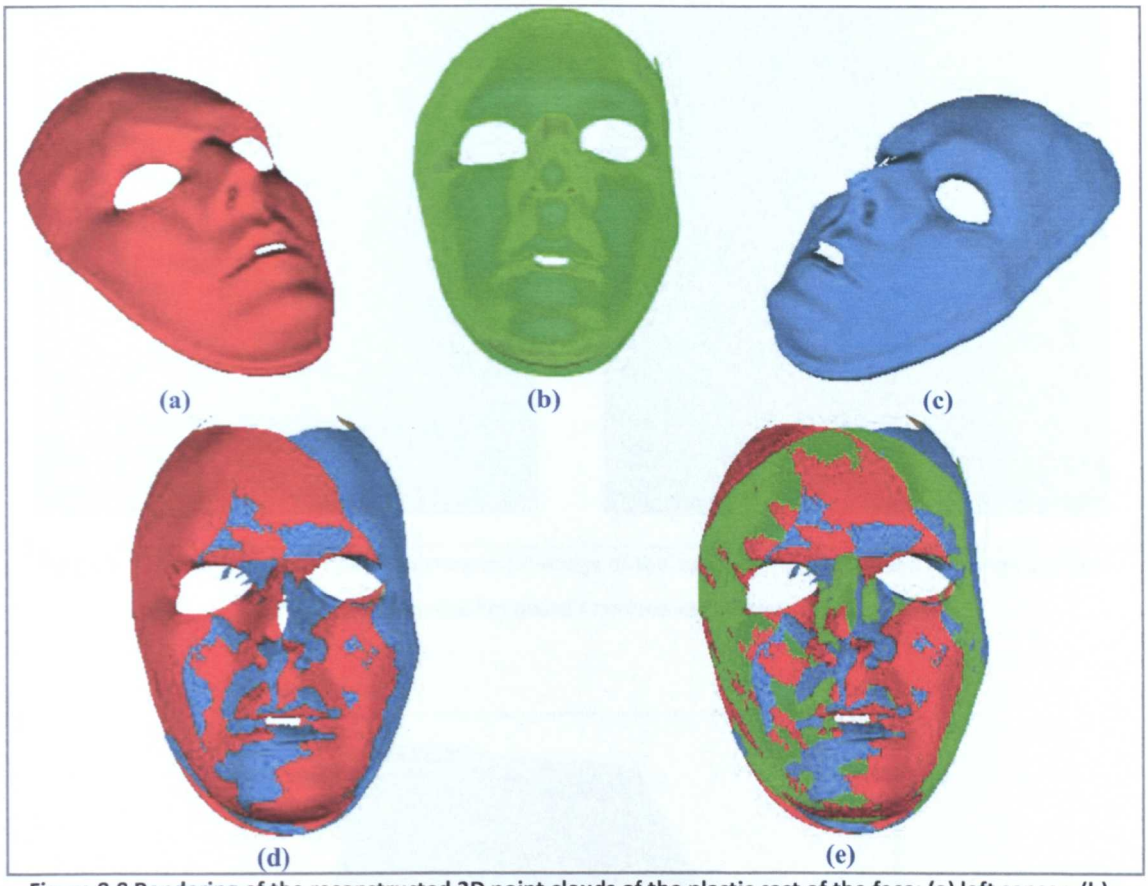

Figure 8.8 Rendering of the reconstructed 3D point clouds of the plastic cast of the face: (a) left sensor, (b) middle sensor, (c) right sensor, (d) left and right sensor, (e) all sensors.

8.1.3 Measurement of More Complex Shapes

As has been demonstrated in Section 4.3.2, various objects were measured using the single and multi-sensor modes. For example, the porcelain figurine of an owl (that was shown in Figure 4.37) features a hard to measure object as it exhibits both shadows and re-entrant features. However, despite the high level of difficulty of this measurement task for an optical system, and as is demonstrated in Figure 4.39 and Figure 4.40, the system was successfully capable of measuring the figurine. However, in order to further test the system's ability to measure more complex objects, a computer keyboard was used as a measurement object (Figure 8.9). The keyboard has approximate dimensions of 162mm (L) × 452mm (W) × 52mm (H) and exhibits an even greater number and extent of shadowed regions, re-entrant and steep features than is the case for the owl figurine.

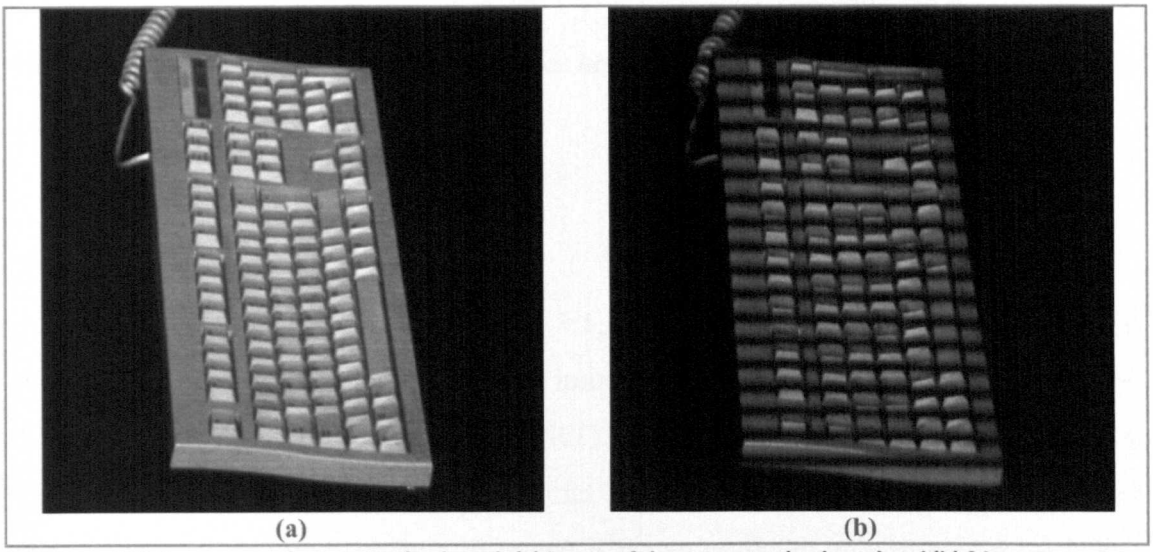

Figure 8.9 The measured computer keyboard; (a) image of the computer keyboard and (b) fringe pattern projected upon the keyboard's surface with 0 phase-shift.

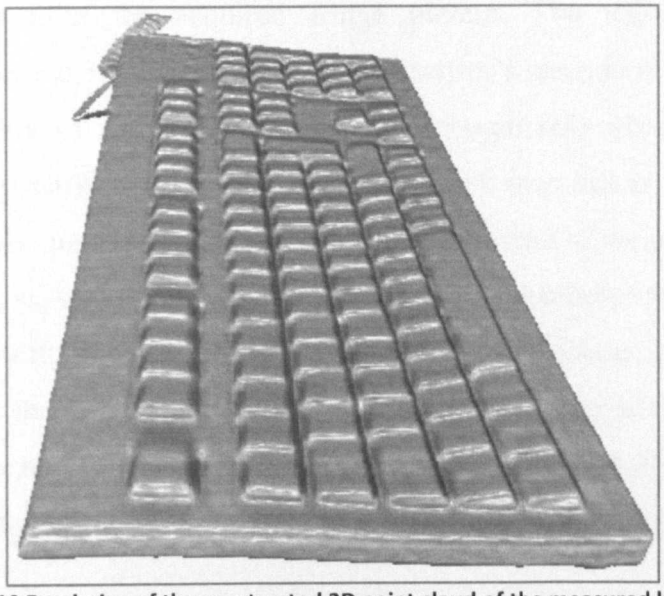

Figure 8.10 Rendering of the constructed 3D point cloud of the measured keyboard.

In the example given above, the keyboard was measured by a single-sensor, using the four-frame phase shifting algorithm for fringe analysis and Flynn's algorithm for phase unwrapping. It can be noticed that the reconstructed 3D surface of the computer keyboard (Figure 8.10) does not contain high frequency details, noticeable for example at the edges of the keyboard keys. Such high frequency detail can be enhanced by reducing the instrument's working distance and thereby increasing the spatial frequency of the fringe pattern. However, the measurement of very small objects such as the keyboard keys was not relevant to the main application of human

body measurement in radiotherapy and hence was not within the scope of this research programme.

8.2 Dynamic Objects

As discussed previously in Section 4.3.1, this research programme has mainly focused on the measurement of the human body surface for the purpose of Metrology Guided Radiotherapy (MGRT). The Fourier Transform Profilometry (FTP) method with the adaptive filter, that was developed by the author, was used for analysis of dynamic objects, because it provides better measurement accuracy than both the conventional FTP and the WTP methods (described in Section 2.3.3). Moreover, the approach was designed to afford the ability to generate both texture and mask maps from the acquired fringe pattern. The texture map can be superimposed over the 3D visualisation of each sensor's measurement results, which adds the capability of providing an instantly recognisable view of any surface features and body markers that are present. The mask map has an important role to play in the phase unwrapping process. This is because it helps to shorten the unwrapping process, sometimes very significantly, and also helps to avoid errors that would result from noisy regions in the unwrapped phase image that are associated with the object's shadow features or with the surrounding regions in the case when we are measuring non full-field objects. The reliability ordering algorithm was used for phase unwrapping in all cases for the measurement of the objects within this section.

For all of the objects being measured, the acquired fringe patterns do not provide a full-field image of the object's surface alone, i.e. the images contain an object that does not fully fill the field of view of the camera ROI, but instead contains a combination of the object and some areas of background. This has obviously made the measurement analysis more difficult and complex. Besides, it also introduces measurement outliers at the boundaries of the objects. In order to reduce the significance of rendered outliers, a Hamming window was pre-applied to the fringe pattern for some of the measurement objects. Additionally, it was noticed that by using a Wiener filter as a noise-suppression algorithm as a pre-processing stage, that this could help to reduce measurement errors in certain cases.

Measurement outliers can destructively affect the merging process of the 3D point clouds from the three sensors. This occurs because the merging process mainly employs an averaging process in the areas of intersection of the three individual measurements. This acts to invalidate good measurement results within the regions where outliers are present. However, the merging process itself is not one of the issues that is addressed in this research programme and hence the analysis of the measurement results are presented as a worst case scenario when performing the measurements using this system.

The different values for the level of detail (which is used in the adaptive filtering mode for the FTP method as described in Section 7.4.1) were chosen in order to minimise surface ripple effects from the individual sensors, while preserving object's high frequency features as much as possible.

8.2.1 Breast Cast

The same plastic resin breast cast (Figure 8.1) that was used for analysis in Section 8.1.1 was again used here. Figure 8.11(a1-a3) shows the fringe patterns that were acquired from the three sensors (left, middle and right sensors, respectively). Single spot triangulation was used to calculate the relative phase map. Figure 8.11(b1-b3) shows the fringe patterns after the locations of the spots were synthetically restored. Figure 8.11(c1-c3) shows the generated texture maps, and Figure 8.11(d1-d3) shows the binary thresholded mask maps.

The level of detail used for the adaptive FTP measurements was; 2, 4 and 3 for the left, middle and right sensors, respectively. Noise-suppression was not used within the analysis for this example, because the breast cast does not exhibit any surface marks, or hair features. Figure 8.12(a-c) shows the 3D point clouds from the measurement results for the left, middle and right sensors, respectively. Figure 8.12(d-e) shows how the measurement results overlay over each other. Under a CAD environment, the 3D point clouds are then merged and aligned to the reference surface of the breast cast (Figure 8.13), where it can be noticed how the merge processes has destructively invalidated some intersecting regions.

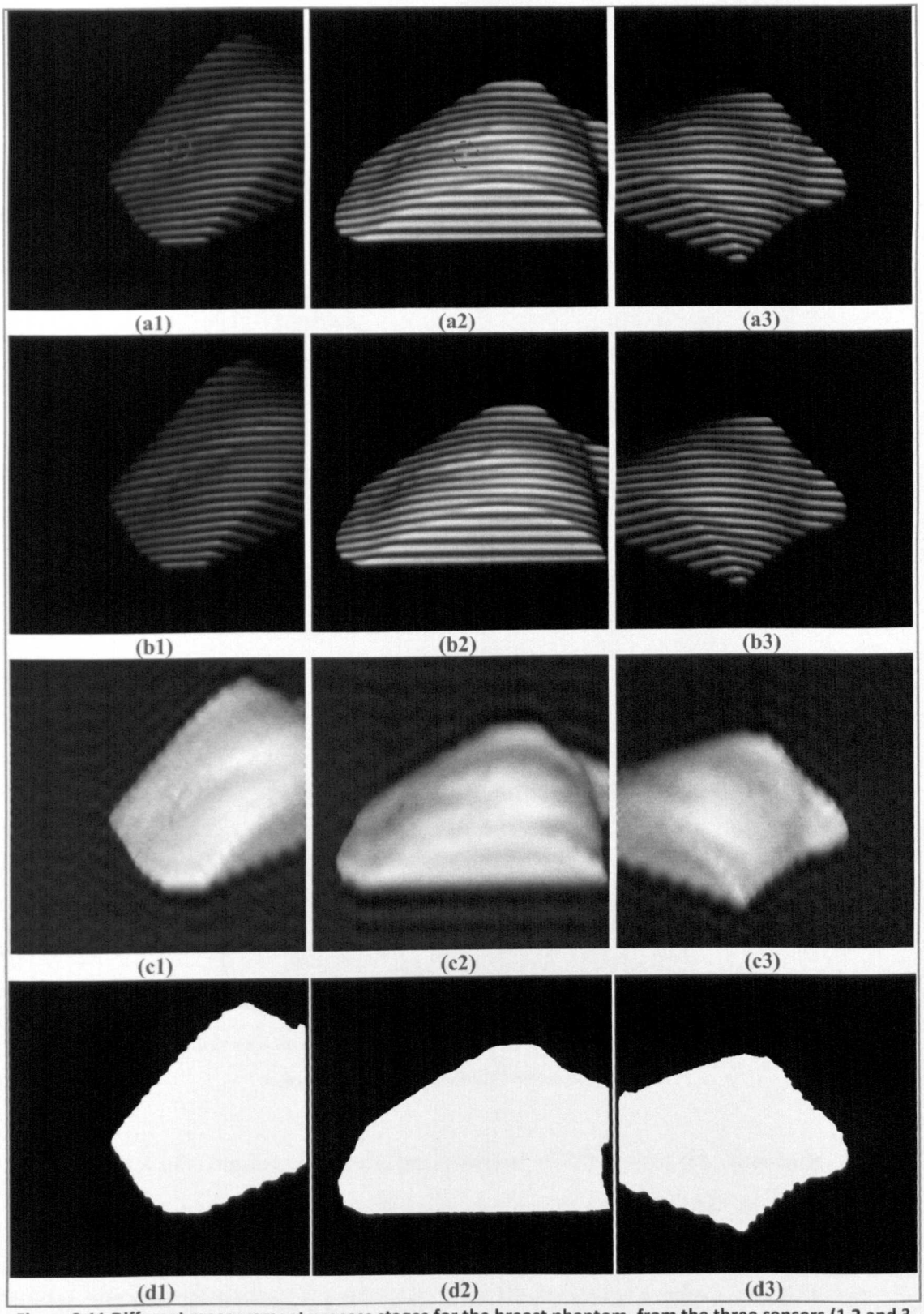

Figure 8.11 Different measurement process stages for the breast phantom, from the three sensors (1,2 and 3 represent the left (red), middle (green) and right (blue) sensors, respectively): (a1-a3) the acquired fringe patterns, the embedded triangulation spots are surrounded with a red circle, (b1-b3) the fringe patterns after the restoration of the locations of the spots, (c1-c3) the generated texture maps, (d1-d3) the generated mask maps.

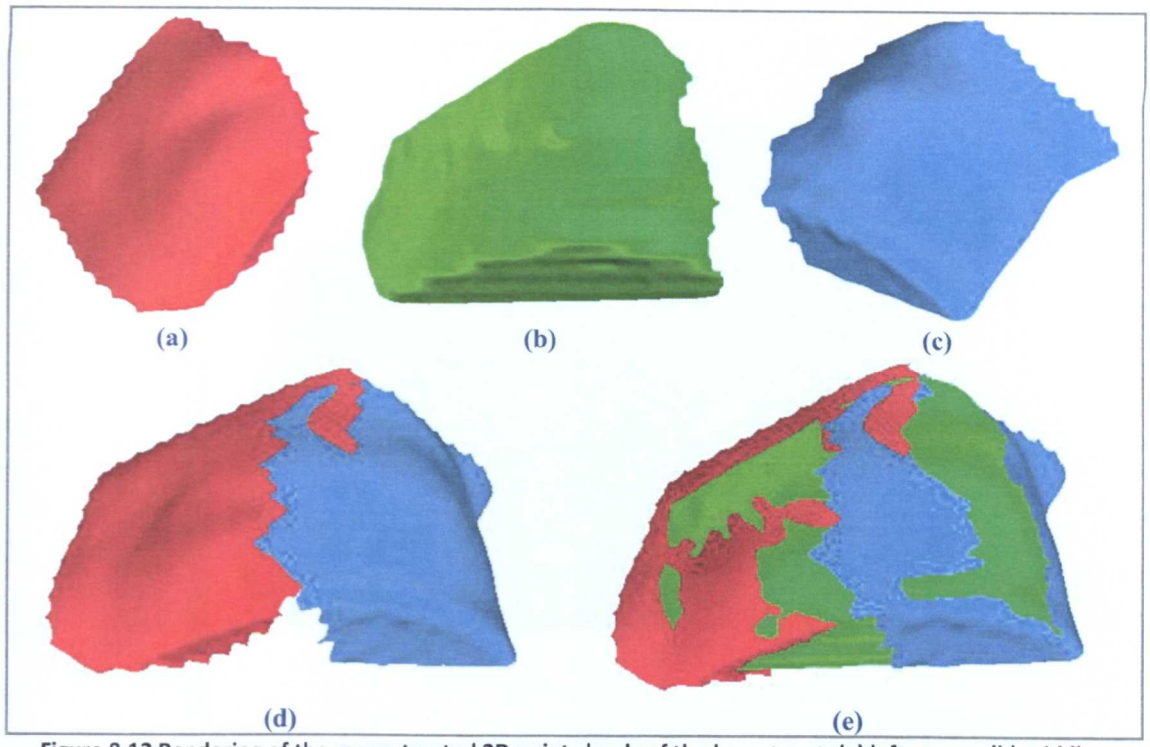

Figure 8.12 Rendering of the reconstructed 3D point clouds of the breast cast: (a) left sensor, (b) middle sensor, (c) right sensor, (d) left and right sensor, (e) all sensors.

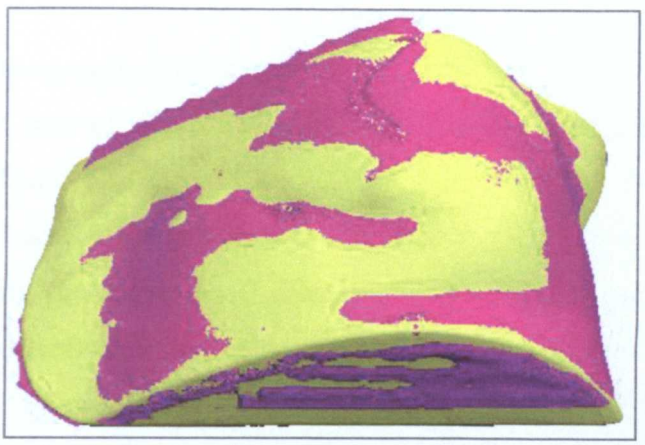

Figure 8.13 A perspective view for the merged three measurement results (in purple) of the breast phantom cast and its CMM reference surface (in yellow).

The same set of Coordinate Measuring Machine (CMM) data that was measured for the breast cast is used here as a reference surface. Using the CAD environment, the 3D deviation map between the three merged surfaces and the reference surface of the breast cast was calculated (Figure 8.14). The 3D deviation results are as follows:

The absolute 3D deviation from the reference surface					
Average (mm)	SD (mm)	PER ≤1.0mm	PER ≤0.5mm	PER ≤0.1mm	PER ≤50μm
0.510	0.695	95.66%	**80.54%**	11.12%	5.59%

Table 8.2 The 3D deviation results between the three merged surfaces and the reference surface of the breast cast.

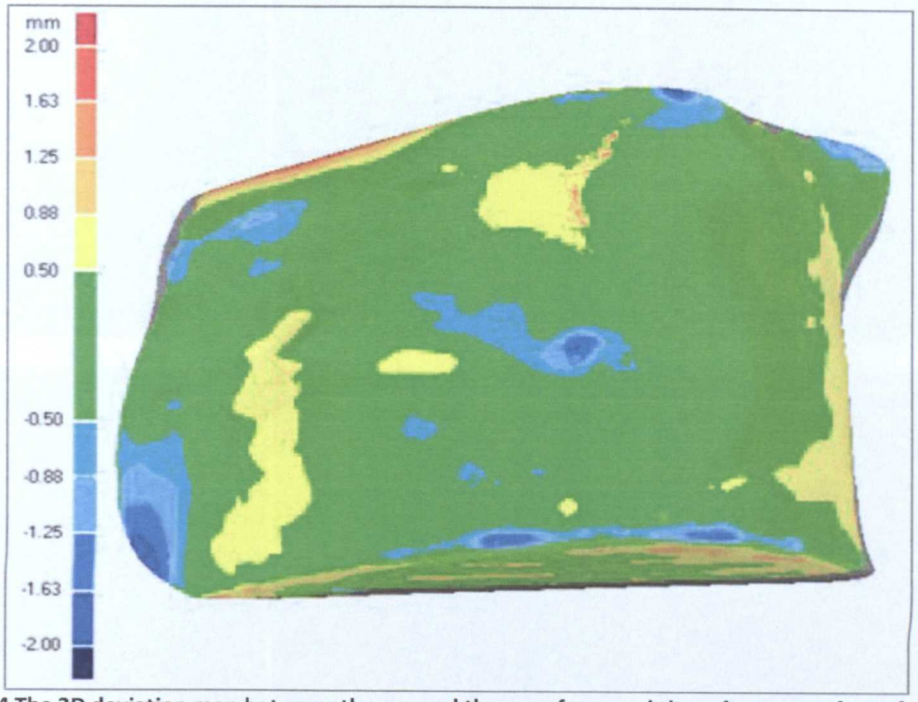

Figure 8.14 The 3D deviation map between the merged three surfaces and the reference surface of the breast cast, the grey colour represents the reference surface of the breast cast.

8.2.2 RANDO Phantom Dorsal Surface

An exterior body cast of a RANDO phantom (Figure 4.31) was used here for measurement analysis. The RANDO phantom was chosen as the ideal reference object for testing, because it was virtually unique in the fact that it offered data in the form of all imaging modalities used in radiotherapy. A CT scan for the RANDO phantom was used here as a reference surface for the system's accuracy analysis (Figure 8.18(a-b)). Figure 8.15(a1-a3) shows the acquired fringe patterns from the three sensors (left, middle and right sensors, respectively). Because the object's surface in this case exhibits marks and shiny features, a multiple triangulation spot approach was used here. Figure 8.15(b1-b3) shows the fringe patterns after the locations of the spots were synthetically restored. Figure 8.15(c1-c3) shows the generated texture maps, and Figure 8.15(d1-d3) shows the binary thresholded mask maps.

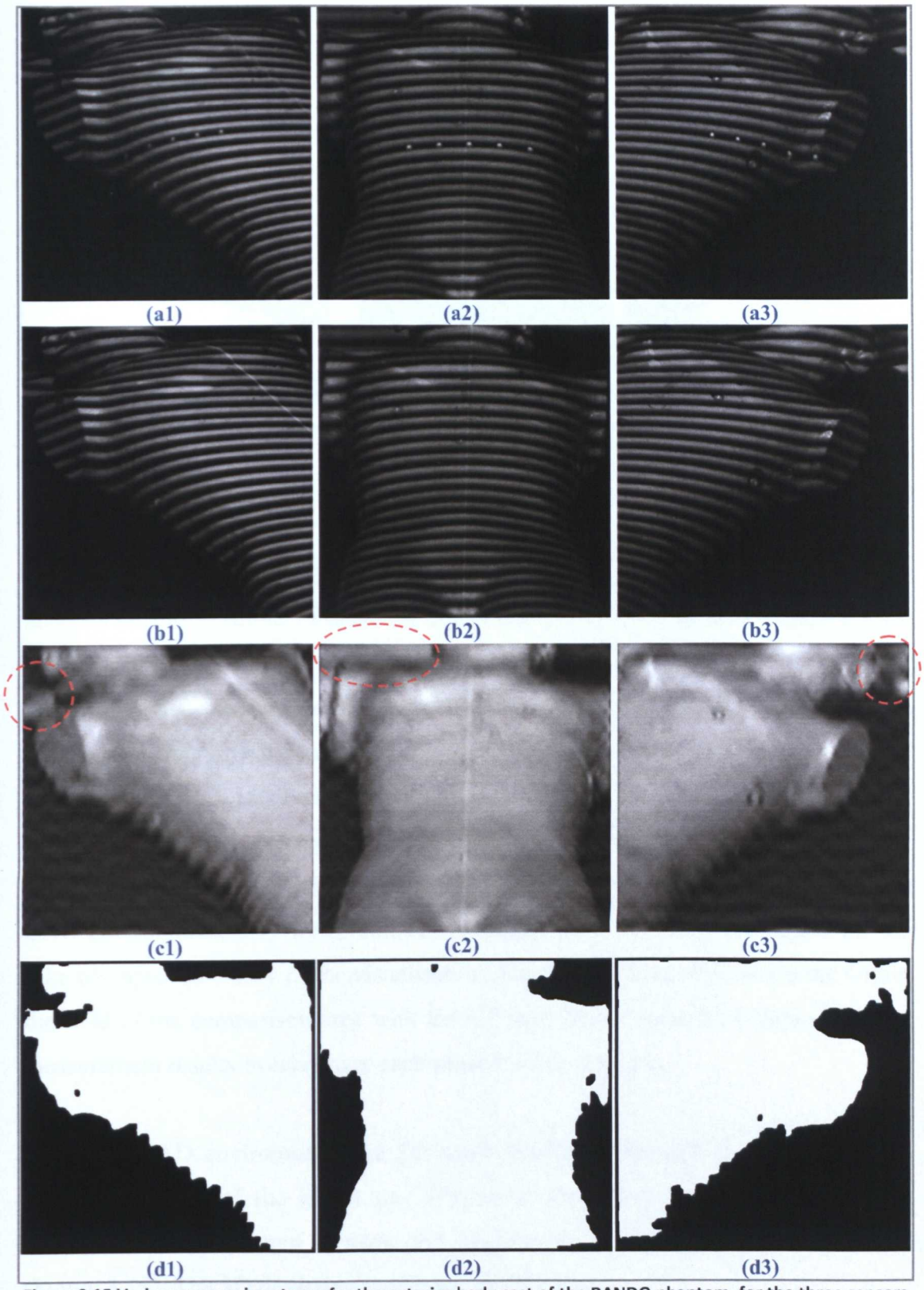

Figure 8.15 Various processing stages for the exterior body cast of the RANDO phantom, for the three sensors (1,2 and 3 represent the left (red) , middle (green) and right (blue) sensors, respectively): (a1-a3) the acquired fringe patterns, (b1-b3) the fringe patterns after restoration of the locations of the spots, (c1-c3) the generated texture maps, (d1-d3) the generated mask maps.

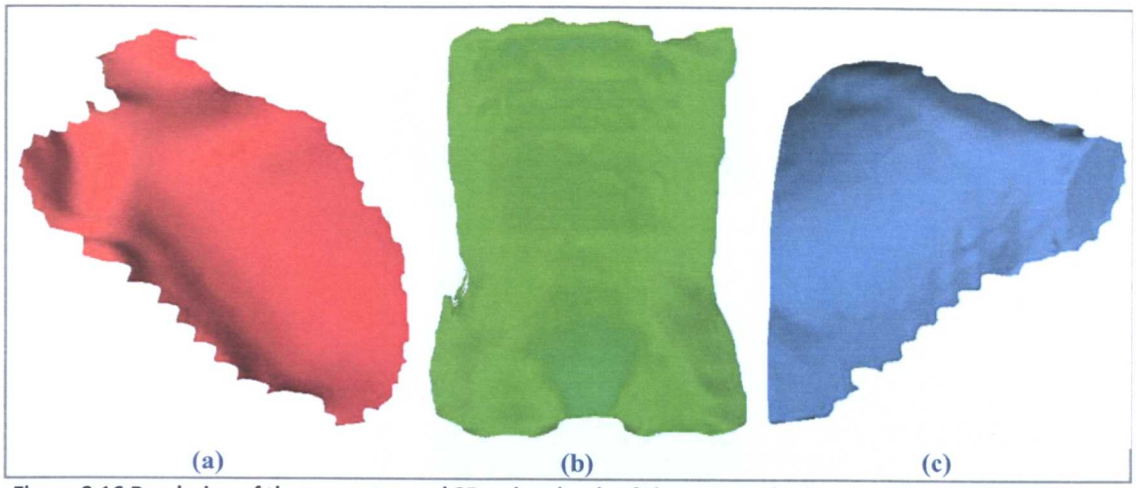

Figure 8.16 Rendering of the reconstructed 3D point clouds of the exterior body cast of the RANDO phantom: (a) left sensor, (b) middle sensor, (c) right sensor.

The level of detail used for the adaptive FTP measurements was; 2, 3 and 2 for the left, middle and right sensors, respectively. Noise-suppression was used for the analysis for this example, because the object has marks on its surface. Figure 8.16(a-c) shows the 3D point clouds that comprise the measurement results for the left, middle and right sensors, respectively. There are some background regions behind the object which were captured within the ROIs of the cameras (surrounded with red circles in Figure 8.15(c1-c3)), which were accidentally included within the mask maps. These regions affected the behaviour of the unwrapping algorithm at the areas around the neck and the head of the RANDO phantom object. Hence, and using the CAD environment, they were removed manually from the 3D point clouds for the sake of improved clarity of the visualisation. Practically, these regions are not within the field of the comparison area with the CT scan data. Figure 8.17 shows how the measurement results overlay over each other for this example.

Using the CAD environment, the 3D point clouds are merged and aligned to the reference surface of the breast cast (Figure 8.18c). Then the 3D deviation map between the three merged surfaces and the reference CT scan data was calculated (Figure 8.19). The 3D deviation results are as follows:

The absolute 3D deviation from the reference surface					
Average (mm)	SD (mm)	PER ≤1.0mm	PER ≤0.5mm	PER ≤0.1mm	PER ≤50μm
0.631	1.255	93.05%	**77.04%**	9.19%	1.90%

Table 8.3 The 3D deviation results between the three merged surfaces and the reference surface of the exterior body cast of the RANDO phantom.

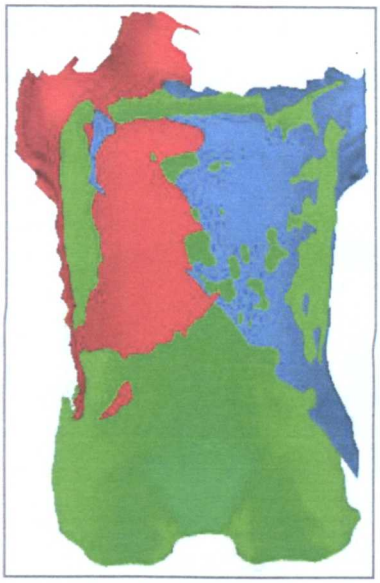

Figure 8.17 Rendering of the reconstructed 3D point clouds of the exterior body cast of the RANDO phantom for the three sensors.

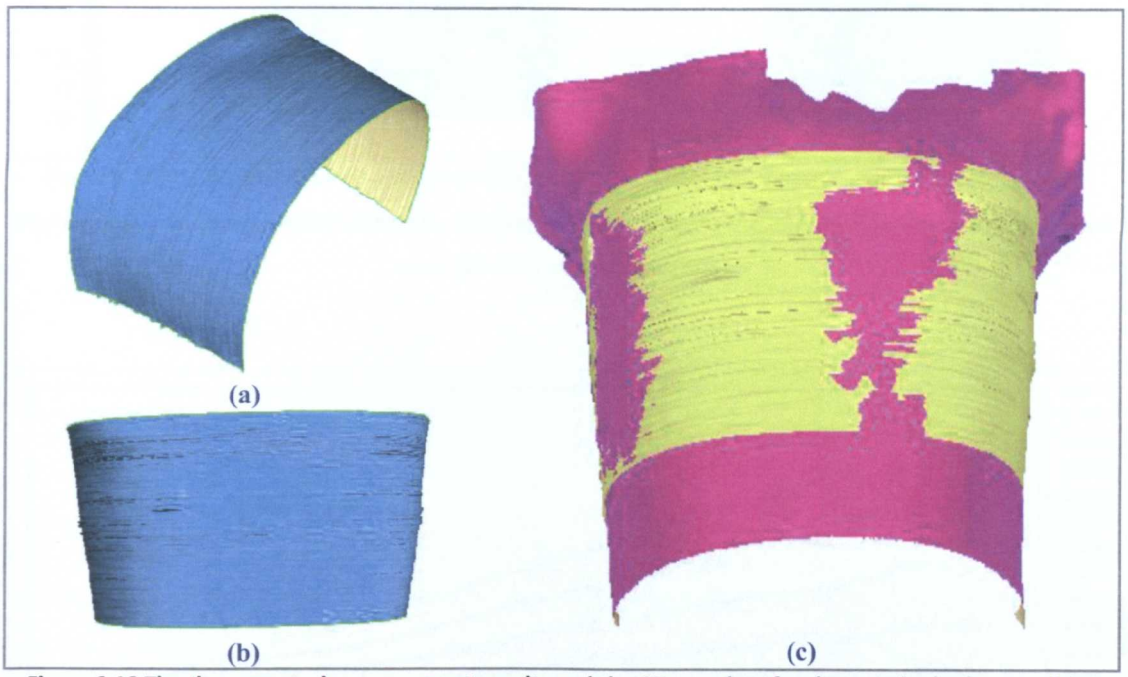

Figure 8.18 The three merged measurement results and the CT scan data for the exterior body cast of the RANDO phantom: (a) and (b) perspective and top views of the CT scan data, respectively, (c) a perspective view for the merged surface (in purple) and the CT reference surface (in yellow).

During the measurement, the RANDO phantom was moved upward and downward by lifting the object's head by about 10cm from its original position in order to give a rough approximation of dynamic respiratory motion. Figure 8.20 shows a 2D plot diagram of cross-sections of 10 merged measurement results of the object's surface. The cross-sections were selected to be throughout the YZ-plane at the object's

centre. The 2D plot covers one cycle of object movement (10 measurements). The blue colour indicates the cross-section of the surface through the upward movement and the red colour indicates downward movement.

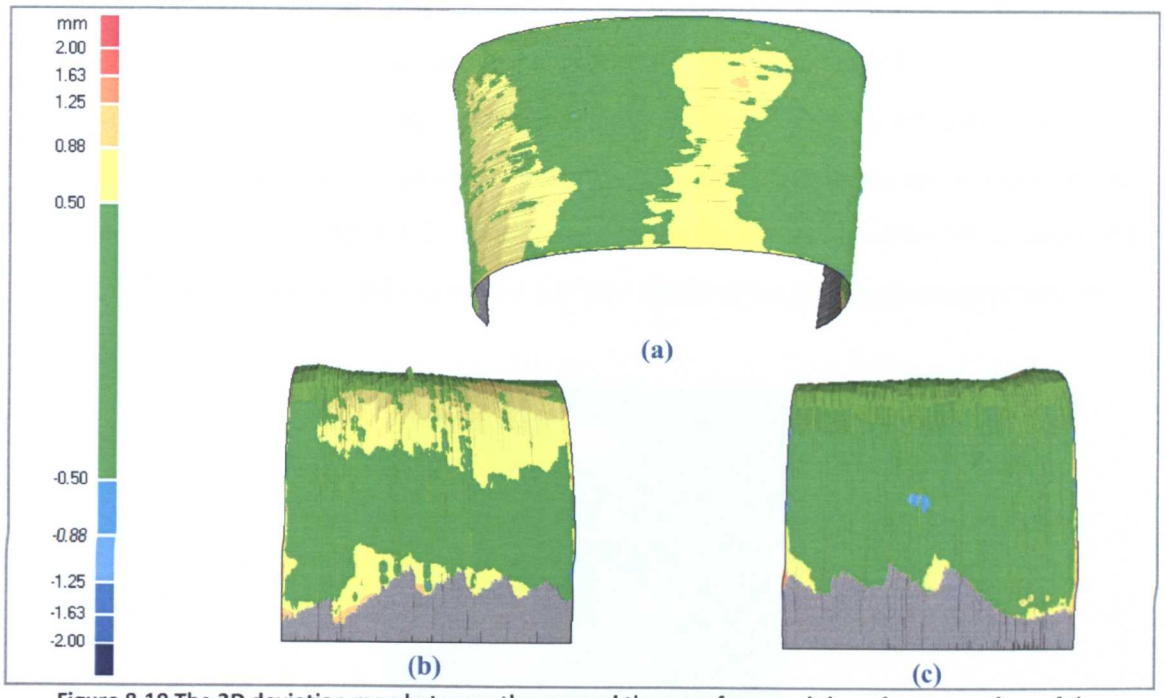

Figure 8.19 The 3D deviation map between the merged three surfaces and the reference surface of the exterior body cast of the RANDO phantom, the grey colour represents the reference surface: (a) perspective-view, (b) left-view, (c) right-view.

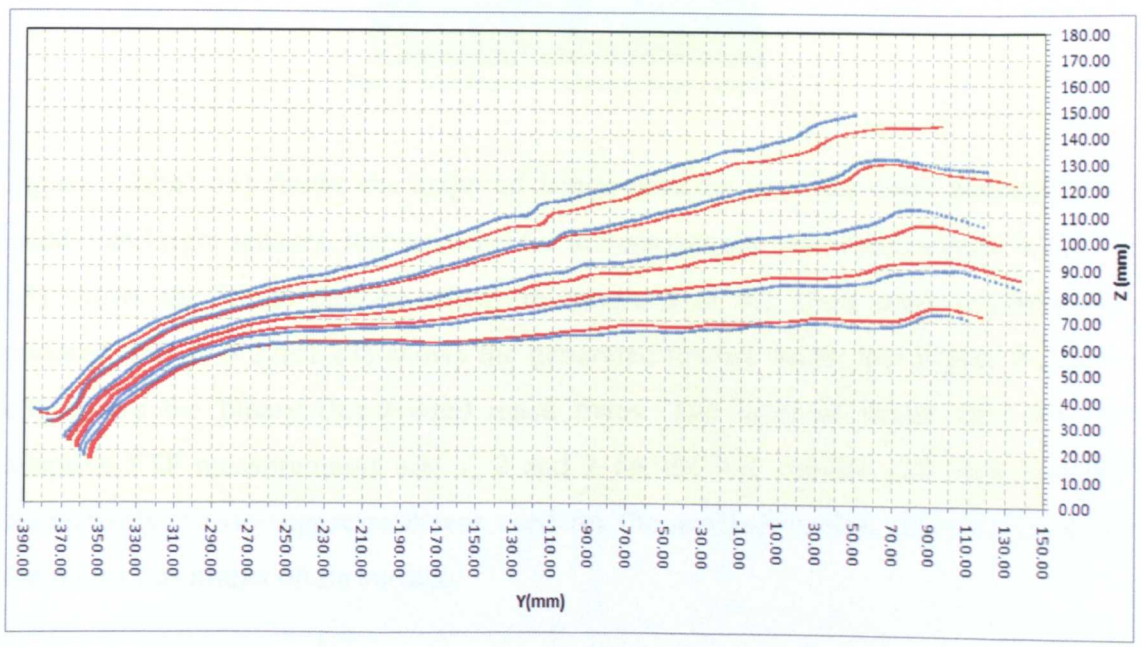

Figure 8.20 A cross-sectional graph of 10 merged measurement results of the exterior body cast of the RANDO phantom, throughout the YZ-plane of the object's centre. The blue colour represents the upward movements and the red colour represents the downward movements.

8.2.3 Female Mannequin

A female mannequin (Figure 8.21) test object represented a cheap laboratory alternative to the anthropomorphic RANDO man that was owned by the Christie Hospital in Manchester. The dummy's surface actually poses a more difficult measurement task than the previous RANDO phantom example; it has steep curvatures and a shiny surface finish, particularly noticeable as saturated reflective areas near the breasts, and a distinct re-entrant navel. The navel is not a deep feature, but its presence certainly could render measurement errors. On the other hand, the shiny surface features could introduce surface ripples into the measurement results.

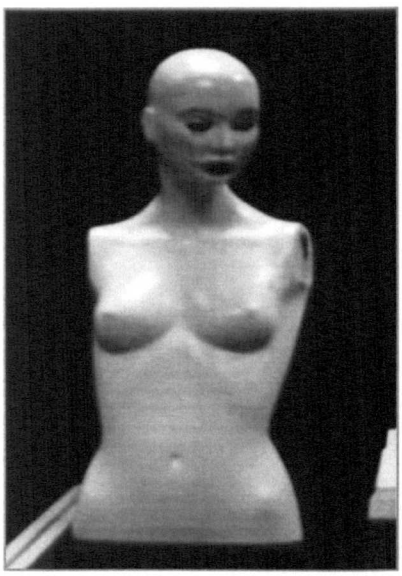

Figure 8.21 Female mannequin test object.

Figure 8.22(a1-a3) shows the acquired fringe patterns from the three sensors (left, middle and right sensors, respectively) for the mannequin test object. Figure 8.22(b1-b3) shows the fringe patterns after the locations of the spots were synthetically restored. Figure 8.22(c1-c3) shows the generated texture maps, and Figure 8.22(d1-d3) shows the binary thresholded mask maps. The level of detail used for the adaptive FTP measurements are; 1, 2 and 2 for the left, middle and right sensors, respectively. Noise-suppression was used for the analysis in this example, because the object has marks on its surface.

Figure 8.23(a-c) shows the 3D point clouds from the measurement results for the left, middle and right sensors, respectively. Figure 8.24 shows how the measurement results overlay each other. Measurement outliers are apparently severe, especially at

the object boundary areas of the three measurements. No editing or trimming was performed upon those outliers for this measurement example.

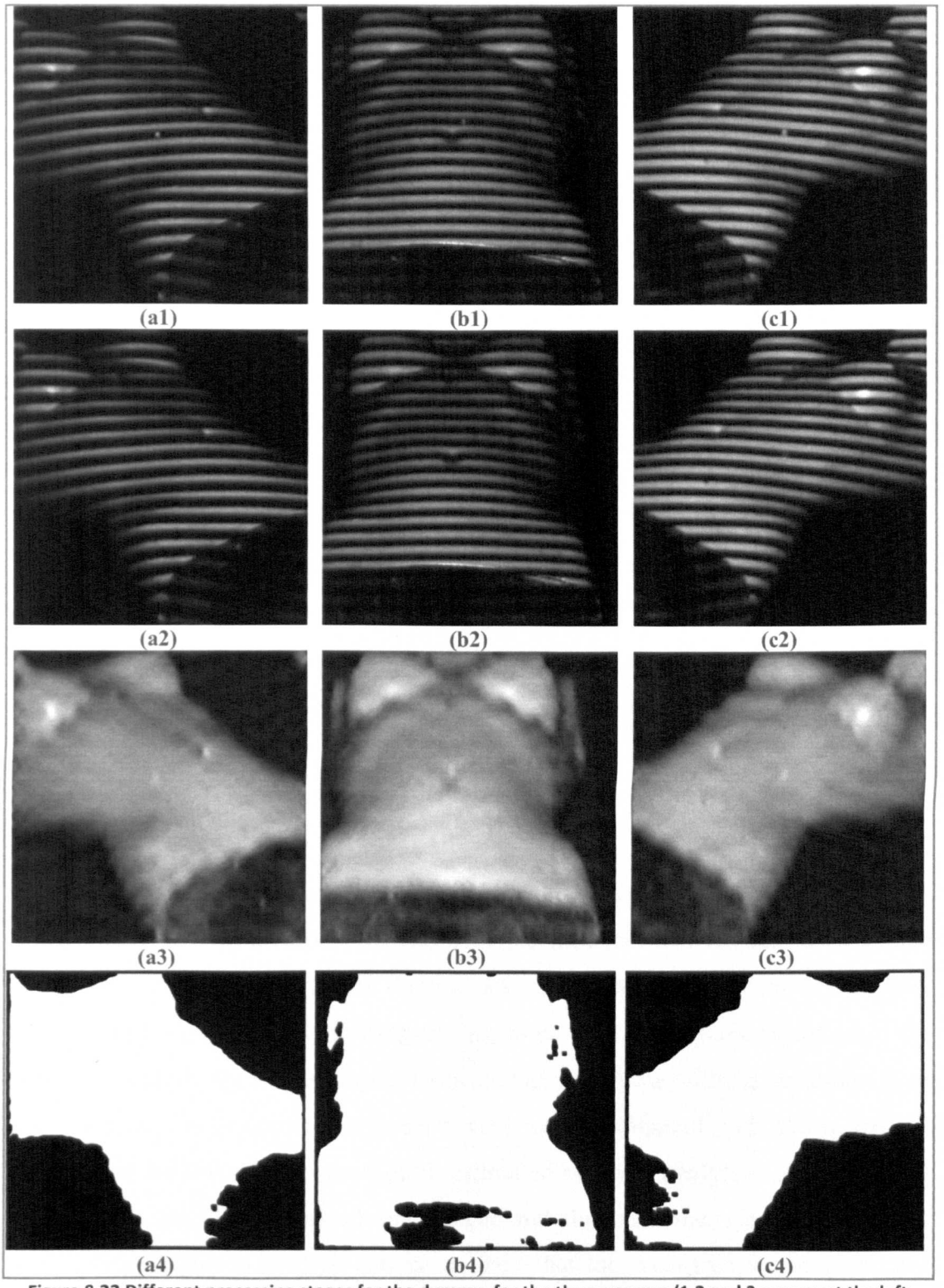

Figure 8.22 Different processing stages for the dummy, for the three sensors (1,2 and 3 represent the left (red) , middle (green) and right (blue) sensors, respectively): (a1-a3) the acquired fringe patterns, (b1-b3) the fringe patterns after the restoration of the locations of the spots, (c1-c3) the generated texture maps, (d1-d3) the generated mask maps.

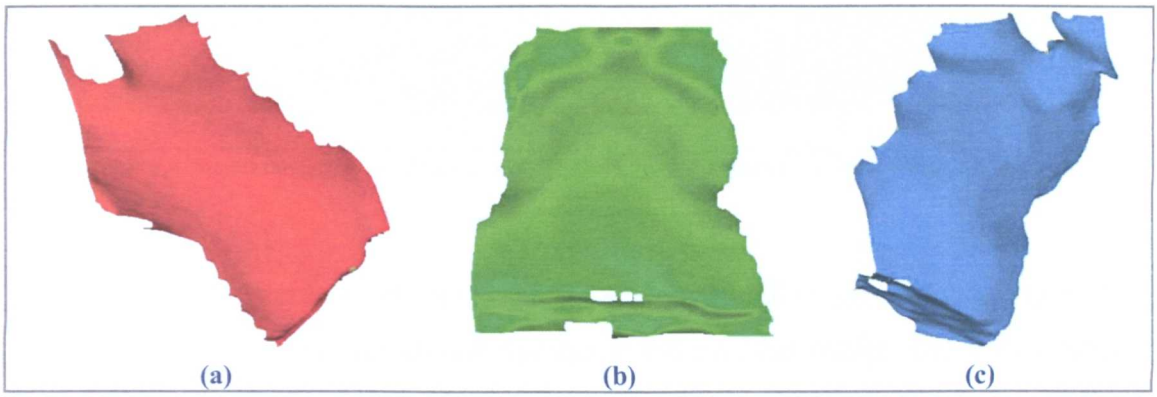

Figure 8.23 Rendering of the reconstructed 3D point clouds from the dummy test object: (a) left sensor, (b) middle sensor, (c) right sensor.

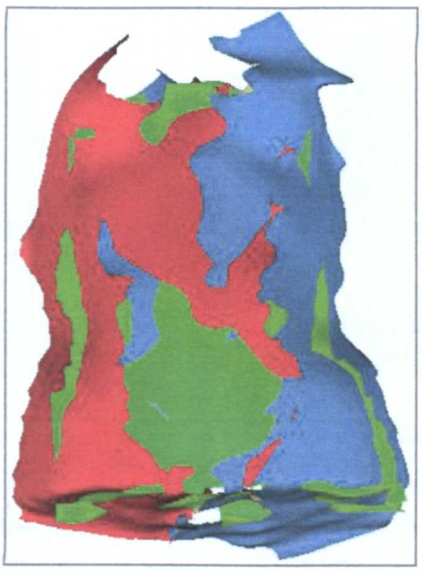

Figure 8.24 Rendering of the reconstructed 3D point clouds of the dummy for the three sensors.

There is no CMM or CT scan data available for the dummy. however, since the four-frame phase shifting method provides accurate measurement results (as described and proven in Section 8.1.1), the dummy was measured using this method (Figure 8.25a) in order for the phase-shifting surface to be used as a reference surface in the accuracy analysis for this example. Even though the phase shifting algorithm does not represent a high accuracy reference result when compared with CMM and CT scans, it can however help to provide an estimated accuracy analysis. Using the CAD environment, the 3D point clouds are merged and aligned to the reference surface of the dummy (Figure 8.25b). *It can be noticed* that the measurement outliers have disrupted the merged surface. The 3D deviation map between the three merged surfaces and the reference surface was calculated and is shown in Figure 8.26. The 3D deviation results are as follows:

The absolute 3D deviation from the reference surface					
Average (mm)	SD[1] (mm)	PER[2] ≤1.0mm	PER[3] ≤0.5mm	PER[4] ≤0.1mm	PER[5] ≤50μm
1.682	3.439	81.75%	**54.40%**	3.31%	1.59%

Table 8.4 The 3D deviation results between the three merged surfaces and the reference surface of the dummy.

Besides the measurement outliers, the testing and difficult to measure features of the female mannequin have introduced significant error to the results. The measurement had a small problem with the navel region, but further errors at the region of the breasts, with deviations from the reference surface ranging from 0.5mm to 2.0mm.

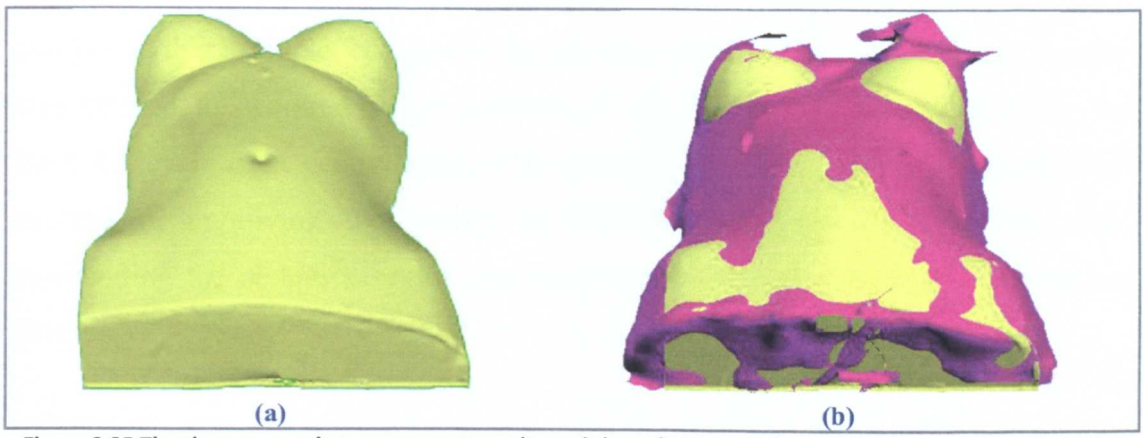

Figure 8.25 The three merged measurement results and the reference surface of the dummy as produced by phase stepping: (a) a perspective-view of the reference surface, (b) A perspective view for the triple sensor merged surface (in purple) and the reference surface (in yellow).

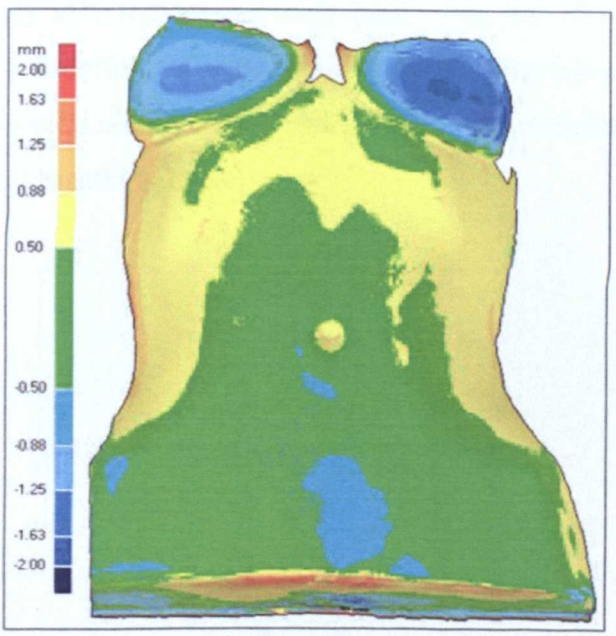

Figure 8.26 The 3D deviation map between the three merged surfaces and the reference surface for the dummy, the grey colour represents the reference surface

8.2.4 Human Abdomen

The abdomen area of a real live male human volunteer test subject was measured in this example. It was interesting to see how the profilometry system would cope with realistic levels of body hair and other features like the navel. Figure 8.27(a1-a3) shows the acquired fringe patterns from the three sensors (left, middle and right sensors, respectively). Figure 8.27(b1-b3) shows the fringe patterns after the locations of the spots were synthetically restored. Figure 8.27(c1-c3) shows the generated texture maps, and Figure 8.27(d1-d3) shows the binary thresholded mask maps. The level of detail used for the adaptive FTP measurements are; 3, 2 and 3 for the left, middle and right sensors, respectively. Noise-suppression was used for the analysis in this example, because of the presence of body hair. A Hamming window was applied to acquired fringe patterns of all the sensors, which increased the intensity levels at the central areas of the generated texture maps. Consequently, this assisted in improving the quality of the mask data by excluding the areas surrounding the abdomen region and hence removing them from the unwrapping process.

Figure 8.28(a-c) shows the 3D point clouds of the measurement results for the left, middle and right sensors, respectively. Figure 8.28(d-e) shows how the measurement results overlay each other. As can be noticed from the results, the system did not seem to be adversely affected by the body hair. This provided vital evidence, in practical terms, as to the effect upon the system of normal levels of body hair. Figure 4.31 shows a cross-sectional graph plotting of the measurement results for this example during a full breathing cycle.

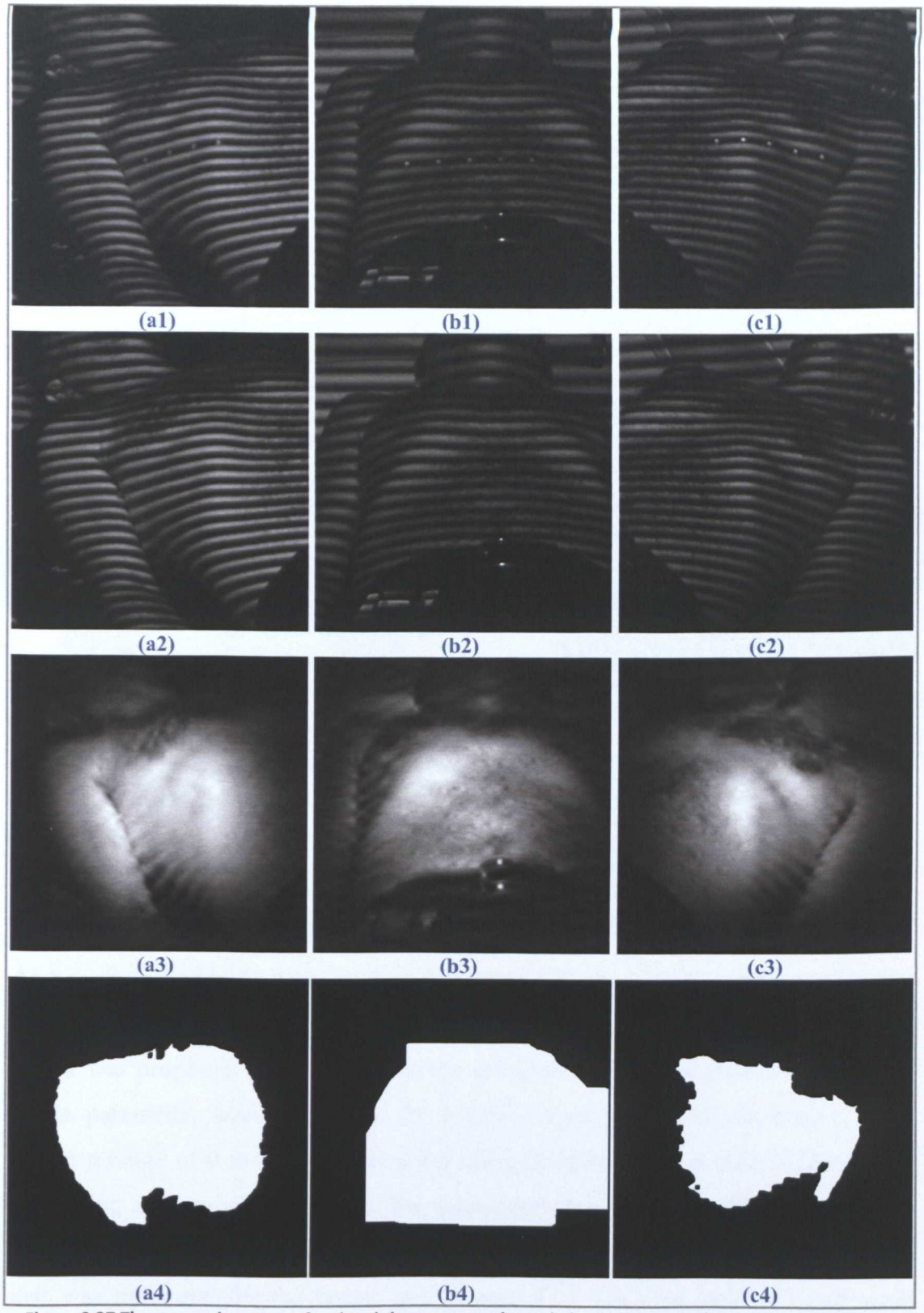

Figure 8.27 The processing stages for the abdomen area of a male human, for the three sensors (1,2 and 3 represent the left (red) , middle (green) and right (blue) sensors, respectively): (a1-a3) the acquired fringe patterns, (b1-b3) the fringe patterns after the restoration of the locations of the spots, (c1-c3) the generated texture maps, (d1-d3) the generated mask maps.

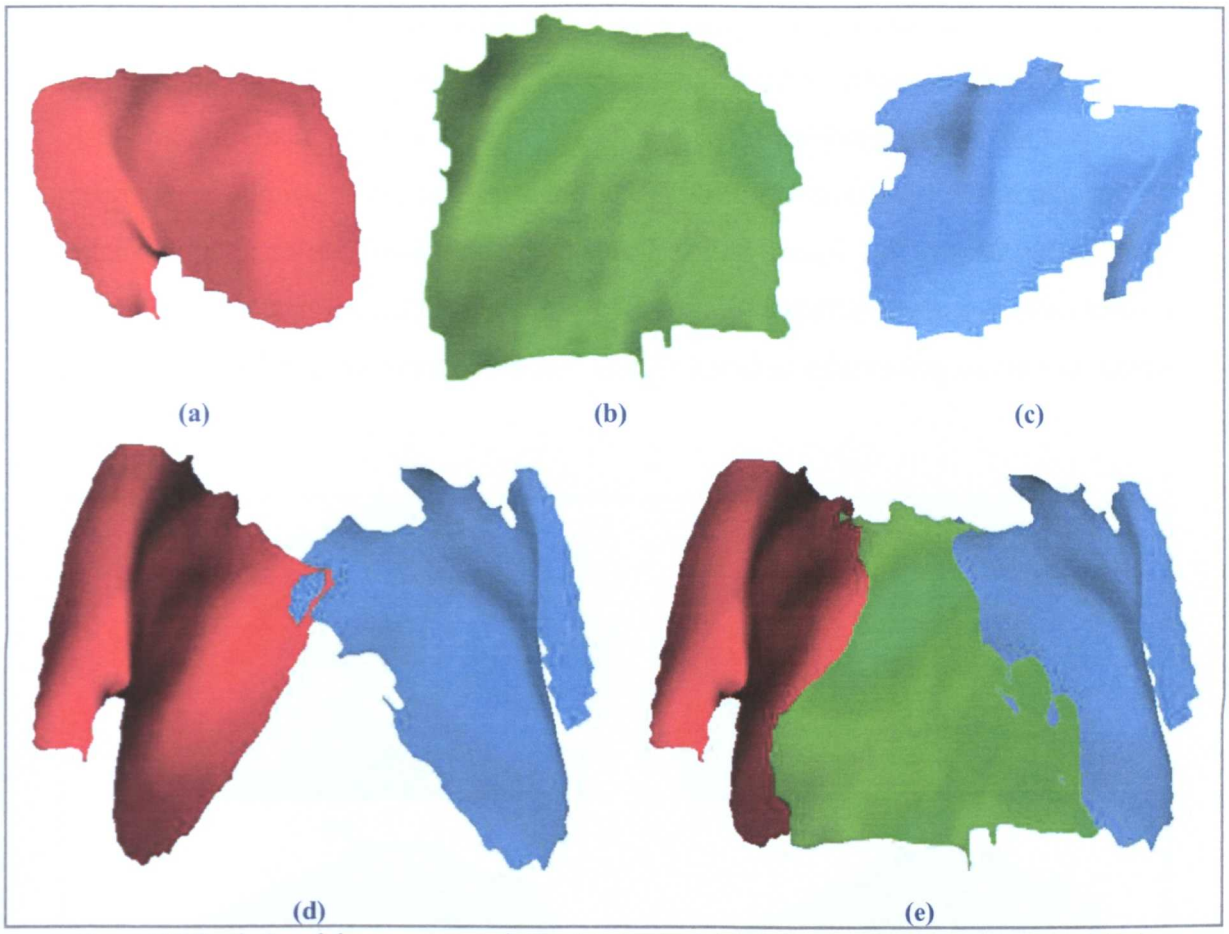

Figure 8.28 Rendering of the reconstructed 3D point clouds of the abdomen area of a male human: (a) left sensor, (b) middle sensor, (c) right sensor, (d) left and right sensor, (e) all sensors.

8.3 Accuracy Analysis of the Proposed Adaptive Mode for the FTP Method

As was discussed in Section 7.4.1, in order to avoid the typical complexity and the iterative calculations involved in the use of adaptive filters for the FTP method, the author has proposed a novel state-of-the-art approach. The approach uses only a single parameter, which indicates the required level of details (an integer value within a range of 0 to 4) to be extracted using the filter. This section is devoted to comparing an accuracy analysis of the measurements when using different levels of details, namely from 1 to 4. A set of Coordinate Measuring Machine (CMM) data that was measured for the breast cast (Figure 8.1) was used here as a reference surface. The use of the lowest level of details (0) is more appropriate for objects with only moderate, or semi-flat features; hence it was excluded from the analysis.

The breast cast was measured here using only the middle sensor (i.e. in single-sensor mode), in order to eliminate the possibility of any errors being incurred due to the

merging process. The measurement was performed using levels of details ranging from 1 to 4. The reliability ordering algorithm was used for phase unwrapping for all of the measurements in this section. Under the CAD environment the measurement results were aligned to the reference surface. Figure 8.29(a-d) shows the aligned 3D point clouds from the measurements, using level of details 1-4, respectively. It can be noticed that using a level of details with a value ranging from 1-3 introduces a greater number of measurement outliers than is the case when using a level of details of 4.

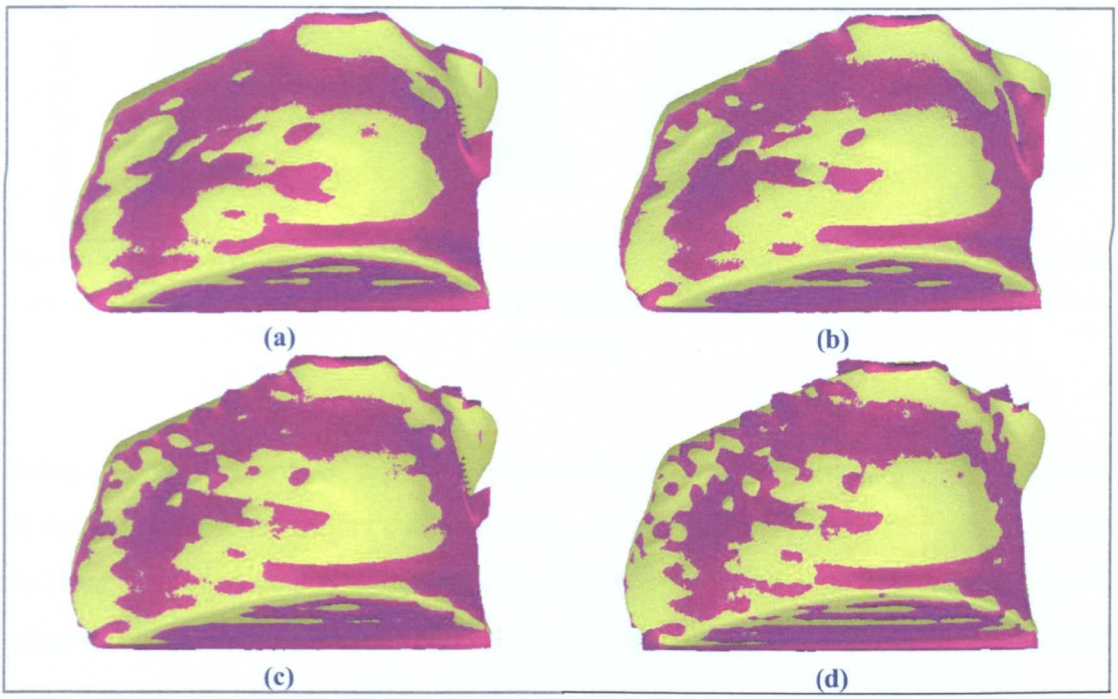

Figure 8.29 A perspective view for the measurement results (in purple) of the breast cast and its CMM reference surface (in yellow): (a-d) using a level of details of 1-4, respectively.

Figure 8.30(a-d) shows the 3D deviation maps between the measurement results, for each of the different level of details ranging from 1 to 4, and the reference surface, respectively. The 3D deviation results are as follows:

	The absolute 3D deviation from the reference surface					
Level of Details	**Average (mm)**	**SD (mm)**	**PER ≤1.0mm**	**PER ≤0.5mm**	**PER ≤0.1mm**	**PER ≤50μm**
1	0.590	1.128	87.17%	**74.22%**	18.10%	9.09%
2	0.567	1.179	88.89%	**78.32%**	17.65%	8.67%
3	0.520	1.054	90.11%	**81.66%**	19.53%	9.80%
4	0.447	0.763	91.63%	**83.61%**	20.02%	9.71%

Table 8.5 The 3D deviation results between the measurement results for each of the different level of details and the reference surface.

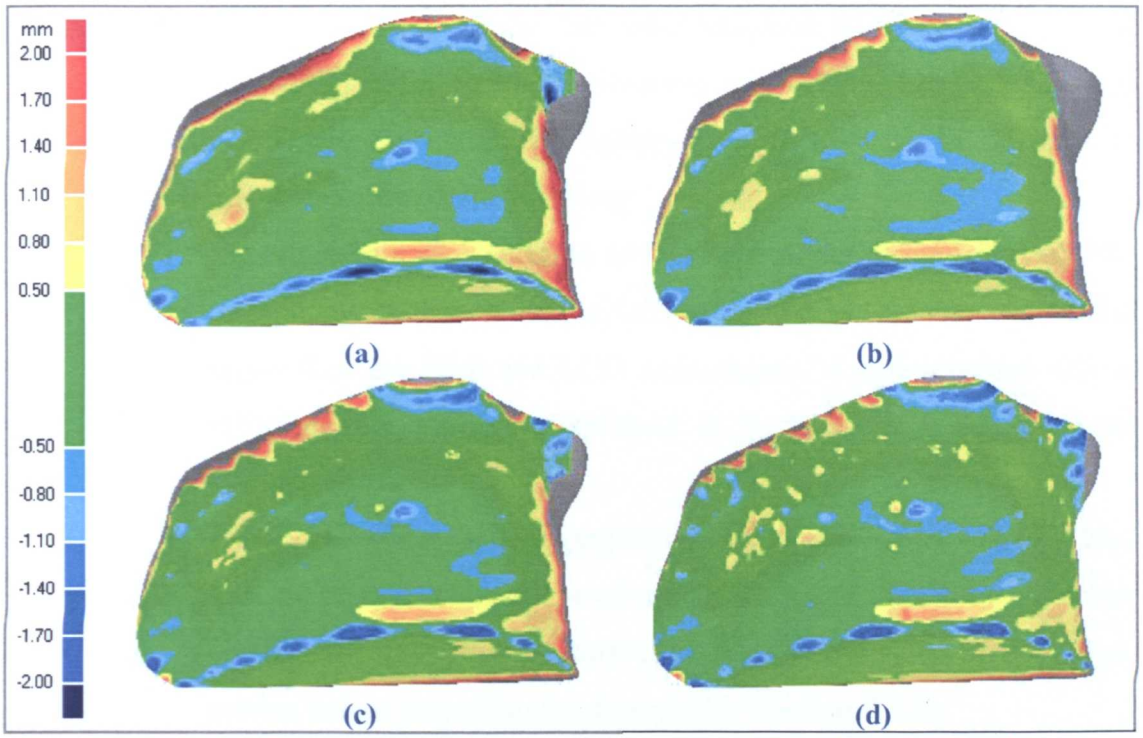

Figure 8.30 The 3D deviation map between the measurement results and the reference surface of the breast cast, the grey colour represents the reference surface of the breast cast: (a-d) using a level of details of 1-4, respectively.

Using a level of details of 4 produced the lowest average error. Due to the presence of the measurement outliers the percentage of the number of the points that within ±0.5mm was used as a comparison index. However, using a higher level of details value does not always guarantee a more accurate result, because it may introduce measurement errors and ripples.

Indeed, the level of details value is independent of the object's shape and there is no need to alter it for each object, but some objects that exhibit hair, or shiny features, demand the use of a lower level of details than is the case for the breast cast that was used here in this analysis.

8.4 Error Sources Considered

Fundamentally, error sources are the disagreements between the practical system and its virtual mathematical representation. These errors are either uncertain in quantity (e.g. random noise) or imprecisely represented. The error sources that may be considered to be the origin of measurement uncertainties for this profilometry system may be enumerated as follows:

A. Errors from the video projector: The video projector that was used was not specifically designed for optical profilometry applications; hence, it does not generate projections of structured lighting patterns precisely as designated. This is mainly because of the following:

   1. Imperfect light projection, in terms of noise introduced by the LCOS technology. Although the LCOS technology provides a higher fill factor than the DLP and LCD technologies, it still provides only a 90% aperture ratio (as explained in Section 5.1.1) and this can produce errors.
   2. Non-linear fringe pattern projection, which introduces errors to the measurement result in shape of ripples. However, this deficiency was significantly mitigated by correcting the gamma value of the fringe pattern before projection (as described in Section 7.2.1).
   3. Dissipated heat from the projector's lamp and electronic components, which causes drifts in image projection position and changes in light levels produced. This may have a great impact on the accuracy of the measurement. For the video projector that was used here a heat stability test was carried out (described in Section 4.2.2) and it was found that it has an effect on the repeatability of the measurement results of the system of ±0.092mm.

B. Errors due to the camera system: This includes both the camera sensor and lens. Since the camera sensor has a finite pixel size, the position of an imaged 3D point actually represents the averaging of the positions of many tiny points upon the object's surface; hence, the imaged 3D point that is generated may not lie exactly on its true position on the surface. In addition, electronic noise can be introduced into the acquired fringe pattern due to the quantization process of the analogue image intensity by the A/D converter of the CCD imaging sensor. A camera bit-depth of 8-bits (256 intensity levels) was used for analysis throughout this work. The error introduced by this quantisation level corresponds to an RMS error of 0.2nm (Robinson and Reid, 1993), which should be satisfactory for the profilometry applications of this system.

C. Imperfection in the chromatic filters: In order to minimise any potential chance for crosstalk amongst the sensors, each camera and projector set are

fitted with colour separation filters (as described in Section 5.1.3). However, these filters may suffer from thermal and photo-effect deterioration over time and this may give rise to a colour leak phenomenon leading to the possibility of crosstalk.

D. Errors due to the synchronisation triggers: This may occur in the cases when multi-sensor measurement mode is being employed. Although the custom designed synchronisation unit can provide a synchronisation error of the order of less than a microsecond (see Section 5.3), it is nevertheless possible that a mismatch between the measurement results from the three sensors may occur. This is mainly because an electronic response lag may be produced by the circuitries of either the camera, or the synchronisation unit.

E. Repeatability of the measurement: as discussed in Section 4.2.1 the precision of measurement is within ±0.353mm.

F. Change of ambient lighting illumination levels: This can introduce a measurement error with an average of up to 0.556mm (as will be discussed later in this chapter in Section 8.4.1).

G. Imprecise system calibration: Although the system is calibrated using empirical methods (that were described in Chapter 3), these methods do however depend upon the degree of the accuracy of the calibration equipment that is used (as discussed in Section 5.4). The errors within this class can be categorised as follows:

    1. Imperfection of the reference plane, including the degree of flatness of the calibration surfaces, and the degree of incline deviation of the calibration surface in both the horizontal and vertical axes.
    2. Imperfection in the elevation steps of the calibration table, which is nominally accurate to 1μm.
    3. Imperfection in the multi-sensor calibration, which addresses the degree of matching between the measurement results at corresponding regions of the object. As will be discussed later in Section 8.4.2, there is an average error of 0.072mm between the corresponding measurement regions of the left and middle sensors and an average error of 0.109mm between the middle and the right sensors.

8.4.1 Errors Due to the Change of Ambient Light Illumination Levels

The calibration process is performed in full darkness, i.e. without the presence of any ambient light, in order to avoid the possibility of introducing any invalid calibration data due to uncontrolled ambient lighting effects. At the measurement stage, and when using a higher ambient light level, the accuracy of the measurement results becomes sensitive to the level of object illumination and hence measurement errors may occur. Besides, common light sources (e.g. fluorescent room lights) suffer from a certain degree of fluctuation in intensity, e.g. mains frequency strobing, which may introduce errors into the measurements, especially in the case when the system is using the temporal phase shifting approach. Waddington and Kofman (2010) demonstrated that if the calibration was carried out under darkness (0 lux) and the measurement was performed under an ambient illumination level of 300 lux, then the measurement error that is introduced can reach a level of up to 0.7mm. Therefore, in order to avoid introducing any additional measurement errors, measurements should be performed under the same well controlled ambient light levels.

However, in some cases the change in ambient light level is inevitable, for example in cases where the profilometry application requires a different illumination level than the one that was used for calibration. To examine the effect of a higher ambient light level on the measurement results, a breast phantom cast (Figure 2.15) was measured (in the laboratory) firstly with the normal fluorescent room lighting switched off (i.e. exactly the same condition as was the case for the calibration stage) and secondly with the room lighting switched on. The fringe analysis methods employed for testing here were as follows; four-frame and seven-frame phase shifting algorithms, and FTP using the adaptive mode filtering. The reliability ordering algorithm was used for phase unwrapping. Under the different illumination levels, the average and standard deviation errors of the absolute 3D deviation maps between the measurements of the breast cast in the presence and absence of the ambient light are as follows:

Measurement Method	Average (mm)	SD (mm)
Four-frame Phase Shifting	0.169	0.223
Seven-frame Phase Shifting	**0.136**	**0.174**
FTP – Adaptive Mode	0.556	0.779

Table 8.6 The average and standard deviation errors of the absolute 3D deviation maps between the measurements of the breast cast in the presence and absence of the ambient light.

In order to avoid image saturation in the fringe pattern, the gain and exposure values of the camera can be adjusted (see Figure 4.8b). It can be noticed that the use of the seven-frame phase shifting method produced the smallest measurement errors, because it is less susceptible to noise than the four-frame method. For the purpose of the measurement of static objects, and depending on the accuracy requirements of the profilometry application, the errors introduced due to the changes in ambient illumination levels can be acceptable. On the other hand, for the purpose of measuring dynamic objects, this introduced error may be relatively high. Thus, it is recommended that the measurement of dynamic objects should be performed under exactly the same ambient lighting levels that were used for the calibration.

8.4.2 Errors Due to Imperfections in the Multi-sensor Calibration

Qualitatively, the generated 3D point clouds (using the multi-sensor measurement mode) appear to be visually well conformed and seem to accurately overlay each other. In addition to affording a visual inspection, this approach helps in a preliminary validation of calibration in order to check if the position of any of the components of the sensors has been altered between measurement sessions, or since calibration. However, an in-depth analysis was also carried out in order to quantitatively determine the degree of matching between the corresponding measurement regions of the individual 3D point clouds that are generated by different sensors.

The breast cast (Figure 8.1) was used here as a measurement example. The four-frame phase shifting method was used for fringe analysis and the reliability ordering algorithm was used for phase unwrapping. Figure 8.31 and Figure 8.32 show horizontal and vertical cross-sectional graphs across the centre of the three reconstructed surfaces of the object, respectively. Under the CAD environment, the 3D deviation map was calculated between the measurement results of the left and middle sensors (Figure 8.33), and between the middle and right sensors (Figure 8.34).

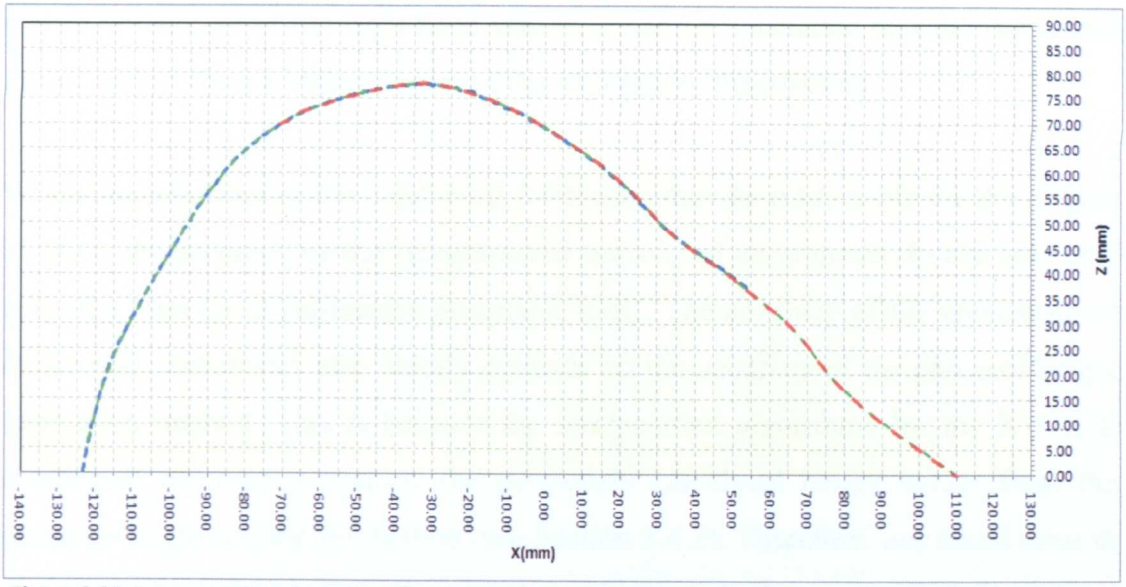

Figure 8.31 A cross-sectional graph of the three measurement results for the breast cast object, throughout the XZ-plane of the object's centre. Red, green and blue colours represent the left, middle and right sensors, respectively.

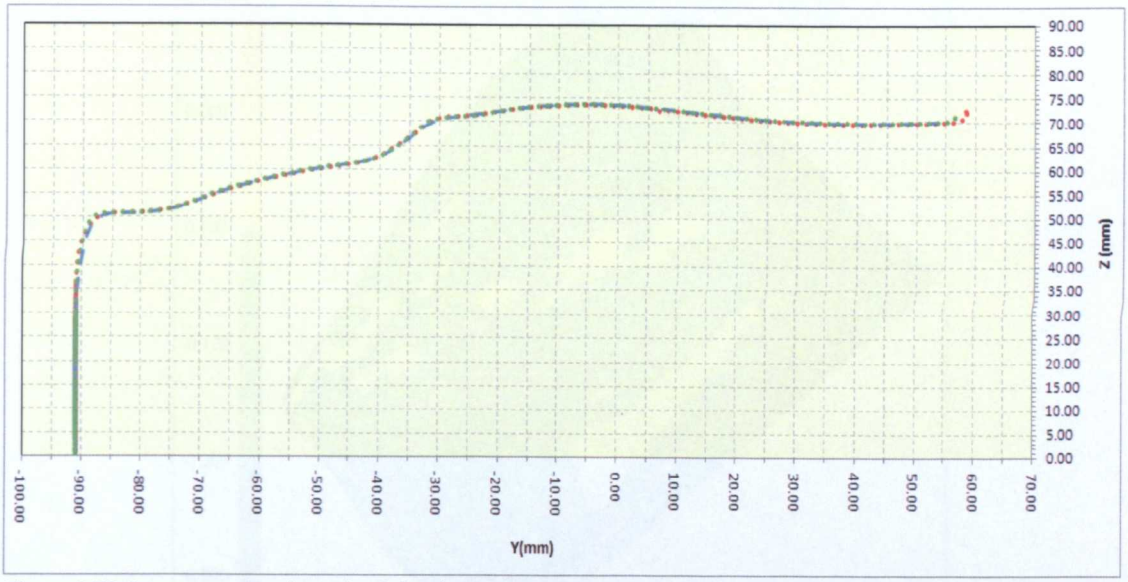

Figure 8.32 A cross-sectional graph of the three measurement results for the breast cast, throughout the YZ-plane of the object's centre. Red, green and blue colours represent the left, middle and right sensors, respectively.

The average and standard deviation errors of the absolute 3D deviation map between the 3D point clouds of the left and middle sensor were 0.072mm and 0.099mm, respectively. On the other hand, the average and standard deviation errors of the absolute 3D deviation map between the 3D point clouds of the middle and right sensor were 0.109mm and 0.148mm, respectively. Because the average error is

higher in the case of the right-hand sensor, it can be concluded that the right-hand sensor suffers from a higher degree of the calibration imperfection.

While imperfections in the transversal calibration may be responsible for this degree of error, the accuracy of the reconstructed transversal coordinates do not only rely upon the transversal calibration procedure itself. The accuracy of the reconstructed transversal coordinates also chiefly depends on the accuracy of the phase-to-height calibration method. This is because the interpolation algorithms for the X and Y transversal coordinates employ the previously calculated height values from the phase-to-height calibration method (see Section 3.4.2). Therefore, any small error in retrieving the height value of a point would also produce erroneous transversal coordinates at that point.

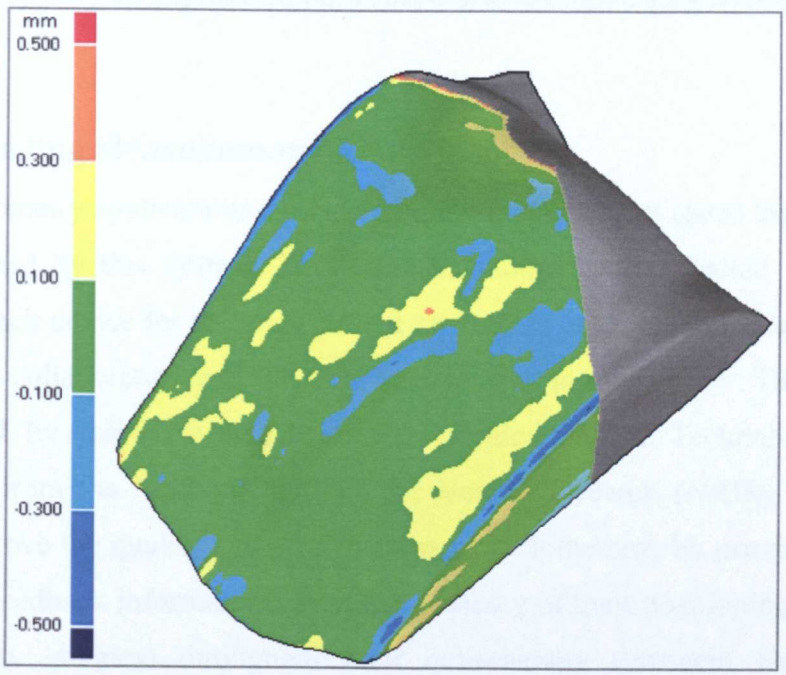

Figure 8.33 The 3D deviation map between the measurement results of the breast cast for the left and middle sensors, the grey colour represents unpaired surface regions of the breast cast.

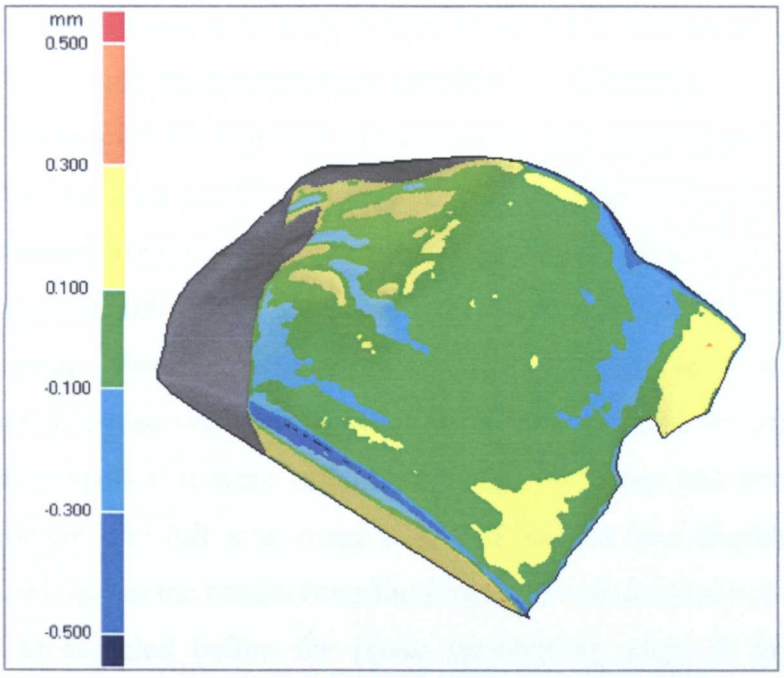

Figure 8.34 The 3D deviation map between the measurement results of the breast cast for the middle and right sensors, the grey colour represents unpaired surface regions of the breast cast.

8.5 Increasing Measurement Speed

Some profilometry applications demand a higher measurement speed than that which can be offered by this system. For instance, another project called "A real-time visual feedback device for reducing patient movement during radiotherapy" has been conducted in collaboration with The Christie Hospital in Manchester. The project has been funded by the New and Emerging Applications of Technology (NEAT) programme from the National Institute for *Health Research (NIHR).* The project aims to improve the quality and effectiveness of radiotherapy, by providing patients with visual feedback information about the accuracy of their positioning (usually via virtual reality goggles) throughout their radiotherapy treatment session, hence allowing them to positively cooperate in minimising their positioning error during treatment. Because it is vital that patients remain as still as possible during treatment, this project will allow them to assist in maintaining their position. For this critical purpose, and when using the reliability ordering algorithm for phase unwrapping, the normal speeds of measurement (~5.35Hz and ~4.5Hz for single-view and multi-view measurements, respectively) were not sufficient to achieve such near real time feedback.

The author's task here was to at least double the speed of measurement. The initial approach for enhancing the measurement speed was to subsample the full size fringe pattern by a factor of 2 (to 256×256 pixels) before it is dispatched into the whole processing pipeline. This simple approach also required the sub-sampling of the X, Y and Z calibration volumes. This enormously increased the measurement speed to ~27.0Hz using the adaptive FTP method and the reliability ordering unwrapper for a single-view mode. However, fringe coalescence occurred in some cases and generated erroneous measurements. Besides, it was difficult to locate the positions of the triangulation spots that were embedded within the fringe patterns. In order to solve this problem, the full size image (512×512 pixels) was dispatched into the processing pipeline, but the results from the fringe analysis method (i.e. the wrapped phase) was sub-sampled before the phase unwrapping stage of the processing pipeline. Because of this use of sub-sampling, the spatial resolution of the reconstructed surface will obviously be reduced when compared to measurements produced using the full image resolution. Hence, the quality of measurement will be compromised to some degree.

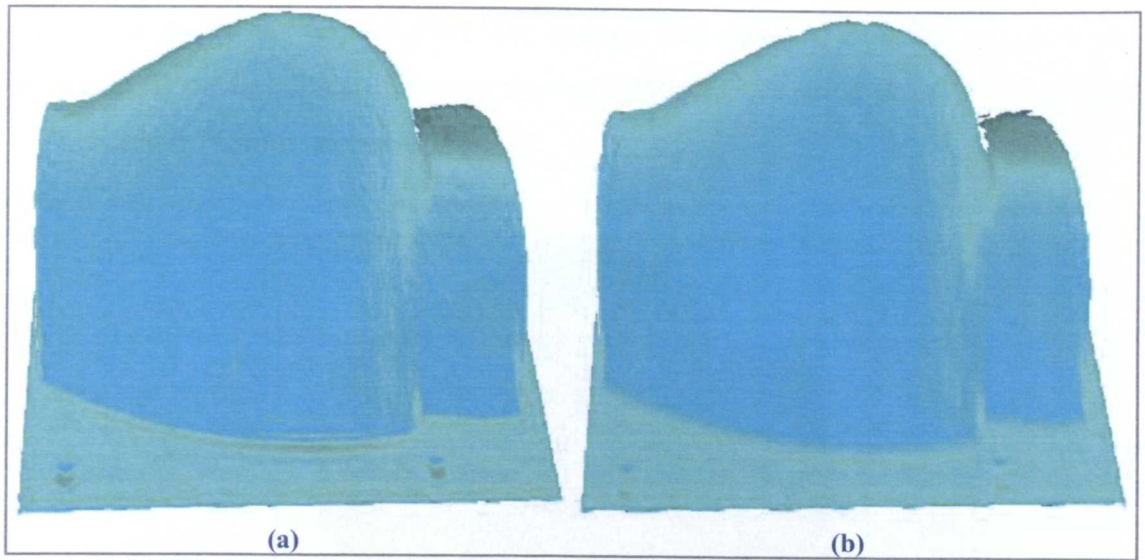

***Figure 8.35** Perspective* **views of the measurement results using the four-frame phase shifting method: (a) with standard resolution (512×512 pixels), (b) with *sub-sampled resolution* (256×256 pixels).**

The measurement speeds that were achieved using the adaptive FTP method and the reliability ordering unwrapper for a single-view mode of the sub-sampling technique was 19.27Hz. On the other hand, for the multi-view measurement mode this was increased to ~9.7Hz. In order to investigate the effects of the sub-sampling technique

upon the accuracy of the measurements, the breast cast (Figure 8.1) was measured using both the normal full resolution and the sub-sampled methods, respectively. The four-frame phase shifting method was used here for fringe analysis and the reliability ordering algorithm was used for phase unwrapping. Figure 8.35(a-b) shows the measurement results for the breast cast using the normal and sub-sampled resolutions, respectively.

It can be noticed from the reconstructed 3D point clouds that the standard resolution method provides higher levels of the object's surface detail than is the case for the sub-sampling method. Figure 8.36 shows how the 3D point clouds of both measurements overlay each other, which implies that the processes of phase unwrapping and the phase-to-coordinates conversion did not have a major impact on the sub-sampled fringe pattern. To determine the degree of the measurement error that is introduced by the sub-sampling technique, the 3D deviation map between the two measurements was calculated and this is shown in Figure 8.37. It is apparent that major errors are introduced in the sub-sampled dataset at the surface regions that exhibit sharp features and such features appear to have been blurred, or low-pass filtered (a shown in Figure 8.35b). The average and standard deviation errors of the absolute 3D deviation map between the two different resolution measurements were 0.1mm and 0.168mm, respectively.

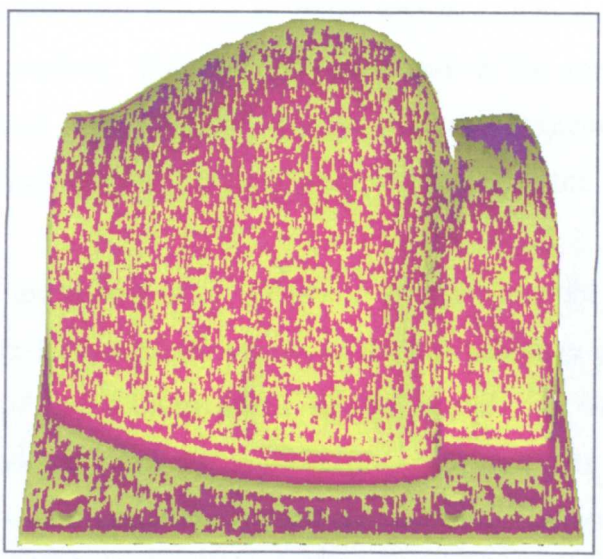

Figure 8.36 A perspective view for the measurement result using the sub-sampling technique (in purple) of the breast phantom cast and its corresponding measurement result using standard resolution (in yellow).

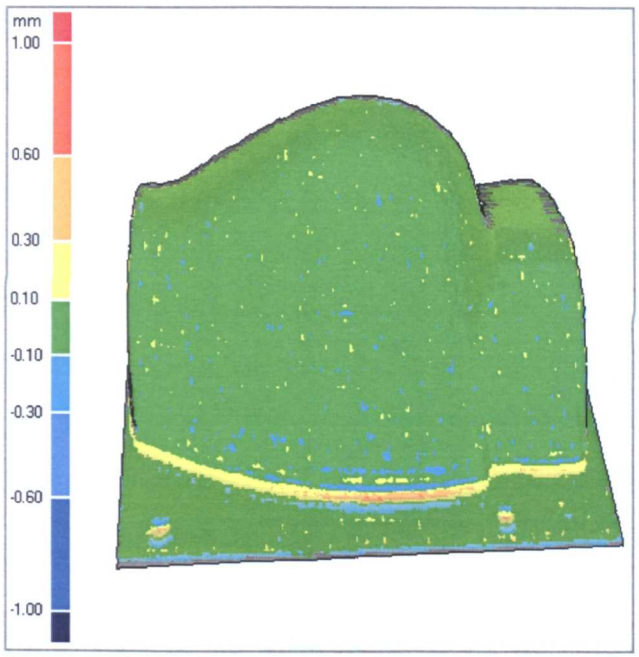

Figure 8.37 The 3D deviation map between the measurement result using the sub-sampling technique and the measurement result using standard resolution imaging for the breast cast, where the grey colour represents the reference surface of the breast cast.

8.6 Discussion

This chapter has presented a logical sequence of experimental results that have gradually increased in terms of measurement complexity and difficulty. Measurement of static objects using the four-frame phase shifting method proved to offer reliable measurement accuracy with an average error of 0.09mm and with 99.36% of the reconstructed 3D points lying within a tolerance band of ±0.5mm from the reference surface. This method succeeded in the measurement of more complicated shapes of static object's, such as the owl porcelain figurine and the computer keyboard examples that were presented in this chapter.

On the other hand, measurement of dynamic objects (using the proposed adaptive filtering mode of the FTP method) compromised the accuracy of the measurement system in favour of speed. Regardless of the complexity of the object being measured, the rendered outliers significantly affected the accuracy of the measurement results, and compromised the accuracy of the merged surface of the measurement results when using the multi-sensor approach. If a robust merging algorithm were to be employed, in terms of avoiding measurement outliers and preserving good measurement results at the intersecting object surface regions that

are covered by different sensors, this would provide more accurate combined measurement results. However, because the process of merging the individual sensor surfaces together is not one of the issues that was addressed in this research programme, the errors that were introduced by these outliers was included within the analysis. Because of the presence of such measurement outliers, the average error was not a reliable index for the overall measurement accuracy. Hence, the percentage number of points located within a tolerance band of ±0.5mm and ±1.0mm from the reference surface was used instead. The percentage number of points varied between 54.40%-80.54% within a tolerance band of ±0.5mm, and between 81.75%-95.66% within a tolerance band of ±1.0mm.

It should be noted that even in the worst scenario for the measurement results of dynamic objects (the female mannequin with an average error of 1.68mm), the measurement system is still very useful for applications such as the Metrology Guided Radiotherapy. This is because the highest average error (of 1.68mm) is still less than a fifth of the radiotherapy Planning Target Volume or PTV (Figure 4.29) linear discrepancy, which is usually estimated to extend 10mm beyond the boundary of the clinically outlined Gross Tumour Volume (Bomford and Kunkler, 2002).

The proposed adaptive FTP method was the fringe analysis algorithm that was used for the measurement of dynamic objects. This is because it provides higher measurement reliability than the other adopted spatial fringe analysis methods, in terms of accuracy and speed. The method has shown significant levels of reliability in the measurement of objects with steep surface curvature and features such as body hair. In addition, it was designed to generate surface texture and mask maps. The texture mask can have an important role in tracking surface marks and features, and the mask map has a great impact on the behaviour of the phase unwrapping process in terms of both speed and quality. It must be born in mind that the other spatial fringe analysis methods that were adopted and implemented in the measurement system (the WTP and the classical FTP methods), though not reviewed in detail here, are still available to be used for profilometry applications other than the ones that were discussed in Chapter Four. The accuracy analysis of the proposed adaptive FTP method has been discussed in this chapter and it was shown that choosing a higher level of details for processing usually provides more accurate results. However,

using a lower level of details for processing eliminates the introduction of measurement errors in cases when measuring objects with surface marks, hair or highly reflective surface features.

A wide range of possible error sources have been considered in this chapter, in addition to the errors caused due to changes of the illumination levels of the ambient light and imperfections in the multi-sensor calibration. It has been shown that using the seven-frame phase stepping algorithm for fringe analysis is less susceptible to changes in ambient lighting illumination levels than is the case when using both the four-frame phase stepping and FTP algorithms. It has also been shown that the average error between the measurements of the left and middle sensor was 0.072mm, and between the middle and the right sensors was 0.109mm.

Finally, the approaches for increasing the measurement speed have been addressed and it has been explained that the adopted approach of sub-sampling the resultant wrapped phase of the fringe analysis results by a factor of 2 did efficiently enhance the system's measurement speed. The measurement speed was increased by 2.16 times using the multi-view mode and by 3.6 times using the single-view mode. However, the sub-sampling approach compromised the measurement accuracy in favour of this speed increase. It has been shown in this chapter that the higher speed sub-sampling approach introduced an average error of 0.1mm to the measurement results.

8.7 References

3DRESHAPER. 2010. *3DReshaper Application* [Online]. 3dreshaper.com. Available: http://www.3dreshaper.com/en1/En_software.htm [Accessed 2 Apr 2010].

BOMFORD, C. & KUNKLER, I. 2002. *Walter & Miller's Textbook of Radiotherapy: Radiation Physics, Therapy and Oncology*, Churchill Livingstone.

NVISION. 2008. *NVision 3D laser scanner* [Online]. nvision3d.com. Available: http://www.nvision3d.com/nvision-products.html [Accessed 2 May 2008].

ROBINSON, D. & REID, G. T. 1993. *Interferogram Analysis, Digital Fringe Pattern Measurement Techniques*, Taylor & Francis.

WADDINGTON, C. & KOFMAN, J. 2010. Analysis of measurement sensitivity to illuminance and fringe-pattern gray levels for fringe-pattern projection adaptive to ambient lighting. *Optics and Lasers in Engineering,* 48, 251-256.

Chapter Nine

Conclusions and Recommendations for Further Work

This chapter presents the conclusions that have been drawn from this programme of research. As part of these conclusions, the main novel intellectual contributions are also highlighted. In view of these conclusions, recommendations for further research in this field are subsequently suggested.

9.1 Conclusions

This research programme has successfully produced a practical 3D optical surface shape measurement system that is based on fringe projection/analysis. The system features real-time (in the context of the timescales associated with radiotherapy), multi-sensor and multi-purpose capabilities. The key advantages of the system are summarised as follows:

- Single, or multi-sensor, modes of measurement available to the user, that are adaptable to the specific requirements of a desired application. Using the single-sensor mode produces a single-view using one of the three sensors. Alternatively, by performing measurements using the multi-sensor mode a larger measurement area may be covered. This provides a multi-view measurement using the three sensors acting cooperatively together and achieves a greater overall measurement speed for the measurement of the entire object due to the inherently parallel measurement.
- A wide-ranging catalogue of fringe profilometry methods and techniques that are available to the user, which enables the reconstruction of 3D information through user selection of 183 different possible main combination paths. In addition, each fringe analysis method has its own set of interactively modifiable processing parameters, in cases when it is critical for the application that a specific fringe profilometry method is employed.

- High degree of flexibility to fit the measurement requirements of various profilometry applications, including both static and dynamic, and full and partial-field surface measurement applications.
- Measurement reliability: The accuracy of the measurements produced by the system has been verified against a set of Coordinate Measuring Machine (CMM) and Computed Topography (CT) scan data.
- Measurement robustness: The measurement process is stable and does not crash during the performance of a measurement, having been tested exhaustively during this programme of research.
- Measurement reproducibility: The measurement system has been implemented and tested upon two different hardware platforms at two different geographical locations, in the GERI laboratories and also in a radiotherapy treatment room at the Christie Hospital.
- The modular structure of the software (as discussed in Chapter Six) that offers the ability to achieve a desired 3D surface measurement for a specific application in the most efficient manner possible that is available for a given set of hardware resources.
- A visual and interactive design, which enables the operator to interact with the system and to select the best possible combinations of processing methods and their parameters in order to meet the measurement requirements of an intended application.
- Real-time display of the results of both the final reconstructed 3D surface and if desired the underlying processing stages. This provides the user with the results of each stage of processing interactively and facilitates in the process of selecting amongst the best combinations of measurement methods.
- Off-the-shelf hardware components with a cost of less than £30,000. Besides, the components of the sensors have proved to be resistant to radiation damage and are still fully functional after spending a period of more than two years in a working radiotherapy treatment room.

The general measurement specifications for the measurement system, with a camera ROI resolution of 512×512 pixels and a projector display resolution of 1024×768 pixels, are as follows:

Z accuracy	< 0.5 mm
Z Precision (see Section 4.2):	
Repeatability	± 0.353 mm
Reproducibility	± 0.452 mm
Heat stability	± 0.092 mm
Number of sampled XYZ points	> 260,000 x,y,z points per sensor > 780,000 x,y,z points for all sensors
Measurement speed	≤ 12 Hz for single-view measurement ≤ 6 Hz for multi-view measurement
Number of measured XYZ points/second	≤ ~3.0 million x,y,z points/sec per sensor ≤ ~4.6 million x,y,z points/sec for all sensors
Field of view	≤ 400 mm × 660 mm
Spatial resolution XY mm/point	≤ 0.78 mm × 1.3 mm per x,y point
Coverage area	~220° around the object's volumetric centre
Maximum measurable body curvature	88° using single-sensor (See Appendix A3) > 90° using multi-sensor

The flexibility and high accuracy of the system have been demonstrated by extensive real experiments. The common sources of errors are identified in Section 8.4, along with their respective significance. It was concluded that any imperfections in the multi-sensor calibration procedure can produce a typical average error of 0.109mm. Finally, measurement speed can be enhanced still further via sub-sampling the wrapped phase (i.e. the result of the fringe analysis method) before the phase unwrapping stage of the processing pipeline. This approach also required the sub-sampling of the X, Y and Z calibration volumes. By sub-sampling the full resolution fringe pattern (512×512 pixels) by a factor of 2 (to give a sub-sampled resolution of 256×256 pixels), the measurement speed was increased to 19.27Hz using the single-sensor mode and to ~9.7Hz using the multi-sensor mode. However, the sub-sampling approach did introduce an additional measurement error with a typical average error of 0.1mm.

9.1.1 Intellectual Contributions

In this research programme the author has made the following main intellectual contributions:

- **Framework for multi-view optical profilometry system**: The thesis presents a novel fundamental structure for the purpose of performing multi-view measurement using fringe projection/analysis, including the associated hardware and software structures, camera synchronisation, crosstalk reduction, and whole system integration.
- **Platform for multi-purpose optical profilometry system**: The thesis presents a comprehensive framework for producing a novel interactive optical profilometry system that can be used and manipulated to fulfil the measurement requirements of a wide variety of profilometry applications.
- **Transversal calibration procedure**: This thesis proposes an advanced transversal calibration method, with sub-pixel accuracy to produce more accurate results. The proposed transversal calibration method also produces absolute X and Y world coordinates (relative to the same central X and Y axes for all sensors), which creates conformed 3D measurement results from all three sensors.
- **Adaptive filtering approach for the FTP method**: This thesis proposes a state-of-the-art adaptive filtering technique for the FTP method, which is used to extract the modulated phase component of the fringe pattern within the frequency domain. The technique avoids the complexity of the relatively small number of existing attempts at producing adaptive filters and uses only a single parameter, which indicates the required level of details (an integer value within a range of 0 to 4) which are desired to be extracted using the filter. At the same time, the technique is able to generate both texture and mask maps within the same process.
- **Triangulation spot restoration**: This thesis presents a method to synthetically restore the locations of the triangulation spots as a pre-processing stage, in order to avoid measurement errors that are rendered due to the embedded spot's presence within the compound source fringe patterns.

9.2 Recommendations for Further Work

Several of the recommendations for further work that are made here are actually being implemented to some degree at the moment, or are planned to be implemented in the near future. This includes the speed and accuracy enhancements when measuring dynamic objects (as discussed in Section 8.5). However, there is a broad set of further research issues that may be conducted and which could achieve a significant further enhancement to the current optical profilometry system. These research areas are mainly as follows:

- Implementation and integration of other fringe profilometry methods, such as: Windowed Fourier Transform Profilometry and Temporal Phase Unwrapping.
- Implementation and integration of Spatial Phase Shifting (SPS) methods, which may improve the accuracy and speed of measurement. SPS methods have been addressed in the literature (Guan *et al.*, 2006, Salvi *et al.*, 2010), where only a single composite fringe pattern is usually used to accommodate the multiple fringe patterns of the three-frame or the four-frame phase shifting methods.
- More improvements on the adaptive filtering technique for the FTP method, which may produce a fully adaptive filter without the need for the level of detail parameter that is currently used. This may be implemented as a pre-measurement stage to automatically detect the level of detail value with the lowest SNR ratio and would then use that parameter for the measurement process.
- Implementation and integration of a surface merging algorithm, which can successfully detect valid measurement points within the corresponding measurement regions for the multi-view measurements, and therefore aids in avoiding the use of invalid measurement points within the surface integration process.
- Re-engineering the projector, in terms of controlling the internal circuitry of the projector that is responsible for pre-processing and therefore increasing the speed of projection. Moreover, re-engineering the cooling system for the projector in order to provide greater heat stability measurement for the measurement, and also re-engineering the projector's lens to allow projection

of finer fringes with necessarily smaller field of view (i.e. making lens assembly physically larger in order to decrease divergence).

9.3 References

GUAN, C., HASSEBROOK, L. G., LAU, D. L. & YALLA, V. 2006. Near-infrared composite pattern projection for continuous motion hand-computer interaction. *Journal of Visual Communication and Image Representation,* 18, 141-150.

SALVI, J., FERNANDEZ, S., PRIBANIC, T. & LLADO, X. 2010. A state of the art in structured light patterns for surface profilometry. *Pattern Recognition,* In Press, Accepted Manuscript.

Appendix

A1 Trajectory Mask Construction for the Triangulation Spot

The trajectory mask is an important element in the process of detecting the location of either single, or multiple, triangulation spots that are embedded within source fringe patterns, because it masks out areas that may be excluded from the spot detection process. It therefore enables more reliable detection of any embedded triangulation spots that are present within the fringe pattern images. The algorithm that was used for constructing the trajectory mask is the same for both the single-spot and multi-spot forms, which is as follows:

1. The X and Y locations that are detected for each spot are used to build up the trajectory mask. This is formed by superposing the individual spot loci for each spot that is embedded within the image. An individual spot's trajectory locus is computed from the locus of its relative position upon a horizontal calibration plane as this changes throughout the process of the plane being translated in a number of discrete height steps over the entire calibration range. The maximum X and Y deviations between each spot's positions in consecutive height steps are calculated for each spot for the whole number of discrete height steps of the elevation table throughout the entire calibration range.
2. The spot locations are set within a black, zero intensity, image frame (see Figure A1.1), with intensity values of 255 (white) denoting the spot trajectories. The size of the black image frame is equal to the measurement image frame dimensions (usually 512×512 pixels).
3. A morphological image processing operation is applied to the resultant image, using a dilation process, in order to enlarge the boundaries of the spot trajectories. The size of the dilatation kernel is defined according to the maximum X and Y deviations for all spots which were obtained in Step 1; where the horizontal kernel size is set to the maximum X deviation and the vertical kernel size is set to the maximum Y deviation. Figure A1.2a shows the result of the dilation, which is used as the trajectory mask.

The trajectory mask is used to determine the *rectangular detection ROI (as shown* in Figure A1.2b) that will be used to locate each spot within the spot-embedded fringe pattern images. The dimensions of each spot's detection ROI is determined by using

the top-left and the bottom-right edges of each individual trajectory mask. The detection ROI for each spot is expanded by an error margin in order to increase the probability of spot detection. The error margin is selected such that it provides a better coverage for spot detection, although it must ensure that the ROIs of the spots do not intersect with each other when in multi-spot form.

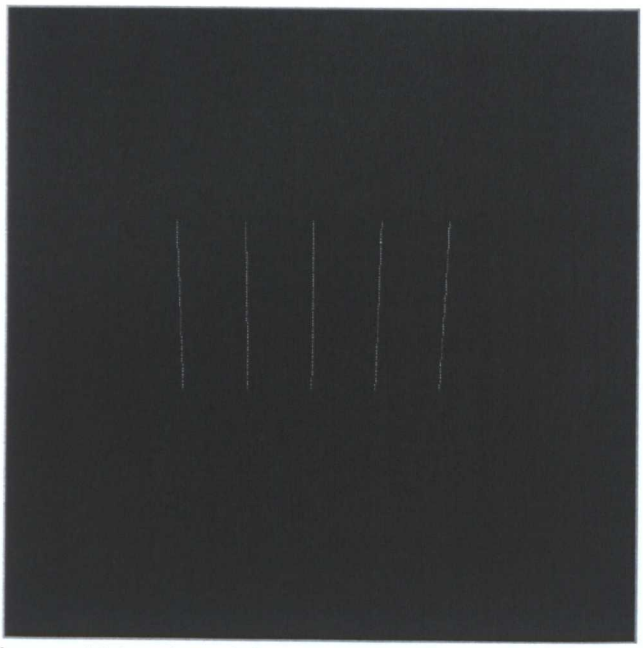

Figure A1.1 the black image with locations of the trajectories of each detected spot (here for five spots) as they move vertically over various elevated planar heights throughout the entire calibration range.

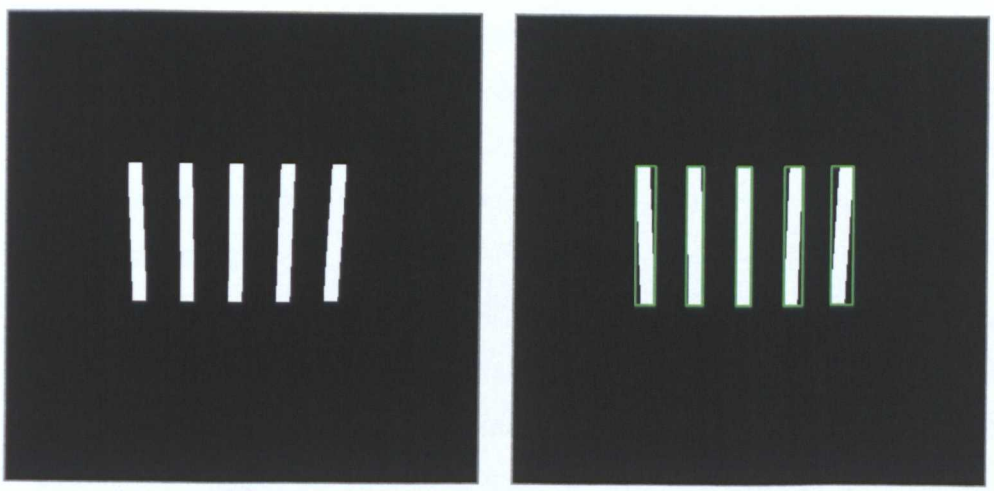

(a) (b)

Figure A1.2 The generated trajectory mask (a), and the rectangular detection ROIs of the spots (b) that are determined from image (a)

A2 Triangulation Spot Visibility Enhancement

This section presents the image processing techniques that were used to enhance the visibility of the embedded triangulation spot within the acquired fringe pattern. The process of triangulation spot visibility enhancement is the same for both the single-spot and the multi-spot forms (which were discussed in Section 3.2).

Figure A2.1 Sample fringe pattern with embedded triangulation spots.

The process of visibility enhancement is as follows:

1. The acquired fringe pattern is smoothed (usually using a mean filter), to reduce noise by eliminating any intensity values that are unrepresentative of their surroundings. Typically, a kernel window with a size of 5×5 pixels is used here. Figure A2.2a shows the smoothed output of the sample image that is shown in Figure A2.1.
2. Laplacian filtering is then applied to the output of the smoothing filter, in order to enhance (sharpen) areas of rapid intensity change within the image (Figure A2.2b). Typically, Laplacian filtering is applied by sliding a convolution kernel (of size 2×2) over the image, and the kernel used for this purpose is;

$$\begin{bmatrix} 1 & -1 \\ 1 & -1 \end{bmatrix}$$

3. Matched filtering is applied to the result of the Laplacian filtering in order to increase the SNR ratio and hence to enhance the peaks within the image (Figure A2.2c). For this purpose the following convolution kernel (of size 6×6) is applied to the output of the Laplacian filtering;

$$\begin{bmatrix} -1 & -1 & -1 & 1 & 1 & 1 \\ -1 & -1 & -1 & 1 & 1 & 1 \\ -1 & -1 & -1 & 1 & 1 & 1 \\ -1 & -1 & -1 & 1 & 1 & 1 \\ -1 & -1 & -1 & 1 & 1 & 1 \\ -1 & -1 & -1 & 1 & 1 & 1 \end{bmatrix}$$

4. The output of the matched filtering is multiplied by the multi-spot trajectory mask (shown Figure A2.2d), and the result (shown Figure A2.3) is used to detect the locations of the spots as *illustrated in Section 3.2.*

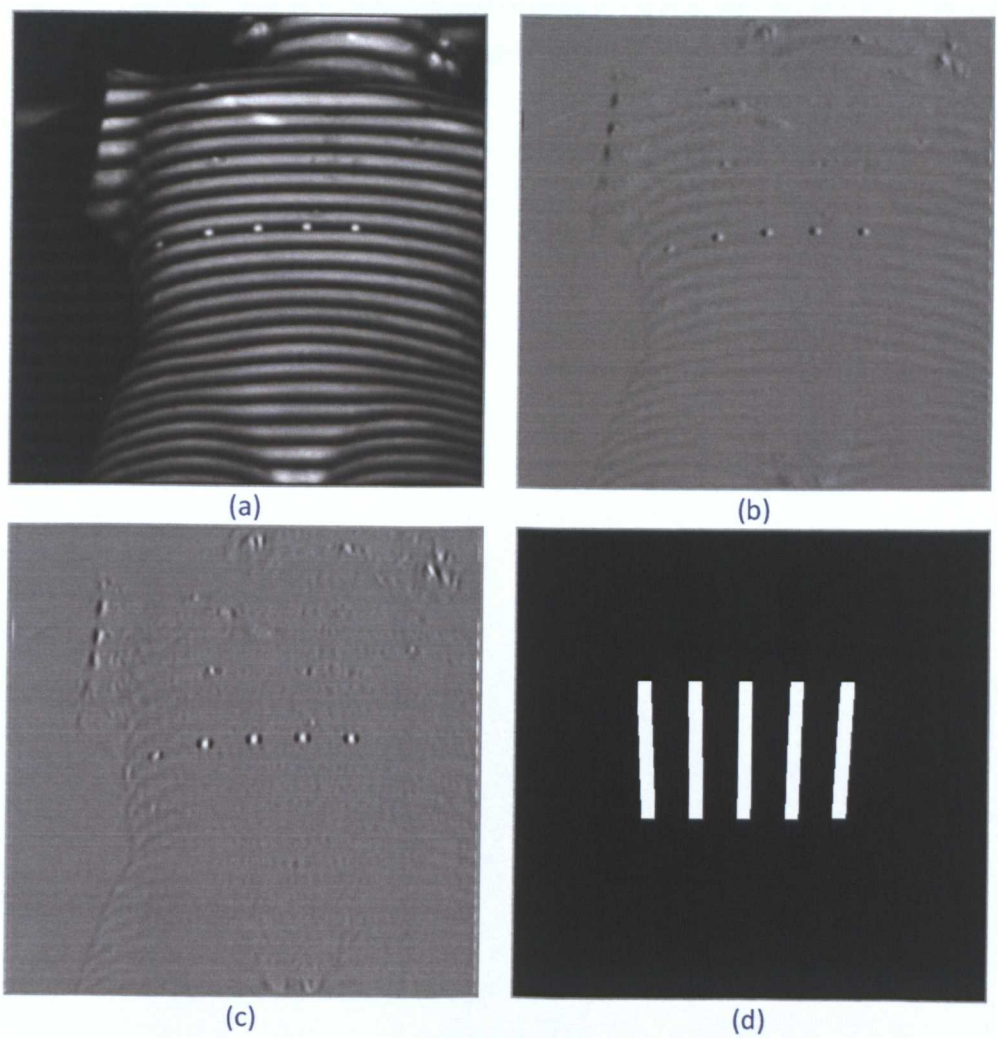

Figure A2.2 Triangulation spot visibility enhancement process: (a) the result of applying the mean filter to the sample image, with a kernel size of 5×5, (b) the result of applying the Laplacian filter to the output of the smoothing filter, with a kernel size of 2×2, (c) the result of applying the matched filter to the output of the Laplacian filter, with a *kernel size* of 6×6, (d) the corresponding trajectory mask for the triangulation spots.

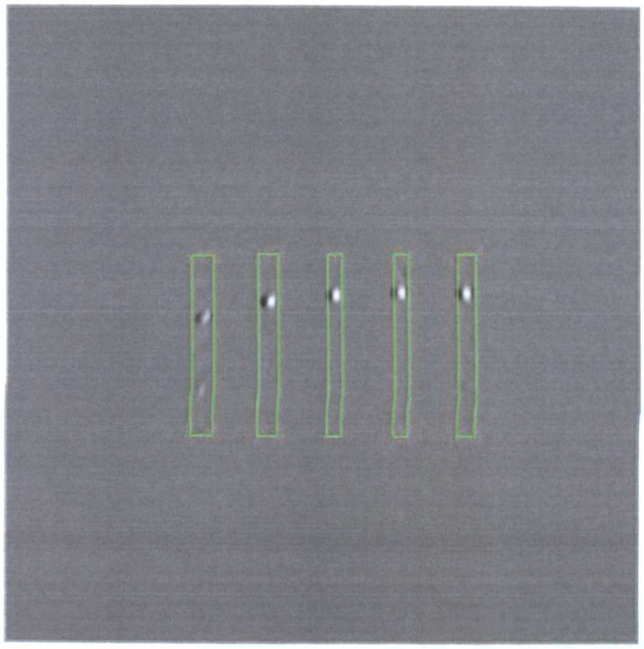

Figure A2.3 The resultant image after multiplication the result of the matched filter with the trajectory mask image and with the rectangular detection ROIs overlaid.

A3 Analysis of Maximum Measurable Body Curvature Using a Single Sensor

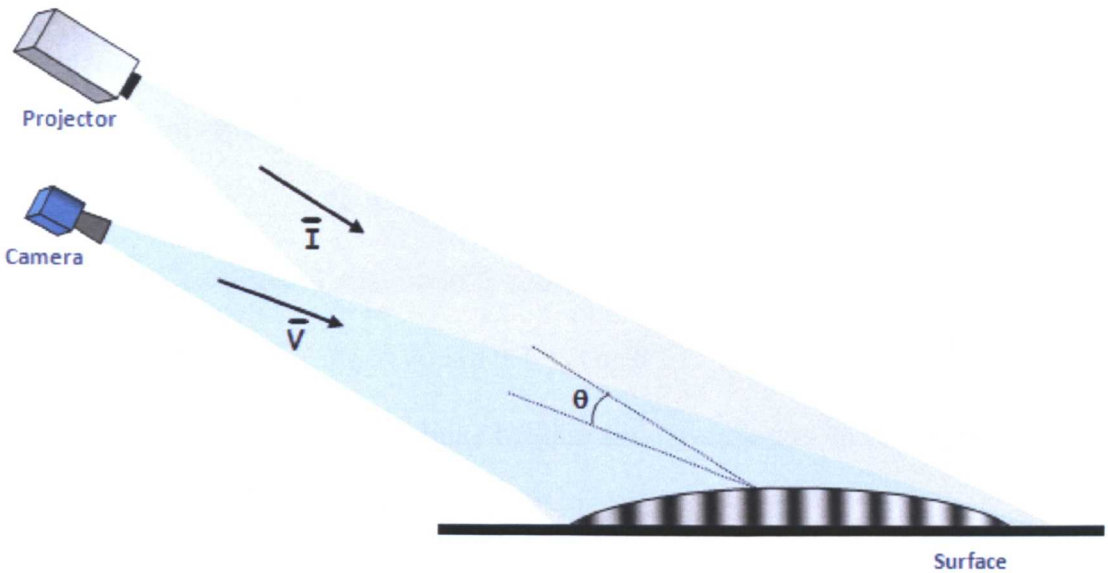

Figure A3.1 Basic optical system geometry.

The camera is considered to be off-axis from the direction of illumination by an angle θ.

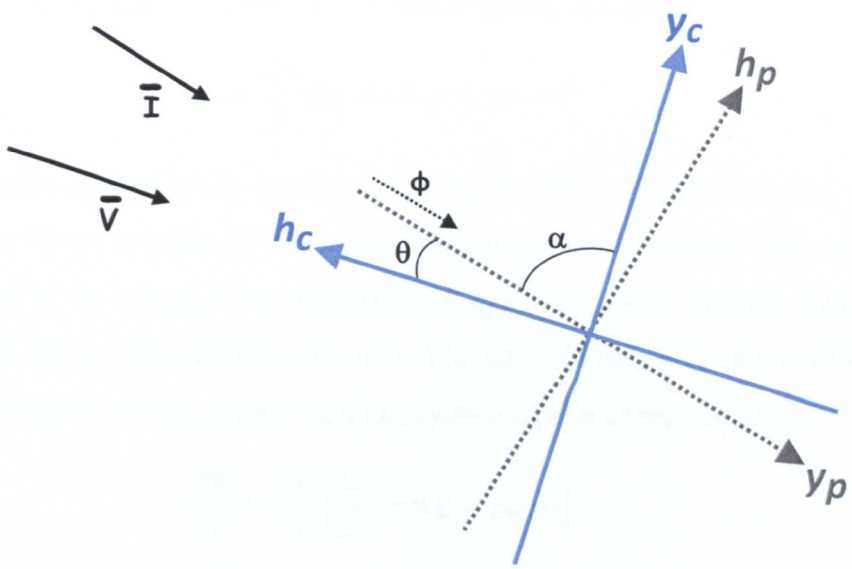

Figure A3.2 Representative vector geometry.

This diagram shows that we have two separate co-ordinate systems. The first is based with respect to the projected fringes and is represented by the axis set (h_p,y_p),

which is aligned with the vector $\bar{\mathbf{I}}$. The second co-ordinate system is based with respect to the viewing camera and is represented by the axis set (h_c,y_c), which is aligned with the vector $\bar{\mathbf{V}}$.

So, by using the standard formula from vector geometry for the rotation of two axis sets about a common origin, we may derive the following equation:

$$h_p = h_c \cos \propto + y_c \sin \propto \qquad \textbf{(A3.1)}$$

Adjusting the equation in relation to θ, results in the following equation:

$$h_p = h_c \sin \theta + y_c \cos \theta \qquad \textbf{(A3.2)}$$

This equation is important as it links heights and co-ordinates in the camera system to the projection system.

If at some particular flat surface, the fringe spacing 'p' was constant across the field of view, then the height could be linked to the phase of the fringe pattern, and as follows:

$$h_p = \frac{\emptyset\, p}{2\pi} \qquad \textbf{(A3.3)}$$

Equating Equations(A3.2) and (A3.3) eliminates h_p and gives:

$$\emptyset = \frac{2\pi}{p}[h_c \sin \theta + y_c \cos \theta] \qquad \textbf{(A3.4)}$$

Although the system being developed for this research programme does not produce a constant fringe spacing 'p' across the field of view, the analysis here will deal with a constant 'p' as it makes the mathematics somewhat more straight forward and the result will not be significantly affected. The rate of change of phase with respect to the y co-ordinate of the camera viewing system can be expressed as:

$$\frac{\delta \emptyset}{\delta y_c} = \frac{2\pi}{p}\left[\frac{\delta h_c}{\delta y_c} \sin \theta + \cos \theta\right] \qquad \textbf{(A3.5)}$$

The Nyquist criterion requires that it is necessary to sample the fringe pattern at least twice in each sample. However, in practice six samples per fringe is the minimum sampling rate that is required to produce a reliable 3D surface reconstruction. For a field-of-view with a distance of 400mm along the Y-axis, sampled by 512 pixels,

1pixel = 400/512 = 0.78mm. As a conservative estimate, a distance of 6mm for y_c actually represents just over 7 pixels. Thus, we have;

$$\frac{2\pi}{6} = \frac{2\pi}{p}\left[\frac{\delta h_c}{\delta y_c}\sin\theta + \cos\theta\right] \qquad \textbf{(A3.6)}$$

Fringe spacing of the projected fringe pattern p = 22.28mm (26 pixels) and $\theta = 4.8°$. Substituting values;

$$\frac{\delta h_c}{\delta y_c} \cong 28.48 \qquad \textbf{(A3.7)}$$

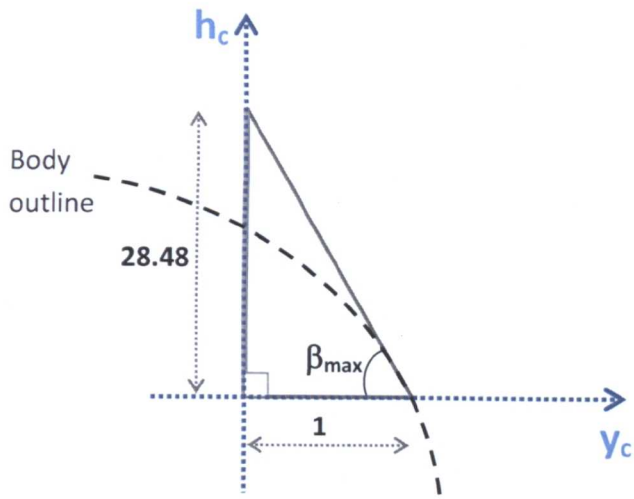

Figure A3.3 Optical geometry.

Thus, considering Figure A3.3, the angle of maximum body curvature that can be measured is given by:

$$\beta_{max} = \tan^{-1}(28.48) \cong 88°$$

β_{max} was measured from the y_c datum plane. For the middle fringe across a horizontal fringe pattern, $\beta_{max} = 88.7°$, whereas theoretically for angles any greater than this, fringe coalescence will occur.

Practically, when measuring tangential surfaces, measurement quality falls off significantly before this theoretical angel of body curvature. This is because when the projected light is tangential to the object's surface, the spatial fringe period becomes infinite, which causes phase distortions and therefore measurement errors.

Tangential regions are typically located near the boundaries of shadowed areas that are insufficiently illuminated by the projector. However, when using the multi-sensor approach for measurement, the regions of an object that are insufficiently illuminated by an individual projector, can be adequately illuminated by another projector and hence produce a valid measurement. Therefore, by using the measurement system in multi-sensor mode it is possible to practically provide a maximum measurable body curvature of $> 90°$.